Thesis for the degree of Doctor from UNIVERSITÉ POLYTECHNIQUE HdF and INSA HdF
Speciality: Micro-nano systèmes et capteurs

Presented by: Victory ELIAS

Doctoral school: École Doctorale Polytechnique Hauts-de-France (ED PHF)

Research team, Laboratory: MAMINA Group, IEMN Valenciennes site

---

An approach based on the μ-vibration concept contributes to the characterization and objective analysis of physiological fluids.

Une approche basée sur un concept de μ-vibratoire pour contribuer à la caractérisation et l'analyse objective des fluides physiologiques.

JURY

Rapporteurs:

Prof. Maryam Siadat, University of Lorraine.

Prof. Norbert Noury, University of Claude Bernard - Lyon.

Examiners:

Prof. Eric Campo, University of Toulouse 2 (Jury President).

Prof. Stéphane Serfaty, University of Cergy Pontoise.

Dr. Jacques Verdier, INSA Lyon.

Guests:

Prof. Emmanuel Dubois, University of Lille.

Prof. Philippe Champagne, INSA HdF.

Dr. Fabrice Lefebvre, INSA HdF.

Thesis Director:

Dr. Nassar Georges, INSA HdF.

Date and Place of the Defense:

Wednesday 20, December 2023, at IEMN, Valenciennes.

© 2023 by Victory Elias is licensed under CC BY-NC-SA 4.0.

Dedications

I want to dedicate this work:

To my family, whose unwavering support and encouragement have been my pillars of strength throughout this challenging journey.

To my friends, for their camaraderie, understanding, and occasional distractions that kept me sane.

To my mentors and advisors, for their guidance, wisdom, and the invaluable lessons they have shared with me.

And to all those who believe in the power of knowledge and the pursuit of excellence, this thesis is dedicated to you.

Thank you for being a part of this remarkable chapter in my life.

Acknowledgments

I would like to express my deepest gratitude to my supervisor, Mr. Nassar, for their unwavering support, guidance, and mentorship throughout my PhD journey. Their expertise and encouragement have been invaluable in shaping my research and helping me grow as a scholar.

I would also like to acknowledge the Minister of Health and Prevention of France for their generous financial support, which made this research possible.

I am grateful to my partner, colleagues, friends, and family for their love and support, which kept me going through the ups and downs of my Ph.D.

Special thanks go to Mr. Philippe CHAMPAGNE, M. Emmanuel DUBOIS, M. Frederic RIVART, M. Nikolay SMAGIN, and Mme Flavie BRAUD for their invaluable contributions to my research. I am deeply appreciative of their time and effort in helping me gather the data for this thesis.

Finally, I would like to extend my sincere gratitude to IEMN CNRS for providing the resources, facilities, and equipment that were essential to the completion of this research.

Contents

1 State-Of-The-Art: Literature Reviews **1**

1.1 Background and motivation . . . 1

1.1.1 Early Detection And Lifestyle Changes For Prevention . . . 2

1.1.2 Novel Genes . . . 4

1.2 Microcantilever as the Chosen Sensor . . . 6

1.2.1 Applications Of Cantilever Micro-beams . . . 10

1.2.2 Scope of applications . . . 10

1.3 MEMS Sensors . . . 12

1.3.1 MEMS Fabrication Techniques . . . 14

1.3.2 Sensing Applications . . . 16

1.4 BioMEMS Sensors . . . 18

1.4.1 BioMEMS Technology Setup . . . 20

1.5 Microcantilever Sensor: Design & Characterization . . . 22

1.5.1 Microcantilever Manufacturing . . . 22

1.5.2 Physical characteristics . . . 23

1.5.3 Working Principle of Micro-cantilever Sensors . . . 25

1.5.4 Micro Cantilever Array Approach . . . 27

1.5.5 Limitations and Challenges . . . 33

2 Modeling approach **46**

2.1 Dynamic Mode Theory . . . 46

2.1.1 Modeling of cantilever behavior . . . 48

2.2 Theory of cantilever beam immersed in fluid . . . 54

2.3 Impedance Correlation . . . 59

2.4 History and description of our Model . . . 62

2.5 Fundamentals and Computational Approaches in Electrostatics and Material Modeling 66

2.6 Cantilever Array Designs . . . 69

2.7 COMSOL Multiphysics Approach . . . 70

2.7.1 Density and viscosity sensing . . . 72

2.7.2 Sensing the adding mass . . . 77

3 Cantilever Microbeam Sensor Development and Characterization **84**
3.1 Introduction . . . 84
3.2 Evolution of the Sensor Design . . . 85
3.2.1 Initial Design and Challenges . . . 85
3.2.2 Proposed Design Using Thin Wafer Tiles . . . 93
3.3 Support Structure and Connection . . . 107
3.4 Creating Devices with Varied Beam Spacing . . . 109
3.4.1 Variation in Beam Number and Spacing . . . 110
3.5 Device Characterization and Validation . . . 112
3.5.1 Numerical Analysis . . . 112
3.5.2 Piezoelectric element charaterics . . . 115
3.5.3 Device Integration . . . 119
3.6 Investigation of Piezoelectric-Structure Interaction Via PSv-400 . . . 120
3.6.1 Structure Mechanical Behavior . . . 122
3.7 Conclusion of the Interaction Study . . . 127

4 Modal Analysis and Frequency Shifts in Fluidic Environments **129**
4.1 Harmonic Mode Shapes Analysis . . . 130
4.1.1 Numerical Analysis: . . . 130
4.2 Experimental Setup . . . 131
4.3 Harmonic Mode shapes: Flexion and Torsion Analyses in Air . . . 135
4.3.1 Frequency Shift Analysis in Air and Water . . . 140
4.3.2 Beam behavior under design . . . 145
4.3.3 Physical affects of beams characterisation . . . 147
4.3.4 Quality Factor Evaluation . . . 151
4.3.5 Sensitivity in Terms of density and viscosity variation . . . 155
4.4 Analysis of Frequency band Shifting . . . 158
4.4.1 Sensitivity . . . 163

List of Figures

1.1 The need for early detection of potential breast cancer 4
1.2 Schematic illustration of exosomes for lipid biopsy. (A) Various body fluids used for the clinical application of exosome-based liquid biopsy in breast cancer. (B) The biogenesis and secretion pathways of exosomes. (C) The structure and content of exosomes.[10] 5
1.3 Rising Analytics Diagram For Our Device 7
1.4 (a) A diagram demonstrating two distinct operational modes for a nanomechanical sensor: static and dynamic. (b) A chronological chart showcasing publication and citation rates in the nanomechanical sensing field.[15] 8
1.5 The mind mapping overview 11
1.6 Cantilever Microbeam Array Sensor Applications 13
1.7 MEMS Configuration[42]. 15
1.8 BioMEMS-Enabled systems (MEMS Packaging for High Volume Products). 19
1.9 Silicon Wafer 22
1.10 Laser micromachining. Link. 23
1.11 Rectangular shape of beam 24
1.12 CMs shapes 25
1.13 Design thinking Process 28
1.14 Arrays of beams[96] 29
1.15 (A) The genetic-probe-modified CM sensor's detection process involves probe immobilization. (B) An advanced electrical signal extraction method is showcased, highlighting the probe-target molecule interaction in an embedded Metal–Oxide–Semiconductor Field-Effect Transistor (MOSFET) cantilever system. (C) The detection of KRAS mutations is depicted using MutS, AuNP, and resonators. (D) HepG2 cell detection using a CMA sensor is illustrated.[98] 30
1.16 A CSAs with Discriminating Cantilever Coatings.(Microcantilever Applications Overview). 31
1.17 Processes of GNPs combine hybridization information.[99] 31

1.18 Nanomechanical method for SARS-CoV-2 detection. (A) Sample collection from infected subjects. (B) RNA extraction from the samples, pinpointing SARS-CoV-2 specific genetic material. (C) Functionalization of CMAs with PNA, enhancing their sensitivity to SARS-CoV-2 presence. Here, four CMs are functionalized with PNA, with another four serving as controls. (D) Use of nanomechanical devices to detect SARS-CoV-2 by directing a stable light beam onto each CM tip and monitoring CM deflection in real-time via a position-sensitive detector. (E) This technique allows for early COVID-19 diagnosis within 60 minutes.[101] 33
1.19 Categorization and Operational Modalities of Micro Cantilever Sensors in Biomedical Diagnostics 35

2.1 The cantilever in a slope detection system is operated at a fixed frequency w_d, that is slightly off-resonance, and it undergoes a change in its resonant frequency from w_0 to w_0' due to a variation in the force gradient. This, in turn, leads to a modification in the steady-state amplitude by an amount of ΔA [1]. 47
2.2 A rectangular cantilever is shown in plan view in a schematic illustration. A beam's clamped end is the origin of the coordinate system. 49
2.3 An infinitesimal element dx of the same cantilever showed in Fig.2.2 longitudinally. . 50
2.4 The passage illustrates a depiction of a typical cantilever (A) and several resonant modes that idealized cantilever sensors exhibit (B-E). These modes include the transverse mode (B), torsional mode (C), lateral mode (D), and longitudinal mode (E). The fundamental mode shape of each mode is presented for clarity, and the displacements are arbitrarily scaled to enhance the mode's clarity. The dashed arrows signify the cantilever's motion throughout the resonant cycle.[12] 52
2.5 First four lateral normal vibration modes of a cantilever beam of the uniform cross-section.[13] 53
2.6 the amplitude (a) and phase (b) response of a forced and damped harmonic oscillator, which varies according to the normalized excitation frequency. The study focuses on CMs vibrating in air or liquid mediums, and specifically examines four different levels of damping (Q) commonly encountered in this context[13]. 58
2.7 This illustration shows a typical CM sensor frequency response near resonance. The phase angle spectrum (□) is shown in (A), while the impedance spectrum(△) is shown in (B). Impedance changes can be detected at a fixed frequency by monitoring at a fixed frequency[20]. 60
2.8 Ultrasonic sensor comprising a steel amplitude transformer, associated with piezoelectric elements. 62
2.9 (a) Conical steel sensor (b) Triangular ceramic sensor 63
2.10 Our Cantilever Microbeam Proposition 64
2.11 Piezoelectric Positioning and Exponential Support Structure for Beams 65

2.12 Meshing of the Cantilever Microbeam Array and Support Structure. 68
2.13 Boundary conditions illustrated in the image: The yellow region on the left represents a fixed constraint, while the blue region on the right denotes a free object. 69
2.14 Cantilever micro-beam array (a) in air (b) in water chamber 70
2.15 Our Model 71
2.16 Our model immersed in the chamber of fluid 71
2.17 Theoretical and numerical shifts eigen frequency were calculated according to[32] at mode 13th. 73
2.18 Variation of the $13th$ natural frequency mode with the potassium level and indicate the range of the patient hypokalemia, normal and hyperkalemia. 74
2.19 Several harmonics mode shapes for cantilever array. 75
2.20 Cantilever array with the insertion of several microcapillaries each containing a different blend in mode $4th$. 76
2.21 Δf Num in fluid for Mode $7th$ while adding lead to a water-filled microcapillary. . . . 77
2.22 Δf Num in fluid for Mode 13th and in vacuum for Mode 16th. 78
2.23 Potassium adsorption on the surface of SiO2 beam. 78

3.1 Our First Proposition - CAD Model 86
3.2 Laser Oxford Etching Silicon Wafer With a Green Wavelength 87
3.3 This is the structure transmitted in DXF format with the different laser passages for ablation for the first Etch. 88
3.4 In the next step, the engraving will be done on the beam. 88
3.5 TEST 1 In 2D View 89
3.6 TEST 2 In 2D view 89
3.7 TEST 3 In 2D View 90
3.8 TEST 3 In 3D View 90
3.9 TEST 3 Slat Is Whole 91
3.10 This Sample Includes Six Beams Ranging From $89\mu m$ to $41\mu m$ 91
3.11 3D view of the sample After Cleanig 92
3.12 Cleaning Samples with Ultrasound Machine 92
3.13 The new design after adjustment 93
3.14 The different Tiles thickness: a and c represent the spacers with thickness $200\mu m$. b represent the spacer with thickness $400\mu m$. e represent the spacers with thickness $140\mu m$ 94
3.15 a: All beams are blue. b: All spacers are blue. c: The piezoelectric is blue. d: The piezoelectric holder 95
3.16 Details of The Tiles that Clamped a Beam 95
3.17 Beam Length and Thickness 96
3.18 Description of The First Spacer With 2 Holes in The Device. 96

3.19 Details of The other Spacers With 4 Holes of The Device: We Have Two Spacers With The Same Shape But Different Thicknesses. . . . 97
3.20 Four different tile shapes must be established in the device. . . . 98
3.21 Assembly a . . . 98
3.22 Resin (A215nXT 50/50) and Cyanolit Liquid . . . 100
3.23 Rectangular Tile etched to establish a Support For Assembling Process . . . 101
3.24 Stacking Tiles In order While using a Microscope and a Precision Tweezers with a: the microscope. b: the Support for assembly. c: the Cantilever micro beam structure. e: The Precision Tweezers . . . 102
3.25 Support for Assembling with an array of four beams already stacked . . . 103
3.26 PZT-5H Homemade Wafer . . . 103
3.27 Details Of a PZT-5H Cut it in Rectangle Shape . . . 104
3.28 The Piezoelectric Is Integrated In The Assembly Structure . . . 104
3.29 SEM image showing the overall structure with the piezoelectric element. . . . 105
3.30 SEM image showcasing the dust welded on the front part of the beam. . . . 105
3.31 SEM image of the beam's side, indicating the dust welded away from the direct jet airflow. . . . 106
3.32 Close-up SEM image of the porous surface of the welded dust. . . . 106
3.33 Computer-Aided Design (CAO) of the sensor holder. . . . 107
3.34 Detailing of the single-sided FR4 printed circuit board (PCB). . . . 108
3.35 Fabricated structure post-copper removal process. . . . 109
3.36 Detailing of the Coaxial Cable with an SMA Connector. . . . 109
3.37 Detailed visualization of the precise interface between the holder and the piezoelectric element, emphasizing the importance of their aligned connection. . . . 110
3.38 Devices with varied beam numbers and spacings. . . . 111
3.39 Device with a crack along its structure. . . . 111
3.40 D5 device with optimal cleanliness and assembly. . . . 112
3.41 The full sensor setup with support holder and electrical connector. . . . 113
3.42 Electrical Excitation of Piezoelectric at Fundamental Frequency . . . 114
3.43 Unfixed Rear View of the Piezoelectric Element . . . 116
3.44 The Piezoelectric fixed in the holder . . . 117
3.45 Resonance frequency of the piezoelectric via the impedance analyzer. . . . 118
3.46 Impedance reactance and resistance plot using MATLAB. . . . 119
3.47 Resistance measurements of the piezoelectric in various mediums. . . . 119
3.48 Shift in Impedance and Reactance (ΔZ) Upon Immersion of Beams in Water . . . 120
3.49 Laser PSV-400 Polytec . . . 121
3.50 The peak frequenciesof the structur measured by the PSV 400 laser . . . 123
3.51 PSV laser scaning the beam while the beam is vibrating . . . 124

3.52 This shows how to register a point to be scanned with PSV software. . . . 125
3.53 The Peak frequencies of the D5 measure with PSV-400 . . . 125
3.54 D8 In Air Sweeping frequency from 10 to 600Khz . . . 126
3.55 The sweeping frequency in water from 30Khz to 100Khz . . . 126
3.56 Water drops on the beams landing on the three beams . . . 127

4.1 Mode Shapes . . . 131
4.2 Experimental Setup for Investigating Beam Vibrations Using LDV-UHF-120 and MATLAB-Controlled Signal Generation . . . 133
4.3 Vibrational Analysis of Microbeam using LDV-UHF-120 Laser Doppler Vibrometer . . . 135
4.4 Workings of the LDV-UHF-120 Laser Doppler Vibrometer via the PSV presentation software, including real-time monitoring of the reflected laser signal. . . . 136
4.5 1st bending mode with the 5 beams . . . 137
4.6 2nd Bending mode with the 5 beams . . . 137
4.7 The 3rd beam shows the 1st Torsion mode with the device with 5 beams . . . 138
4.8 The 1st beam shows the 2nd Torsion mode with the device with 5 beams . . . 138
4.9 3rd Bending mode with the 5 beams . . . 139
4.10 Using the devices with 5 beams, the 2nd beam shows the 3rd Torsion mode . . . 139
4.11 Using the devices with 5 beams, the 3rd and the 5th beams shows the 4th flexion mode 140
4.12 Laser-Assisted Underwater Analysis of Microbeam Vibrations . . . 141
4.13 Comparative Resonance Analysis of Multi-beam Device: Air vs. Water Environments (First Mode in Air Vs Water with resonance frequencies 84Khz and 51Khz, respectively) 141
4.14 Flexional Mode 2 Resonance Shift Analysis: Multi-beam Device in Air vs. Water Environments (566Khz and 391Khz for Air and Water, respectively) . . . 142
4.15 Third Flexional Mode Analysis: Resonance Shift of Multi-beam Device in Air and Water (1.509Mhz and 1.070 Mhz for Air and Water, respectively) . . . 143
4.16 Fourth Flexional Mode Shift: Air to Water Frequency Transition in Multi-beam Device (2.834Mhz and 1.978 Mhz for Air and Water, respectively) . . . 144
4.17 Depiction of the out-of-plane mode shapes observed during the experimental phase. Flexion bending mode shapes are encapsulated in sub-figures (a, c, e, f, and h), and torsion mode shapes in sub-figures (b, d, and g). . . . 145
4.18 Dust influence on torsion mode. . . . 146
4.19 Spacing between the beams set at 800μm . . . 147
4.20 Mode shape Beams In Air . . . 149
4.21 Beams In Water . . . 150
4.22 Quality Factor Air . . . 152
4.23 Quality Factor Water . . . 153
4.24 Frequency Shift for each Harmonic Modes . . . 157

4.25 Amplitude and Frequency Variations Across Different Mediums: A Comparative Analysis from 10 kHz to 2 MHz 158
4.26 Displacement Variations in Air and Ethanol over a Specified Frequency Range 159
4.27 Frequency Shift by variation of 25% of Viscosity On the Third mode of Flexion Bending 161
4.28 Frequency Shift by variation of 25% of Viscosity On the Third mode of Flexion Bending 162
4.29 Delta f For The third Beam 165
4.30 Comparison of modeled and experimental displacement amplitudes as a function of frequency. 167
4.31 Amplitude response in water (blue), and in vacuum (black). 167
4.32 Amplitude response in vacuum (blue), and with 8 μg added to the beams (black). . . 168
4.33 Amplitude response in water (blue), and with 8 μg added to the beams (black). 169

List of Tables

1.1 Presents a comparison between the dynamic and static modes of sensing using a cantilever as the mechanical platform for chemical and biological sensing applications. . . 9
1.2 Area of Applications of CM . . . 12
1.3 Table of materials used for sensing applications[100]. . . . 32
1.4 A summary of the important parameters discovered in previous investigations of microcantilevers for detecting mass in liquid surroundings. based on the research presented in [110] . . . 34

2.1 Material properties of silicon. . . . 67

3.1 Machining parameters of the three tests . . . 89
3.2 Comparison of Different Methods of Joining Tiles. . . . 99
3.3 Resistance measurements in different environments . . . 116

4.1 Vibration mode data for different beams in air . . . 148
4.2 Vibration mode data for different beams in water . . . 149
4.3 Quality factor data for different beams in air . . . 151
4.4 Quality factor data for different beams in water . . . 153
4.5 Density and viscosity measurements of various mixtures . . . 155
4.6 Mode shapes and their corresponding peak frequencies in air for Beam 3 . . . 155
4.7 Mode shape data for the Beam 3 in different mediums . . . 156
4.8 Frequency deviation (Δf) in mode 5 of the third beam for different mediums . . . 164
4.9 Density, Viscosity, and Frequency Shift for Various Mediums. . . . 165

Acronyms

AFM Atomic Force Microscopy 6

Bio-MEMS Biomedical Microelectromechanical Systems XIV

CFD Computational Fluid Dynamics 14

CM Cantilever Microbeam XIV

CMA Cantilever Microbeam Array 2

CSAs Chemical Sensor Arrays 30

CVD Chemical Vapor Deposition 22

DMA Dynamic Mechanical Analyzer 17

DRIE Deep Reactive Ion Etching 23

FEA Finite Element Analysis 70

FM Frequency Modulation 27

FSI Fluid-Structure Interaction 54

IC Integrated Circuit 13

IP In Plane 34

LDV laser Doppler vibrometry 27

LOC Lab On Chip 32

MEMS Micro Electro Mechanical Systems XIV

MMIC Integrated Circuits For Microwave Applications XIV

MOSFET Metal–Oxide–Semiconductor Field-Effect Transistor . . . . . V, 30

NEMS Nano Electro Mechanical Systems 15

OoP Out Of Plane 34

PSD Phase-Sensitive Detection 27

Q-factor Quality Factor 48

SHO Simple Harmonic Oscillator 51

General Introduction

Cantilever Microbeam (CM) is a transformative technology with vast potential in healthcare and environmental monitoring. Resonant CMs enable the quantification of biochemical substances in biological fluids, paving the way for early disease detection and diagnosis. Likewise, they play a crucial role in the identification of dangerous materials in fluids, improving our comprehension of environmental pollution, and proposing mitigation techniques. The mechanical characteristics of interacting materials or substances are revealed by this response. By utilizing this idea, scientists have created resonant CMs that can identify particular biochemical components present in biological samples. Such developments have great potential for use in drug discovery, environmental surveillance, and medical diagnostics.

A key factor in improving patient outcomes and reducing healthcare costs is early disease detection. By examining biomarkers and other biochemical components in biological samples, resonant CMs offer a non-invasive, effective method for illness identification. With the use of this technology, doctors can identify illnesses early on, reducing the need for invasive procedures and increasing the likelihood that patients will recover. Such devices are useful for environmental monitoring in addition to the healthcare industry since they can detect dangerous materials in fluid media. By accurately identifying contaminants in water, air, and other liquids, mitigation measures for their negative effects on the environment and human health can be developed. With a consistent approach to early disease detection and improved environmental surveillance, resonant CMs have the potential to completely transform environmental monitoring and healthcare. To effectively utilize this technology, more research and advances in this area are required.

With the CM sensor, you can detect prognostic biomarkers present in serum and urine, in order to avoid probable pathologies in patients. The CM sensor is a revolutionary Biomedical Microelectromechanical Systems (Bio-MEMS) gadget. MCs play vital roles in timekeeping, imaging, sensing, and biological/biomedical systems. They are among the most basic miniaturized devices used in microelectromechanical systems. Additionally, such sensors can also be manufactured and built as Micro Electro Mechanical Systems (MEMS) sensors, which are widely used in the commercial and industrial domains to measure physical and environmental conditions. The natural development of electronic components Integrated Circuits For Microwave Applications (MMIC) and the constant demand for miniaturization, weight and cost reduction, and the creation of more efficient devices gave

rise to this technology. The examination of the potential use of alternative transduction methods is motivated by the reduction in sensor size, pushed by an improvement in performance. Utilizing MEMS technology for biological detection, laboratory research focuses on dielectric transduction at the intersection of microelectronics and biology.

This work is the development of a MEMS CM sensor based on an array of silicon beams excited by an external source to vibrate. The device's operation relies on the natural frequency shift that occurs when the micro-beam is immersed in an incompressible fluid, allowing it to detect changes in density or the presence of specific analytes. This technique employs embedded piezoelectric elements to excite the system and a readout solution using silicon for manufacturing the structure of the sensor. Our underlying objective is to combine predictive indicators with the theory of vibration beams. We have chosen the CM as our technological medium for biomarker identification in order to accomplish this. We present a novel design that makes use of piezoelectric excitation in the CM domain. This design presents new obstacles in addition to surpassing the capability of current models in use. In order to achieve improved self-sensing and accuracy, the study attempts to investigate the feasibility of incorporating a dielectric transduction approach into vibrating Bio-MEMS CM sensors. The physicochemical characteristics of the sensor can be altered by chemical sorption onto a sensitive layer, which will alter the mass of the system and, in turn, its resonance frequency. By applying a specialized polymer coating or receptor material to the top surface of the CM, we can selectively bind it to the analyte of interest and investigate all signs discovered in a particular medium. This device has the potential to be useful in many disciplines, such as determining in situ disease severity through the analysis of natural frequency shifts in body fluids and detecting changes in density or the presence of markers in fluids. The primary objective of my thesis research, however, was to develop a sensor with sensitivity and functionality to justify our proposal. We additionally made sure that it was affordable and compatible with the tools we already have.

To accomplish our goal, this project was carried out in multiple phases, which included: The recognition of the potential of micro-cantilever-based sensors in substance detection was the driving force behind the creation of this research. Micro-cantilever sensors have become a viable solution due to the growing demand for accuracy and speedy detection, especially when it comes to drug identification. The background of the research was clarified by the basic roles that background and motivation played. The necessity of novel diagnostic techniques was made clear by the crucial significance of early detection and lifestyle modifications for prevention, which provided additional impetus for our investigation. After a review of the state of current research, our project identified a critical role for Microcantilever-Array with Biomarkers, where a quantum leap in detection fidelity was promised by the interface between biomarkers and microcantilevers. The specificity and sensitivity of the sensor were further improved by the selection of the Coating Proposition.

This concept may be used for a wide range of tasks, from industrial monitoring to medical diagnostics. We conducted a thorough analysis of current approaches and their drawbacks, focusing on MEMS and BioMEMS sensors in particular, identifying the intrinsic drawbacks and difficulties. We then took a closer look at cantilever micro-beam sensors in our quest. CM was examined, the complexities of fabricating CM were explored, CM sensors were characterized, and their operation was clarified. Combining downsizing and multiplexing was made possible by the Micro Cantilever Array Approach and Lab on Chip technology. Dynamic Mode Theory was used to model cantilever behavior in a comprehensive way. It was crucial to investigate a complex theory of the cantilever beam submerged in fluid and impedance correlation. We used FEM for computational modeling with the History and description of our model as a backdrop. Robust simulations were produced by the Sensing mechanism using the COMSOL-Multiphisics tool. Additionally, this phase focused on the influence of sensing the added mass on sensor dynamics as well as density and viscosity sensing. The development of our sensor, from its original design challenges to an enhanced design utilizing thin wafer tiles, has been described in the section on Cantilever Microbeam Sensor Development. Support structures and adjustable beam spacing improved this design. We integrated the device using piezoelectric and numerical analysis. We investigated the relationship between the piezoelectric elements and the microbeam, which resulted in measurements in Newtonian fluids. Extensive experiments, ranging from sensitivity analyses to frequency shifts, confirmed the accuracy of our theoretical frameworks.

During my thesis, we collaborated with Sahlgrenska Cancer Centre (since 2012), which is a biomedical research center with 15 research groups and about 100 scientists. It was founded by a collaboration of several institutes at Sahlgrenska Academy at the University of Gothenburg, which expanded and integrated their research activities on a single campus. Cell culture, virus transfection, bacterial culture, and a FACS cell sorter are all available at the center. So, we take advantage of this opportunity in order to make a bio-surrounding for our device to detect biological entities. Cancers can be detected early, allowing the identification of new genetic and epigenetic biomarkers. Detecting cancer before it metastasizes by the detection of trace biological entities in the serum, can save a patient, prevent disease progression, and give the possibility of diagnosing the pathology at its very first stage before spreading. To fully realize the potential of CMs as sensors, understanding their dynamic responses in dissipative media and their bending and mass-changing capabilities is necessary. Despite the significant theoretical and practical advancements in the last two decades, there is still a challenge to overcome to unlock the full potential of these microdevices.

The background for this manuscript is provided by the broad application of microelectromechanical systems (MEMS) technology and its transformational effects on numerous fields. In the upcoming chapters, we will explore this field in detail, emphasizing the vital significance of cantilever microbeams (CM) and providing an in-depth theoretical and experimental analysis of their numer-

ous applications.

Chapter 1 presents a comprehensive introduction to MEMS technology, outlining its historical development and emphasizing its critical role in fields including nanotechnology, electronics, and biomechanics. The story focuses on cantilever microbeams (CM) and their crucial function in detection and actuation applications. This chapter devotes a good deal of space to discussing the use of CM in biomarker sensing and breast cancer detection. It also delves deeper into the complex processes involved in creating a CM sensor, covering excitation and measurement methodologies. As we go, we also identify the constraints this sensor faces and compare it to other industry choices.

Chapter 2 unravels the mysteries of CM while providing a solid theoretical framework. The vibrational theory of beams, which provides insights into resonance frequency calculations and impedance theory, lies at the heart of this chapter. This chapter must be read through in order to have a clear knowledge of the physics behind CM behavior. A thorough modeling section confirms our selection of the model and its behavior, particularly when submerged in a Newtonian fluid environment, under ideal circumstances as well as when more mass is added to the beams.

Chapter 3 describes in detail the methodical development that underlies the emergence of our sensor. It tells the story of the path taken to refine the sensor, starting with the early phases of design and highlighting the difficulties faced and solutions developed. This chapter concludes with a thorough exploration of the subtleties of piezoelectric-structure interactions, all of which are crucial to comprehending the origins and development of our sensor.

Chapter 4 reveals the experimental results of our investigation. We provide results from extensive testing, mainly concentrating on possible uses of the CM in Newtonian fluids and evaluating beam sensitivity. In fluidic situations, modal analysis and the observable frequency shifts are emphasized. The story does not hold back when examining beam behaviors that are greatly impacted by design factors. Throughout, our go-to measuring equipment of choice has been the LDV-UHF-120 Polytec doppler vibrolaser, demonstrating its indispensable nature in our scientific pursuits.

Chapter 1

State-Of-The-Art: Literature Reviews

In this chapter, we discuss the modern field of medical diagnostics, emphasizing the pressing problem of early disease detection and prevention. The importance of pathologists' identification of the markers found in body fluids—markers that frequently indicate the onset of possible diseases—is emphasized in this chapter. Further, we address the potential role that biomarkers derived from human body fluids may have in preventing the development of diseases such as breast cancer. The CM, a technical wonder that unites the fields of Micro Electro Mechanical Systems (MEMS) and BioMEMS sensors, is central to this discussion. Its ability to function as both a MEMS and a BioMEMS sensor gives it unmatched versatility in the medical industry. This section of the study discusses the complicated techniques involved in the fabrication and characterization of the CM, as well as describes its uses. It breaks down the many approaches to measuring these devices in both static and dynamic modes and looks at the wide range of fabrication processes that are out there. The chapter provides a comprehensive overview of the state of the art in this field, highlighting the potential of CMs to revolutionize disease detection and prevention.

1.1 Background and motivation

The vital role of detecting and measuring concentrations of biochemical substances and dust particles is showcased in its multifaceted applications related to human health, environmental conservation, and streamlined industrial operations. Identification of these biochemical markers, which include proteins, enzymes, hormones, and metabolites, is critical for prompt diagnosis, precise treatment approaches, and careful observation of many illnesses. On the other hand, the focus on dust particle identification highlights the health risks that come with respiratory problems, especially for people who already have medical disorders. Monitoring the quality of the air and water allows for the proactive reduction of environmental contaminants that are harmful to human health. But the conventional approaches to measuring these concentrations have many drawbacks, including low sensitivity, long response times, and complex sample preparations.

This situation calls for the improvement of current approaches to promote increased sensitivity, quick findings, and simplified sample preparation. Accepting this challenge, the potential of Cantilever Microbeam Array (CMA) becomes apparent and offers hope. They offer a significant change in the detection of biological compounds and dust particles by combining sensitivity, specificity, and speed. The CM sensors, gaining traction for their label-free, real-time detection capabilities, rest their principles on the deviation or resonance frequency shift upon analyte adsorption or binding. This change is then directly associated with the concentration of the target. The CMAs exhibit several advantages. They possess **enhanced sensitivity and selectivity**, surpassing their traditional counterparts. Their unique coatings on multiple microbeams enable selective detection, even in intricate environments like biological fluids. Moreover, the non-invasive nature of these sensors means that there is **less risk of disturbing or touching potential cancer cells**, thereby minimizing the chance of inducing metastasis. Furthermore, they offer **real-time, label-free detection**, which eliminates the need for exhaustive sample preparation or labeling, yielding instantaneous outcomes. Their structural design demands **minimal sample volumes**, making them ideal for applications in medical diagnostics or environmental monitoring. These arrays also excel in **multiplexed detection**, recognizing multiple analytes at the same time, allowing for a more comprehensive study. Lastly, their fabrication through MEMS technology allows for **scalability and integration**, seamlessly blending with other microscale devices such as lab-on-a-chip platforms.

For this purpose, developing a CMA could transform precise, sensitive, and effective detection in a variety of fields, including environmental monitoring and medical diagnostics. Breast cancer, predominantly afflicting women, represents 30% of fresh diagnoses. In 2020, the disease witnessed 2.3 million cases, resulting in 685,000 fatalities, thus ranking fifth in global cancer mortalities [1]. Despite a promising 5-year relative survival rate at 90%, advancing stages see a sharp decline in these numbers [2].Given the serious consequences of breast cancer, prompt actions are required. In addition to innate signs like as breast lumps or discharge, therapeutic approaches include radiation, chemotherapy, hormone therapy, and surgery. Early detection is pivotal, underscoring the relevance of self-exams, clinical exams, mammograms, and innovative methods like smart bra. Women, especially post the age of 50 or with a familial history of the ailment, should adhere to regular screenings, supplemented with advanced imaging for precise evaluations.

1.1.1 Early Detection And Lifestyle Changes For Prevention

Risk Factors

Breast cancer, a potentially life-threatening condition, is influenced by numerous risk factors. A family history of breast cancer is a significant risk factor, particularly for women who have first-degree relatives diagnosed with the disease. Some subtypes of breast cancer may be hereditary. Lifestyle choices also influence breast cancer risks. Smoking, obesity, excessive alcohol consumption, and physical inactivity elevate the risk. Hormonal factors further contribute; post-menopausal

women, those with higher BMIs, and those who have undergone hormone replacement therapy are at an increased risk. It is crucial to discuss the pros and cons of hormone therapy with a medical professional. According to Tan et al.[3], identifying and adopting preventive measures can help mitigate the risk. Recognizing these risk factors and adopting preventative actions can lower a woman's likelihood of developing breast cancer. Regular mammograms, healthy lifestyle practices, and preventive medications like Tamoxifen are beneficial for high-risk individuals. Researchers, as elucidated by Dong et al.[4], are also investigating potential vaccines and naturally occurring compounds with anti-cancer properties. Breast cancer prevention research is advancing rapidly, focusing on enhancing screening techniques, pinpointing risk factors, and strategizing prevention. Developing these strategies will reduce breast cancer incidences and better the outcomes for those diagnosed. NCI-supported researchers are making significant strides in understanding breast cancer's prevention, detection, and treatment [5]. Early detection of breast cancer enhances the chances of successful treatment and a favorable prognosis. Recognizing the importance of proactive breast health monitoring is vital. Discussing individual risk factors with healthcare professionals and establishing a tailored screening regimen, considering one's age, health history, and other factors, is essential. The figure1.1 underscores the significance of early detection and the steps associated with it, starting from self-examination and moving through clinical exams, genetic testing, and maintaining a healthy lifestyle. To ensure rapid action, screening and awareness campaigns are essential. Women should continue to be watchful about their breast health and seek medical attention at the first sign of irregularities. Better screening techniques and more potent therapies for breast cancer are made possible by ongoing research and technological developments. The creation of blood tests targeted at early-stage diagnosis through the identification of biomarkers suggestive of breast cancer cells represents a promising research option. These kinds of advancements have the potential to improve breast cancer diagnostic accuracy and reliability.

This research encompasses new screening techniques and treatments, delving into cancer subtypes, and assessing which treatments will benefit specific patient groups [6]. Moreover, studies are examining breast cancer risk prediction, the effectiveness of preventive treatments, and the impact of lifestyle and environmental factors on breast cancer development [7]. Such endeavors are paramount to curtail the disease's spread and enhance survivors' life quality. Breast cancer is categorized into three subtypes—hormone receptor-positive/human epidermal growth factor receptor-2 gene (ERBB2) negative, ERBB2 positive, and triple-negative—which inform recurrence rates and treatment plans [8]. Treatment options encompass radiation therapy, surgery, chemotherapy, endocrine therapy, or a combination thereof. Potential side effects include asthenia, edema, myalgia, osteoporosis, leukemia, hot flashes, and uterine cancer. Surgical procedures vary from excising the tumor to removing the entire breast and axillary lymph nodes, contingent on cancer spread. Surgery might lead to lymphedema by impacting nerves or disrupting lymphatic drainage. Especially post-mastectomy, radiation therapy proves effective in reducing local recurrence and enhancing overall survival. Nonetheless, sustained studies indicate possible loco-regional recurrence and issues like



Figure 1.1: The need for early detection of potential breast cancer

arm lymphedema with severe symptoms [9]. To alleviate standard treatment side effects, many cancer patients explore complementary and alternative medicine.

1.1.2 Novel Genes

The Sahlgrenska Cancer Centre, a biomedical research institution comprising 15 research groups and approximately 100 scientists, was established through a collaboration of several institutes within the Sahlgrenska Academy at the University of Gothenburg. The center is equipped with a range of research tools, including cell culture facilities, virus transfection capabilities, bacterial culture systems,

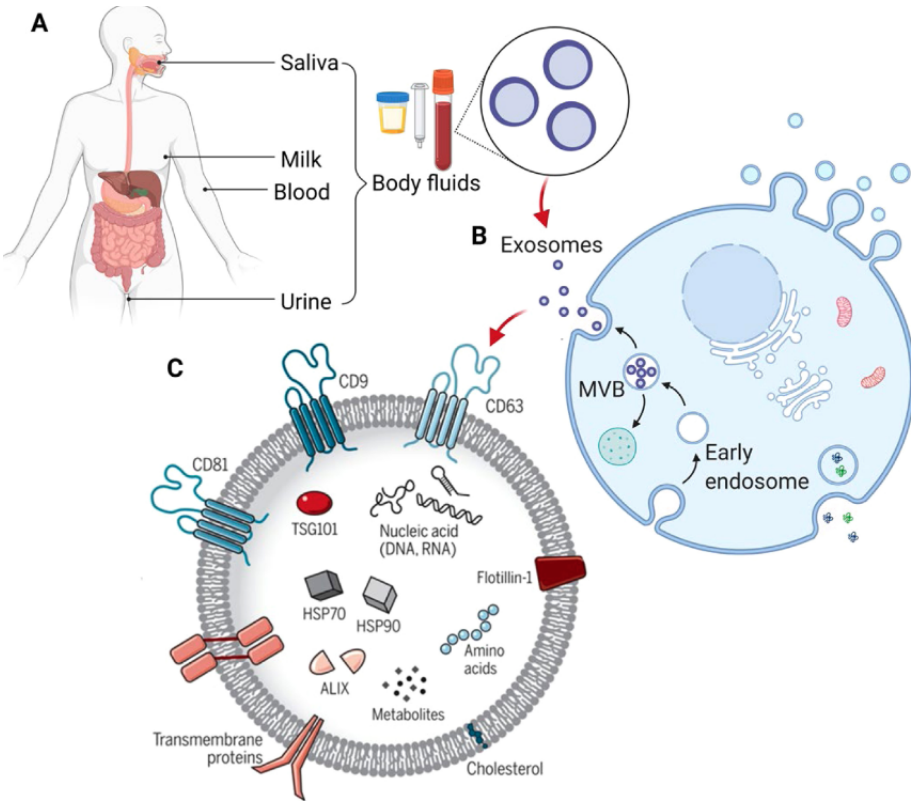

Figure 1.2: Schematic illustration of exosomes for lipid biopsy. (A) Various body fluids used for the clinical application of exosome-based liquid biopsy in breast cancer. (B) The biogenesis and secretion pathways of exosomes. (C) The structure and content of exosomes.[10]

and a FACS cell sorter. These resources can be employed to create an ideal environment for devices designed to detect biological entities. Biermann and colleagues conducted a study at the Gothenburg Oncology Department to identify potential biomarkers related to the prognosis of breast cancer [11]. They employed a statistical model and gene expression microarray profiles from 136 primary breast tumors and identified 18 genes. The predictive capabilities of these biomarkers were further validated using three publicly available RNA microarray datasets. To understand the role of these biomarkers in breast cancer progression, protein expression levels were analyzed using a tissue microarray consisting of 71 primary breast carcinomas, and optimized antibodies from nine invasive breast carcinomas were used. Early detection of cancer remains paramount; it facilitates the identification of new genetic and epigenetic biomarkers. Diagnosing cancer before it metastasizes, by identifying minute biological entities in the serum, can inhibit disease progression and potentially save the patient's life.

On the other hand, Liquid biopsy has been recognized as a pivotal tool for the early screening and diagnosis of breast cancer. Recent studies by Zhao et al.[10] emphasized the significance of breast cancer-derived exosomes as potential biomarkers for its early detection. This review sheds light on the latest advancements in exosome research pertaining to breast cancer, drawing comparisons between various isolation methodologies and elaborating on different exosome biomarkers. The review also underscores innovative techniques for detecting exosomes in clinical diagnostics.

Although more research is required, the current findings are promising, suggesting the potential of targeting specific breast cancer markers for detection and monitoring. Notwithstanding, challenges such as optimizing efficient exosome isolation techniques must be addressed to fully realize the potential of next-generation exosome-driven liquid biopsies. In recent studies, scientists analyzed the physiological serum of breast cancer patients and identified distinct exosomes, absent in healthy individuals, that could act as non-invasive and highly sensitive biomarkers for early breast cancer detection. These findings, while encouraging, necessitate further investigation and practical applications. Apart from these screening methodologies, there are several biomarkers indicative of breast cancer presence. Elevated levels of protein markers such as CA 15-3 or CA 27.29, anomalies in breast tissue identified via imaging, gene mutations like BRCA1 and BRCA2, and unusual growths or lumps in the breast are all potential indicators. The discovery of novel exosomes that can serve as biomarkers for early breast cancer detection is a significant breakthrough. Exosomes are minuscule vesicles excreted by cells, encapsulating various molecules indicative of the cell's health.

1.2 Microcantilever as the Chosen Sensor

MEMS cantilevers, also known as CMs, are among the most prevalent MEMS types. The utilization of vibrating CMs for mass detection began in the 1980s. In 1994, Gimzewski et al. [12] introduced a novel calorimeter that leveraged a CM to detect chemical reactions. A cantilever resembles a diving board: one end is clamped while the other is suspended. The development of MEMS cantilever involves fabricating a microbeam, which is subsequently coated with a material that can adsorb the target chemical. Silicon is the most commonly used material for MEMS cantilever sensors. In the late 1980s, Howe and Muller demonstrated [13] its suitability for mechanical structures.

For more than twenty years, Atomic Force Microscopy (AFM) has used microfabricated cantilevers to create topographical photographs of non-conductive surfaces. Due to their compactness, sensitivity, and quick response times, tipless cantilever beams have recently emerged as multifunctional sensors in industries like chemistry, physics, biochemistry, and medicine. These sensors work well in a variety of conditions, including vacuums, liquids, and gases. They can imitate human nostrils in gaseous media to distinguish between various vapors, and they can detect biochemical reactions and bigger organisms, like as fungi and bacteria, in liquid media. By detecting changes in fluid properties like viscosity, density, and surface tension, CMs function as mechanical fluid sensors [14]. They can operate in two modes: dynamic and static, each with their own benefits and drawbacks.

In Fig.1.4 (a), the nanomechanical sensor can function in static or dynamic modes. The static mode detects resonance frequency shifts when analytes attach to the sensor's surface. Meanwhile, the dynamic mode identifies oscillation amplitude and phase changes due to analyte attachment. Both modes operate similarly for biological purposes, with the sensor typically coated with biological recognition elements like antibodies, DNA, or aptamers. Part (b) displays publication and citation

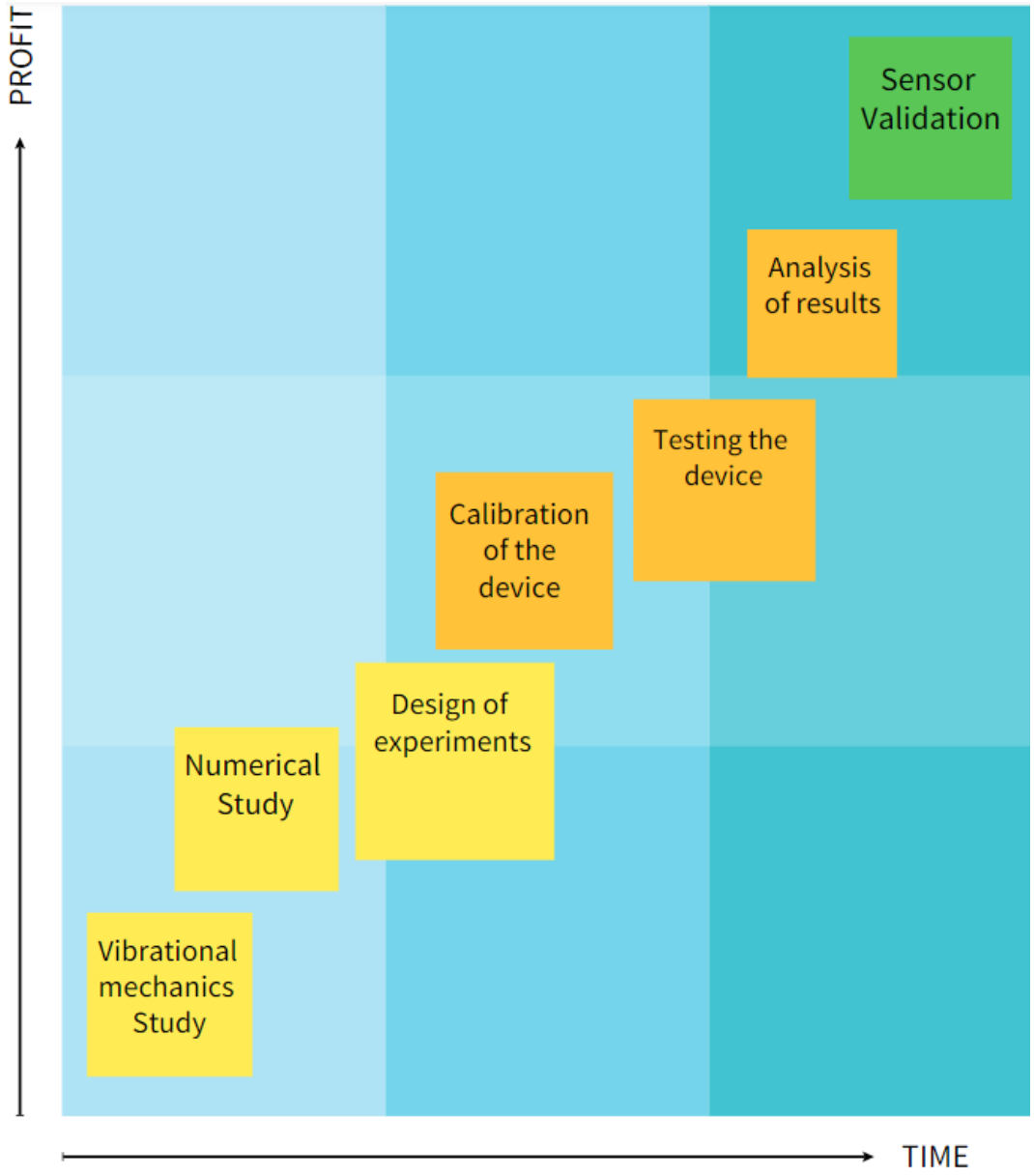

Figure 1.3: Rising Analytics Diagram For Our Device

trends in nanomechanical sensing, bifurcated by static (red) and dynamic (black) operational modes.

A stationary CM is used in the static mode to measure beam deflection brought on by environmental changes. By observing the capacitance change between the beam and a nearby fixed electrode, one can determine how much force is applied to the beam and how much it bends. This capacitance shift helps determine the magnitude of the applied force and correlates with beam deflection. Receptor layer coatings on cantilevers in static mode typically attach to target entities selectively, changing the cantilever's resonance frequency or deflection. The primary benefit of the static mode is its increased sensitivity to minute changes in the environment, which permits even single-particle detection. On the other hand, it usually identifies particles with significant receptor layer affinity and requires longer testing times.

The dynamic mode uses several ways to vibrate the CM. Environmental changes can be seen by

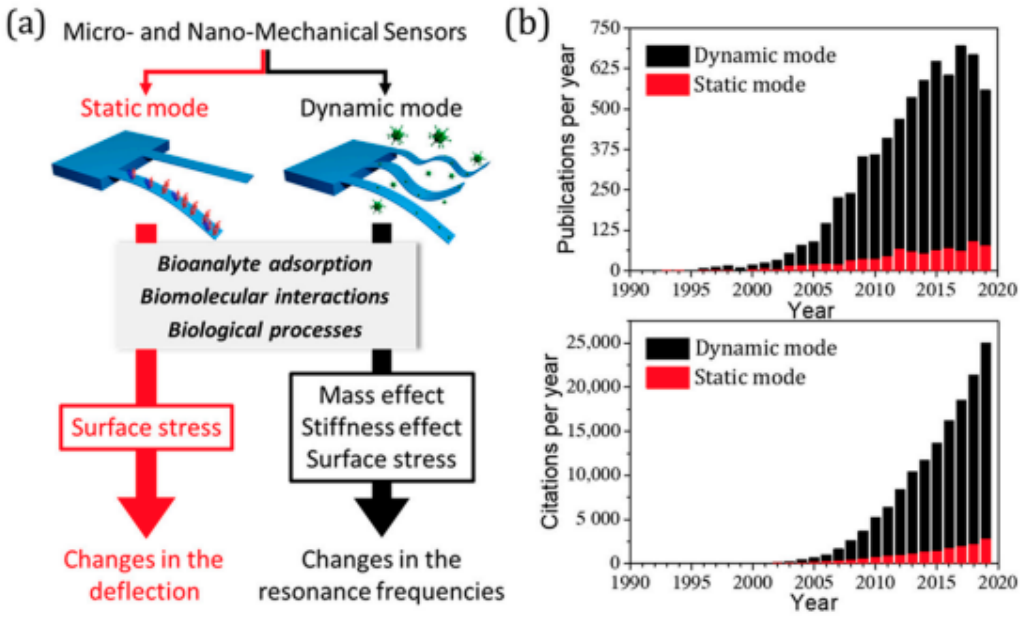

Figure 1.4: (a) A diagram demonstrating two distinct operational modes for a nanomechanical sensor: static and dynamic. (b) A chronological chart showcasing publication and citation rates in the nanomechanical sensing field.[15]

tracking the resonance frequency and amplitude of the oscillating cantilever. In this mode, vibration frequency, amplitude, or phase observations are used to identify mass and stiffness fluctuations in the beam caused by the surroundings. These revelations can reveal aspects of the environment, such as the mass of a molecule or the viscosity of a fluid.

Parameters	Dynamic sensing modes	Static sensing modes
Sensing principle	Measurement of change in resonant frequency due to change in mass and/or spring constant. Measurement of resonant frequency due to change in surface stress.	Measurement of CM displacement due to change in surface stress.
Features	Receptors are immobilized on either one side or both sides of the cantilever. Sensitivity can be improved by operating the cantilever at higher modes.	Receptors are immobilized on one side of the cantilever. Sensitivity can be improved by incorporating stress concentration regions.

Parameters	Dynamic sensing modes	Static sensing modes
Limitations	Erroneous due to adsorbate-induced changes in stiffness. Susceptible to fluid damping effect. Susceptible to material damping effect. Dependence of change in resonant frequency on the position of the target molecule on the cantilever.	Structural nonlinearity due to large deflection of the cantilever. Dependence of surface stress generation on immobilization protocols.
Suitability for measurements Liquid / Air	Low / High	High / High
Resolution	Mass: $10^{-24}g$ [16]	CM Deflection: 4Å [17]

Table 1.1: Presents a comparison between the dynamic and static modes of sensing using a cantilever as the mechanical platform for chemical and biological sensing applications.

Table 1.1 presents a comparison between the dynamic and static modes of sensing using a CM as the mechanical platform for chemical and biological sensing applications. When it comes to sensitivity and precision, the static mode of operation outperforms the dynamic mode. Because polymers have a large intrinsic material loss, material damping causes a significant decline in sensitivity, especially for polymeric cantilevers. Although using higher vibration modes can improve cantilever performance in dynamic mode, the readout becomes more complex due to the reduced oscillation amplitude. Moreover, the mass of the target molecules along with the stiffness-induced resonant frequency shift brought about by adsorbates limits the immobilization area. As a result, when in dynamic mode, biological sensitivity is affected. One application of micro-electromechanical systems (MEMS) technology is resonant microbeams, which use tiny vibrating beams to measure the physical, chemical, and biological properties of various materials. These microbeams, which are made of silicon, glass, or polymers, have a diameter of only a few micrometers.

Both static and dynamic modes are prominent techniques in particle detection systems. Although static mode is simpler and more direct, dynamic mode promises greater sensitivity and rapid detection, positioning it as a prime choice for real-time observation of dynamic systems [18]. The dynamic mode's strength lies in its capacity to detect minute changes in the surrounding environment, making it adept at identifying particles that exhibit weaker bonds to the receptor layer. Contrarily, static mode typically showcases superior sensitivity. Both modes have proven effective for particle detection in fluid media. The choice between them largely hinges on the application in question and the characteristics of the particles under scrutiny. For instance, particles with a robust bond to the receptor layer, present in sparse concentrations, are best detected using static mode. On the other hand,

when dealing with particles of weaker affinities or those in abundant concentrations, dynamic mode emerges as the preferred method [19]. In conclusion, while dynamic mode holds advantages in speed and sensitivity, making it the preferred choice for numerous real-time monitoring applications, static mode remains a dependable choice for specific particle detection scenarios.

1.2.1 Applications Of Cantilever Micro-beams

The evolution of resonant CM, illustrated in figure 1.5, offers potential solutions to challenges in substance detection, especially within medical diagnostics. Detecting minute biochemical substances in bio-fluids is a significant challenge for medical professionals, highlighting the potential of micro-beams to bridge this detection gap. Furthermore, accurately distinguishing between structurally similar biochemical compounds is crucial. There's also a demand in the medical community for economical and precise methodologies. Speed is essential as real-time, label-free detection demands rapid results without extensive sample preparations. When it comes to diagnostic instruments, dependability is critical. The potential of resonant CM in addressing these challenges is vast. However, comprehensive understanding is required before their deployment, as outlined by the mind map in figure 1.5.

1.2.2 Scope of applications

The resonant CM, renowned for its sensitivity, selectivity, and real-time detection capabilities, finds diverse applications as depicted in fig1.6. In *Medical Diagnostics*, CMs detect biomarkers in fluids, aiding early diagnosis and personalizing medicine. In *Environmental Monitoring*, they assess air and water quality, while in *Food Safety and Quality*, they identify food contaminants. They also play roles in *Threat Detection*, detecting chemical and biological threats, and in *Pharmaceutical Research*, accelerating drug discovery through studying drug-biomolecule interactions. Furthermore, in *Industrial Monitoring*, they oversee processes to enhance efficiency and quality. Distinguished as BioMEMS, which focuses on biological entities, and MEMS, which measures physical quantities, CM's primary strength lies in its unparalleled sensitivity, observable in both its dynamic and static modes. This versatility, represented in table1.2, spans applications from healthcare to aerospace, showcasing CM's transformative potential across sectors. The primary advantage of CM is its unparalleled sensitivity. This sensitivity allows for the detection of environmental changes by measuring the microbeam's dynamic and static modes. Its wide range of applications, as demonstrated in table1.2, extends from healthcare to environmental monitoring and aerospace. This sensitivity positions CM as an essential tool for progress in various sectors.

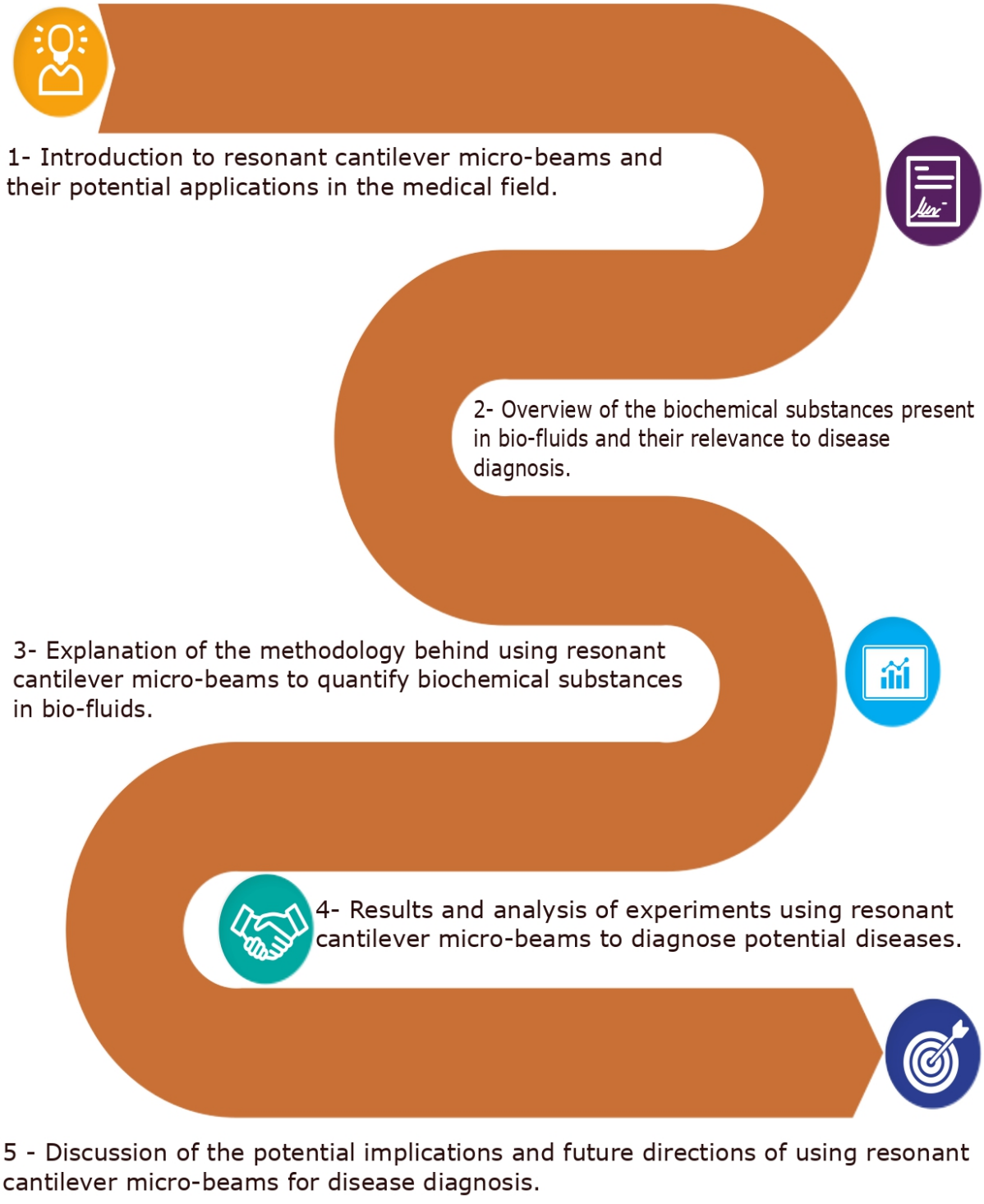

Figure 1.5: The mind mapping overview

Area of Applications	Examples
Area of Applications	**Examples**
Biomedical applications [20]	Biosensors (DNA, antibodies proteins, viruses, and microorganisms), Diagnostics, pH sensors
High-frequency resonators [21]	Chemical sensors
Food production and safety [22, 23]	Detection of heavy metals in the water to detect concentrations of herbicides, Changes in pH
RF switching [24]	Broadband switches, Switches for wireless communication
Atomic force microscopy [25]	Live cells, Reaction processes of DNA Biomolecules
Environmental monitoring [26, 27]	Temperature detection, Humidity detection, Heat changes
Energy [28]	Energy harvesters

Table 1.2: Area of Applications of CM

CM sensor devices are available in an array of designs, each tailored for specific applications. These devices operate dynamically, wherein the structure's vibration and any alterations in the beam's mechanical characteristics induce changes in its resonance frequency and energy dissipation. Some prevalent types of CM sensor devices are resonant [14], piezoresistive[26], optical [29], and electrochemical sensors [30]. Given the distinct benefits and limits of each type, the selection of a sensor device depends on the intended application and measurement requirements. Dynamic mode shifting, or the deviation of the beam's oscillation frequency beyond its inherent frequency presents interesting applications for CM. Design optimization, nonlinear analysis, feedback control, state-of-the-art fabrication methods, and application-specific considerations can all help achieve this. Higher-order modes can be induced by design optimization, and nonlinear analysis identifies nonlinear influences that may have an impact on dynamic mode shifting. Modern fabrication processes give increased control over the resonant frequencies, while feedback control allows for real-time manipulation of the beam's activities. Moreover, there may be application-specific factors that require attention. Factoring in these elements provides a competitive advantage in leveraging cantilever micro-beams for dynamic mode shifting.

1.3 MEMS Sensors

MEMS, or Micro-Electro-Mechanical Systems, incorporate micro-sized components including sensors, transducers, actuators, and electronic circuits. Originating in the 1960s, MEMS swiftly found

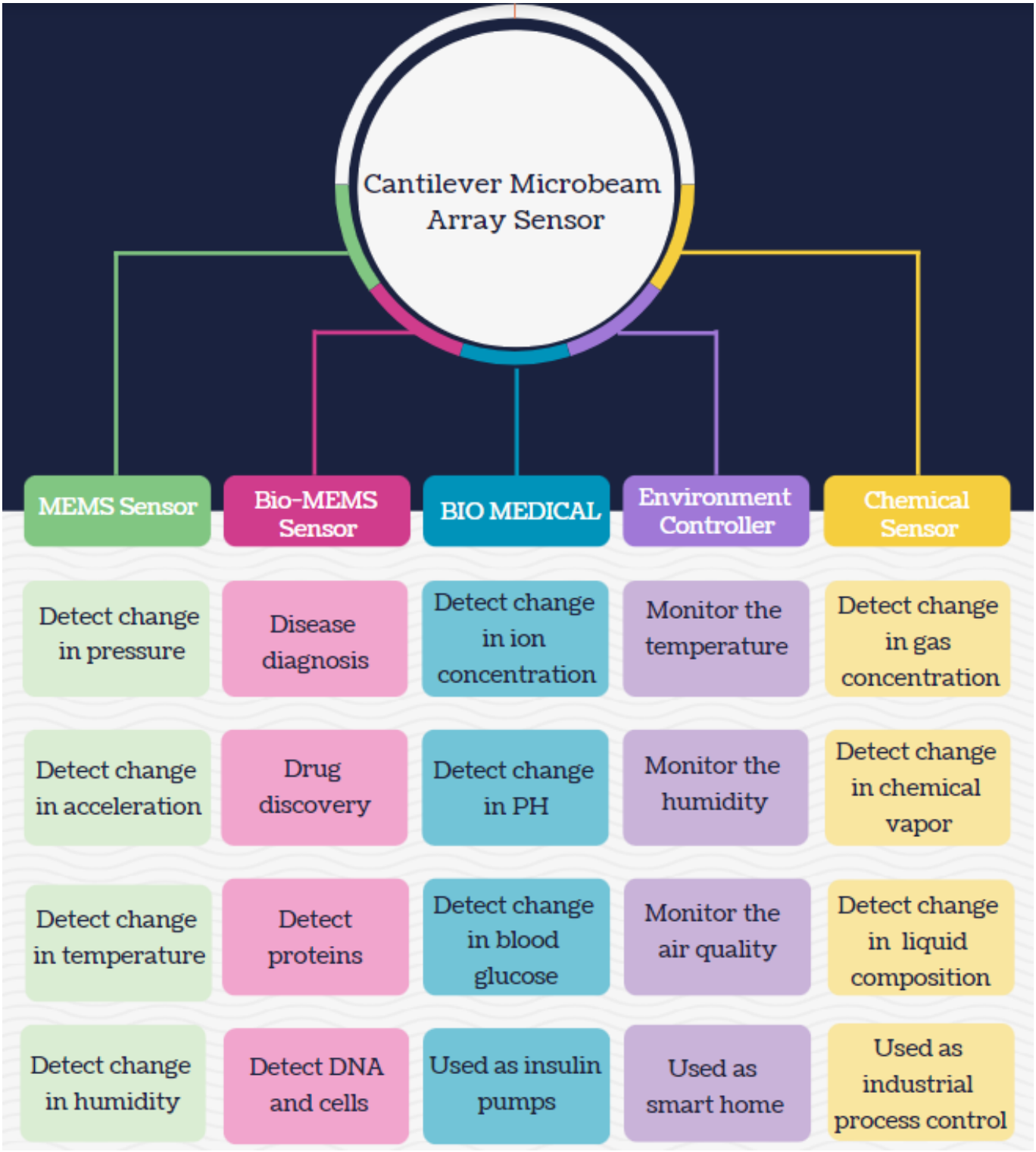

Figure 1.6: Cantilever Microbeam Array Sensor Applications

integration into electronic products. These devices predominantly employ micro and nanofabrication techniques that have evolved from the microelectronics sector. While they can be fabricated from materials familiar to microelectronics, polymers and biological components are also commonly utilized. MEMS harness Integrated Circuit (IC) fabrication methods to construct mechanically de-

formable devices on the micro-metric scale. This melds silicon-based microelectronics with micro-machining technology, encompassing a plethora of circuits and devices today [31]. The applications of MEMS technology have grown exponentially, prompting vast research across numerous domains like electronics [32], micro-mechanics [33], optics [34], fluidics [35], chemistry [36], and biology [37], to name a few.

The process of designing MEMS devices involves several steps that are based on fundamental ideas. The conceptual design is the first step in the process, during which the device's overall concept and specifications are outlined. The next step is material selection, which determines the components for different parts of the device, such as the substrate, structural parts, or electro-mechanical parts that are essential to its functionality. The following stages involve modeling and simulation, which make use of computer-aided tools to predict and optimize device performance. Tools like FEA and Computational Fluid Dynamics (CFD) are instrumental in simulating the device's mechanical and thermal attributes. Fabrication is the hands-on phase, where the envisioned device takes form via techniques like photolithography, etching, and deposition. Here, stringent process control is paramount to guarantee device performance and reliability. After that, the gadget is tested and characterized to confirm its functionality and identify any abnormalities. This could include analyses of the mechanical, electrical, and chemical properties. In summary, MEMS devices are usually packaged to protect them from outside influences and guarantee strong mechanical and electrical interfaces.

1.3.1 MEMS Fabrication Techniques

In the fabrication of MEMS devices, several methods are utilized. Lithography [38].
leverages light to transfer patterns onto substrates. Deposition involves layering materials onto a substrate using techniques such as PVD, CVD, or electrodeposition [39]. Etching, which is used to remove material from a substrate, can be performed through chemical, dry, or wet processes [40]. Additionally, bonding joins two substrates together, achieved through anodic, fusion, or adhesive techniques [41]. Each of these methods offers its unique advantages, disadvantages, and applications. The selection of a specific method often hinges on the desired device characteristics and the materials being used.

Characterization of MEMS Devices

MEMS devices undergo evaluation through methods like impedance spectroscopy and thermal imaging to ascertain their electrical, mechanical, thermal, and optical attributes. As previously highlighted, they find applications in sectors such as consumer electronics, healthcare, and aerospace, serving purposes ranging from sensors to drug delivery systems. The salient features

of MEMS devices include their compactness (often within the micrometer to millimeter scale), integration of multiple functionalities on a single chip (including sensors, actuators, and electronics),

low power consumption, high precision, and cost-effective mass production using microfabrication techniques.

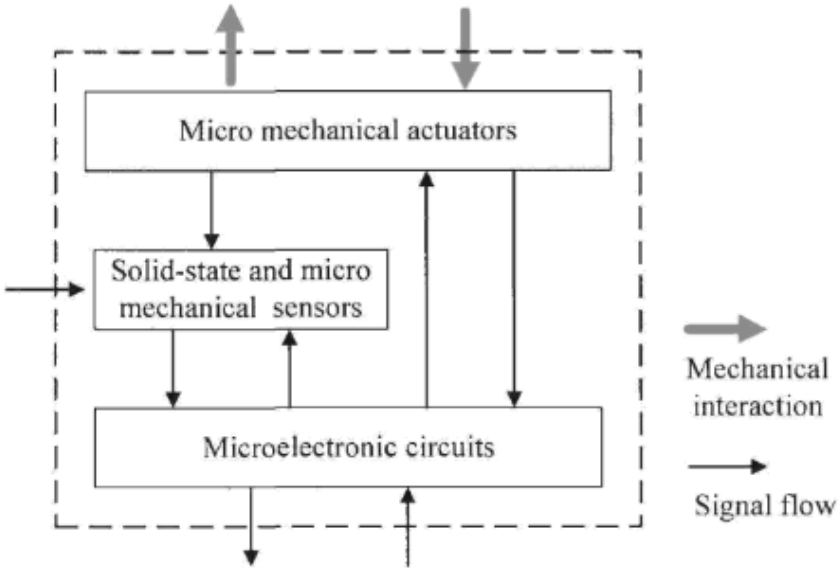

Figure 1.7: MEMS Configuration[42].

Figure 1.7 delineates a MEMS sensor configuration, encompassing both solid-state and micro-electro-mechanical actuators, coupled with microelectronic circuits. This design is primed to detect mechanical engagements with the external environment and ensure seamless signal transference within the apparatus. Bold arrows signify mechanical interactions between the device and its surroundings, while slender arrows denote electrical or other non-mechanical communications within the device components and the exterior. Thanks to its heightened sensitivity, this MEMS configuration can discern even minimal mechanical engagements. These are then converted into electrical signals for processing by the microelectronic circuits, making the system adept for a broad spectrum of applications.

Material selection for CMs MEMS devices is guided by specific prerequisites like operating temperature, mechanical robustness, and electrical conductivity. Advancements have leveraged the pressure, acceleration, and deformation sensitivity of certain thin-layered materials. The quest for harnessing MEMS for chemical detection, especially within biochemistry, continues to gain momentum. Emulating the miniaturization trajectory of the microelectronics domain, MEMS technologies have evolved into nanometric dimensions, referred to as Nano Electro Mechanical Systems (NEMS). The detection threshold of such devices, when employed as gravity sensors, has now reached the diminutive scale of a singular molecule or, in certain extreme scenarios, even a lone proton. A critical challenge for electromechanical nanosystems remains the incorporation of electromechanical transduction mechanisms. This pertains to the electrical instigation and discernment of mechanical motion inherent within the device.

1.3.2 Sensing Applications

As we mentioned bellow, sensors are employed to detect and measure diverse physical, chemical, and biological parameters across a plethora of industries. They play pivotal roles in environmental monitoring, detecting air quality, water quality, temperature, humidity, and atmospheric pressure to safeguard the environment [43]. In industrial control, sensors help regulate temperature, pressure, flow rate, and chemical composition to optimize processes [44]. In medicine, sensors track body temperature, blood glucose, heart rate, and blood pressure for diagnostics and treatments [14, 45, 46]. For urban infrastructure in smart cities, sensors gauge traffic flow, air quality, and energy consumption [47]. In agriculture, they monitor soil moisture, pH, and temperature to enhance crop yield [48]. In the automotive sector, sensors measure parameters like speed and acceleration for enhanced vehicle performance and safety [49]. Robotics use sensors to detect position, movement, and force for efficient robot navigation [50]. In security, sensors help detect motion, temperature, and chemical composition to mitigate potential threats [51].

In Fluid Media

Sensing within fluid media is essential for tracking changes in fluid properties such as viscosity, temperature, and composition with the aim of monitoring or controlling fluid behavior. Various methodologies are employed, including mechanical sensing which uses physical probes to measure fluid reactions [52, 53, 14], optical sensing that uses light to identify fluid changes [54], electromagnetic methods employing electric or magnetic fields [55], and acoustic sensing based on sound waves [56]. Other techniques include chemical sensors that use reactions to identify fluid property changes [57], microfluidic sensing with small fluid systems [34], and numerical modeling to simulate fluid behavior [58]. Specific sensor types include optical sensors that leverage light for fluid particle detection and employ lasers for measuring particle dimensions [59], ultrasonic sensors using sound waves [60], electric-field-based sensors for particle detection [60], magnetic sensors in medical applications like blood analysis [61], and MEMS sensors that measure attributes such as capacitance and resistance, though they have challenges like susceptibility to vibrations [62]. The choice of sensing technology depends on factors like sensitivity, fluid type, and particle composition, with MEMS sensors favored for their compactness and cost-effectiveness, but considerations regarding their limitations are essential.

Rheology Study

Rheology has diverse applications in fields such as materials science, engineering, geophysics, physiology, human biology, and pharmacology [57, 63]. Rheological measurements using rheometers determine properties like viscosity and elasticity, enabling control and prediction of material behavior in industries such as food and pharmaceuticals. Various rheometers are available for measurements, including rotational rheometry, oscillatory rheometry, and dynamic mechanical analysis.

MEMS sensors rely on fluids for rheology and sensing applications, and the interaction between the sensor and the medium is critical for high accuracy [57]. Different rheology sensors include viscometers, rheometers, strain sensors, capillary rheometers, oscillating rheometers, Dynamic Mechanical Analyzer (DMA), and extensional rheometers [63, 34]. For example, some MEMS sensors use cantilevers to measure material deformation under stress. These cantilevers are coated with a thin layer of the material under study. When force is applied, the cantilever bends, resulting in a change in electrical resistance or capacitance. Analyzing these changes enables the sensor to determine material properties like elasticity and yield stress.

In Viscous Media

MEMS sensors are increasingly utilized for their precise measurement of physical and chemical properties, notably viscosity. CMs, a subset of MEMS sensors, are distinguished by their sensitivity and selectivity, operating through the detection of resonant frequency changes in a cantilever beam due to surrounding fluid viscosity variations. Such sensors have been deployed in biomedical environments for detecting blood viscosity alterations, suggesting potential in diagnosing cardiovascular diseases [64]. Furthermore, Chen et al. [65] applied cantilevers to observe viscosity changes in fluids, assisting in monitoring pollution levels. In industrial contexts, where viscosity plays a pivotal role, particularly in fuel and polymer production, MEMS sensors discern fluid property shifts and evaluate factors such as density, temperature, and pressure. They employ various techniques, from timing fluid flow in narrow conduits to analyzing the natural frequencies of immersed vibrating elements. Additionally, microfluidic sensors gauge viscosity using medium flow within microchannels on their chips. Their precise assessments enable timely detection of variations in factors like flow rate and temperature.

By Density Variation

MEMS technology has progressed swiftly, providing an array of sensor technologies boasting precision, sensitivity, and accuracy. Especially, MEMS sensors designed to identify density changes have garnered interest due to their prospective use in sectors like aerospace, automotive, and medical [66, 67]. These sensors function by recognizing resonant frequency alterations in vibrating structures, caused by the presence of an analyte or environmental changes. MEMS density sensors encompass types such as piezoelectric sensors, surface acoustic wave sensors, and bulk acoustic wave sensors. Each type possesses its own set of benefits and constraints. By understanding each type's merits and limitations, researchers can select the most suitable sensor technology for specific tasks. The cantilever sensor has stood out as a highly promising MEMS sensor, especially for chemical and biological sensing, as illustrated by Ghatkesar et al.[68]. The cantilever sensor's distinct design, featuring a thin, flexible beam fixed at one end, facilitates the sensitive detection of mass changes on the beam's surface. This asset, paired with the ease of integration with electronic readout systems, has established MEMS cantilever sensors as a top choice for diverse sensing tasks. Density sensing

plays an essential role across industries, employing MEMS devices that translate fluid or gas density into electrical signals. These instruments find uses in contexts like automobile fuel-air mixture regulation and air quality assessment. Numerous techniques, such as hydrometry, pycnometry, laminar flow analysis, NMR, NQR, and ultrasound, are available for density measurement, each presenting unique advantages and disadvantages. Accurate density measurements can unveil information about a substance's composition, temperature, or concentration.

By Adding Mass In Fluid Media

Furthermore, MEMS sensors are renowned for their ability to detect mass changes with high precision and accuracy. Among these, micro-vibrating elements have shown great promise for detecting and measuring mass changes in fluid media. Their distinctive design, comprising a thin, flexible beam anchored at one end, allows for the highly sensitive detection of mass changes on the beam's surface. When particles adhere to the cantilever's surface, they induce slight deflection, which is detectable and quantifiable. Easily integrated with electronic readout systems, MEMS sensors have become a preferred choice for diverse sensing applications in chemical and biological fields. Additionally, these sensors can discern changes in mass direction, making them invaluable in arenas like industrial process control, environmental monitoring, and healthcare. They play a pivotal role in innovating new treatments, monitoring vital signs, and elucidating biological processes. Mass sensing is also indispensable in environmental and biomedical research, enabling experts to discern environmental characteristics and gauge human environmental impact. Various mass sensing methodologies exist, such as balance, strain gauge, SAW-based sensors, MEMS sensors [59], and optical sensors. Each method provides a distinct measurement range, accuracy, and ideal application scenario. Some are best suited for laboratory contexts, while others excel in field applications.

1.4 BioMEMS Sensors

BioMEMS sensors are a subset of MEMS sensors designed for biomedical applications. These miniaturized devices, known for their low power consumption, can be either implanted within the body or integrated into external devices to monitor various physiological parameters, including temperature [69], blood pressure [70], and glucose levels [71]. Externally, BioMEMS sensors find applications in wearable health monitors [72] and specialized diagnostic equipment [73, 14]. As illustrated in figure 1.8, BioMEMS devices serve multiple medical applications, such as manipulating and analyzing small fluid volumes, including blood or saliva [74, 75]. Constructed from biocompatible materials like silicon [76] and various polymers, these devices are tailored to minimize potential bodily rejections or irritations upon implantation.

BioMEMS stands out as an ever-evolving domain, holding immense promise in medical and biological arenas. Its growth is spurred by the increasing need for efficient diagnostic and treatment methodologies. The mounting concerns surrounding food security [77], environmental pollution like

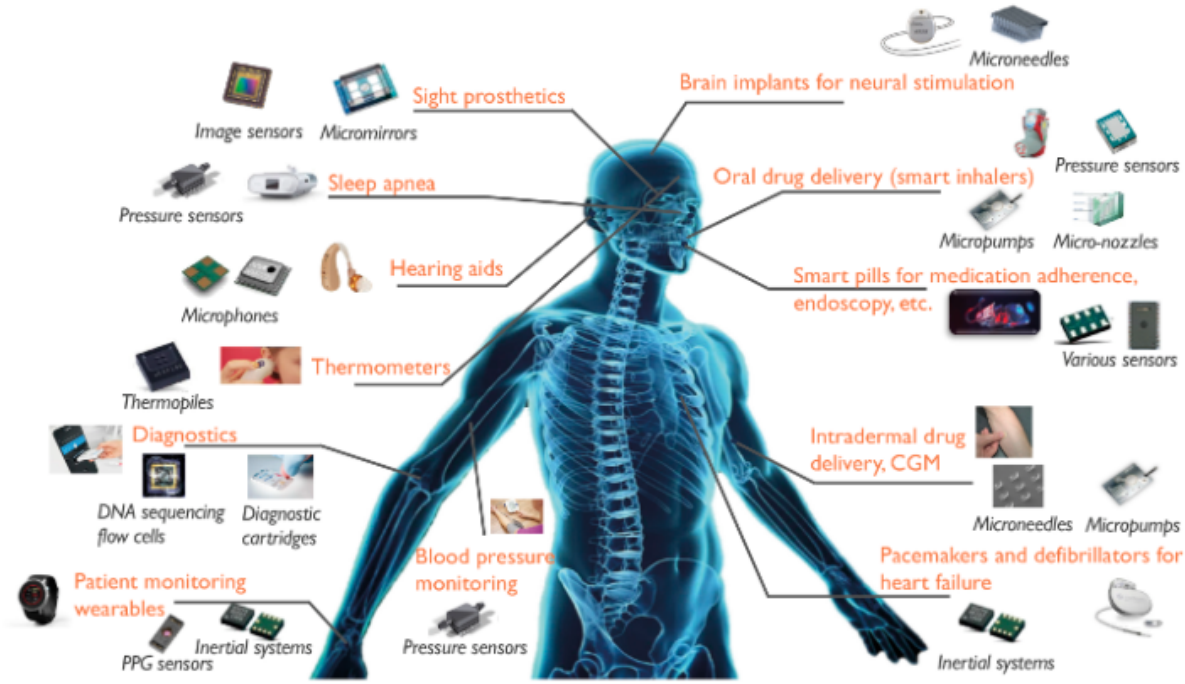

Figure 1.8: BioMEMS-Enabled systems (MEMS Packaging for High Volume Products).

soil and water contamination [78], potential threats from chemical or microbial agents [79], and the prevalence of health conditions such as diabetes and cardiovascular diseases emphasize the urgency for rapid, affordable, and robust biological measurement tools.

In healthcare, the shift towards "point of care" testing [80] rapid diagnostic procedures conducted near patients—can radically enhance patient care quality. Traditional biological assessments largely rely on laboratory-centric methodologies using advanced equipment like spectrometers. The process of collecting, transporting, and preparing samples for such analyses often consumes significant time, coupled with the imperative need for optimal storage to thwart sample degradation or contamination. Addressing these challenges, bioassays and biosensors have emerged as viable alternatives, offering portability, affordability, and speed. Though bioassays like blood glucose and disease-specific immunochromatography tests are popular for their out-of-lab applicability, they typically yield qualitative or semi-quantitative results.

In contrast, this concept based on cantilever mechanisms (CM-based) [81], offers rapid, precise diagnostic data. These sensors feature a thin cantilever beam anchored at one end, sensitive to variations in mass, stress, and other physical parameters. In point-of-care contexts, BioMEMS CMs excel in swiftly detecting biomolecules and cells in body fluids, such as blood or urine. Their compact design is especially beneficial for settings with limited resources, including remote locations with restricted access to conventional laboratory diagnostics. Moreover, the seamless integration potential of BioMEMS CMs with electronic systems facilitates real-time health monitoring, proving indispensable for tracking disease progression and evaluating treatment outcomes.

1.4.1 BioMEMS Technology Setup

BioMEMS devices employ several fabrication techniques, each with unique merits and drawbacks. Photolithography, widely recognized for its precision, enables nanoscale feature development [82]. Soft lithography, a more affordable and swift process introduced by George M. Whitesides in the 1990s [83], is suited for crafting microfluidic channels and microelectronic elements using pliant materials like elastomers. Electrospinning, a technique harnessing electric fields to produce nanofibers, is applied in areas like tissue engineering [84]. While photolithography excels in precision, soft lithography offers speed and cost-effectiveness, and electrospinning is adept at generating minuscule features.

Varieties of BioMEMS Devices

BioMEMS devices play a pivotal role in medical and biological research[85]. These devices range from lab-on-a-chip devices that consolidate multiple laboratory functions onto a single chip to microfluidic devices adept at the precise manipulation of fluids using microchannels[85]. Microelectrode arrays, with their intricate electrode arrangements, cater to both the stimulation and recording of cellular activity. On the other hand, implantable devices have been designed for either monitoring or modulating various physiological processes within the human body. Biosensors stand out by their ability to accurately quantify a wide range of biological molecules, leveraging diverse sensing mechanisms. Additionally, drug delivery systems are renowned for their controlled release of therapeutic agents. The hallmark of these devices lies in their unparalleled sensitivity, portability, and cost-effectiveness, revolutionizing medical diagnosis, treatment, and monitoring.

Characterization of BioMEMS Devices

Diving deeper into BioMEMS devices, they can be viewed as specialized MEMS fine-tuned for biomedical applications. These microsystems are meticulously designed to interface and interact with biological materials, serving various purposes such as diagnosis, ongoing patient monitoring, and drug delivery[85]. A few standout characteristics of BioMEMS devices include their miniaturized nature, allowing them to operate seamlessly at the microscale level of cells and tissues. Their biocompatibility ensures minimal adverse effects on biological systems, making them especially vital for devices intended for body implantation. Furthermore, these devices often incorporate sensors to detect physiological signals and actuators to physically interact with or manipulate biological entities. A synergy with electronic components ensures efficient data acquisition and transmission, while their multiplexing capability facilitates the simultaneous detection of multiple biological targets. Such technological feats in the realm of BioMEMS are transforming healthcare. For instance, technologies like CM, built upon an array of minute cantilevers, are making waves in the industry. These cantilevers are sensitive to molecular changes, especially when a target molecule binds to them. This innovation holds immense potential for disease diagnosis, drug discovery, and even

environmental monitoring, underlining the boundless possibilities of BioMEMS in the healthcare sector.

Applications In Biofluids

BioMEMS technology, through its miniaturization, has become indispensable in biomedical and healthcare. Primarily used for diagnostics, these devices can measure vital signs and detect pathogens, enabling swift medical interventions. In the realm of biofluids, BioMEMS sensors serve varied roles, from monitoring blood glucose levels and blood pressure to detecting infectious agents and cancer biomarkers. They also aid in precise drug delivery, analyze cerebrospinal fluid for neurological disorders, monitor electrolyte balances, and detect toxins, among other functions. Beyond healthcare, BioMEMS devices enhance industrial automation, handling tasks too minute for human execution, thus boosting efficiency and product quality. Overall, BioMEMS devices, with their precision and versatility, are transforming both medical treatments and industrial processes[86].

Diagnostic Pathology with BioMEMS Sensors:

BioMEMS sensors are revolutionizing diagnostic pathology, offering swift, accurate, and cost-effective methods for biomarker measurement, vital sign monitoring, and disease detection. These sensors leverage machine learning algorithms to enhance diagnostic precision by drawing insights from historical data. They play a crucial role in tailoring medical treatments to individual needs by tracking disease progression. In the realm of research and development, BioMEMS sensors provide invaluable data for discovering and validating new treatments. A notable application of this technology is microarrays for gene expression analysis. These platforms contain a vast array of DNA probes, enabling the simultaneous study of numerous genes. The process involves examining patient tissue samples, extracting RNA, converting it to cDNA, and subsequently analyzing the fluorescence signals indicative of gene expression levels. Such microarrays are instrumental in disease classification, particularly in identifying gene expression patterns in cancer cells, thereby facilitating enhanced diagnosis and treatment monitoring.[87]

Biofluids

Biofluids like blood, saliva, and urine, are reservoirs of valuable diagnostic information. By integrating BioMEMS devices with these fluids, precise disease diagnostics can be achieved. For instance, urine samples can help identify urinary tract infections, blood can reveal diseases like HIV, hepatitis, and heart ailments, and saliva can be used to diagnose oral conditions. BioMEMS can even measure biomarker levels for monitoring health metrics like glucose and cholesterol. Moreover, these detectors are adept in diagnosing neurological disorders from spinal fluid, lung conditions from pleural fluid, and joint problems from synovial fluid. The overarching benefit of BioMEMS is their accuracy, speed, and cost-effectiveness. As the technology evolves, its adoption in diagnostic

pathology is anticipated to expand, heralding swift and precise diagnoses and thereby improved health outcomes[86].

1.5 Microcantilever Sensor: Design & Characterization

1.5.1 Microcantilever Manufacturing

Generally, the process of creating a CM sensor involves several steps, each essential to ensure the final product's accuracy and reliability. The first step is preparing the silicon wafer, as shown in figure 1.9, by removing any contaminants. Impurities can affect the CM's mechanical properties. Subsequently, thin films of materials, including silicon nitride or silicon oxide, are deposited onto the wafer using methods like Chemical Vapor Deposition (CVD) or sputtering.



Figure 1.9: Silicon Wafer

Photolithography[1] is employed to create a patterned mask on the thin films, outlining the CM beam and other necessary structures. This stage is pivotal to the CM's accuracy and precision. The superfluous material is then removed through etching, the method of which depends on the materials being etched.

[1]Process used to define a CM by selectively exposing a photosensitive material using a patterned mask and then chemically etching the material to shape.



Figure 1.10: Laser micromachining. Link.

There are various etching methods for CM beams in MEMS sensors, such as wet etching, Deep Reactive Ion Etching (DRIE), the Bosch process, and laser micromachining, as depicted in figure 1.10. After etching, the cantilever beam is released from the substrate by removing a sacrificial layer, leaving it suspended. Metal electrodes are added subsequently to use the cantilever beam as a sensor.

1.5.2 Physical characteristics

CMs, generally fabricated from silicon or other materials, can have various shapes, such as rectangular or triangular. The precise shape of a CM sensor may depend on its specific application and the fabrication technique.

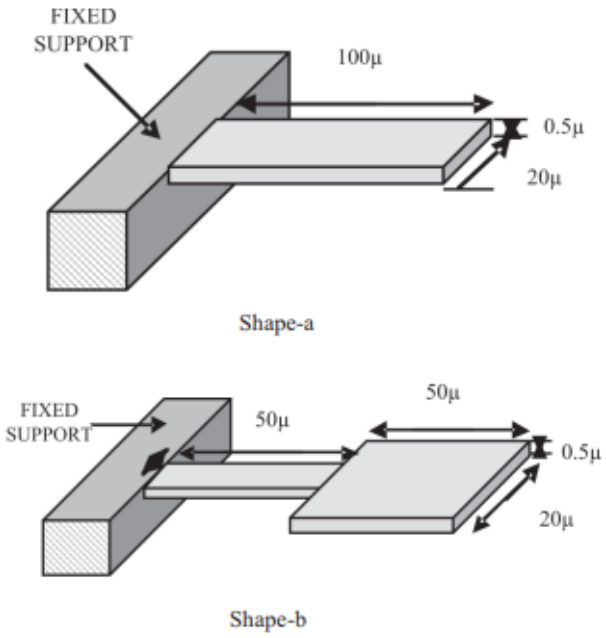

Figure 1.11: Rectangular shape of beam

The choice of shape can influence the dynamic modes of the microbeam and factors like sensitivity and resonant frequency. Common shapes include (shown in figure 1.11) and 1.12:

- **Rectangular**: This is the most prevalent shape for sensing applications due to its simplicity and well-defined mechanical behavior.
- **Tuning fork**: Comprising two rectangular beams connected at the base extending oppositely. It's used for mass sensing applications.
- **Triangular**: Offers higher sensitivity and better mechanical stability than the rectangular shape due to its geometrical symmetry.

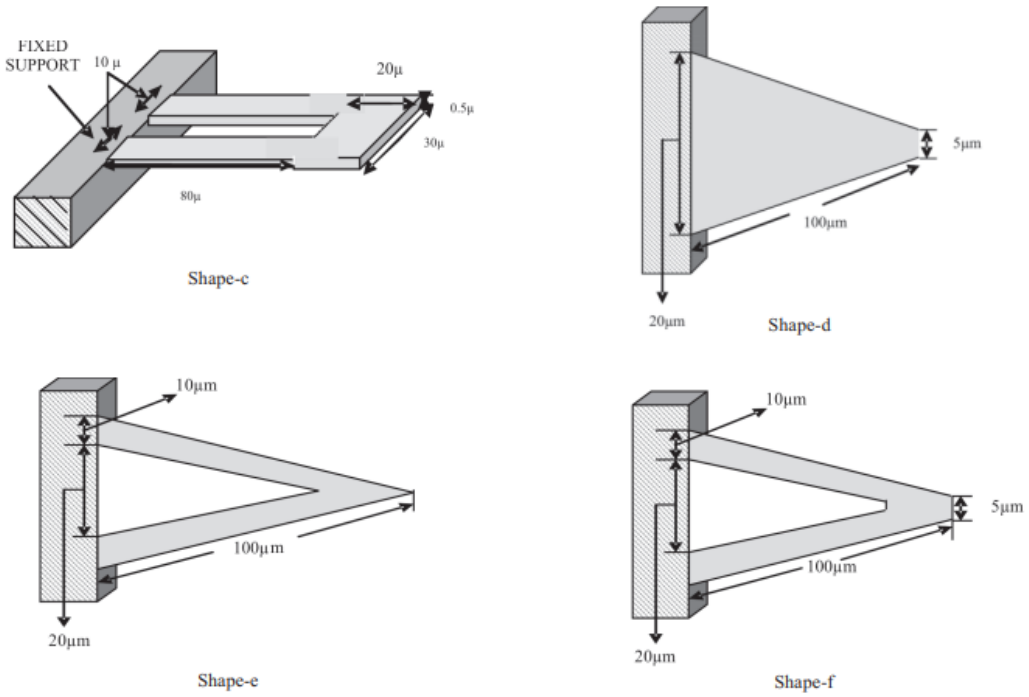

Figure 1.12: CMs shapes

The beam's thickness is vital, influencing the performance of CMs in multiple applications. Thinner beams are more sensitive, while thicker beams offer increased stability. The exact thickness required depends on the specific application and the balance between sensitivity and stability. Factors such as beam thickness, resonant frequency, and sensitivity are interrelated and can be affected by other parameters like material properties, boundary conditions, and the nature of the external stimulus.

1.5.3 Working Principle of Micro-cantilever Sensors

In dynamic mode, the fundamental operation of a CM sensor is based on inducing vibrations in the cantilever beam at its resonant frequencies. The resonant frequency is influenced by the beam's dimensions, geometry, and inherent mechanical properties, such as stiffness and mass. When exposed to a specific environment or sample, changes in the CM's physical or mechanical properties result in shifts in its resonant frequency. Such variations can be observed by tracking the deflection or displacement of the beam using sensitive instruments like optical interferometers or piezoresistive sensors. The observed deflections or displacements may stem from several factors, including molecular adsorption on the beam's surface, thermal fluctuations, pressure variations, or externally applied stresses. As a result, CM sensors are adept at detecting and quantifying a diverse range of analytes in real time, encompassing gases, liquids, and biological molecules.

Ways of Excitation

Several methods are available for vibrating a microbeam, with the following being the most prevalent:**Electrostatic actuation** [88]: This method involves applying an electrical potential difference across a cantilever to induce bending. Excitation is achieved by applying an AC voltage between the beam and a counter electrode situated beneath it. **Piezoelectric actuation** [14]: This approach uses an electrical potential applied to piezoelectric materials to produce a mechanical force. Typically, the piezoelectric layer is either integrated with the microbeam or located at its base, and its deformation due to the applied voltage causes the beam to move. **Thermal actuation** [89]: Here, a temperature gradient established across the cantilever, often via an electrical heat source, causes the cantilever to bend, similar to the bi-metal effect. **Acoustic excitation** [90]: Sound waves are employed to exert mechanical force on a cantilever, causing it to vibrate, a mechanism beneficial in applications like AFM for probing material surfaces. **Optical actuation** [91]: This method involves subjecting a cantilever to light, often from a laser, which induces either a photothermal or photoelastic effect, causing the cantilever to move. **Magnetic and electromagnetic actuation** [92]: While magnetic actuation utilizes a magnetic field, electromagnetic actuation employs the Laplace force on a cantilever in a magnetic field when there's an electric current flowing over its surface.

These techniques play a crucial role in modern microsystems by providing versatile ways to induce controlled movements in microscale structures. Piezoelectric excitation boasts several distinct advantages over other methods, enumerated as follows: **High efficiency**: This is attributed to the notable electromechanical coupling coefficients of piezoelectric materials [93]. **Broad operational frequency range**: It spans from a few hertz up to multiple megahertz. **Low power requirements**: This characteristic makes piezoelectric excitation suitable for portable or battery-driven devices. **Precise control**: Both amplitude and vibration frequency can be controlled precisely via adjustments to the input voltage. **Compatibility with fabrication processes**: The method aligns well with micro/nanofabrication processes, rendering it ideal for MEMS and NEMS devices. **Embedded vibrating source**: Piezoelectric excitation can either be embedded or integrated within the device, offering flexibility in design and application.

Measurement Methods

MEMS sensors often utilize CMs as sensing elements, measuring their deflection or resonance frequency in response to external stimuli. CM measurement techniques can be bifurcated into two modes: static and dynamic.

In static mode, the beam remains stationary while an external stimulus is applied. Its deflection is ascertained using optical lever deflection, capacitive sensing, or piezoresistive sensing. Optical lever deflection directs a laser beam onto a cantilever, reflecting a deflection angle proportional to the applied external stimulus. Capacitive sensing employs a parallel plate capacitor formed between the cantilever and a fixed electrode. As the cantilever deflects, the gap alters the capacitance, enabling measurements. Piezoresistive sensors on the cantilever measure resistance, which varies with the

deflection, enabling stimulus measurements.

Dynamic mode vibrates the beam at a selective resonance frequency. The frequency is measured pre and post-stimulus application using laser Doppler vibrometry (LDV), frequency modulation, or phase-sensitive detection. LDV measures cantilever dynamic vibration non-invasively by reflecting a laser beam from the cantilever to a detector. Frequency Modulation (FM) couples an oscillating circuit to the cantilever's dynamic system, detecting frequency changes as the cantilever vibrates. In contrast, Phase-Sensitive Detection (PSD) ascertains resonance frequency by measuring the phase difference between the cantilever's drive and response signals. Compared to FM, PSD is more precise as it can identify minute phase signal changes. LDV, FM, and PSD are non-invasive methods used to measure cantilever dynamic vibration.

1.5.4 Micro Cantilever Array Approach

The CMA approach promises profound advancements in MEMS and BioMEMS sensing. This method employs an array of CMs that deflect or vibrate when exposed to external stimuli. These cantilevers, when coated with specific materials or functionalized with biological molecules, become effective at detecting various substances or biomolecules in samples.

For MEMS sensing, the CMA presents several benefits:

- Due to their miniaturized size, CMs necessitate lesser sample volumes, especially useful when sample quantity is constrained.
- Their heightened sensitivity enables the detection of minuscule sample changes.
- Arrays facilitate concurrent detection of multiple substances, optimizing them for multiplexed sensing scenarios.

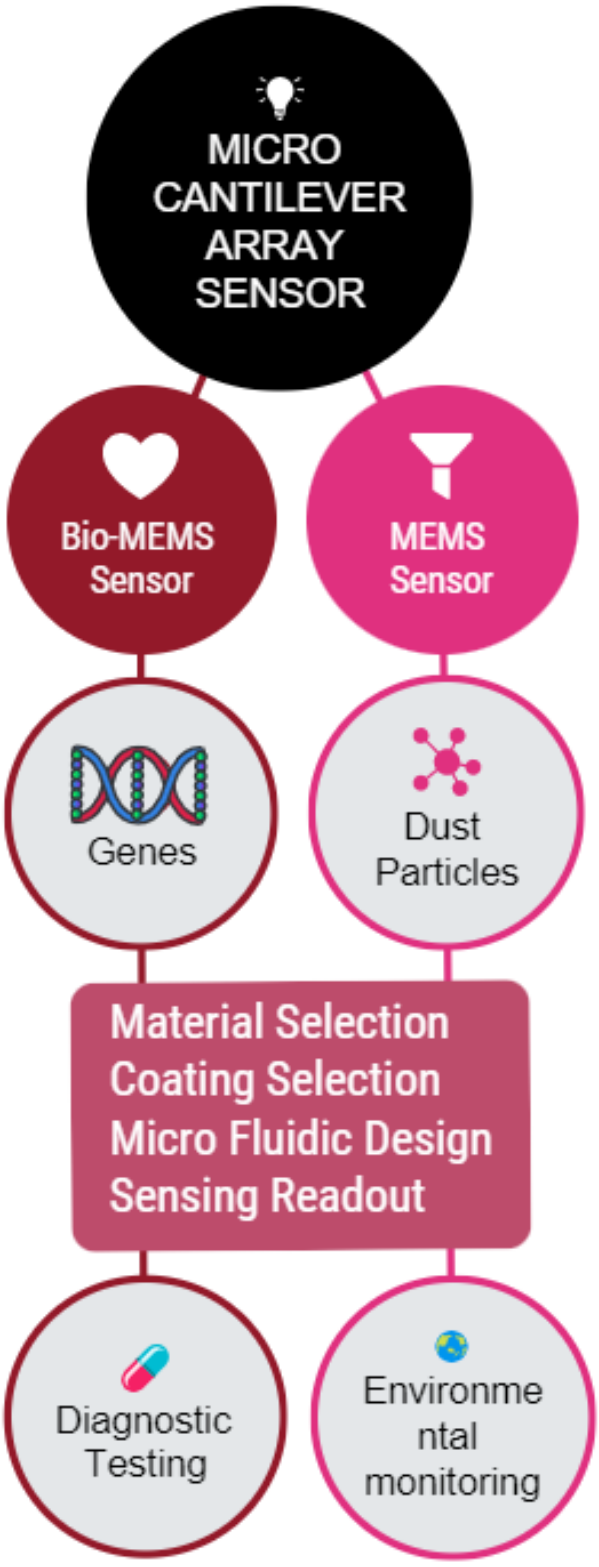

Figure 1.13: Design thinking Process

The Cantilever Microarray (CMA) is ready to revolutionize medical diagnostics. When CMs are functionalized with biological molecules, such as antibodies, they enable the detection of biomarkers in bio-fluids like blood and urine, offering advantages over traditional diagnostic technologies such

as ELISA. Notably, CMAs excel in multiplexed biomarker detection, high sensitivity, and label-free operation, and they hold promise for advancements in environmental monitoring, and detecting contaminants in water or air. CMAs offer multiple advantages over single-beam cantilevers: they boast enhanced sensitivity due to diverse cantilever geometries; they permit higher throughput with simultaneous multi-sample analysis; they provide redundancy ensuring reliability; and they exhibit versatility across varied applications [94, 95]. Conversely, while single-beam cantilevers are simpler and more economical, they may have limited sensitivity and selectivity.

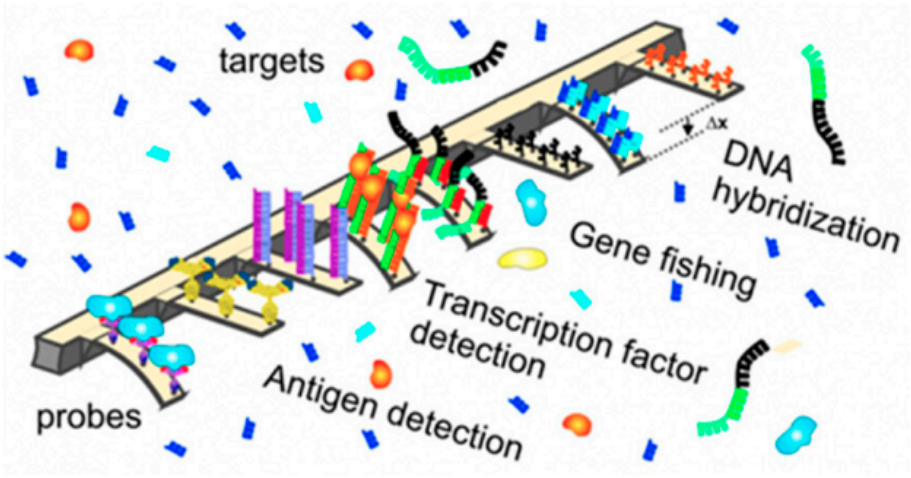

Figure 1.14: Arrays of beams[96]

The power of CMA lies in the synergy of multiple cantilevers, which amplifies sensitivity and accuracy. Furthermore, the failure of one doesn't incapacitate the entire system. Their flexibility, evidenced in figure 1.14, allows for diverse coatings on individual beams, catering to varied applications.

However, complexities in array fabrication might elevate costs and affect user-friendliness. High-density configurations could induce cross-talk between beams, potentially diminishing sensitivity and selectivity.

Resonant silicon microbeams, demonstrated as micro rheometers, excel in analyzing fluid properties over a broader frequency range compared to traditional rheometers. The resonant frequency, influenced by fluidic properties like viscosity and density, is a crucial parameter for these sensors.

Functionalization and Applications of Genetic-Probe-Integrated Microcantilever Arrays

Functionalizing the free end of a CM with a genetic probe expands its applicability to fields like chemical analysis, biological assays, pharmaceutical evaluations, and environmental assessments. Zhang et al.[97] elaborate on the CM sensor's genetic probe integration, detailing processes like probe immobilization, target hybridization, and signal processing.

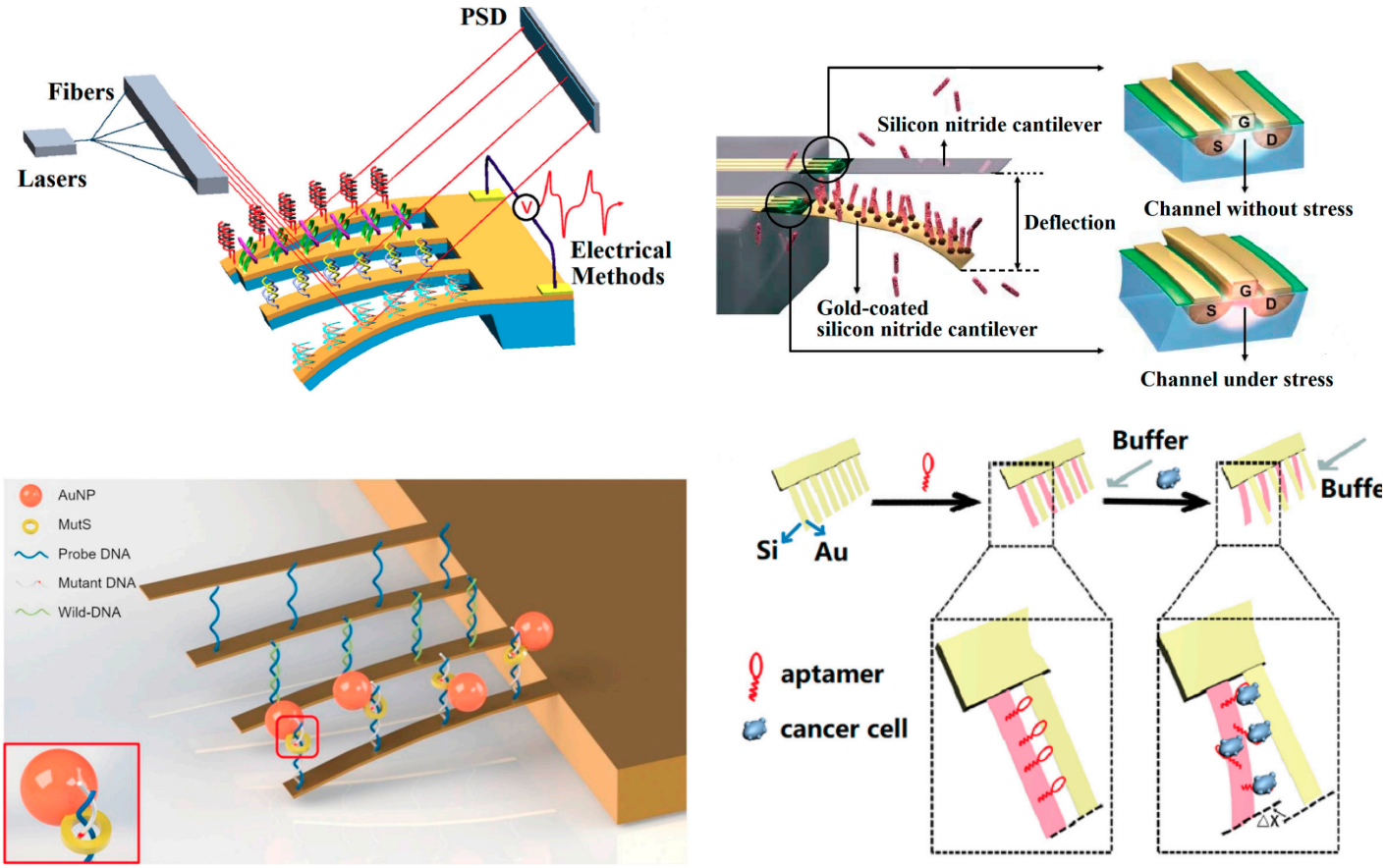

Figure 1.15: (A) The genetic-probe-modified CM sensor's detection process involves probe immobilization. (B) An advanced electrical signal extraction method is showcased, highlighting the probe-target molecule interaction in an embedded Metal–Oxide–Semiconductor Field-Effect Transistor (MOSFET) cantilever system. (C) The detection of KRAS mutations is depicted using MutS, AuNP, and resonators. (D) HepG2 cell detection using a CMA sensor is illustrated.[98]

This review emphasizes the potential of genetic-probe-modified CMs integrated with microfluidic chips, aiming to refine the CM design, elucidate its sensitivity mechanism, optimize design methodologies, broaden application scopes, and foster its real-world adoption.

When a CM is coated with a specific chemical receptor or sensing material, it is typically referred to as a "functionalized" or "modified" CM. The coating is designed to selectively interact with a specific target molecule, causing a change in the cantilever's mechanical or physical properties, which can then be measured and used to detect the presence and/or concentration of the target molecule. The specific coating used on a CM will depend on the target molecule being detected and the specific application of the sensor system.

Chemical Sensor Arrays (CSAs) based on cantilever technology is a type of sensor system that use arrays of CMs to detect and quantify the presence of various chemical species in a sample. Each cantilever in the array is coated with a specific chemical receptor that is designed to interact with a particular target molecule. When a target molecule binds to the receptor, it causes the cantilever to bend as depicted in fig.1.16 or change its resonance frequency, which can be detected and measured. CSAs are highly sensitive and can be used for a wide range of applications, including environmental

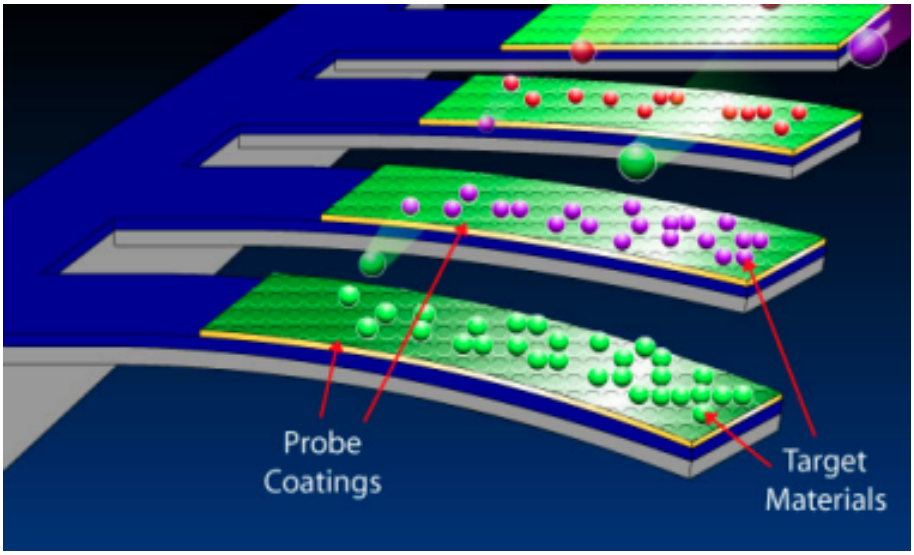

Figure 1.16: A CSAs with Discriminating Cantilever Coatings.(Microcantilever Applications Overview).

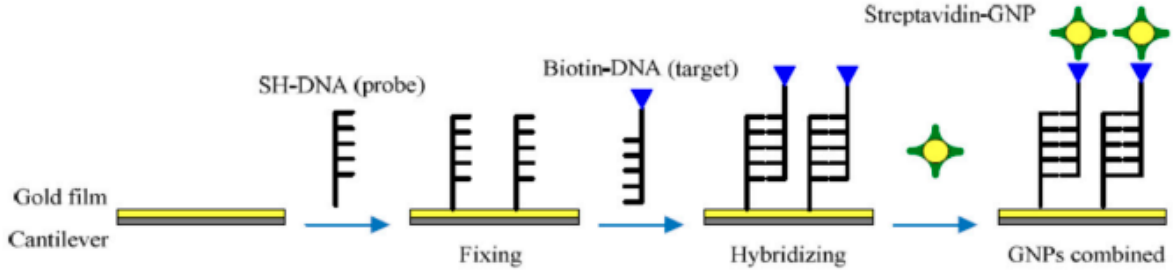

Figure 1.17: Processes of GNPs combine hybridization information.[99]

monitoring, food and water quality control, and biomedical diagnostics. One advantage of CSAs is their ability to detect multiple analytes simultaneously, allowing for more comprehensive and accurate analysis of complex samples. Additionally, the cantilever-based CSAs technology is label-free, meaning that it does not require the use of fluorescent or radioactive labels, which can simplify and speed up the analysis process. CM-based biosensors are a promising research area in the field of biosensors for detecting breast cancer biomarkers. In this approach, specific molecules are coated onto the CMs to bind to the biomarkers present in a sample, which alters the mechanical properties of the cantilever, and this change can be detected by advanced sensors. The advantages of this biosensor include high sensitivity and specificity, rapid response time, and portability, making it suitable for point-of-care testing and remote monitoring. To detect breast cancer biomarkers in dynamic mode, biological recognition molecules such as antibodies or aptamers are commonly used to specifically bind to the target biomarker, and the cantilever's mechanical response is measured as it binds and releases the target.

Here's the revised paragraph:

The selection of coating materials for CMs is paramount in determining their efficacy and function. Contrary to the claim, gold is often used as a coating material for CMs, particularly for surface

Material	Material Property		
	Young's Modulus(GPa)	Poisson's Ratio(V)	Density (Gm/Cc)
Silicon	170	0.26	2.32
Sio2	64	0.25	2.22
Al203	415	0	4
Porous Silicon	106.8	0	2.32
Ploy Silicon	160	0.22	2.32
Silica	73	0.17	2.20
Si3N4	315	0.27	3.18

Table 1.3: Table of materials used for sensing applications[100].

plasmon resonance (SPR) sensing, due to its ability to facilitate biological recognition when combined with specific capture molecules. A multitude of techniques, including cleaning, activation, immobilization, and characterization, are employed to graft biological recognition molecules onto silica CMs. Several materials, including silicon, polymers like PDMS and SU-8, gold, and graphene, have been utilized for CMs in exosome detection. Silicon stands out owing to its high stiffness, low thermal expansion coefficient, and fabrication ease, while polymers are favored for their biocompatibility and manufacturing simplicity. Additionally, graphene-based CMs are recognized for their high sensitivity and selectivity, a result of their substantial surface-to-volume ratio coupled with functionalization using exosome-specific capture molecules. The choice of material for CM beams targeting exosome detection in serum is influenced by a combination of factors, including application specificity, material expense, availability, and the requisite sensitivity and selectivity. An array of materials has been investigated for CM sensors. Predominantly, silicon and its derivatives like silicon nitride and silicon dioxide are preferred due to their elevated Q-values and minimal energy dissipation during resonance. Beyond these standard materials, magnetoelastic and piezoelectric materials offer distinct actuation and sensing attributes. Piezoelectric substances appear in various configurations, encompassing single crystals (e.g., Quartz), piezoceramics (PZT), thin films (like sputtered ZnO), and polymers, notably polyvinylidene fluoride (PVDF) and SU8.1.3 [100] provides a comprehensive list of commonly used materials for sensing applications. In general, materials that are biocompatible and have a high surface-to-volume ratio are preferred for detecting exosomes in serum. The surface of the CM is functionalized by attaching recognition molecules such as antibodies or aptamers to selectively bind to exosomes in the serum. Finally, an optical method such as surface plasmon resonance imaging (SPRi) is used to detect exosomes present in the sample.

A Lab On Chip (LOC) tailored for CM-based MEMS sensors amalgamates multiple lab processes onto a singular chip. This includes microfluidic channels for sample delivery, a CM for sensing dynamics, a signal transducer for resonance frequency detection, and integrated electronics for signal processing and analysis, as illustrated in figure 1.18. Consolidating these functionalities into one chip not only minimizes the sensor's footprint but also augments its sensitivity and accuracy. The entire developmental phase of a CM MEMS sensor LOC, spanning from design to application, mandates

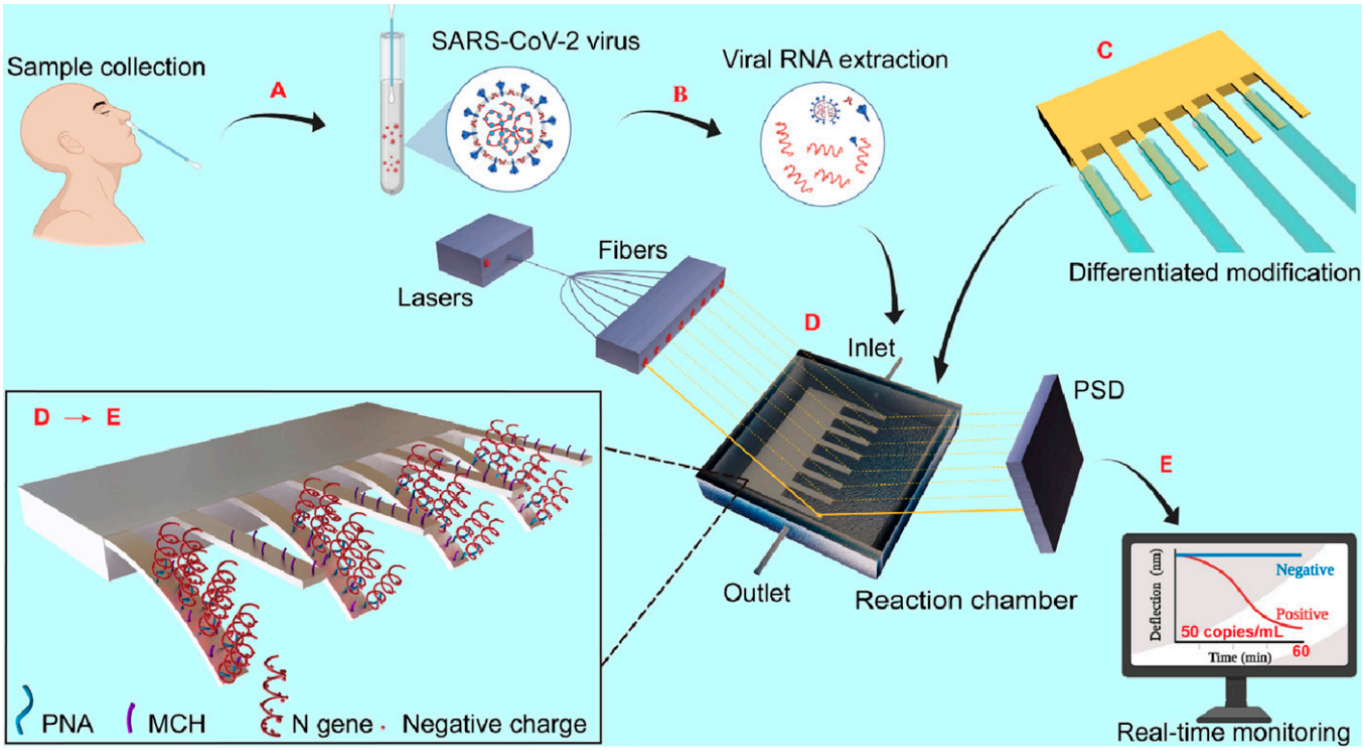

Figure 1.18: Nanomechanical method for SARS-CoV-2 detection. (A) Sample collection from infected subjects. (B) RNA extraction from the samples, pinpointing SARS-CoV-2 specific genetic material. (C) Functionalization of CMAs with PNA, enhancing their sensitivity to SARS-CoV-2 presence. Here, four CMs are functionalized with PNA, with another four serving as controls. (D) Use of nanomechanical devices to detect SARS-CoV-2 by directing a stable light beam onto each CM tip and monitoring CM deflection in real-time via a position-sensitive detector. (E) This technique allows for early COVID-19 diagnosis within 60 minutes.[101]

proficiency in microfabrication, sensor blueprinting, and signal analysis. The overarching aim is to produce a compact, integrated apparatus capable of discerningly and accurately identifying specific analytes or attributes in a given sample.

1.5.5 Limitations and Challenges

Because of their exceptional sensitivity and selectivity, CM-based sensors are widely used in a wide range of applications. To the fullest extent possible, they must overcome a multitude of obstacles and limitations that they face. The sensitivity of CM-based sensors is a major challenge, as table 1.4 illustrates. Although they are extremely sensitive to changes in mass, stiffness, and surface stress, they are also affected by environmental factors, most notably temperature and humidity. Such factors could compromise the sensor's accuracy and result in erroneous readings.

Authors	Dimensions (μm^3)	Frequency (KHz)/Mode	Responsivity	Read-Out
Braun et al. [102]	500 x 100 x 1 μm^3	750/13th OoP	400Hz/ng	*Optical*
Braun et al. [103]	500 x 100 x 1 μm^3	685/14th OoP	200Hz/ng	*Optical*
Davila et al. [104]	20 x 9 x 0.2 μm^3	–	100Hz/ng	*Optical*
Jensen et al. [105]	500 x 100 x 1 μm^3	640/14th OoP	250Hz/ng	*Optical*
Leahy et al. [106]	320 x 70 x 10 μm^3	1160/7th OoP	3KHz/ng	*Optical*
Tao et al. [107]	190 x 270 x 5 μm^3	436 IP	8.8Hz/ng	*Piezoresistive*
Tseng et al. [108]	500 x 100 x 1 μm^3	–	8.7Hz/ng	*Optical*
Walther et al. [109]	500 x 100 x 1 μm^3	370/10th OoP	220Hz/ng	*Optical*

Table 1.4: A summary of the important parameters discovered in previous investigations of microcantilevers for detecting mass in liquid surroundings. based on the research presented in [110]

Efforts are consistently made to enhance the sensitivity of CM-based sensors. New coatings aim to boost sensor specificity, while active feedback systems mitigate environmental disturbances. Challenges arise due to the need for precise fabrication of CMs, which can lead to disparities between devices. Additionally, drift in CMs could compromise long-term sensor stability. To counter this, enhancements in fabrication techniques and the adoption of active control strategies aim to preserve the cantilever's resonance frequency. Cutting-edge nanofabrication techniques are pursued to augment precision and uniformity while integrating CMs with electronics and microfluidics can enrich functionality. For example, electronics integration simplifies onboard signal processing, and pairing with microfluidics allows for continuous monitoring of intricate biological samples. We anticipate that future CM technology innovations will revolve around the development of novel materials offering superior sensitivity and selectivity, as well as the incorporation of emerging areas like optoelectronics and nanoelectronics. The potential for innovative applications, such as wearable and implanted devices, underscores the sustained relevance of CMs in sensing.

Undoubtedly, CM-based sensors have established a stronghold in materials science and biology. However, extant challenges inhibit their optimal performance. Future horizons encompass blending CM technology with avant-garde techniques, synthesizing unique materials, and exploring pioneering CM-based sensors. CMs, without a doubt, will be instrumental in the evolution of future sensing and measurement technologies.

CONCLUSION

The provided diagram1.19 offers a comprehensive overview of CM sensors, emphasizing their operational modes and readout methodologies. Central to the diagram is the Micro Cantilever, which primarily operates in two modes: Static and Dynamic. In the Static mode, the cantilever's position changes are detected using Piezoelectric, Piezoresistive, Optic (with OBDT and Diffraction sub-methods), and Capacitive methods. Conversely, the Dynamic mode explores the cantilever's oscillations, focusing on its Resonance Frequency and Impedance Sweeping, the latter of which delves into Harmonics Modes, Admittance, Reactance, and Resistance. Furthermore, the dynamic mode outlines various bending mechanisms like Lateral, Vertical, and Torsion bending. An integral part of this chart, Cantilever Readout, signifies the interpretation of these oscillations or deflections, primarily aiming at Detection Biomarkers. This capability underlines the sensor's importance in Biomedical Diagnostic applications, where specific biomarkers indicative of certain biological states, often related to diseases, can be identified.

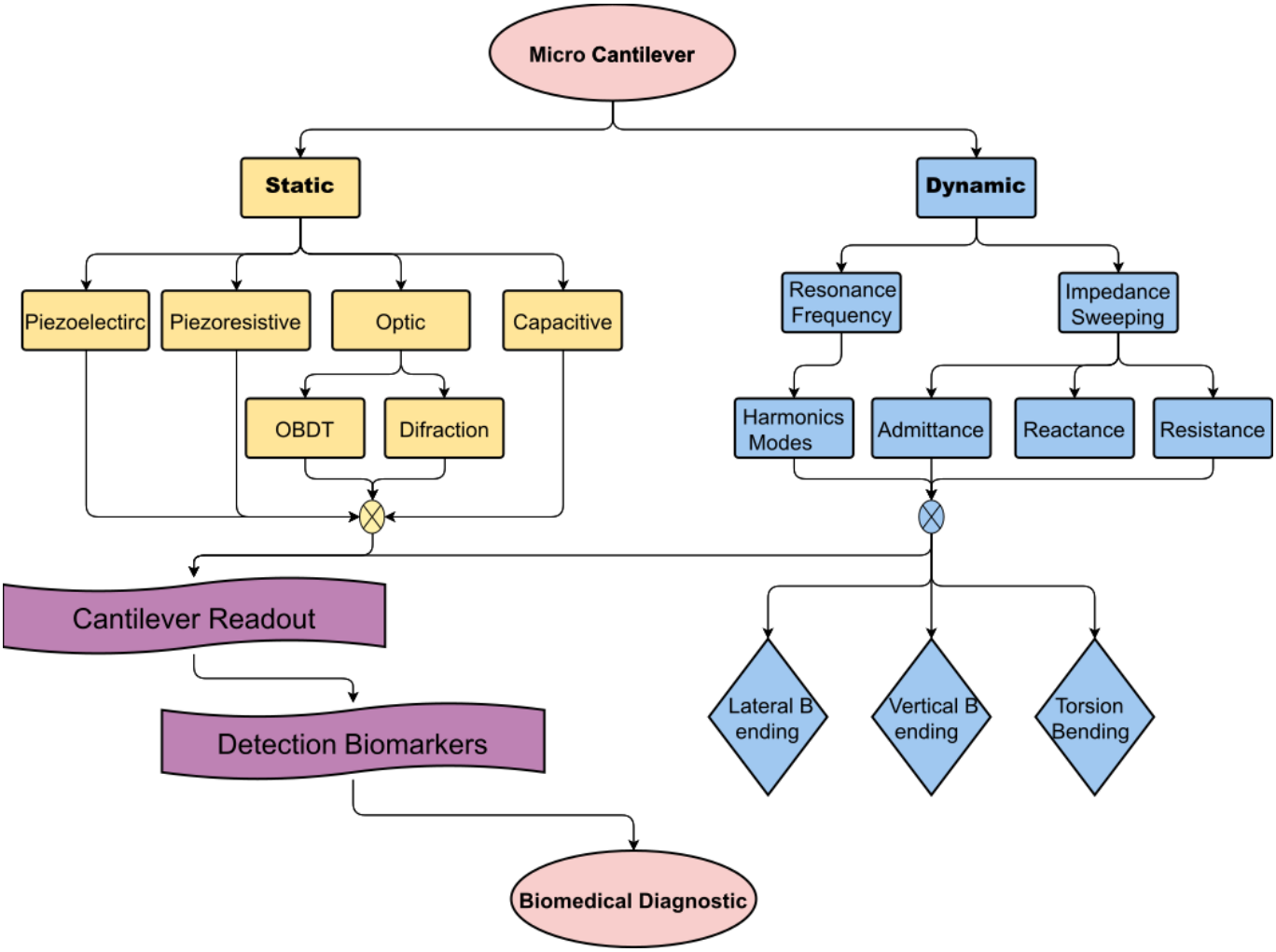

Figure 1.19: Categorization and Operational Modalities of Micro Cantilever Sensors in Biomedical Diagnostics

The rise of Micro Electro Mechanical Systems (MEMS) and BioMEMS technologies has driven

the demand for precise, affordable sensors suitable for tasks like environmental monitoring, chemical analysis, and biomedical diagnostics. Among these, Cantilever-based sensors (CMs) are distinguished by their exceptional sensitivity and vast detection range, making them suitable for detecting various chemicals and biomolecules. Their adaptability is evident in their widespread use in industries like medicine, food processing, and environmental research. Historically, researchers like Petersen et al. [111] and Howe et al.[112] in the 1980s emphasized silicon's potential as a mechanical material. The operational modes of CMs, both static and dynamic, have been rigorously explored, with various readout techniques, such as piezoresistive and optical methods, being examined. While advancements in fabrication techniques have streamlined the production of MEMS devices, challenges in sensitivity and integration persist. CMs excel in dynamic mode, capturing minute beam deflections due to particle interactions, indicating their potential in fluidic scenarios. Future research on CM and BioMEMS devices suggests a shift towards lab-on-a-chip systems and early disease detection, with a notable focus on detecting cancer biomarkers in body fluid using specialized sensors. The trip begins with the fundamental component in the drawn diagram: the CM. As we go, it becomes clear that the dynamic mode is where the CM functions most frequently, an area that highlights the complex oscillatory characteristics that characterize these sensors. Particular attention is given to the resonance frequency in this dynamic mode, which is an important characteristic that determines the cantilever's intrinsic vibration frequency. When we explore the resonance frequency further, we come across the harmonics mode, a complex subset that looks at the different overtones and undertones that exist outside of the fundamental frequency. Most importantly, the Laser Doppler Vibrometer (LDV), a precision device that can pick up even the smallest vibrations and deflections, is used to measure the harmonics mode. Our research contributes to micro-cantilever sensor technology through the development of a novel silicon CM sensor embedded with an electromechanical source. This innovative design significantly enhances fluid characterization by elevating the sensitivity and accuracy in detecting viscosity and density variations. We strategically employed vibratory microbeams as diagnostic sensors, favoring dynamic over static measurement modes. Notably, our approach of applying bidirectional stress and energy transfer to the microbeam, diverging from conventional unidirectional models, results in a more dynamic interaction and potentially heightens the sensor's responsiveness. This pioneering work in micro-cantilever technology, integrating advances in piezoelectric material positioning and hinge design, represents a substantial leap forward with wide-ranging applications in chemical analysis, biological testing, and environmental monitoring. Our design optimizes energy transfer and stress distribution, potentially revolutionizing the efficiency and precision of MEMS sensors.

Bibliography

[1] Hyuna Sung et al. "Global cancer statistics 2020: GLOBOCAN estimates of incidence and mortality worldwide for 36 cancers in 185 countries". In: *CA: a cancer journal for clinicians* 71.3 (2021), pp. 209–249.

[2] Rebecca L Siegel, Kimberly D Miller, and Ahmedin Jemal. "Cancer statistics, 2019". In: *CA: a cancer journal for clinicians* 69.1 (2019), pp. 7–34.

[3] HS Tan et al. "Risk factors for persistent pain after breast cancer surgery: a multicentre prospective cohort study". In: *Anaesthesia* (2023).

[4] Songtao Dong et al. "Emerging role of natural products in cancer immunotherapy". In: *Acta Pharmaceutica Sinica B* 12.3 (2022), pp. 1163–1185.

[5] Mary Beth Nierengarten. *Annual report to the nation on the status of cancer: This latest report, a collaboration from the American Cancer Society, the Centers for Disease Control and Prevention, the National Cancer Institute, and the North American Association of Central Cancer Registries, shows that cancer mortality rates have accelerated, and incidence rates remain stable, with pancreatic cancer showing an increase in both incidence and mortality*. 2023.

[6] Hao Jin et al. "Risk factors from Framingham risk score for anthracyclines cardiotoxicity in breast cancer: A systematic review and meta-analysis". In: *Frontiers in Cardiovascular Medicine* 10 (2023).

[7] Louiza S Velentzis et al. "Breast Cancer Risk Assessment Tools for Stratifying Women into Risk Groups: A Systematic Review". In: *Cancers* 15.4 (2023), p. 1124.

[8] Adrienne G Waks and Eric P Winer. "Breast cancer treatment: a review". In: *Jama* 321.3 (2019), pp. 288–300.

[9] Fabien Mignot et al. "Ten-year outcomes of hypofractionated postmastectomy radiation therapy of 26 Gy in 6 fractions". In: *International Journal of Radiation Oncology* Biology* Physics* 112.5 (2022), pp. 1105–1114.

[10] Junjie Zhao et al. "Exosome-driven liquid biopsy for breast cancer: recent advances in isolation, biomarker identification and detection". In: *Extracellular Vesicle* 1 (2022), p. 100006.

[11] Jana Biermann et al. "A Novel 18-Marker Panel Predicting Clinical Outcome in Breast Cancer-Predictive Model for Clinical Outcome in Breast Cancer". In: *Cancer Epidemiology, Biomarkers & Prevention* 26.11 (2017), pp. 1619–1628.

[12] James K Gimzewski et al. "Observation of a chemical reaction using a micromechanical sensor". In: *Chemical Physics Letters* 217.5-6 (1994), pp. 589–594.

[13] RT Howe and RS Muller. "Polycrystalline and amorphous silicon micromechanical beams: annealing and mechanical properties". In: *Sensors and Actuators* 4 (1983), pp. 447–454.

[14] Victory Elias et al. "Investigation of the Eigen Frequency of a Cantilever Microbeam Immersed in a Fluid Under the Piezoelectric Effect". In: (2021).

[15] JJ Ruz et al. *A Review on Theory and Modelling of Nanomechanical Sensors for Biological Applications. Processes 2021, 9, 164*. 2021.

[16] Julien Chaste et al. "A nanomechanical mass sensor with yoctogram resolution". In: *Nature nanotechnology* 7.5 (2012), pp. 301–304.

[17] Jacob Thaysen et al. "Polymer-based stress sensor with integrated readout". In: *Journal of Physics D: Applied Physics* 35.21 (2002), p. 2698.

[18] Cornelis A Van Eysden and John E Sader. "Resonant frequencies of a rectangular cantilever beam immersed in a fluid". In: *Journal of applied physics* 100.11 (2006), p. 114916.

[19] Alexa W Hudnut. "High-Resolution Optical Instrumentation for Biosensing and Biomechanical Characterization". PhD thesis. University of Southern California, 2018.

[20] Giulio Brunetti et al. "Nanotechnological immunoassay for rapid label-free analysis of candidate malaria vaccines". In: *Nanoscale* 13.4 (2021), pp. 2338–2349.

[21] I Stachiv et al. "Exploiting NiTi shape memory alloy films in design of tunable high frequency microcantilever resonators". In: *Applied Physics Letters* 111.21 (2017), p. 213105.

[22] Daniela Kunkel Muenchen et al. "Pesticide Detection in Soil Using Biosensors and Nanobiosensors." In: *Biointerface Research in Applied Chemistry* 6.6 (2016).

[23] Carlo Ricciardi et al. "Microcantilever resonator arrays for immunodetection of β-lactoglobulin milk allergen". In: *Sensors and Actuators B: Chemical* 254 (2018), pp. 613–617.

[24] N Siddaiah and T Vamsi Aravind Swamy. "Material optimization of the novel cantilever based RF MEMS switch for mobile communication". In: *Transactions on Electrical and Electronic materials* 20 (2019), pp. 350–358.

[25] Daniel J Müller et al. "Atomic force microscopy-based force spectroscopy and multiparametric imaging of biomolecular and cellular systems". In: *Chemical Reviews* 121.19 (2020), pp. 11701–11725.

[26] Jiushuai Xu et al. "Piezoresistive microcantilevers for humidity sensing". In: *Journal of Micromechanics and Microengineering* 29.5 (2019), p. 053003.

[27] Jiushuai Xu et al. “Fabrication of ZnO nanorods on MEMS piezoresistive silicon microcantilevers for environmental monitoring”. In: *Proceedings*. Vol. 1. 4. MDPI. 2017, p. 290.

[28] Masaaki Aramaki et al. “Demonstration of high-performance piezoelectric MEMS vibration energy harvester using BiFeO3 film with improved electromechanical coupling factor”. In: *Sensors and Actuators A: Physical* 291 (2019), pp. 167–173.

[29] Kirill Zinoviev et al. “A novel optical waveguide microcantilever sensor for the detection of nanomechanical forces”. In: *Journal of Lightwave Technology* 24.5 (2006), p. 2132.

[30] Lee MacKenzie Fischer et al. “Development of a microfabricated electrochemical-cantilever hybrid platform”. In: *Sensors and Actuators B: Chemical* 157.1 (2011), pp. 321–327.

[31] Louizos-Alexandros Louizos, Panagiotis G Athanasopoulos, and Kevin Varty. “Microelectromechanical systems and nanotechnology: a platform for the next stent technological era”. In: *Vascular and endovascular surgery* 46.8 (2012), pp. 605–609.

[32] Jiri Marek. “MEMS for automotive and consumer electronics”. In: *2010 IEEE International Solid-State Circuits Conference-(ISSCC)*. IEEE. 2010, pp. 9–17.

[33] Mahammadrafeeq Manvi and KB Mruthyunjaya Swamy. “Microelectronic materials, microfabrication processes, micromechanical structural configuration based stiffness evaluation in MEMS: A review”. In: *Microelectronic Engineering* (2022), p. 111854.

[34] Jian Zhang et al. “Real-time Cd2+ detection at sub-femtomolar level in various liquid media by an aptasensor integrated with microfluidic enrichment”. In: *Sensors and Actuators B: Chemical* 329 (2021), p. 129282.

[35] Shuyun Wu et al. “MEMS flow sensors for nano-fluidic applications”. In: *Sensors and Actuators A: Physical* 89.1-2 (2001), pp. 152–158.

[36] John-Ojur Dennis, Abdelaziz-Yousif Ahmed, and Mohd-Haris Khir. “Fabrication and characterization of a CMOS-MEMS humidity sensor”. In: *Sensors* 15.7 (2015), pp. 16674–16687.

[37] Anwarul Hasan et al. “Recent advances in application of biosensors in tissue engineering”. In: *BioMed research international* 2014 (2014).

[38] Aviru Kumar Basu et al. “Fabrication processes for sensors for automotive applications: A review”. In: *Sensors for automotive and aerospace applications* (2019), pp. 123–142.

[39] IV Shishkovsky and PN Lebedev. “Chemical and physical vapor deposition methods for nanocoatings”. In: *Nanocoatings and ultra-thin films*. Elsevier, 2011, pp. 57–77.

[40] Kang Rao et al. “A MEMS micro-g capacitive accelerometer based on through-silicon-wafer-etching process”. In: *Micromachines* 10.6 (2019), p. 380.

[41] J Braeuer et al. “A novel technique for MEMS packaging: Reactive bonding with integrated material systems”. In: *Sensors and Actuators A: Physical* 188 (2012), pp. 212–219.

[42] Minhang Bao. "Chapter 1 - Introduction to MEMS Devices". In: *Analysis and Design Principles of MEMS Devices*. Ed. by Minhang Bao. Amsterdam: Elsevier Science, 2005, pp. 1–32. ISBN: 978-0-444-51616-9. DOI: https://doi.org/10.1016/B978-044451616-9/50002-3. URL: https://www.sciencedirect.com/science/article/pii/B9780444516169500023.

[43] Seung Eon Moon et al. "Semiconductor-Type MEMS Gas Sensor for Real-Time Environmental Monitoring Applications". In: *Etri Journal* 35.4 (2013), pp. 617–624.

[44] Robert Neal Dean and Antonio Luque. "Applications of microelectromechanical systems in industrial processes and services". In: *IEEE Transactions on Industrial Electronics* 56.4 (2009), pp. 913–925.

[45] Gastone Ciuti et al. "MEMS sensor technologies for human centred applications in healthcare, physical activities, safety and environmental sensing: A review on research activities in Italy". In: *Sensors* 15.3 (2015), pp. 6441–6468.

[46] Dennis L Polla. "MEMS technology for biomedical applications". In: *2001 6th International Conference on Solid-State and Integrated Circuit Technology. Proceedings (Cat. No. 01EX443)*. Vol. 1. IEEE. 2001, pp. 19–22.

[47] Xiaofeng Wei et al. "Positioning Algorithm of MEMS Pipeline Inertial Locator Based on Dead Reckoning and Information Multiplexing". In: *Electronics* 11.18 (2022), p. 2931.

[48] Neeti Sharma, BD Pant, and Jyoti Mathur. "MEMS devices used in agriculture—a review". In: *Journal of Biosensors and Bioelectronics* 10.1 (2019), pp. 1–4.

[49] Geeta Bhatt et al. "MEMS sensors for automotive applications: A review". In: *Sensors for Automotive and Aerospace Applications* (2019), pp. 223–239.

[50] Claudio Abels et al. "Nitride-based materials for flexible MEMS tactile and flow sensors in robotics". In: *Sensors* 17.5 (2017), p. 1080.

[51] Roman Berevsik, Jozef Puttera, and Frantisvek Nebus. "Seismic sensor system for security applications based on MEMS accelerometer". In: *2014 International Conference on Applied Electronics*. IEEE. 2014, pp. 31–36.

[52] Maxence Rube et al. "Unconventional protocol for SAW sensor: multi-physic response enrichment in liquid medium". In: *IEEE Sensors Journal* 22.12 (2021), pp. 11345–11354.

[53] Karen M Goeders, Jonathan S Colton, and Lawrence A Bottomley. "Microcantilevers: sensing chemical interactions via mechanical motion". In: *Chemical reviews* 108.2 (2008), pp. 522–542.

[54] Matas Calcerrada, Carmen Garca-Ruiz, and Miguel Gonzlez-Herrez. "Chemical and biochemical sensing applications of microstructured optical fiber-based systems". In: *Laser & Photonics Reviews* 9.6 (2015), pp. 604–627.

[55] Shavkat Nizamov, Simona Dimchevska Sazdovska, and Vladimir M Mirsky. "A review of optical methods for ultrasensitive detection and characterization of nanoparticles in liquid media with a focus on the wide field surface plasmon microscopy". In: *Analytica Chimica Acta* (2022), p. 339633.

[56] Moussa Hoummady, Andrew Campitelli, and Wojtek Wlodarski. "Acoustic wave sensors: design, sensing mechanisms and applications". In: *Smart materials and structures* 6.6 (1997), p. 647.

[57] Isabelle Dufour et al. "Unconventional uses of microcantilevers as chemical sensors in gas and liquid media". In: *Sensors and Actuators B: Chemical* 170 (2012), pp. 115–121.

[58] Qazi Adnan Ahmad et al. "Numerical simulation and modeling of a poroelastic media for detection and discrimination of geo-fluids using finite difference method". In: *Alexandria Engineering Journal* 61.5 (2022), pp. 3447–3462.

[59] Tao Wang et al. "Second-order correlation function supported optical sensing for particle detection". In: *IEEE Sensors Journal* 21.18 (2021), pp. 19948–19958.

[60] Rasmus Johansen et al. "An in-line, high-flowrate, and maintenance free ultrasonic sensor with a high dynamic range for particle monitoring in fluids". In: *IEEE Sensors Journal* 18.6 (2018), pp. 2299–2304.

[61] Yi-Ting Chen et al. "Biosensing using magnetic particle detection techniques". In: *Sensors* 17.10 (2017), p. 2300.

[62] Sophia Nazir and Oh Seok Kwon. "Micro-electromechanical systems-based sensors and their applications". In: *Applied Science and Convergence Technology* 31.2 (2022), pp. 40–45.

[63] Parul Singh, Pankaj B Agarwal, et al. "A comprehensive review on MEMS-based viscometers". In: *Sensors and Actuators A: Physical* (2022), p. 113456.

[64] Gopikrishnan Soundararajan et al. "MEMS shear stress sensors for cardiovascular diagnostics". In: *The 26th Annual International Conference of the IEEE Engineering in Medicine and Biology Society*. Vol. 1. IEEE. 2004, pp. 2420–2423.

[65] Tingting Chen et al. "Design and analysis of particulate matter air-microfluidic grading chip based on MEMS". In: *Micromachines* 10.8 (2019), p. 497.

[66] Keiichi Higashino et al. "Self-excited vibrational cantilever-type viscometer driven by piezoactuator". In: *Journal of Vibration and Acoustics* 137.6 (2015).

[67] Tomas Manzaneque et al. "Piezoelectric MEMS resonator-based oscillator for density and viscosity sensing". In: *Sensors and Actuators A: Physical* 220 (2014), pp. 305–315.

[68] Murali Krishna Ghatkesar et al. "Multi-parameter microcantilever sensor for comprehensive characterization of Newtonian fluids". In: *Sensors and Actuators B: Chemical* 135.1 (2008), pp. 133–138.

[69] Y Oni et al. “Effects of temperature on diffusion from PNIPA-based gels in a BioMEMS device for localized chemotherapy and hyperthermia”. In: *Materials Science and Engineering: C* 31.2 (2011), pp. 67–76.

[70] Florent Cros. “BioMEMS”. In: *Biomedical Materials* (2021), pp. 581–620.

[71] M Birkholz et al. “Sensing glucose concentrations at GHz frequencies with a fully embedded Biomicro-electromechanical system (BioMEMS)”. In: *Journal of Applied Physics* 113.24 (2013), p. 244904.

[72] Hung Cao et al. “Development and characterization of a novel interdigitated capacitive strain sensor for structural health monitoring”. In: *IEEE Sensors Journal* 15.11 (2015), pp. 6542–6548.

[73] Ioanna Giouroudi, Jurgen Kosel, and Cornie Scheffer. “BioMEMS in diagnostics: A review and recent developments”. In: *Recent patents on engineering* 2.2 (2008), pp. 114–121.

[74] Sam Kassegne et al. “High-efficiency microarray of 3-D carbon MEMS electrodes for pathogen detection systems”. In: *Optomechatronic Technologies 2008*. Vol. 7266. SPIE. 2008, pp. 358–363.

[75] Zeynep Caglayan, Yagmur Demircan Yalgn, and Haluk Kulah. “A prominent cell manipulation technique in BioMEMS: dielectrophoresis”. In: *Micromachines* 11.11 (2020), p. 990.

[76] Sheeny Lan, Mandana Veiseh, and Miqin Zhang. “Surface modification of silicon and gold-patterned silicon surfaces for improved biocompatibility and cell patterning selectivity”. In: *Biosensors and Bioelectronics* 20.9 (2005), pp. 1697–1708.

[77] Jiahui Cai and Aurelian Bidulescu. “The association between food insecurity and cognitive impairment among the US adults: The mediation role of anxiety or depression”. In: *Journal of Affective Disorders* (2023).

[78] Suiling Wang and Catherine N Mulligan. “Occurrence of arsenic contamination in Canada: sources, behavior and distribution”. In: *Science of the total Environment* 366.2-3 (2006), pp. 701–721.

[79] Robert Langs. *Death anxiety and clinical practice*. Routledge, 2018.

[80] Stanislav L Karsten et al. “Point-of-care (POC) devices by means of advanced MEMS”. In: *Talanta* 145 (2015), pp. 55–59.

[81] A Adami et al. “Development of MEMS microcantilever detectors for DNA single nucleotide polymorphism detection in autoimmune diseases diagnostic”. In: *Sensors and Microsystems: AISEM 2009 Proceedings*. Springer, 2009, pp. 335–338.

[82] LP Lee et al. “High aspect ratio polymer microstructures and cantilevers for bioMEMS using low energy ion beam and photolithography”. In: *Sensors and Actuators A: Physical* 71.1-2 (1998), pp. 144–149.

[83] Younan Xia and George M Whitesides. “Soft lithography”. In: *Annual review of materials science* 28.1 (1998), pp. 153–184.

[84] Jae Ho Lee, James Castracane, and Anand Gadre. "Structural and electrical properties of conductive polymeric aligned nanofibers via electrospinning". In: *Microfluidics, BioMEMS, and Medical Microsystems V*. Vol. 6465. SPIE. 2007, pp. 221–229.

[85] Yudhishthir Pandey and Surya Prakash Singh. "Recent Advances in Bio-MEMS and Future Possibilities: An Overview". In: *Journal of The Institution of Engineers (India): Series B* 104.6 (2023), pp. 1377–1388.

[86] Ayobami Elisha Oseyemi, Ion Stiharu, and Muthukumaran Packirisamy. "Design and parametric study of a tapered polymer-based suspended microfluidic channel for enhanced detection of biofluids and bioparticles". In: *Microsystem Technologies* 29.5 (2023), pp. 715–727.

[87] Khalid Mohd Ibrahimi et al. "Enhanced Design and Analysis of the Microcantilever-Based Bio-Sensor to Detect Carcinoembryonic Antigen Tumor Biomarkers". In: *Computer Assisted Methods in Engineering and Science* 30.3 (2023), pp. 347–367.

[88] Dumitru I Caruntu and Israel Martinez. "Reduced order model of parametric resonance of electrostatically actuated MEMS cantilever resonators". In: *International Journal of Non-Linear Mechanics* 66 (2014), pp. 28–32.

[89] Marius Pustan, Véronique Rochus, and Jean-Claude Golinval. "Mechanical and tribological characterization of a thermally actuated MEMS cantilever". In: *Microsystem technologies* 18 (2012), pp. 247–256.

[90] Chuming Zhao, Katherine E Knisely, and Karl Grosh. "Design and fabrication of a piezoelectric MEMS xylophone transducer with a flexible electrical connection". In: *Sensors and Actuators A: Physical* 275 (2018), pp. 29–36.

[91] Matthieu Gaudet and Steve Arscott. "Optical actuation of microelectromechanical systems using photoelectrowetting". In: *Applied Physics Letters* 100.22 (2012), p. 224103.

[92] Karolina Orlowska et al. "A method of magnetic field measurement in a scanning electron microscope using a microcantilever magnetometer". In: *Metrology and Measurement Systems* 27.1 (2020), pp. 141–149.

[93] Qing-Ming Wang et al. "Electromechanical coupling and output efficiency of piezoelectric bending actuators". In: *IEEE transactions on ultrasonics, ferroelectrics, and frequency control* 46.3 (1999), pp. 638–646.

[94] Mohd Zahid Ansari et al. "Comparison between deflection and vibration characteristics of rectangular and trapezoidal profile microcantilevers". In: *Sensors* 9.4 (2009), pp. 2706–2718.

[95] Sandeep Kumar Vashist. "A review of microcantilevers for sensing applications". In: *J. of Nanotechnology* 3 (2007), pp. 1–18.

[96] Gengfeng Zheng et al. "Multiplexed electrical detection of cancer markers with nanowire sensor arrays". In: *Nature biotechnology* 23.10 (2005), pp. 1294–1301.

[97] He Zhang et al. “A Genosensor Based on the Modification of a Microcantilever: A Review”. In: *Micromachines* 14.2 (2023), p. 427.

[98] Chanho Park et al. “Highly sensitive and selective detection of single-nucleotide polymorphisms using gold nanoparticle MutS enzymes and a micro cantilever resonator”. In: *Talanta* 205 (2019), p. 120154.

[99] Yue Tao Ge et al. “Study on gold nanoparticles aggravating MEMS cantilever gene detection biosensor”. In: *Applied Mechanics and Materials*. Vol. 336. Trans Tech Publ. 2013, pp. 148–152.

[100] A Nallathambi and T Shanmuganantham. “Performance analysis of cantilever based MEMS sensor for environmental applications”. In: *2014 International Conference on Smart Structures and Systems (ICSSS)*. IEEE. 2014, pp. 118–122.

[101] Yu Wang et al. “Nanomechanical assay for ultrasensitive and rapid detection of SARS-CoV-2 based on peptide nucleic acid”. In: *Nano Research* (2022), pp. 1–13.

[102] Thomas Braun et al. “Quantitative time-resolved measurement of membrane protein–ligand interactions using microcantilever array sensors”. In: *Nature nanotechnology* 4.3 (2009), pp. 179–185.

[103] Martin Hegner. “Quantitative time-resolved measurement of membrane protein–ligand interactions using microcantilever array sensors”. In: (2009).

[104] Angelica P Davila et al. “Microresonator mass sensors for detection of Bacillus anthracis Sterne spores in air and water”. In: *Biosensors and Bioelectronics* 22.12 (2007), pp. 3028–3035.

[105] Jason Jensen et al. “Quantitative, label-free detection of the aggregation of α-synuclein using microcantilever arrays operated in a liquid environment”. In: *Journal of Sensors* 2012 (2012).

[106] Stephane Leahy and Yongjun Lai. “A cantilever biosensor exploiting electrokinetic capture to detect Escherichia coli in real time”. In: *Sensors and Actuators B: Chemical* 238 (2017), pp. 292–297.

[107] Yihan Tao et al. “Resonant cantilever sensors operated in a high-Q in-plane mode for real-time bio/chemical detection in liquids”. In: *Sensors and actuators B: Chemical* 157.2 (2011), pp. 606–614.

[108] You-Chen Tseng et al. “3, 4-Methylenedioxymethylamphetamine detection using a microcantilever-based biosensor”. In: *Sensors and Actuators A: Physical* 182 (2012), pp. 163–167.

[109] Michael Walther et al. “An optimized measurement chamber for cantilever array measurements in liquid incorporating an automated sample handling system”. In: *EPJ Techniques and Instrumentation* 2 (2015), pp. 1–24.

[110] Florian Patocka et al. “Novel resonant MEMS sensor for the detection of particles with dielectric properties in aged lubricating oils”. In: *Sensors and Actuators A: Physical* 315 (2020), p. 112290.

[111] Kurt E Petersen. “Silicon as a mechanical material”. In: *Proceedings of the IEEE* 70.5 (1982), pp. 420–457.

[112] RT Howe and RS Muller. “Polycrystalline silicon micromechanical beams”. In: *Journal of the Electrochemical Society* 130.6 (1983), p. 1420.

Chapter 2

Modeling approach

The theoretical basis and modeling of a suggested cantilever microbeam submerged in an incompressible Newtonian fluid and measured in dynamic mode are presented in this chapter. This arrangement allows for the accurate identification and measurement of dust particles and biological compounds in fluids. We can determine the composition of the fluid by using equations that regulate resonant systems, such as resonance frequency and $Q - factor$. Likewise, taking into account the mechanical characteristics of the CMs, like mass and rigidity, offers additional understanding of the nature of the fluid. Gaining an in-depth knowledge of fluid mechanics is essential to determine how materials in the fluid affect the CMs' resonance frequency. By use of mathematical modeling, we anticipate the behavior of the system in different scenarios, so improving our understanding of the detection mechanism. This part of work provides also a thorough explanation of the history and intricate ideas behind cantilever microbeam arrays, which are well-known for being effective instruments in the study of physics, chemistry, and microbiology. We discuss the dynamic behavior of cantilever microbeams in air, vacuum, and fluid environments. The material includes theoretical explanations of the observed variations in dust particle or biochemical concentration that result from microbeam interactions with fluidic velocity, density, and viscosity. Readers will gain a thorough understanding of the fundamental concepts and operation of cantilever microbeam arrays from this session.

2.1 Dynamic Mode Theory

CM beams are small beam-like structures that are used in the research of MEMS and nanotechnology. Lord Rayleigh proposed them in the late 1800s, but they only became a research tool in the 1980s with the development of microfabrication techniques. Researchers began investigating the use of CM beams as sensors in the 1990s, specifically for chemical and biological detection, after initially using them for AFM. They are now used for a variety of purposes, including microfluidics and energy harvesting. CMA sensors were first introduced in the late 1990s to detect small molecules in a highly sensitive and selective manner. Surface functionalization, nanomechanical resonators, and

piezoelectric sensing elements have improved these sensors, allowing them to be widely used in environmental monitoring, chemical sensing, biomedical diagnostics, and other applications. Dynamic mode research entails key concepts and theories such as dynamics, feedback, control systems, stability, and stability analysis. Mathematical models, such as differential equations and transfer functions, are used to analyze and predict the system's response to various inputs and disturbances. The frequency response of a system characterizes its ability to respond to different frequencies of input, indicating its adaptability. The ability of a system to respond and adjust to changes determines its dynamic mode, which can be evaluated using mathematical models and frequency response.

The first reference by Albrecht et al. in 1991[1] describes the use of frequency modulation detection using high-Q cantilevers to achieve sub-Angstrom sensitivity in the detection of surface forces. This technique was a significant improvement over traditional contact mode AFM, which had limited sensitivity due to the relatively low $Q - factor$ of the cantilever oscillation. The subsequent references by Hansma et al. [2], and Betzig et al. [3] discuss various applications of dynamic mode AFM, including imaging of biological molecules and breaking the diffraction barrier in optical microscopy. Together, these references demonstrate the broad impact of dynamic mode AFM in advancing our understanding of materials and biological systems at the nanoscale.When the CM is excited, it vibrates at a natural frequency that is determined by its physical properties, such as its length, thickness, and material composition. When the CM is brought close to a sample surface, it can interact with the surface through various physical mechanisms, such as van der Waals forces, electrostatic forces, or chemical interactions. This interaction can cause a change in the natural frequency of the CM, which is known as a frequency shift as depicted in fig2.1.

The dynamic mode of a CM is a key concept for the quantification of biochemical substances in

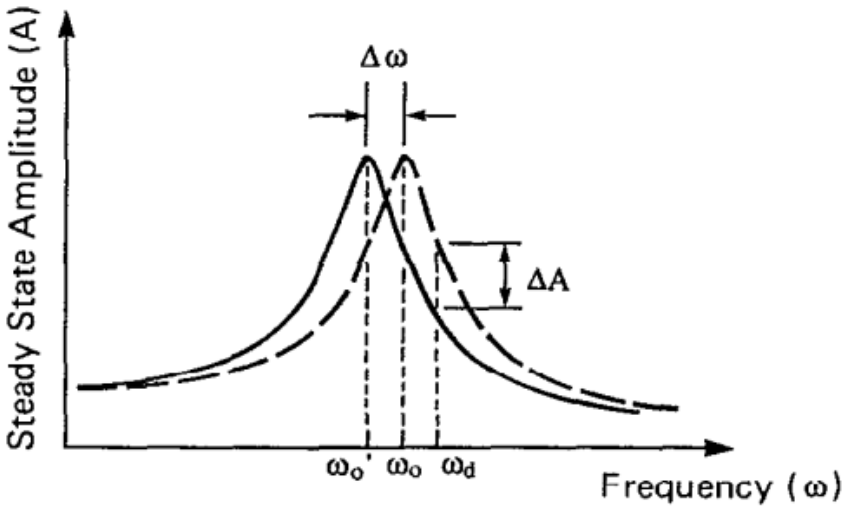

Figure 2.1: The cantilever in a slope detection system is operated at a fixed frequency w_d, that is slightly off-resonance, and it undergoes a change in its resonant frequency from w_0 to w_0' due to a variation in the force gradient. This, in turn, leads to a modification in the steady-state amplitude by an amount of ΔA [1].

a specific medium. In this mode, the microbeam is designed to vibrate at its natural resonant frequency, and changes in resonant frequency are measured as the substance binds to its surface. This method can be used for the early diagnosis of diseases, where the presence of specific biochemical substances can indicate disease onset. However, there are challenges associated with using resonant microbeams for biochemical detection in biological fluids, such as the need to minimize non-specific binding and interference from other substances present in the fluid. Furthermore, additional research and development are needed to optimize the design and performance of the biosensor for clinical applications. This process provides a highly sensitive and specific detection method for quantifying biochemical substances in a specific medium.

To achieve an effective quantification process using a CM, it is crucial to understand the dynamic mode and the factors that affect it. One important factor is the damping effect, which can affect in the amplitude of the microbeam's oscillation and its resonant frequency. The damping effect is dependent on the medium surrounding the microbeam and the properties of the substance being detected. Another important factor is the Quality Factor (Q-factor) of the microbeam, which is a measure of its energy dissipation per oscillation cycle. A higher $Q-factor$ corresponds to a narrower resonance peak and a higher sensitivity for detecting small changes in the resonant frequency [4]. The $Q-factor$ is dependent on the CM physical properties and the surrounding medium characteristics. The dynamic mode of a CM can be analyzed using mathematical models such as the Euler-Bernoulli beam theory and the harmonic oscillator model. These models can provide insight into the microbeam's behavior and help optimize its design for specific applications. Understanding the dynamic mode of a CM is crucial for the quantification of biochemical substances in a specific medium. The damping effect and $Q-factor$ are important factors to consider when designing and optimizing the microbeam for specific applications, and mathematical models can be used to analyze and predict its behavior.

2.1.1 Modeling of cantilever behavior

Several works have investigated vibrating cantilever beams immersed in fluid as it has a wide range of practical applications. Chu [5] uses an incompressible and inviscid fluid where the cantilever is totally immersed, which makes it a useful theoretical model for cantilevers of macroscopic size. The effects of fluid viscosity have become increasingly important in recent developments in microelectromechanical systems MEMS and applications such as the atomic force microscope AFM. Several practical applications have led to a vast history of research into vibrating cantilever beams immersed in a fluid. In addition to ultrasensitive mass measurements, CM beams are used in molecular and atomic scale imaging [6]. A rectangular CM immersed in a viscous fluid was derived by Sader [7]. The model for rectangular cantilevers vibrating in various mediums is described in this section. Many assumptions regarding the model are made to make the analysis practicable. To begin as shown in figure2.2, it is assumed that the cross-section of the beam is uniform along its length and

rectangular in shape. The beam's length L is considerably greater than its breadth b, and its width is much greater than its thickness h. This simplifies the analysis and makes analytical expressions possible. Finally, because the amplitude of oscillation is far less than any geometric length scale, the Navier-Stokes equations are linearized. When compared to fluid dissipative effects, internal dissipative effects are negligible, and the fluid is assumed to be unbounded in space and incompressible. It is crucial to note that the fluid environment in which a CM operates, whether gas or liquid, can have a substantial impact on its dynamic response. The cantilever is operated at its eigenfrequency in many applications, which may be utilized to precisely quantify mass changes. If the elastic characteristics of the cantilever stay unchanged and damping effects are minor during molecule adsorption, the eigenfrequency equals the resonance frequency. But, when mass is added to the cantilever surface, the cantilever's eigenfrequency decreases, and this change may be utilized to calculate the mass of the adsorbed material.

To analyze the behavior of a rectangular CM beam in a dynamic mode, analytical expressions are presented. It should be noted that beam dimensions, excited modes, medium densities, viscosities, and adsorption particles can all have an impact on the beam's behavior. Therefore, it is important to consider these factors when designing and optimizing the CM for specific applications. The theoretical model presented in this section provides a foundation for understanding the behavior of rectangular CMs in various media and can be used to develop more complex models for specific applications. Assume that the beam's width b exceeds its thickness h more than ten times (see Fig2.2).

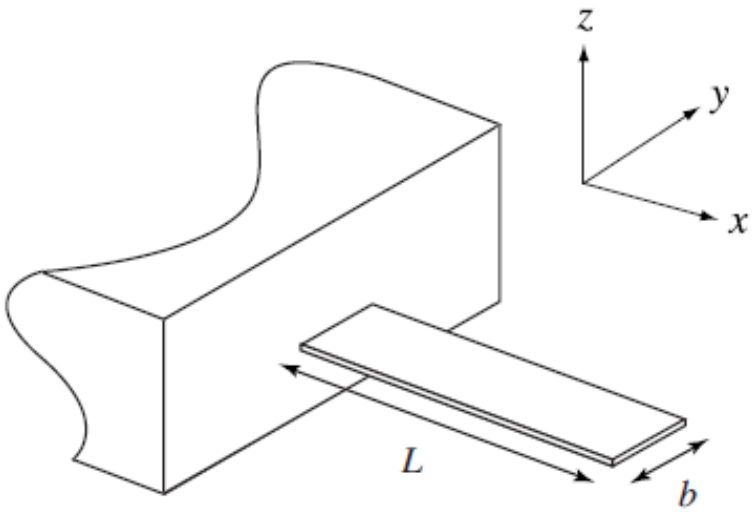

Figure 2.2: A rectangular cantilever is shown in plan view in a schematic illustration. A beam's clamped end is the origin of the coordinate system.

The deflection of CM sensors indicates sensing. For applications in sensing, CM deflections can be static or dynamic. A dynamic mode is used in our case, where the cantilever vibrates and its resonant frequency is monitored. In this section, a theoretical description is given of how CMs behave in the flexural, and torsional modes when used as sensors. The Euler-Bernoulli beam theory is well known for explaining the flexural vibrations of thin uniform beams. Four main assumptions are made in this

model: the cantilever aspect ratios are large, the deflections are small compared to the beam dimensions, the material of the cantilever is linearly elastic and homogeneous, and no dissipation occurs during deformation. This figure illustrates how a cantilever under external force per unit length Q looks schematically. A beam of infinitesimal length dx exhibits shear forces F_z and bending moments M_y as a result of the external load, as shown in figure2.3.

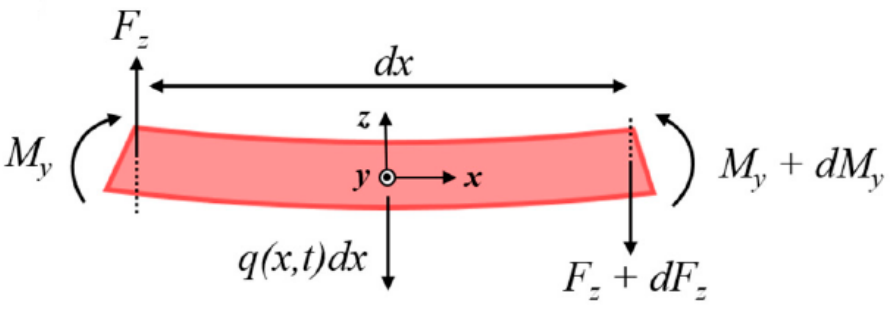

Figure 2.3: An infinitesimal element dx of the same cantilever showed in Fig.2.2 longitudinally.

$$\begin{cases} F_z + dF_z - F_z + q(x,t)dx = \rho A dx \frac{\partial^2 W(x,t)}{\partial^2} \\ M_y + dM_y - M_y - F_z dx + q(x,t)dx\frac{dx}{2} = 0 \end{cases} \Rightarrow \begin{cases} \frac{dF_z}{dx} + q(x,t) = \rho A \frac{\partial^2 W(x,t)}{\partial t^2} \\ \frac{dM_y}{dx} = F_z \end{cases} \tag{2.1}$$

We will present the equations that describe the beam's vibration in the air. Next, we will discuss the damping effects of measuring viscous gases and liquids. In a vacuum, an undamped motion of a homogeneous bar of length L is described using the differential equation for its amplitude $Y(x,t)$, at position x and time t. The equation of motion for flexural vibrations is a differential equation of fourth order [8, 9]:

$$EI\frac{\partial^4 Y(x,t)}{\partial x^4} + m_B \frac{\partial^2 Y(x,t)}{\partial t^2} = 0 \tag{2.2}$$

Where E is the modulus of elasticity for the bar and m_B it's mass per unit of length, the rectangular cross-section of the bar has an area $A = WT$ according to its width W and thickness T, while $I = WT^3/12$ is its moment of inertia. An end-clamped bar will vibrate with a frequency determined by its nth eigenmode.

$$\omega_n^{\text{vac}} = \frac{\alpha_n^2}{L^2}\left(\frac{EI}{m_B}\right)^{1/2}, \quad n = 1, 2, \ldots, \tag{2.3}$$

with tabulated numbers αn. The resonance frequencies of the various harmonics of a cantilever sensor vibrating in vacuum in flexural mode are represented as:[10]

$$f_{R,n}^{\text{theo}} = \frac{\alpha_n^2}{2\pi}\sqrt{\frac{EI}{m_c l^3}} \tag{2.4}$$

The resonance frequency of a vibrating cantilever depends on various parameters. Here, E represents the material's elastic modulus, I is the cantilever's moment of inertia, l its length, b its width,

and h its thickness. The mass of the cantilever is denoted by m_c. The constants $\alpha_1, \alpha_2, \alpha_3$, and α_4 have values 1.875, 4.694, 7.854, and 11.0 respectively, with α_{n-5} being defined as $\Pi(n - 0.5)$. The first mode, termed the fundamental mode, corresponds to $n = 1$.

Real-world cantilevers may have imperfections due to fabrication processes, leading to differences between actual and theoretically calculated resonance frequencies. Introducing a correction factor C into Equation :

$$f_{R,n}^{\text{theo}} = C\frac{\alpha_n^2}{2\pi}\sqrt{\frac{EI}{m_c l^3}} \tag{2.5}$$

Where,

$$C = \frac{f_{R,n}\alpha_1^2}{f_{R,1}\alpha_n^2} \tag{2.6}$$

Using $f_{R,n}$ and $f_{R,1}$ to represent the experimentally determined resonance frequencies for mode n and mode 1 respectively, we can note that C is set to 1 for a perfect cantilever across all modes. By aligning the respective frequency spectrum with a Simple Harmonic Oscillator (SHO) function, as illustrated in equation 1.5, the resonance frequency and $Q - factor$ for each mode can be deduced. The fitting parameters include A_0, $f_{R,n}$, and Q [11].

$$A(f) \approx \frac{A_0 f_{R,n}^2}{\sqrt{f^2 - f_{R,n}^2 + \frac{f^2 f_{R,n}^2}{Q^2}}} \tag{2.7}$$

Here, A_0 represents the amplitude of the response at zero frequency, while Q denotes the mode's $Q - factor$. It's important to mention that the SHO criterion is met when $Q \geq 1$, $L/b \geq 4$, and in the absence of nonlinearities in vibration [11].

By activating a cantilever at its eigenfrequency, precise mass variations can be gauged. This eigenfrequency is the resonance frequency of the vibrating cantilever if the cantilever's elasticity remains constant during molecular adsorption and damping influences are negligible. Dynamic mode is the term used to describe this approach. As additional mass accumulates on the cantilever's surface, there will be a downward shift in its intrinsic frequency. The alteration in frequency with respect to mass on a rectangular cantilever is determined as outlined in:

$$\frac{\Delta f}{\Delta m} = \frac{1}{4\pi n_l l^3 w} \times \sqrt{\frac{E}{\rho^3}} \tag{2.8}$$

In this context, ρ represents the mass density of both the microcantilever and the added mass, defined as $\rho = \frac{m}{lwt}$. Additionally, n_l, which is approximately equal to 1, serves as a geometric factor. The alteration in mass can be deduced from the frequency shift, as detailed in:

$$\Delta m = \frac{k}{4\pi^2} \times \left(\frac{1}{f_1^2} - \frac{1}{f_0^2} \right) \tag{2.9}$$

In the equation, f_0 represents the original eigenfrequency prior to any mass alteration, while f_1 indicates the eigenfrequency following the mass adjustment. Processes such as adsorption, desorption, and decomposition, especially during temperature variations, lead to mass modifications on the picogram scale. These alterations can be simultaneously monitored by observing shifts in the resonance frequency.

The harmonic modes refer to the different vibration patterns that the cantilever can exhibit, each corresponding to a different resonant frequency. These modes include the transverse mode, torsional mode, lateral mode, and longitudinal mode as depicted in fig.2.4. The first harmonic mode is typically the mode of interest, as it has the lowest resonant frequency and the largest amplitude of vibration. The second harmonic mode corresponds to the next highest resonant frequency and has a more complex vibration pattern than the first mode. The higher harmonic modes continue in this

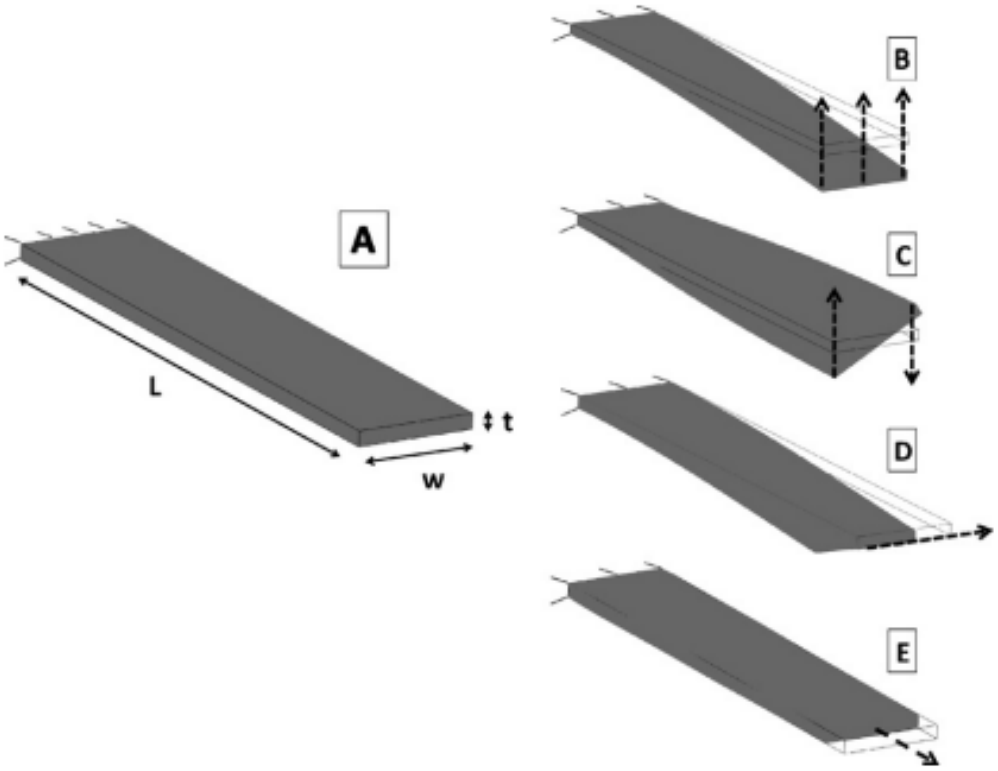

Figure 2.4: The passage illustrates a depiction of a typical cantilever (A) and several resonant modes that idealized cantilever sensors exhibit (B-E). These modes include the transverse mode (B), torsional mode (C), lateral mode (D), and longitudinal mode (E). The fundamental mode shape of each mode is presented for clarity, and the displacements are arbitrarily scaled to enhance the mode's clarity. The dashed arrows signify the cantilever's motion throughout the resonant cycle.[12]

pattern, with each mode having a higher resonant frequency and a more complex vibration pattern than the previous mode. Based on fig2.5, it can be seen that the number of nodes near the base of the

cantilever increases as n increases. These are the transverse modes (B) in figure2.4.

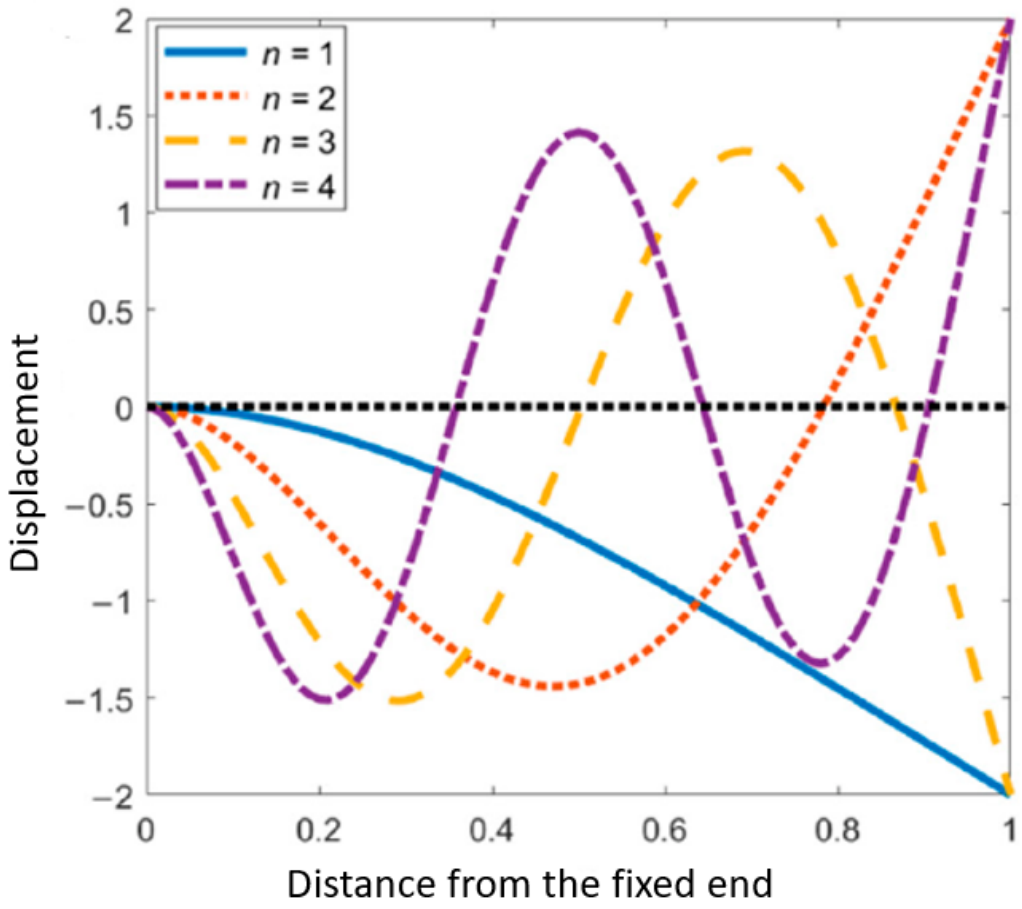

Figure 2.5: First four lateral normal vibration modes of a cantilever beam of the uniform cross-section.[13]

Steps to follow:

Theoretical approach: Start with the fundamental equation of motion for a cantilever beam, which is a second-order differential equation that relates the deflection of the beam to the applied load. Apply the boundary conditions to this equation to obtain the natural frequencies of the beam, which are the frequencies at which the beam will resonate. Use analytic CM methods to model the effect of various factors, such as temperature or mass loading, on the natural frequencies of the beam. Calculate the shift in resonance frequency by comparing the natural frequency of the beam under different conditions.

Experimental approach: Mount the CM beam in a setup that allows for precise measurements of its resonance frequency, such as a laser Doppler vibrometer or an atomic force microscope. Apply a stimulus, such as a piezoelectric actuator or an acoustic wave, to the beam and measure its response. Record the resonance frequency of the beam under different conditions, such as changes in temperature or pressure, and compare them to the baseline resonance frequency. Calculate the shift in resonance frequency by comparing the resonance frequency of the beam under different conditions.

Numerical approach: Use finite element analysis software to model the CM beam and its environment, including any factors that may affect its resonance frequency. Apply a stimulus to the beam

and simulate its response. Use the simulation results to calculate the resonance frequency of the beam under different conditions. Calculate the shift in resonance frequency by comparing the resonance frequency of the beam under different conditions. Overall, tracking the shift in resonance frequency of a CM beam requires a combination of theoretical modeling, experimental measurement, and numerical simulation. By comparing the results obtained from these different approaches, you can gain a more complete understanding of the factors that affect the resonance frequency of the system.

2.2 Theory of cantilever beam immersed in fluid

The behavior of a cantilever beam immersed in a fluid derives from principles in fluid dynamics and beam mechanics. Immersing the beam in fluid subjects it to forces causing bending. The force magnitude and direction rely on fluid properties (density, viscosity, and flow velocity) and the beam's geometry (length, width, and cross-sectional shape). One approach to modeling this is to utilize the equations of motion for beams surrounded by fluid, considering fluid pressure, velocity, viscous forces, and the beam's inherent properties. The resultant equations provide beam displacement and velocity with respect to time and position. Additionally, the fluid can be represented as a boundary layer, a thin fluid layer adjacent to a solid surface where flow dynamics are notably influenced by the solid. The boundary layer's thickness enlarges as fluid traverses the surface, slowing the fluid velocity. Another modeling technique involves the concepts of Fluid-Structure Interaction (FSI).

FSI simulations offer insights into cantilever beams' dynamic behavior in fluid flows, revealing natural frequencies, mode shapes, and damping ratios. This is vital for designing structures in fluid settings, like bridges, offshore constructs, and aircraft wings. FSI also predicts micro- and nanoscale device performance, e.g., microfluidics, drug delivery systems, and biosensors, emphasizing fluid-structure interactions. Moreover, FSI simulations, combined with computational fluid dynamics (CFD), investigate the cross-section of the cantilever beam, enabling fluid flow feature analysis, including turbulence, vortices, and pressure distribution. These simulations guide beam design optimization for particular flow scenarios or examine flow impact on structural behavior. Lastly, FSI simulations evaluate environmental influences, such as wind or waves, on cantilever beams in fluid settings, crucial for coastal or offshore structure design, where fluid-structure interactions significantly influence structure safety and efficacy. The behavior of a cantilever beam immersed in a fluid can be modeled using equations of motion for beams in a fluid, boundary layer theory, and fluid-structure interaction. These models take into account the properties of the fluid and the geometry of the beam, and can be used to predict the displacement of the beam and velocity of the fluid as a function of time and position. When a cantilever is stimulated in a fluid, the fluid-structure interaction causes the wave propagation on the cantilever to resist and dissipate. The interaction force can be expressed as follows [7]:

$$F(x,\omega) = \frac{\pi}{4}\rho\omega^2 b^2 \Gamma(\omega) w(x,\omega) \tag{2.10}$$

where ρ is the density of the fluid, ω is the radial frequency, b is the width, and $\Gamma(\omega)$ is the hydrodynamic function of the cantilever. The hydrodynamic function is affected by the Reynolds number [14]. $Re = \frac{\rho\omega^2}{4\eta}$, where η is the viscosity of the fluid. The hydrodynamic function of a cantilever with a rectangular cross-section Γ_{rect} must be revised numerically from that of a cantilever with a circular cross-section Γ_{circ}. The rectangular beam's hydrodynamic function may therefore be represented as[7]:

$$\Gamma_{\text{rect}}(\omega) = \Omega(\omega)\Gamma_{\text{circ}}(\omega) = \Omega(\omega)\left[1 + \frac{4iK_1(-i\sqrt{i\,\text{Re}})}{\sqrt{i\,\text{Re}}K_0(-i\sqrt{i\,\text{Re}})}\right] \tag{2.11}$$

in the range, $Re \in [10^{-6}, 10^4]$, Where K_0 and $K_1 1$ are the modified Bessel functions of the third type and the correction function, respectively, andω is written as fractional polynomial functions of $\log_{10} Re$. As a result of the Reynolds number and cantilever bending stiffness, the $Q - factor$ for cantilevers immersed in fluid differs from microscale-thickness to nanoscale-thickness cantilevers. A microscale-thickness cantilever completely immersed in a liquid would not induce standing waves because its decay rate would be too large. The effects of the shear deformation and the rotary inertia are negligible if the cantilever has a small thickness and width compared to the lengthwise dimension. Cantilever sections with fluid-immersed flexural modes of vibration have the following governing equation for elastic deformation as follows[15]:

$$EI\frac{\partial^4 w(x,t)}{\partial x^4} + \mu\frac{\partial^2 w(x,t)}{\partial t^2} = F(x,t) \tag{2.12}$$

where $w(x,t)$, is the deflection function of the beam in the z direction, E is Young's modulus, I is the moment of inertia of the beam cross section,μ is the mass per unit length of the beam. F(x, t) is the external applied force per unit length in the z direction, x is the spatial coordinate along the length of the beam, and t is time. For a rectangular cantilever beam, $I = \frac{bh^3}{12}$. The well-known inviscid model is a suitable approximation for describing resonance frequencies for a rectangular shape submerged in fluid. It is assumed that the liquid is incompressible in nature. The resonance frequencies in a fluid, f_{nl}, are given by this model.

$$f_{nl} = f_n\left(1 + \frac{\pi\rho_l w}{4\rho_c t}\right)^{-1/2} \tag{2.13}$$

where ρ_l and ρ_c are the density of the fluid medium and cantilever. This equation is used to compute [16]. The properties of the materials and fluids were selected to align with the test conditions. The elasticity modulus of Si stands at 169 GPa, while its density ρ_{Si} is 2330 kg/m^3. In terms of air's properties at room temperature, its density ρ_{air} is 1.1839 kg/m^3, its viscosity is 1.78×10^{-5} kg/(m s), and the sound travels at a speed of 346.18 m/s. The standard formulas to determine the resonance frequency and the $Q - factor$ for a specific mode can be found in references [17, 18].

$$f_{R,n} = \frac{f_{vac,n}}{\sqrt{1 + \left(\frac{\pi \rho_{air} b}{4 \rho_{Si} t}\right) \Gamma_r \left(f_{R,n}, n\right)}} \tag{2.14}$$

And

$$Q = \frac{\left(\frac{4 \rho_{Si} t}{\pi \rho_{air} b}\right) + \Gamma_r \left(f_{R,n}, n\right)}{\Gamma_i \left(f_{R,n}, n\right)} \tag{2.15}$$

In the given equation, t represents the cantilever's thickness, while b denotes its width. The term $f_{vac,n}$ stands for the cantilever's mode n vacuum resonance frequency. Meanwhile, the term $\Gamma_r \left(f_{R,n}, n\right)$ is a hydrodynamic function without dimensions, where the indicators r and i pinpoint the real and imaginary portions, respectively. To compute the $Q - factor$ and resonance frequencies, it's essential to determine the hydrodynamic function for each model. Notably, this component is influenced by the fluid's compressibility. This process entailed addressing the linear equation systems as outlined in references [28] and [29]. As a result, the oscillation's $Q - factor$, Q, diminishes, making the tracking of resonance frequency shifts with precision a challenge. The $Q - factor$, a dimensionless metric, provides insight into energy dissipation in the vibrating system. It indicates the rate of energy loss, with a higher Q suggesting reduced energy losses due to aspects like fluid damping. The $Q - factor$ represents the "sharpness" of the resonance peak, making it crucial in evaluating the efficiency of mechanical resonators such as cantilever beams. This factor describes an oscillator's or resonator's underdamped nature and defines a resonator's bandwidth in relation to its central frequency. A high Q signifies that the oscillations diminish more gradually due to a lower energy loss rate in comparison to the resonator's stored energy. When a cantilever microbeam is submerged in a fluid (like water or air), its $Q - factor$ tends to decrease because of the fluid's damping effects. During the dynamic mode, where the cantilever vibrates at its resonant frequency, the $Q - factor$ can be determined either through experiments or simulations.

In a Newtonian in-compressible fluid, the oscillation of a cantilever can be characterized using the model of a driven, damped harmonic oscillator:

$$m^* \frac{d^2 x}{dt^2} + \gamma \frac{dx}{dt} + kx = F \cos(2\pi f t) \tag{2.16}$$

In this context, $m^* = \text{const}(m_c + m_l)$ represents the cantilever's effective mass, where, for a rectangular cantilever, the constant is set at 0.25. Notably, in liquid environments, the liquid's co-moved mass m_l considerably contributes to the cantilever's mass m_c. This expression $\gamma \frac{dx}{dt}$ signifies the drag force caused by damping, $F \cos(2\pi f t)$ corresponds to the driving force produced by the piezo-electric actuator, and k is the cantilever's spring constant.

However, it is critical to underline that the hydrodynamic function utilized for computing the $Q - factor$ and resonance frequencies, $\Gamma_r(f_{R,n}, n)$, is impacted by the fluid's compressibility, rendering it a complex function of the cantilever's size, the fluid's properties, and the vibrating mode. The eigen

frequency characterized by this equation below in the absence of damping with:

$$f_0 n = \frac{\alpha_n^2}{2\pi}\sqrt{\frac{k}{2\left(m_c + m_1\right)}} \tag{2.17}$$

Where f_n are the eigenfrequencies of the $n-th$ mode, α_n are constants depending on the mode and related to the different eigenvalues of the harmonics: α_1 = 1.8751, α_2 = 4.6941, α_n = π (n - 0.5), k is the spring constant of the cantilever given by $k = 3\frac{EI}{L^3}$ where $EI$is the flexural rigidity, with E Young's modulus and I the moment of inertia and L is the length of the cantilever.

$$f_n = \sqrt{f_{on}^2 \frac{-\gamma^2}{2\pi}} \tag{2.18}$$

Where the damping factor γ is defined by:

$$\gamma = \frac{c_0 + c_v}{\left(\frac{2}{L}\right)\left(m_c + m_l\right)} \tag{2.19}$$

where c_v is the dissipation coefficient, c_0 is the intrinsic damping coefficient per unit length that describes internal losses. If adsorption adds mass to the cantilever, the effective mass will change as follows:

$$m^* = \mathrm{C}\left(m_c + m_1 + \Delta m\right) \tag{2.20}$$

Assume that Δm is the additional mass adsorbed. It is common for the liquid's co-moved mass to be much larger than its adsorbed mass.

$$f_{on} = \frac{\alpha_n^2}{2\Pi}\sqrt{\frac{k}{2\left(m_c + m_l + \Delta_m\right)}} \tag{2.21}$$

Basically, the eigenfrequency and natural frequency of a CM are different theoretical concepts that describe the response of the beam to external disturbances and its inherent properties, respectively. Both can be experimentally determined by exciting and observing the vibration of the beam but using different methods. When a CM is immersed in a fluid, the amplitude of its deflection can be influenced by the drag force exerted by the fluid. The formula for the amplitude of the CM immersed in a fluid theoretically can be derived from the following equation:

$$A(f) = A_{\mathrm{bl}} + \frac{A_0 f_{R,n}^2}{\sqrt{\left(f^2 - f_{R,n}^2\right)^2 + f^2 f_{R,n}^2 / Q^2}} \tag{2.22}$$

Figure 4.30 displays the amplitude and phase curves of CMs with varying Q-values, where Equation 2.18 provides the amplitude response of the cantilever, and Equation 2.19 denotes the phase

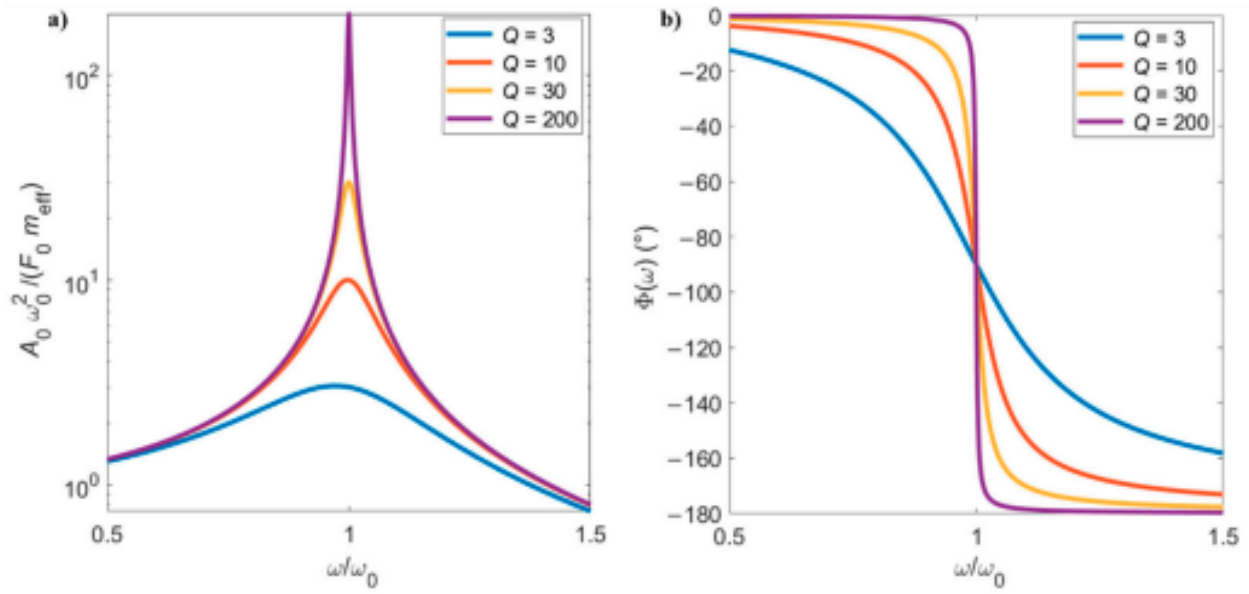

Figure 2.6: the amplitude (a) and phase (b) response of a forced and damped harmonic oscillator, which varies according to the normalized excitation frequency. The study focuses on CMs vibrating in air or liquid mediums, and specifically examines four different levels of damping (Q) commonly encountered in this context[13].

difference between the driving force and the cantilever's motion.

$$\phi = \text{atan}\left(-\frac{\omega_0\omega}{Q\left(\omega_0^2-\omega^2\right)}\right) \tag{2.23}$$

This formula takes into account the effect of the fluid drag force on the beam's deflection, which is proportional to the square of the fluid velocity and the length of the beam immersed in the fluid. The formula assumes that the fluid is in-compressible and the beam is submerged in the fluid to a depth of one-third of its length. In practice, the actual amplitude of the deflection may differ from the theoretical value due to factors such as turbulence, boundary layer effects, and other fluid dynamics phenomena. The sensitivity of a CM beam immersed in a fluid is a measure of how much the beam's deflection changes in response to a small change in the fluid's properties, such as viscosity or density. The sensitivity formula for a CM beam immersed in a fluid can be expressed as:

$$S = \frac{\Delta f}{\Delta m} = \frac{f_{nl}}{2m_c} \tag{2.24}$$

It also assumes that the deflection of the beam is small, so the linearized Euler-Bernoulli beam theory can be used to model the beam's behavior. In practice, the sensitivity of a CM immersed in a fluid can be measured experimentally by subjecting the beam to small changes in the fluid's properties and measuring the resulting deflection. The sensitivity can then be calculated using the above formula. Optimizing the geometry and materials of the microbeams themselves is one way to improve sensitivity. Because the resonant frequency of a cantilever beam is determined by its geometry, you

can improve the device's sensitivity by carefully designing the beam shape and dimensions. Furthermore, choosing the right materials for the microbeams can improve the device's sensitivity. Certain materials, such as graphene or carbon nanotubes, have high surface area-to-volume ratios, which can enhance interaction between the beam and the target particles. Signal amplification techniques are another method for increasing sensitivity. This can be accomplished through electronic amplification of the sensor signal, which can increase signal strength and improve the device's detection limits. You could also use physical amplification by designing the device to increase the mass of the particles being detected. This could be accomplished through a variety of methods, including increasing the size of the microbeams or incorporating additional structures that can increase particle mass. Finally, in order to ensure the highest sensitivity and accuracy of the measurements, it is critical to carefully control the device's operating conditions, such as temperature, pressure, and flow rate. To ensure that the signal from the sensor is as strong and consistent as possible, any external factors that could affect the resonance of the microbeams should be minimized.

2.3 Impedance Correlation

Impedance is a measure of the opposition to the flow of alternating current (AC) in an electrical circuit. In the context of a piezoelectric CM sensor, impedance measurements can be used to detect changes in the mechanical properties of the cantilever due to a change in the environment or the presence of a target analyte. The resonance frequency of a system is determined by its impedance, which is directly related to its impedance. In a resonant circuit, the impedance is at a minimum at the resonance frequency, allowing for the maximum flow of current. The impedance of a circuit can be represented graphically by a vector in the complex plane, with the real axis representing resistance and the imaginary axis representing reactance.

The impedance of a circuit can be affected by various factors, such as the frequency of the applied voltage, the properties of the circuit elements, and the properties of the surrounding medium. Understanding the impedance of a circuit is important for designing and analyzing electrical systems, as it can provide insight into the circuit's performance and stability. For a cantilever with uniform cross-section in an inviscid fluid, the resonant frequency is:

$$\frac{f_{R_{\text{fluid}}}}{f_{R_{\text{vac}}}} = \left(1 + \frac{\pi \rho b}{4 \rho_c h}\right)^{-1/2} \tag{2.25}$$

In these equations, $f_{R_{\text{fluid}}}$ and $f_{R_{\text{vac}}}$ are resonant frequencies in fluids and vacuums, c is the cantilever's density, b and h are its width and thickness, and is its surrounding fluid's density. It has been shown using approximations that the ratio of resonant frequency of water and aqueous solutions is[19]:

$$\frac{f_{Rw}}{f_{Rx}} = \frac{\sqrt{1 + \gamma \rho_x}}{\sqrt{1 + \gamma \rho_w}} \tag{2.26}$$

CM sensors have non-uniform thickness due to the γ parameter. Water's resonant frequency f_{Rw} and solute mass fraction X's resonant frequency f_{Rx} refer to resonant frequencies in solution. Gamma is typically reported as ∼2. CM sensors resonant frequency decreases with increased liquid density, according to equation(2.20).

The frequency response of a typical CM sensor near resonance is shown in fig.2.7. The phase angle

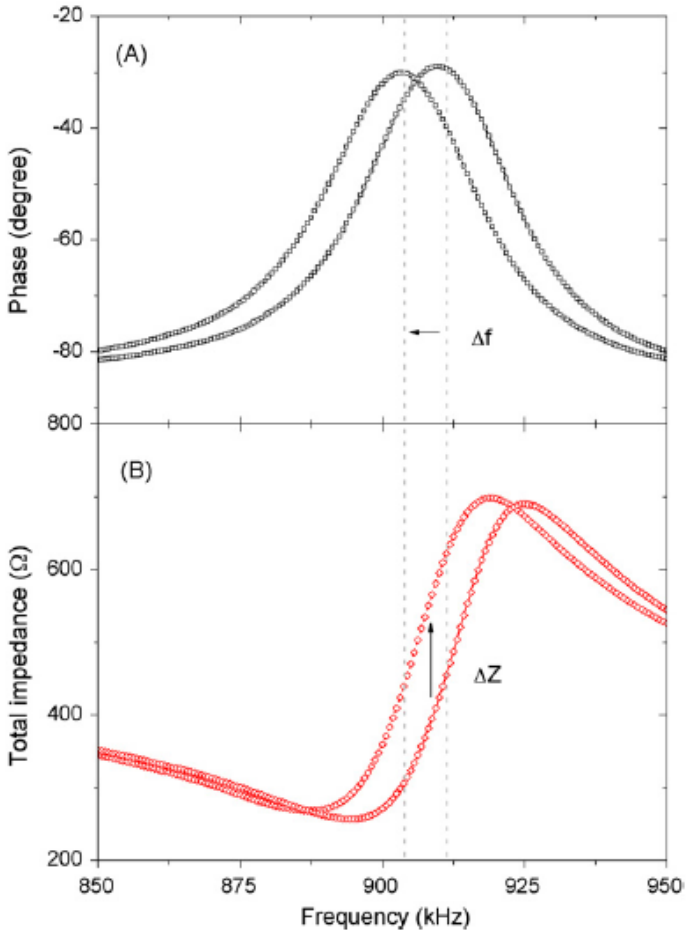

Figure 2.7: This illustration shows a typical CM sensor frequency response near resonance. The phase angle spectrum (□) is shown in (A), while the impedance spectrum(△) is shown in (B). Impedance changes can be detected at a fixed frequency by monitoring at a fixed frequency[20].

is measured using an impedance analyzer at steady state and represents the vectorial difference between the excitation voltage and the current signal. The shift in resonant frequency associated with detection in a typical detection experiment is a few kHz. Binding of antigens such as E. coli O157:H7 at 100 cells/mL causes a frequency decrease of 1 kHz [21], whereas binding of Staphylococcus enterotoxin B (SEB) at 100 fg caused a decrease of 250 Hz [22]. As a result, resonant frequency movement is well within the frequency bound of (f_r -α) and (f_r +α). Impedance at frequency f_r in the vicinity of f_r may be estimated as: where the formula $\partial|Z|/\partial f|_{f=f_{Rx}}$ represents the slope-dependence of impedance near f_r and f is an arbitrary frequency near resonant frequency. When there is a slight change in fluid density or binding of the target analyte, the impedance spectrum in the (f_r - α) and

(f_r +α) area moves in a parallel pattern, as shown in fig2.7 As a result, we propose that measuring impedance change at a fixed frequency is a viable way for monitoring sensor responsiveness. By combining Eqs. (2.20) and (2.21), and defining $|Z(f_{nr}|)$ as impedance measured at a fixed non-resonant monitoring frequency f_{nr}, it is possible to formulate $|Z(f_{nr}|)$ as a function of fluid density as:

$$|Z(f)| = |Z(f_R)| + \left.\frac{\partial |Z|}{\partial f}\right|_{f=f_R} (f - f_R) \tag{2.27}$$

By combining Equations (2.20) and (2.21) and defining $|Z(f_{nr}|)$ as impedance measured at a fixed frequencyf_{nr}, one can form the following expression for $|Z(f_{nr}|)$ with fluid density:

$$\frac{f_{Rw}}{f_{Rx}} = \frac{\partial|Z|/\partial f|_{f=f_{Rx}} \left(|Z(f_R)|_w + (\partial|Z|/\partial f)|_{f=f_{Rw}} \cdot f_{nr} - |Z(f_{nr})|_w\right)}{\partial|Z|/\partial f_{f=f_{Rw}} \left(|Z(f_R)|_x + (\partial|Z|/\partial f)|_{f=f_{Rx}} \cdot f_{nr} - |Z(f_{nr})|_x\right)} = \frac{\sqrt{1+\gamma\rho_x}}{\sqrt{1+\gamma\rho_w}} \tag{2.28}$$

where $\partial|Z|/\partial f|_{f=f_{Rx}}$, $\partial|Z|/\partial f|_{f=f_{Rw}}$, $|Z(f_R)|_{w'}$, $|Z(f_R)|_x$ are constant values in the region(f_r - α) $\leq$ $f \leq$(f_r +α). Simplifying equation 2.29 by introducing $A_x = \partial|Z|/\partial f|_{f=f_{Rx}}$, $A_w = \partial|Z|/\partial f|_{f=f_{Rw}}$, $B_x = |Z(f_{Rx})| + (\partial|Z|/\partial f)|_{f=f_{Rx}} \cdot f_{nr}$, $B_w = |Z(f_{Rw})| + (\partial|Z|/\partial f)|_{f=f_{Rw}} \cdot f_{nr}$, one gets

$$\frac{f_{Rw}}{f_{Rx}} = \frac{A_x(B_w - |Z(f_{nr})|_w)}{A_w(B_x - |Z(f_{nr})|_x)} = \frac{\sqrt{1+\gamma\rho_x}}{\sqrt{1+\gamma\rho_w}} \tag{2.29}$$

In equation (2.30), $|Z(f_{Rw})|$ grows when density increases, and vice versa. It is critical to understand that the aforementioned connection is only valid in the (f_r - α) $\leq$ f $\leq$(f_r +α) range. With density change experiments. When particles in the medium bind to the cantilever beam, they alter the beam's resonance frequency and impedance, which can be measured to detect the presence of the particles. The relationship between impedance and resonance frequency in this setup is that the impedance of the cantilever beam is at a minimum when it is driven at its resonance frequency. This is because the impedance of the beam is mainly due to its mechanical properties, which are frequency-dependent. At the resonance frequency, the mechanical properties of the beam are optimized, and the impedance is at its minimum value. When particles in the medium bind to the beam, they change their mass and stiffness, which alters the resonance frequency and impedance of the beam. By tracking the changes in the frequency and impedance of the beam, it is possible to detect the presence of particles in the medium and quantify their properties. Therefore, in this setup, the resonance frequency and impedance of the cantilever beam are closely related, and tracking both of these parameters can provide valuable information about the presence and properties of particles in the fluid medium.

2.4 History and description of our Model

Criteria of the choice of conical and triangular sensors

Conventional ultrasonic techniques for characterization generally rely on the use of a piezoelectric transducer resonating in a thickness mode [23]. Since the resonance frequency of a transducer is proportional to its size, it becomes significant for frequencies in the order of tens of kHz. To achieve the set objective, we prefer to proceed differently. Our technique thus involves resonating the entirety of a mechanical structure of reduced size, one end of which is tapered and immersed in the material to be analyzed [24]. Ensminger [25] studied the propagation of longitudinal waves in a cone without loss, where the lateral dimensions are small compared to the length, based on the following differential equation:

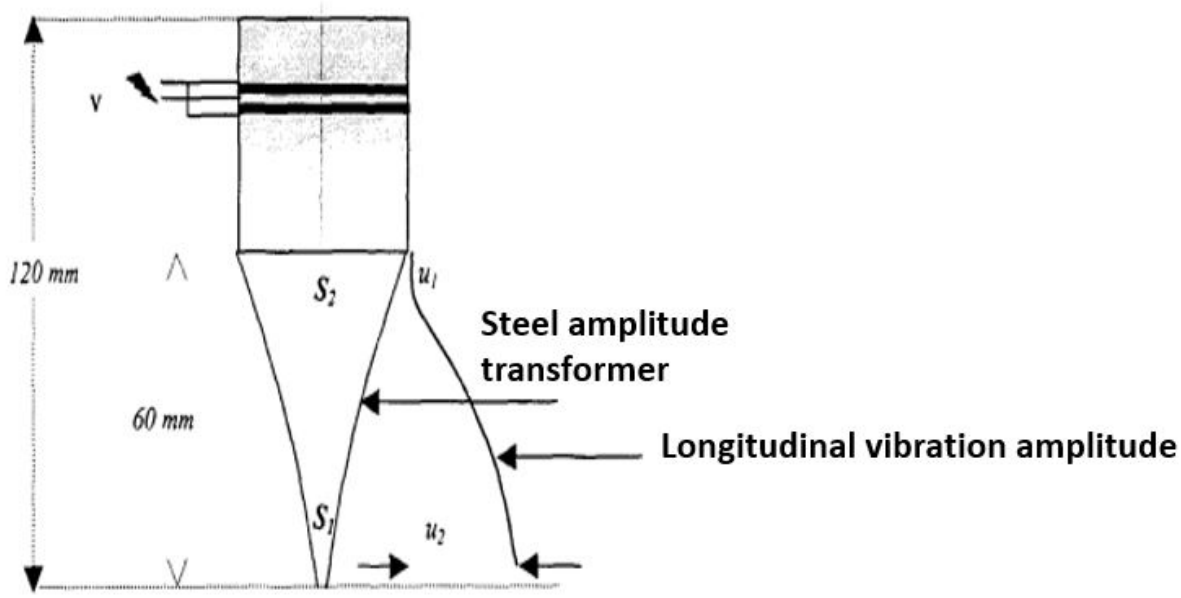

Figure 2.8: Ultrasonic sensor comprising a steel amplitude transformer, associated with piezoelectric elements.

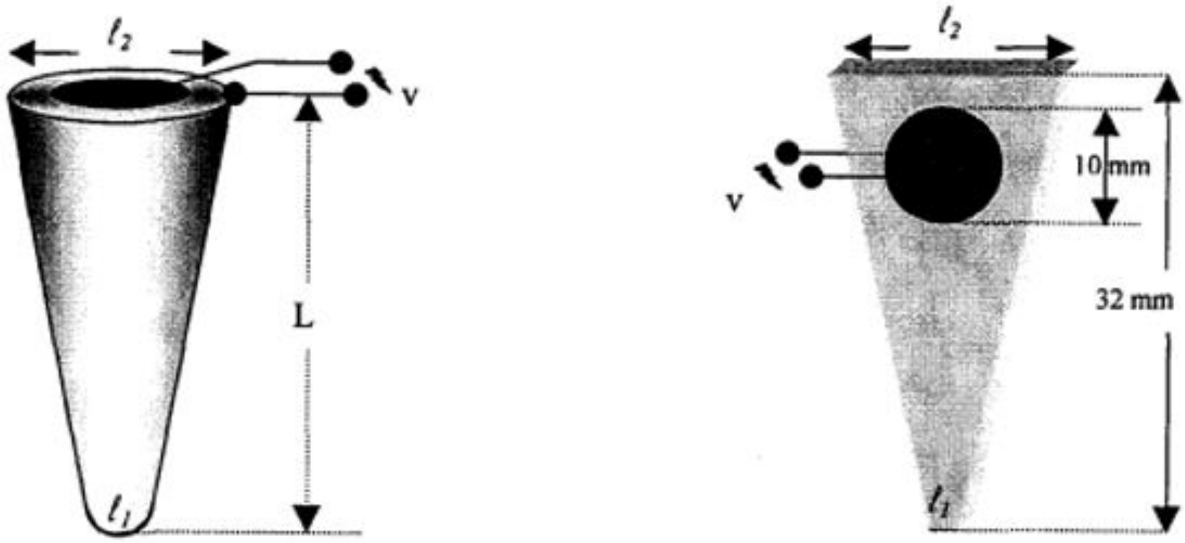

Figure 2.9: (a) Conical steel sensor (b) Triangular ceramic sensor

This analytical part concerns the study of the propagation of the difficult mode in the triangular and conical parts alone of our sensors. Its objective is to determine the resonance frequency of the longitudinal mode as well as its amplification ratio. The theoretical developments of Ensminger [25] for the study of the conical part, to which we proposed an extension for the study of the triangular part.

$$\frac{\partial^2 v}{\partial x^2} + \frac{1}{S}\frac{\partial S}{\partial x}\frac{\partial v}{\partial x} + \frac{\omega^2}{c^2}v = 0 \tag{2.30}$$

With:

v : velocity of the particles.

ω : angular frequency.

c : speed of the longitudinal wave in the material constituting the vibrating element.

and $S = \pi R^2(x)$ gives

$$S = \pi \ell^2 \left(\frac{x_1 + x}{4x_1}\right)^2 \tag{2.31}$$

Substituting the value of S into equation (III-2), we get:

$$\frac{\partial^2 v}{\partial x^2} + \frac{2}{x_1 + x}\frac{\partial v}{\partial x} + \frac{\omega^2}{c^2}v = 0 \tag{2.32}$$

This differential equation has a general solution given by:

$$v = \frac{1}{x_1 + x}\left[A\cos\left(\frac{\omega(x_1 + x)}{c}\right) + B\sin\left(\frac{\omega(x_1 + x)}{c}\right)\right] \tag{2.33}$$

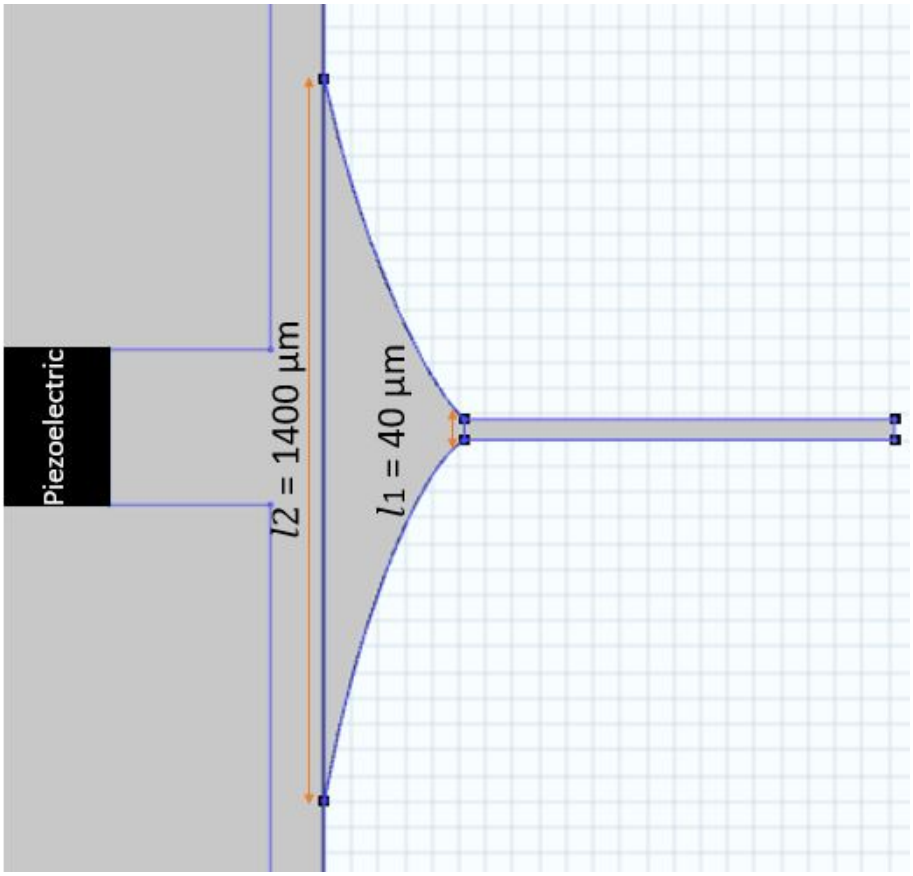

Figure 2.10: Our Cantilever Microbeam Proposition

This velocity v reaches its maximum value at resonance in two positions: the first is at the end $x = 0$, i.e., V_1 and the second at $x = L$, i.e., V_2. Applying the boundary conditions to calculate the constants A and B (Appendix III-1), the expression for the velocity then appears in the following form:

$$v = \frac{V_2}{(x_1 + x)} \left[(x_1 + L) \cos\left(\frac{\omega(x-L)}{c}\right) + c \sin\left(\frac{\omega(x-L)}{\omega c}\right) \right] \tag{2.34}$$

For $x = 0$, $v = V_1$, which allows deducing the velocity amplification ratio at the ends. Applying the boundary conditions to calculate constants A and B (Appendix III-1), the expression for the velocity thus appears in the following form:

$$v = \frac{V_2}{(x_1 + x)} \left[(x_1 + L) \cos\left(\frac{\omega(x-L)}{c}\right) + \frac{c}{\omega} \sin\left(\frac{\omega(x-L)}{c}\right) \right] \tag{2.35}$$

For $x = 0$, $v = V_1$, which allows us to deduce the velocity amplification ratio at the extremities.

$$\frac{V_1}{V_2} = \frac{1}{(x_1 + L)} \left[\cos\left(\frac{\omega L}{c}\right) - \frac{c}{\omega} \sin\left(\frac{\omega L}{c}\right) \right] \tag{2.36}$$

The similarity ratio (III-1) allows expressing (III-7) as a function of L, ℓ_1, and ℓ_2:

$$\frac{V_1}{V_2} = \ell_2 \cos\left(\frac{\omega L}{c}\right) - \frac{c(\ell_2 - \ell_1)}{\omega \ell_1} \sin\left(\frac{\omega L}{c}\right) \tag{2.37}$$

At the resonance frequency, the product $\omega L/c$ takes the value π. It then appears that the ratio of the speed of displacement at the end of the cone and that at the base is directly proportional to the ratio l_2/l_1. In the particular case of the sensor in figure2.10, the transformation ratio takes the value -7 and the resonance frequency is $f = 1$ MHz. For a conical volume where $x_1 = 0$, the general equation of speed is written as:

$$v = \frac{V_2}{x}\left[L \cos\left(\frac{\omega(x-L)}{c}\right) + c \sin\left(\frac{\omega(x-L)}{c}\right)\right] \tag{2.38}$$

At the resonance frequency, the condition $\frac{dv}{dx} = 0$ when $x = 0$ and $x = L$, leads to the following relationship:

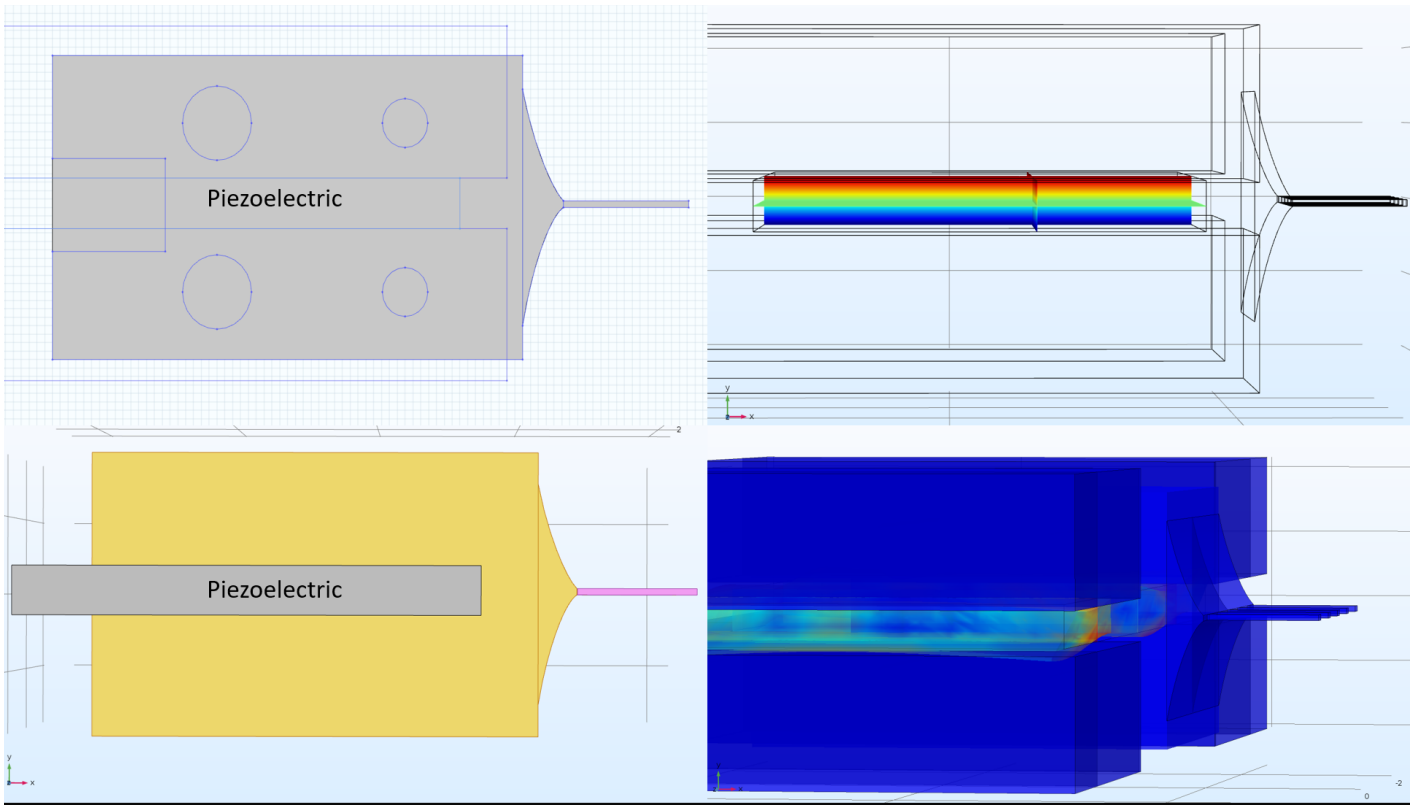

Figure 2.11: Piezoelectric Positioning and Exponential Support Structure for Beams

2.5 Fundamentals and Computational Approaches in Electrostatics and Material Modeling

Charge Conservation in Electrostatics

In the study of electrostatics, the conservation of electric charge and the relationship between the electric field, electric potential, and electric displacement field are governed by the following fundamental equations:

Gauss's Law for Electricity: The divergence of the electric displacement field, **D**, in a region of space is equal to the volume charge density, ρ_v, in that region. Mathematically, this is expressed as:

$$\nabla \cdot \mathbf{D} = \rho_v \tag{2.39}$$

Relationship between Electric Field and Electric Potential: The electric field, **E**, is related to the gradient of the electric potential, V, as follows:

$$\mathbf{E} = -\nabla V \tag{2.40}$$

These equations play a pivotal role in the simulation studies of electrostatic phenomena and are crucial for ensuring the conservation of electric charge.

Parameters of Lead Zirconate Titanate (PZT-5H)

Elasticity Matrix

Ordering: xx, yy, zz, yz, xz, xy

$$\begin{bmatrix} 1.27205 \times 10^{11} & 8.02122 \times 10^{10} & 1.27205 \times 10^{11} \\ 8.46702 \times 10^{10} & 8.46702 \times 10^{10} & 1.17436 \times 10^{11} \\ 0 & 0 & 0 \\ 2.29885 \times 10^{10} & 0 & 0 \\ 0 & 0 & 2.29885 \times 10^{10} \\ 0 & 0 & 2.34742 \times 10^{10} \end{bmatrix}$$

Coupling Matrix

$$\begin{bmatrix} 0 & 0 & -6.62281 \\ 0 & 0 & -6.62281 \\ 0 & 0 & 23.2403 \\ 0 & 17.0345 & 0 \\ 17.0345 & 0 & 0 \\ 0 & 0 & 0 \end{bmatrix}$$

Relative Permittivity

$$\begin{bmatrix} 1704.4 \\ 1704.4 \\ 1433.6 \end{bmatrix}$$

Property	Value
Density	$2330\,\mathrm{kg/m^3}$
Young's Modulus	$130 - 170\,\mathrm{GPa}$
Poisson's Ratio	0.28

Table 2.1: Material properties of silicon.

Mathematical Formulation of Linear Elasticity: Linear elasticity is a cornerstone of solid mechanics that provides a relationship between stress and strain for materials under small deformations. In this section, we elucidate the governing equations and their implications. **Conservation of Momentum**: The fundamental equation representing the conservation of momentum is given by:

$$-\rho\omega^2\mathbf{u} = \nabla \cdot \mathbf{S} + \mathbf{F}_{ve}\phi, \tag{2.41}$$

Where: ρ represents the material density, ω denotes the angular frequency, $\mathbf{u}$ signifies the displacement vector, $\mathbf{S}$ stands for the stress tensor, $\mathbf{F}_{ve}$ is the external force vector, and ϕ is the scalar modulation function. Additionally, the eigenvalue problem is described by:

$$-ikz = \lambda. \tag{2.42}$$

Decomposition of Stresses: The additional stress, $\mathbf{S}_{ad}$, can be decomposed into various components as:

$$\mathbf{S}_{ad} = \mathbf{S}_0 + \mathbf{S}_{ext} + \mathbf{S}_q. \tag{2.43}$$

Strain-Displacement Relationship: The link between the displacement field and the strain tensor is

provided by the strain-displacement relationship:

$$\boldsymbol{\varepsilon} = \frac{1}{2}(\nabla \mathbf{u} + \nabla \mathbf{u}^T). \tag{2.44}$$

Understanding these mathematical formulations is imperative for simulating the behavior of elastic materials under different loadings. Employing such equations allows for accurate predictions and insights into material behavior, thereby aiding in design and analysis tasks.

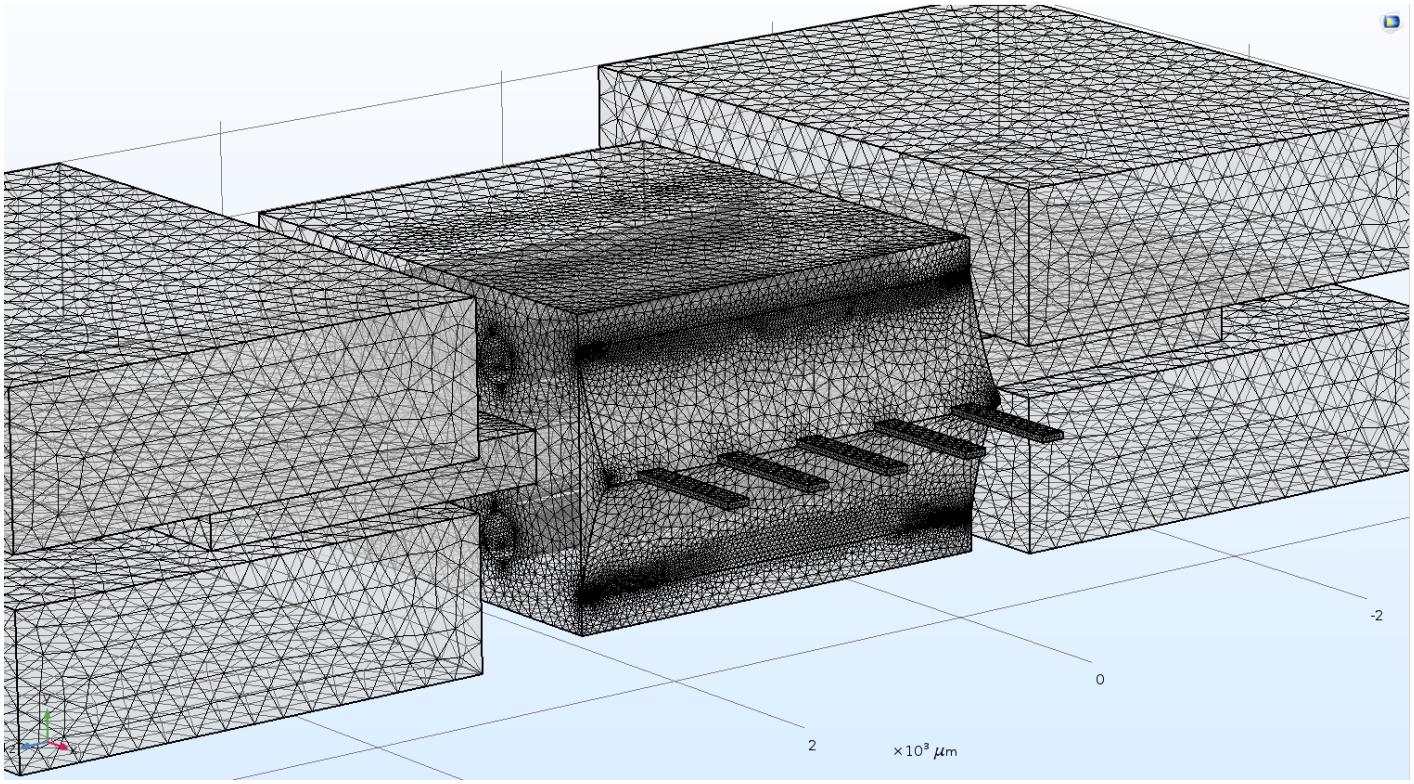

Figure 2.12: Meshing of the Cantilever Microbeam Array and Support Structure.

In Figure 2.12, the meshing strategy employed for the cantilever microbeam array and its support structure is depicted. Notably, a finer mesh is adopted for the beams to capture intricate details and to ensure a precise simulation. This is critical due to the beam's inherent thin structure and its consequent susceptibility to higher gradients of stress and displacement. In contrast, the rest of the structure, being less susceptible to rapid changes in these parameters, is meshed with a standard granularity. This approach effectively balances computational efficiency with the required precision for the simulation.

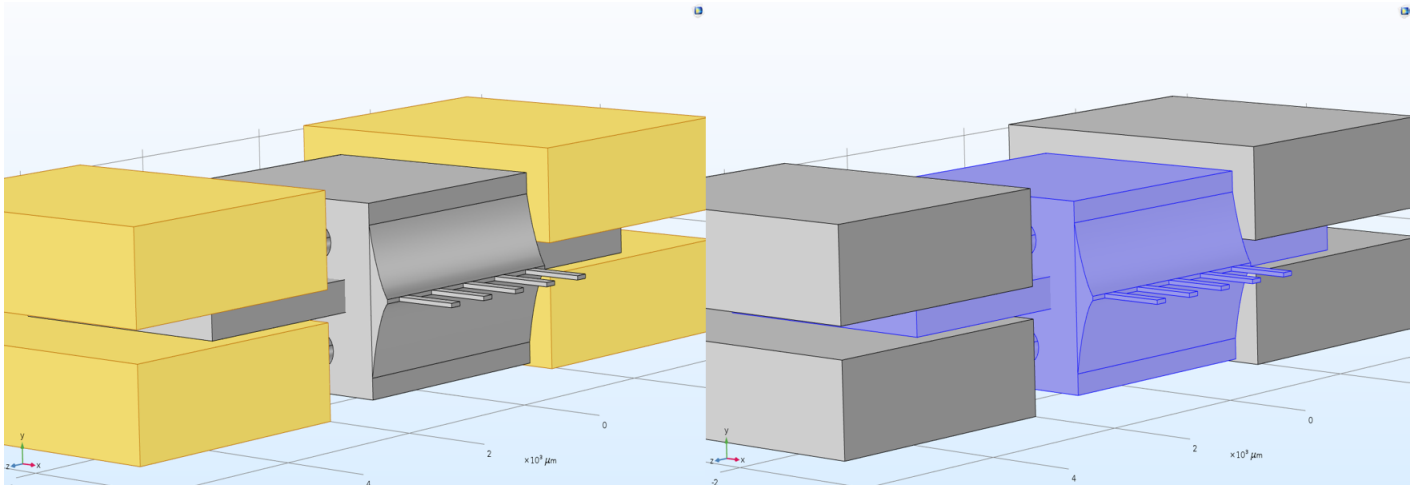

Figure 2.13: Boundary conditions illustrated in the image: The yellow region on the left represents a fixed constraint, while the blue region on the right denotes a free object.

The figure 2.13 illustration showcases the boundary conditions set for a microstructural assembly. The regions delineated in yellow signify areas that are firmly anchored, implying that they are subjected to constraints preventing any form of movement or displacement. This essentially means that these zones are maintained in a static position, acting as the foundational support for the structure. On the other hand, the regions highlighted in blue depict areas that are free. These zones are not bound by any restraints, allowing them to experience movement and flexion under applied forces. The distinction between these boundary conditions is crucial, as it facilitates a clearer understanding of how different parts of the system respond under varying external influences.

2.6 Cantilever Array Designs

A CMA design is the organization of many cantilevers in a sensor. Cantilever array designs have been suggested and used for a variety of purposes. Linear arrays, in which cantilevers are arranged parallel to each other in a one-dimensional pattern, and two-dimensional arrays, in which cantilevers are arranged in a rectangular or square grid, are two common designs. Cantilevers are arranged in a cube or sphere in three-dimensional arrays to provide multiple detection layers. Random arrays are also used to detect numerous analytes across a vast region by randomly arranging cantilevers over a substrate. Hybrid arrays are made up of different cantilever array designs that are combined to improve the sensor's sensitivity and selectivity. CM sensors can be designed with a single beam or an array of beams to achieve different sensing properties as we can notice in figure2.14. Theoretical models can be used to predict the effects of these design choices on the sensor's performance. When designing a CM sensor with a single beam, the shape of the beam can have a significant impact on its performance. The beam's shape affects its stiffness, resonant frequency, and sensitivity to different physical phenomena. For example, a rectangular beam will have a greater resonance frequency than a beam with the same length and thickness, but a triangular beam may be more sensitive to

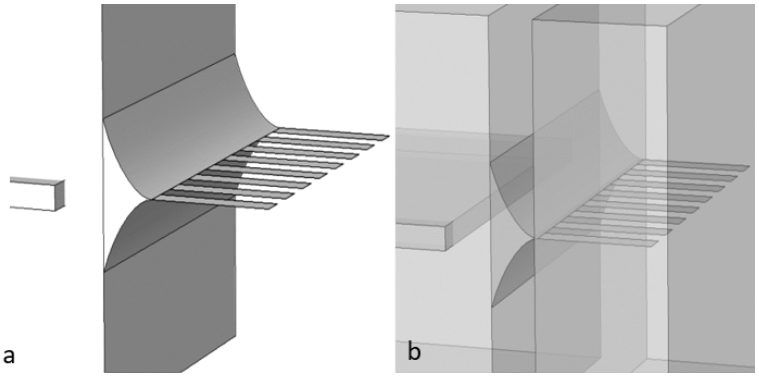

Figure 2.14: Cantilever micro-beam array (a) in air (b) in water chamber

changes in mass at its tip. An array of CM beams can be used to improve the sensor's sensitivity and selectivity. By arranging the beams in a specific pattern, the sensor can detect multiple analytes or physical phenomena simultaneously. The size and spacing of the beams in the array can be optimized to achieve the desired sensitivity and selectivity. The theoretical modeling of CM sensors involves the use of mathematical equations to describe the mechanical properties of the beams and their interactions with the surrounding environment. Finite Element Analysis (FEA) is a common tool used for the theoretical modeling of CM sensors. FEA simulations can be used to predict the resonant frequency, stiffness, and deflection of the beams, as well as the effects of different physical phenomena on the sensor's performance.

In summary, the design of a CM sensor can be optimized by considering factors such as the shape of the beam and the arrangement of an array of beams. Theoretical modeling using FEA can be used to predict the sensor's performance and optimize its design.

2.7 COMSOL Multiphysics Approach

Our Methodology begins by using numerical technology and simulating the physical concept with charges effects to illustrate the functional analysis of the results (frequency deviations and electrical signal properties) using Multiphysics software. Then, the accuracy of the proposed model is validated by close comparison studies of the theoretical calculations to our numerical work using the models of Van Eysden and Sader[7].

In this part, our approach is based on the eigenfrequency shift when the micro-beam is totally immersed in an incompressible fluid. The density variation of the fluid is deduced and solved according to the behavior of the eigenfrequency. The material used for the manufacturing of the cantilever beam is Silicon Dioxide or Silica which is a porous material. Moreover, if the fluid contains particles, they can be adsorbed on the pores of the micro-beam and cause a change in the mass. Examination of theoretical computation by simulation approach was done using COMSOL Multiphysics software.

Several types of excitation are used to make the beam vibrate, the source can be the effect of the electromagnet, thermal noise, or piezoelectric like in our case. Preliminary studies have resulted in

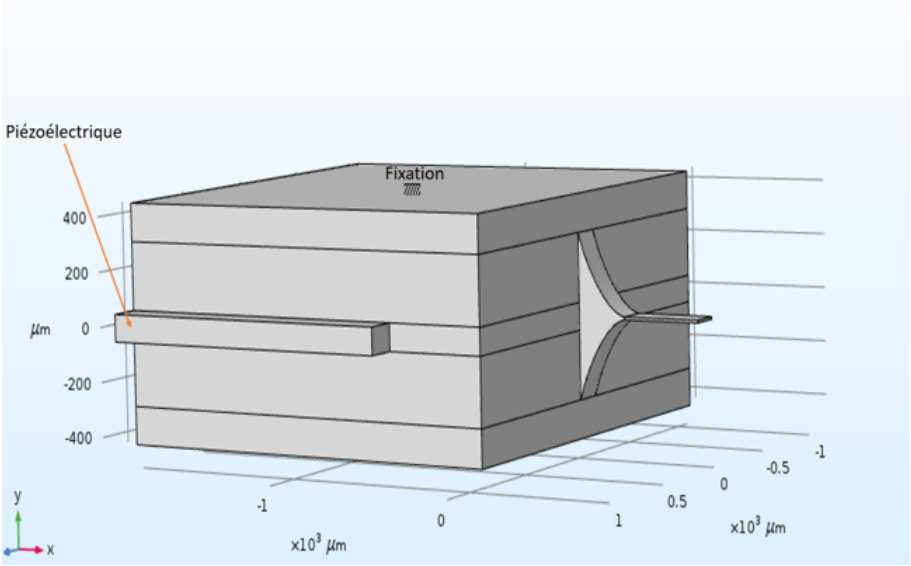

Figure 2.15: Our Model

the assumption that placing the piezoelectric as a layer under the beam causes the metal to melt at the desired frequencies. Furthermore, this placement also might be causing many reactions with the environment of the experiment since the piezoelectric is in contact with the medium. To avoid these risks, we proposed an adapted model of the structure depicted in the figure2.15, where the piezoelectric with $10\mu m$ of width is sandwiched in a box of silica. And this box is engraved in an exponential shape ended by a thin beam having a length of $400\mu m$, width of $140\mu m$, and thickness of $10\mu m$. This design participates in the transfer of stresses from the box to the beam in an efficient way, by reducing the loss and increasing the $Q - factor$. The maximum frequency of the peak depends on the mass and the rigidity of the structure. The used cantilever has the dimensions of (400 x 140 x 10) μm^3. A periodic pulse excitation signal is generated by an external source on the piezoelectric while only immersing the beam in a chamber volume of $1.76\mu L$ of incompressible fluid as shown in figure2.16. The

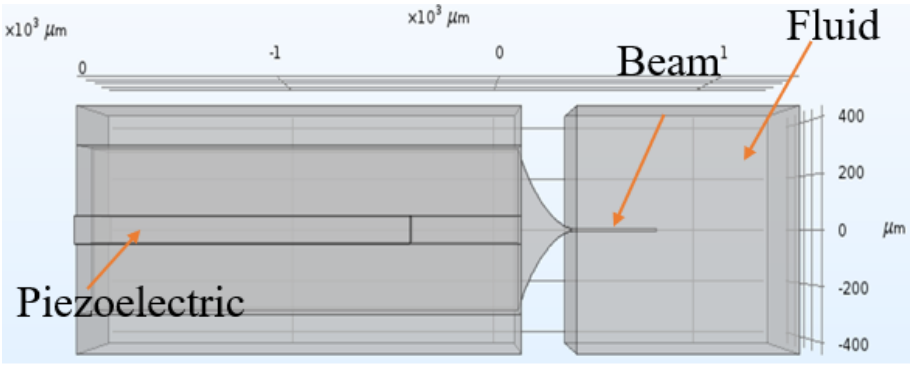

Figure 2.16: Our model immersed in the chamber of fluid

maximum displacement of the beam represents the fundamental frequency of the system and creates acoustic pressure on the surrounding fluid. Any change in the resonant frequency for the next pulse is a function of the change in the environmental characteristics, whether it is the mass of viral parti-

cles adsorb to the surface of the cantilever beam or a change in fluid density. Unlike other methods of measurement by optical reflection [26], deflection of the actuated cantileverelectrode [27],piezoresistive [28] or shifting in resonance frequency [29], our way of measuring depends on analyzing what can be detected. A frequency value is read on the piezoelectric, depending on the damping mode caused by the beam that vibrates, in addition to the shifting frequency for two consecutive eigenfrequencies. With this system, installation and nano-wire complicity are reduced. According to a study done by Ghatkesar et al.[30], the peak frequency is notably scattered in the function of time as for the eigenfrequencies, they are recorded orderly. These findings drove us to rely on the eigenfrequencies. According to our simulation, the deviation between the peak frequency and the eigenfrequency is small while increasing in harmonic mode. A harmonic mode in a CM refers to a specific vibration pattern that the cantilever can exhibit when excited. Cantilevers are slender beams utilized for various sensing applications, such as detecting biomolecules or measuring the mechanical properties of materials. The harmonic modes of a CM are influenced by its geometry, material properties, and excitation frequency. The first harmonic mode, commonly referred to as the fundamental mode, represents the lowest frequency mode and is typified by the entire cantilever bending uniformly. Higher harmonic modes exhibit more intricate vibrations, including multi-directional bends or twists. In our experiments, we observed the vibrational behavior for the 1st, 2nd, 3rd, 5th, and 13th normal modes in a fluid medium. Additionally, the 16th mode was analyzed in the surrounding air. The observed movements indicated favorable nodal positions, suggesting potential for adsorption on the beam while minimizing particle displacement from its pores.

2.7.1 Density and viscosity sensing

The micro-cantilever beam is more sensitive to changes in density than in viscosity while using a beam with $1\mu m$ of width according to Ghatkesar et al.[31].To move towards greater precision in density and viscosity changes we compared the $5th$ harmonic mode with the $13th$ harmonic mode by who has the biggest shift in eigenfrequency while changing in density and viscosity. while using our exponential model which ends with a beam width of 10 μm. Taking water with 997 $Kg/m^{-}3$ of density and 0.913 of viscosity as a reference to examine the frequency changes and to illustrate the sensation variation between our device of 10 μm of width with other thinner devices. According to our tests done before, as we go up in harmonic mode, there is an increase in the changing frequencies, than with the fluids surrounding tests in this paper, we use the $13th$ mode as an eigen value. The eigen frequency characterized by this equation below in the absence of damping with the equation 2.13. Where fn are the eigenfrequencies of the $n-th$ mode, α_n are constants depending on the mode and related to the different eigenvalues of the harmonics: α_1 = 1.8751, α_2 = 4.6941, $\alpha_n = \pi$ (n - 0.5), k is the spring constant of the cantilever given by $k = 3\frac{EI}{L^3}$ where EI is the flexural rigidity, with E Young's modulus and I the moment of inertia and L is the length of the cantilever.

The study showed that in 5% of glycerol test and 5% of ethylene glycol test, we inferred that the viscosity is constant, per contra in 5% of glycerol test and 12% of ethylene glycol the density is constant.

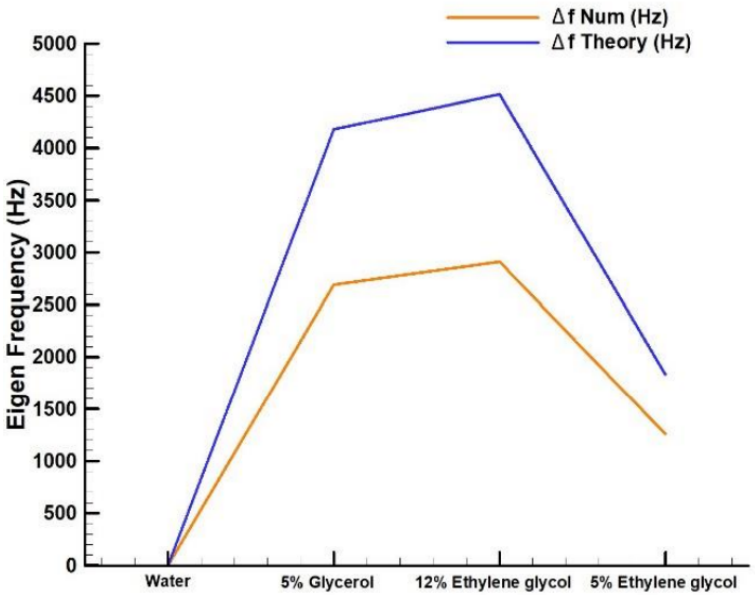

Figure 2.17: Theoretical and numerical shifts eigen frequency were calculated according to[32] at mode 13th.

These tests in Fig are carried out to make a comparison between the density and the viscosity at the level of frequency sensitivity. As we can see in Fig.2.17, in 5% of glycerol, the numerical eigenfrequencies shifted in the center of 680 kHz by 2690 Hz, in 12% of ethylene glycol, it shifted by $2910Hz$ and in 5% of ethylene glycol, it shifted by 1260 Hz Correspondingly, in 5% of glycerol, the analytical eigenfrequencies shifted in the 13th mode by 4178Hz, in 12% of ethylene glycol, it shifted by $4514.6Hz$ and in 5% of ethylene glycol, it shifted by 1833.8 Hz. We have noticed that the change in density is 0.055% and the change in viscosity is 4.41%. Our findings suggest that the beam thickness used with this model has better density sensitivity than previous models. The self-sensing microcantilever obtained in a vacuum is around $390Hz/ng$ measured at a center frequency of 960 kHz and with a density resolution of 0.055% in fluid measured at a center frequency of 680 kHz.

Potassium is a chemical element that exists in the form of an ion in the body. It is present in the serum and too much or too little potassium in the blood plasma can lead to cardiac complications. The normal value of the potassium level should be between 3.5 and $5mmol/L$, for all human beings. A decrease in potassium levels called "hypokalemia"(<3.5$mmol/L$) is often caused by digestive problems, and can cause fatigue, and muscle cramps [33]. Too much potassium in the blood is called "hyperkalemia"(>4.5$mmol/L$) and can cause serious heart problems, which can lead to cardiac arrest and death without emergency chelation therapy. Several studies on cardiac disease are done to detect a specific marker in serum the C-reactive protein for this pathology [34]. In fact, our model is based on the density variation caused by the potassium rate. The potassium level in $mmol/L$ can affect the serum density in $Kg/m^{-}3$ according to this equation:

$$Cm = CM \times MM \tag{2.45}$$

where C_m is mass concentration in g/L, C_M is molar concentration in mol/L and MM is the potas-

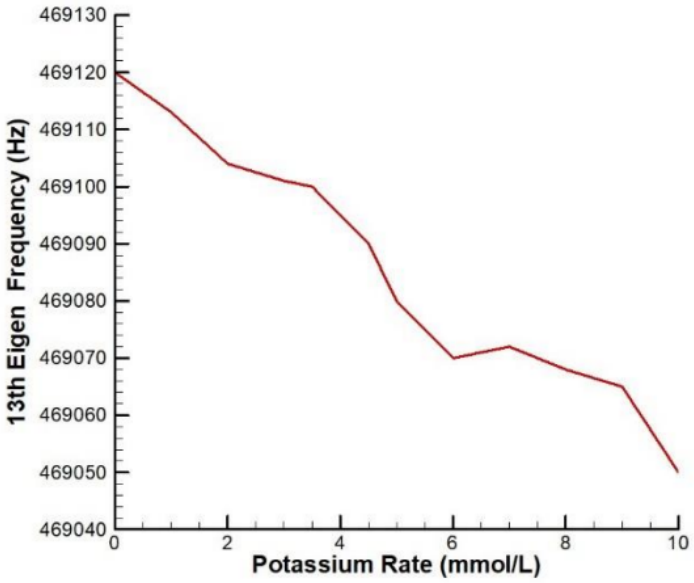

Figure 2.18: Variation of the 13th natural frequency mode with the potassium level and indicate the range of the patient hypokalemia, normal and hyperkalemia.

sium molar mass, equal to 39.1 g/mol. We took a serum density of 1024.136 kg/m^3 as an arbitrary value for a normal patient as an example, who has an eigenfrequency between 640510 Hz and 640530 Hz. The density increases while increasing the amount of potassium and decreases while decreasing the amount of potassium as shown in fig.2.18. The frequency shift is from 640510 Hz to 640460Hz with 0.254 g/L of density for hyperkalemia disease ($> 5mmol/L$) and from 640530 Hz to 640400 Hz with -0.136 g/L of density for hypokalemia disease ($< 3mmol/L$) insofar as shown in fig.2.18. We have noticed that the change is 20 $Hz/mmol.L^{-}1$.

Microcantilever Array

Our advanced concept is shaped by laser engraving in a 2mm thick silicon wafer and this is in accordance with a numerical model resulting from a Multi-physics numerical approach $(COMSOL)$. Through the latter, we were able to illustrate the physical vibration behavior by charge effects on micro-beams of size (500 x 140 x 10)μm^3 excited by a PZT source integrated with the mass of the sensor. An exponential form distinguished on the basis of micro-beam has been adopted in order to favor the amplification of the vibratory modes by purely mechanical means. From a physical point of view, the resonant frequencies of the beams will be affected by the properties of the analysis medium. This assignment which results from the load effect will give access to a law of variation translating the link between the density and/or the viscosity of the medium and the frequency drift of resonance modes. With our design [35], stresses are efficiently transferred from the box to the beams, reducing loss and increasing $Q-factor$s. A preliminary result shows that the beam has an appropriate movement for the order of vibration of the 1st, 2nd, 3rd, 4th, 5th,6th, and 7th harmonic modes immersed in water (as a referential medium) as shown below in figure2.19.

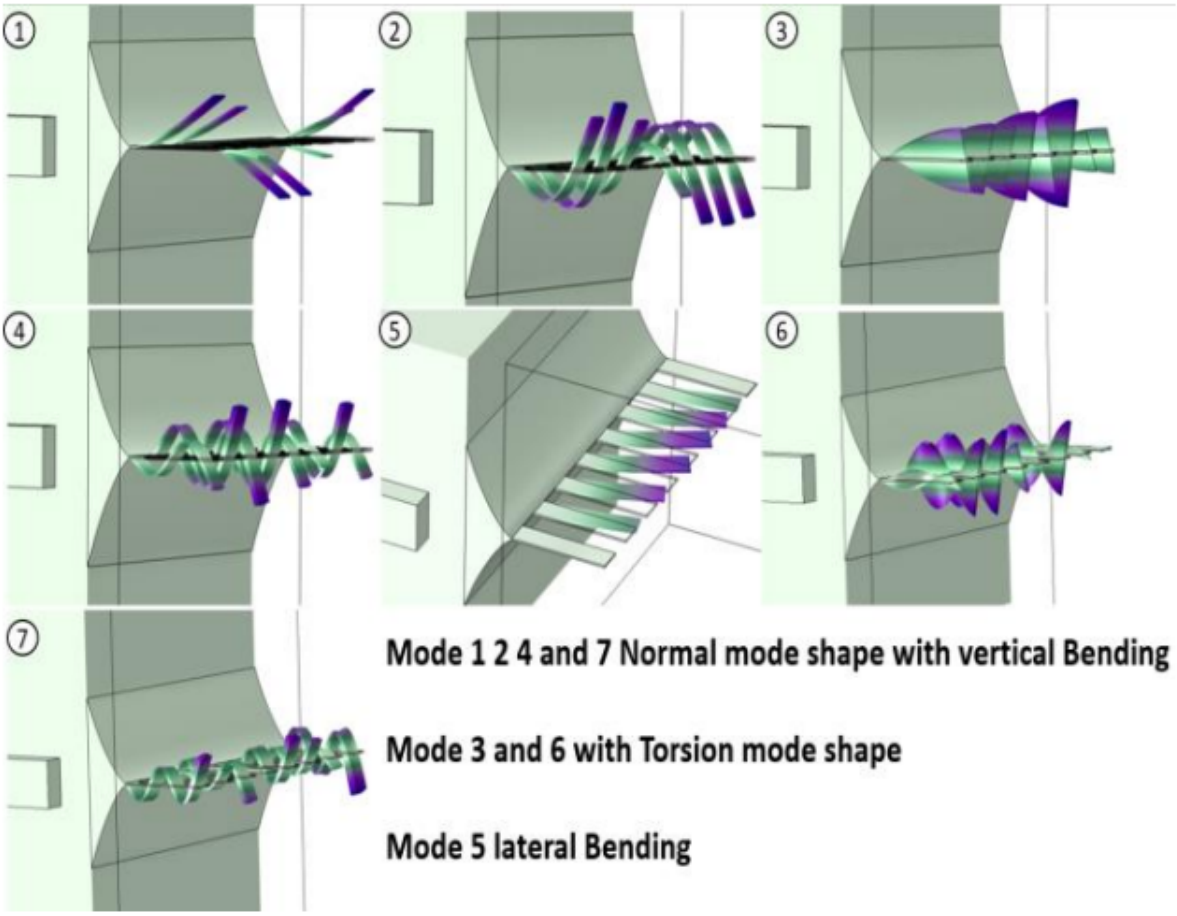

Figure 2.19: Several harmonics mode shapes for cantilever array.

We have also been able to observe that this frequency drift is proportional to the ascending rank of the harmonic components, enabling us to better notice if any medium features have changed.

For specific molecular applications, functionalization of the surfaces of the beams will be necessary in order to create a coating (often based on a polymer) playing the role of a specific and selective bio-sensor for the analyte of interest. In addition, the microbeams can be oxidized to create SiO2, which is a porous material, whose pore dimensions can be of the same order as certain pollutants in a solution (lead for example) thus giving this device the power and the potential to detect by frequency drift by added mass. In order to assess the impact of the (bio-chemical) composition of the medium, the cantilever network was immersed in different micro-capillaries with various biochemical properties. As shown in Figure2.20, the resonance in the $4th$ harmonic mode of micro-beams is largely influenced by the nature and composition of the medium (incompressible fluid). In addition, the micro-beams which have not been subjected to the constraint of the environment display permanent stability thus confirming that the natural frequency depends on the nature and characteristics of its environment. The cantilever beam is made out of silicon (Si) engraved by a laser etching machine in an exponential shape ending with a thin array of eight cantilevers with a size of (500 x 140 x 10) μm^3. Based on the behavior of the natural frequency, it is possible to estimate the variation of the density of a fluid or the presence of markers in a gas or liquid. To select the target

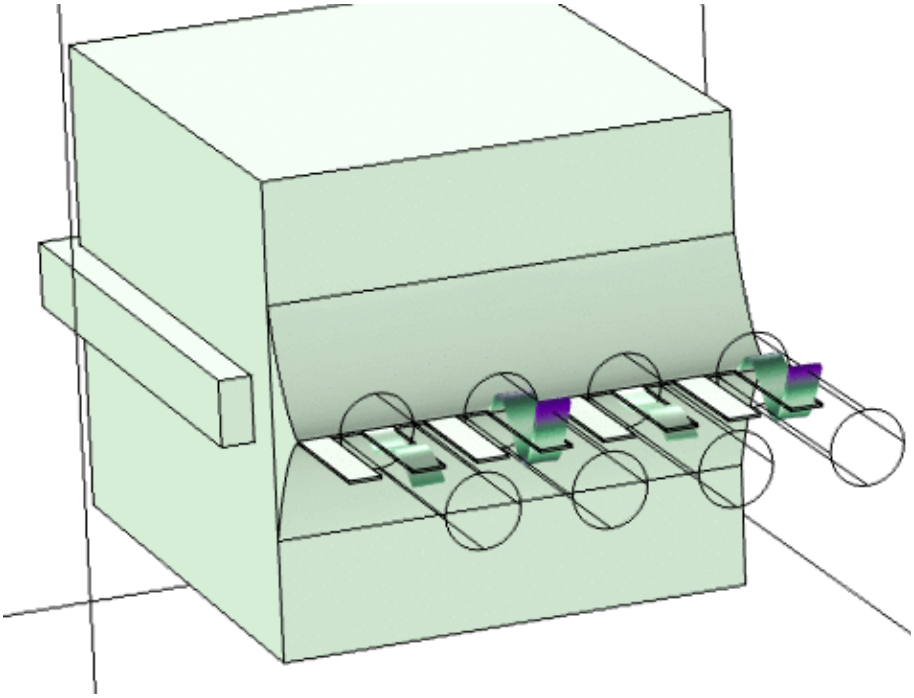

Figure 2.20: Cantilever array with the insertion of several microcapillaries each containing a different blend in mode $4th$.

analyte, it is necessary to identify the binding site as well as the covalent or non-covalent interactions between the functional monomer and the analyte. It can monitor natural, industrial, and residential areas by analyzing the eigenfrequency change when the micro-beam is immersed in a sample of these mediums. The numerical analysis using COMSOL Multiphysics software conducted was based on theoretical computations. The frequency resolution of the self-sensing micro-cantilever achieved in the fluid is $50Hz/mmol.L^1$ with mode $7th$ around $1.14MHz$ However, we have noticed that this device can detect changes in density up to 0.054%. We deduced that the $1st$, $2nd$, $4th$, $7th$ harmonics modes are normal with vertical bending, which helps us to reach the possibility of adsorption on the beam while avoiding the fall of particles from the pores with an appropriate bending of the beam. Following that, we will compare the theoretical calculation results to our numerical work based on Van Eysden and Sader's [36] models to verify the accuracy of the proposed model. From the practical point of view, the lead level in $mmol/L$ for example can affect the water density kg/m^3 according to this equation 2.46. where C_m is mass concentration in g/L, C_M is molar concentration in mol/L and MM is the potassium molar mass, equal to 207.2 g/mol. The density of water is $997kg/m^3$ is associated with an average value of a resonant frequency of 1,126,450 Hz. Thus, Figure 2.21 shows a linear law which is established between the molar variation of the lead content in water and the frequency drift. Indeed, the variation in the lead level between 0 and 10 $mmol/L$ induces sensitivity to the frequency drift around $500Hz$. Such sensitivity opens up the prospect of a multitude of potential applications both on the quality of the environment as in cell biology and/or chemistry domain.

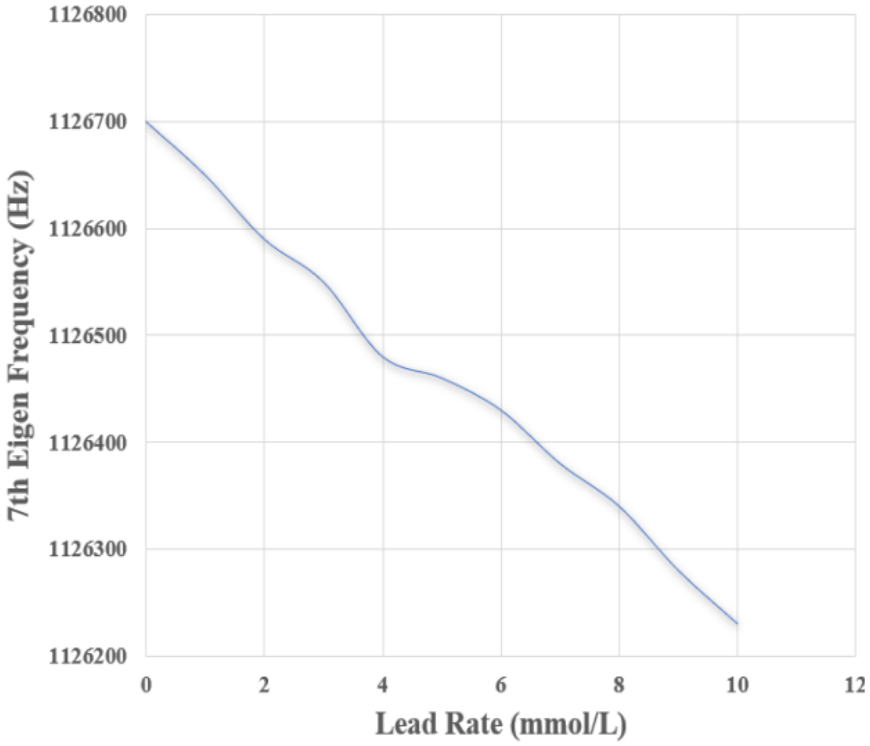

Figure 2.21: Δf Num in fluid for Mode $7th$ while adding lead to a water-filled microcapillary.

2.7.2 Sensing the adding mass

For additional optimization, we made several numerical estimations of δf variation for two different methods of added masses on the beam as shown in Fig2.22. For accuracy, this test is validated by a close comparison of the studies of the theoretical calculations with our numerical works by using equation 2.17. Where Δm is related to the loaded mass distributed on the surface of the cantilever and the eigen frequency $f_{0n}$is characterized by this equation in the absence of damping. As shown in Fig.2.22, the first test was at the center of 640 KHz (13th Mode) surrounded by a fluid, and the mass was added on the whole surface with an accuracy of 90Hz/ng.

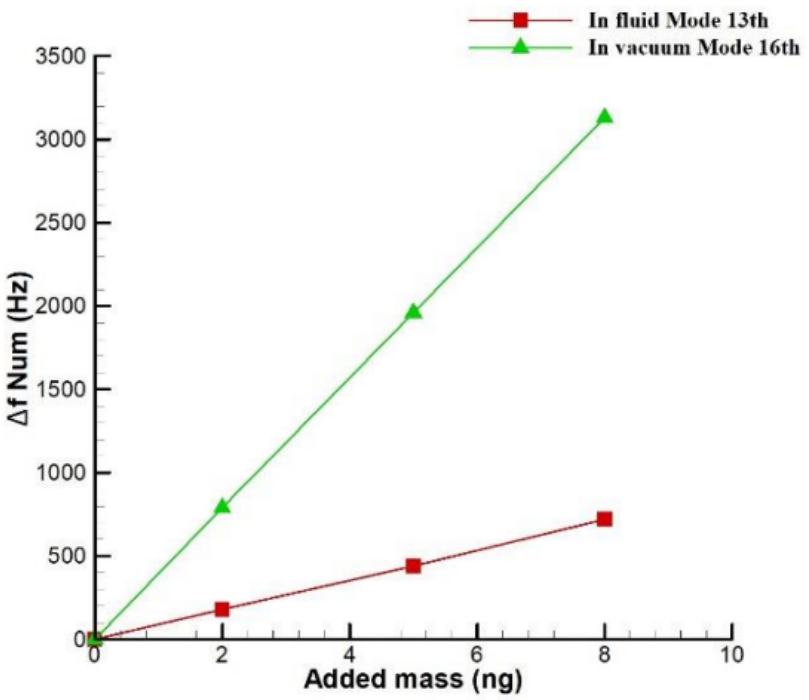

Figure 2.22: Δf Num in fluid for Mode 13th and in vacuum for Mode 16th.

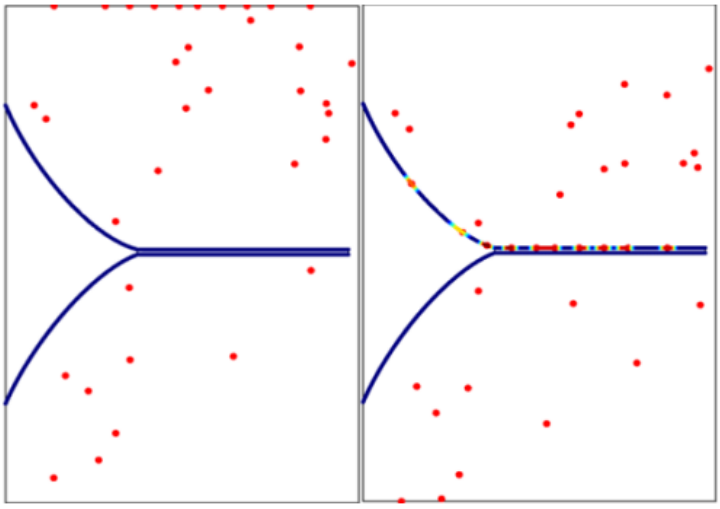

Figure 2.23: Potassium adsorption on the surface of SiO2 beam.

The second test was at the center of 961KHz $(16thMode)$ under vacuum and the mass was added on the whole surface with an accuracy of 390 Hz/ng. Our numbers show that in a liquid medium the shifting frequency is much more pronounced than in a vacuum owing to the influence of hydrodynamic force on the cantilever. By examining the curve shown in Figure 2.18, it can be noticed that the change in frequency is shifted by 140 Hz in a change of 0.39 g/L of potassium. Moreover, the $SiO2$ is a porous material where the average pore diameter is between 2.6 and 68.3 nm [37] compatible with the diameter of potassium particles of 550 pm. Based on the aforementioned, these potassium beads

may be adsorbed on the beam during the vibration, and this will be a great incentive to change the eigenfrequency. The validation was done using *COMSOLMultiphysics* software as depicted in figure 2.23 with the red beads being the potassium particles and the bleu lines being the beam clamped on one edge. The change in the eigenfrequency as a function of the mass of particles attached to the surface of the cantilever beam could be the basis of the detection scheme.

Conclusion

This chapter discusses the importance of resonance frequency and impedance in detecting the presence and properties of particles in a fluid medium using a dynamic mode cantilever microbeam setup. The relationship between impedance and resonance frequency is explained, where the impedance is at a minimum when the cantilever beam is driven at its resonance frequency. Tracking the changes in frequency and impedance can detect and quantify particles in the medium. The choice of tracking ΔF depend on the particles' properties and experimental conditions, and it is essential to consider the signal-to-noise ratio of the measurement. We also highlight the significance of the theory of cantilever beam behavior in MEMS sensors, including CM beam sensors that can detect the presence of added mass by measuring either a shift in resonant frequency or a change in impedance. CM array designs enable the measurement of multiple physical quantities simultaneously, making them ideal for various applications, such as biomedical, environmental, industrial control, and structural health monitoring.

Despite their advantages, MEMS sensors face challenges, such as signal-to-noise ratio issues and the need for calibration. However, ongoing research and development in this field is improving their performance. This chapter also indicates the study's aim to use numerical techniques to simulate the physical concept of charge effects for functional analysis of the results, including frequency deviations and electrical signal properties. The proposed model's accuracy will be validated by comparing theoretical calculations to numerical work using Van Eysden and Sader's models [7].

Bibliography

[1] Thomas R Albrecht et al. "Frequency modulation detection using high-Q cantilevers for enhanced force microscope sensitivity". In: *Journal of applied physics* 69.2 (1991), pp. 668–673.

[2] Helen G Hansma et al. "Atomic force microscopy of DNA in aqueous solutions". In: *Nucleic acids research* 21.3 (1993), pp. 505–512.

[3] EJKTDJSRL Betzig et al. "Breaking the diffraction barrier: optical microscopy on a nanometric scale". In: *Science* 251.5000 (1991), pp. 1468–1470.

[4] Cornelis A Van Eysden and John E Sader. "Resonant frequencies of a rectangular cantilever beam immersed in a fluid". In: *Journal of applied physics* 100.11 (2006), p. 114916.

[5] WH Chu. "Technical report no. 2". In: *DTMB, Contract NObs-86396 (X), Southwest Research Institute, San Antonio, Texas* (1963).

[6] R Berger et al. "Micromechanics: A toolbox for femtoscale science:"Towards a laboratory on a tip"". In: *Microelectronic Engineering* 35.1-4 (1997), pp. 373–379.

[7] John Elie Sader. "Frequency response of cantilever beams immersed in viscous fluids with applications to the atomic force microscope". In: *Journal of applied physics* 84.1 (1998), pp. 64–76.

[8] K Uno Ingard. *Theoretical acoustics*. McGraw Hill, 1968.

[9] Harris CM, Crede CE, and ELECTR ENG ARCHIT. *Shock and vibration handbook*. McGraw-Hill, New York, 1976.

[10] U Rabe, K Janser, and Wt Arnold. "Vibrations of free and surface-coupled atomic force microscope cantilevers: Theory and experiment". In: *Review of scientific instruments* 67.9 (1996), pp. 3281–3293.

[11] James WM Chon, Paul Mulvaney, and John E Sader. "Experimental validation of theoretical models for the frequency response of atomic force microscope cantilever beams immersed in fluids". In: *Journal of applied physics* 87.8 (2000), pp. 3978–3988.

[12] Jiushuai Xu et al. "Piezoresistive microcantilevers for humidity sensing". In: *Journal of Micromechanics and Microengineering* 29.5 (2019), p. 053003.

[13] Joao Mouro et al. "Microcantilever: Dynamical response for mass sensing and fluid characterization". In: *Sensors* 21.1 (2020), p. 115.

[14] L Landau. *Em Lifshitz Fluid Dynamics*. 1987.

[15] LD Landau and EM Lifshitz. *Theory of Elasticity (Pergamon Press, Oxford, 1959)*. 1970.

[16] Dror Sarid et al. "Scanning force microscopy-with applications to electric, magnetic and atomic forces". In: *Microscopy Microanalysis Microstructures* 2.6 (1991), pp. 649–649.

[17] Cornelis A Van Eysden and John E Sader. "Frequency response of cantilever beams immersed in viscous fluids with applications to the atomic force microscope: Arbitrary mode order". In: *Journal of applied physics* 101.4 (2007).

[18] Cornelis A Van Eysden and John E Sader. "Frequency response of cantilever beams immersed in compressible fluids with applications to the atomic force microscope". In: *Journal of applied physics* 106.9 (2009).

[19] Kishan Rijal and Raj Mutharasan. "Piezoelectric-excited millimeter-sized cantilever sensors detect density differences of a few micrograms/mL in liquid medium". In: *Sensors and Actuators B: Chemical* 124.1 (2007), pp. 237–244.

[20] Sen Xu and Raj Mutharasan. "A novel method for monitoring mass-change response of piezoelectric-excited millimeter-sized cantilever (PEMC) sensors". In: *Sensors and Actuators B: Chemical* 143.1 (2009), pp. 144–151.

[21] David Maraldo and Raj Mutharasan. "10-minute assay for detecting Escherichia coli O157: H7 in ground beef samples using piezoelectric-excited millimeter-size cantilever sensors". In: *Journal of food protection* 70.7 (2007), pp. 1670–1677.

[22] David Maraldo and Raj Mutharasan. "Detection and confirmation of staphylococcal enterotoxin B in apple juice and milk using piezoelectric-excited millimeter-sized cantilever sensors at 2.5 fg/mL". In: *Analytical Chemistry* 79.20 (2007), pp. 7636–7643.

[23] WP Mason and RF Wick. "Ferroelectrics and the dielectric amplifier". In: *Proceedings of the IRE* 42.11 (1954), pp. 1606–1620.

[24] Edward Eisner. "Design of sonic amplitude transformers for high magnification". In: *The Journal of the Acoustical Society of America* 35.9 (1963), pp. 1367–1377.

[25] Dale Ensminger. "Solid Cone in Longitudinal Half-Wave Resonance". In: *The Journal of the Acoustical Society of America* 32.2 (1960), pp. 194–196.

[26] Chun-Hao Chen et al. "A wireless bio-MEMS sensor for C-reactive protein detection based on nanomechanics". In: *IEEE Transactions on Biomedical Engineering* 56.2 (2008), pp. 462–470.

[27] Masoud SoltanRezaee and Mahdi Bodaghi. "Simulation of an electrically actuated cantilever as a novel biosensor". In: *Scientific reports* 10.1 (2020), pp. 1–14.

[28] Kyung Wook Wee et al. "Novel electrical detection of label-free disease marker proteins using piezoresistive self-sensing micro-cantilevers". In: *Biosensors and Bioelectronics* 20.10 (2005), pp. 1932–1938.

[29] Jeong Hoon Lee et al. “Immunoassay of prostate-specific antigen (PSA) using resonant frequency shift of piezoelectric nanomechanical microcantilever”. In: *Biosensors and Bioelectronics* 20.10 (2005), pp. 2157–2162.

[30] Thomas Braun et al. “Micromechanical mass sensors for biomolecular detection in a physiological environment”. In: *Physical Review E* 72.3 (2005), p. 031907.

[31] Murali Krishna Ghatkesar et al. “Multi-parameter microcantilever sensor for comprehensive characterization of Newtonian fluids”. In: *Sensors and Actuators B: Chemical* 135.1 (2008), pp. 133–138.

[32] Cornelis A Van Eysden and John E Sader. “Frequency response of cantilever beams immersed in viscous fluids with applications to the atomic force microscope: Arbitrary mode order”. In: *Journal of applied physics* 101.4 (2007), p. 044908.

[33] Philippe Veroli. *Le Potassium Mode d’emploi: Contrôlez l’acidité de votre corps avec le potassium*. Thierry Souccar, 2015.

[34] Riccardo Castagna. “Detection of Angiogenic Growth Factor by Microcantilever Biosensors”. In: (2011).

[35] Victory Elias et al. “Investigation of the Eigen Frequency of a Cantilever Microbeam Immersed in a Fluid Under the Piezoelectric Effect”. In: (2021).

[36] Cornelis A Van Eysden and John E Sader. “Frequency response of cantilever beams immersed in compressible fluids with applications to the atomic force microscope”. In: *Journal of applied physics* 106.9 (2009), p. 094904.

[37] Takehisa Mochizuki et al. “Effect of SiO2 pore size on catalytic fast pyrolysis of Jatropha residues by using pyrolyzer-GC/MS”. In: *Catalysis Communications* 36 (2013), pp. 1–4.

Chapter 3

Cantilever Microbeam Sensor Development and Characterization

3.1 Introduction

We explained in the numerical approach that the underlying objective of our project is to characterize serum to prevent health problems (breast cancer). To detect biomarkers that have a negligible mass reliably, it was essential to create beams with a thickness of less than $10\mu m$, and there would also be nanometric layers such as gold from which grafting and planting of the antibodies of the desired antibody can be done for diagnosis. Hence, our initial proposal was to make thin beams (400 x 140 x 10) μm^3 with a pitch of $140\mu m$. However, after analysis, we opted for a slightly larger structure for several reasons:

1. Validate the design of the structure carrying the cantilever micro-beams, ensuring that we could manipulate the structure using available means with the least possible cost.

2. Ensure that we could engrave with the ablation laser within the limits of the technology.

After discussing with the implementation team to understand the limits ($10\,\mu m$ of precision) of our ablation laser in terms of precision, we chose the following dimensions $500 \times 120 \times 40\,\mu m^3$ with a pitch of $180\,\mu m$. For technical reasons, the dimensions adopted are $800 \times 120 \times 40\,\mu m^3$ with a pitch of $400\,\mu m$. More details will be provided in the subsequent sections.

This chapter explores the methodical progression behind our sensor's development, providing insights into both its design evolution and the rigorous steps taken to bring it to fruition. Our first attempt involved the ablation procedure for the structure with the ablation laser, aiming to engrave the structure in one go, but unfortunately, this did not work. As a result, we decided to embark on a second procedure where the structure was divided into several parts and then assembled, which produced perfect results but required creating a support to stack the engraved tiles. After engraving the beams and assembling them with the support we developed, we proceeded with integrating the piezoelectric into the structure after cutting it with the laser. It's worth noting that we employed

various assembly methods and checked the surface condition with FEM photos to verify and validate the assembly between the pieces and the piezoelectric and to ensure the cleanliness of the beams before proceeding to the analysis, given the critical nature of the beams' condition. In the next step, we explain how we developed a support to hold the assembled samples (the cantilever beams and the piezoelectric in the slot of the box holding these beams) and simultaneously assume the electric connection. After this implementation phase, we moved on to verify several aspects: The interaction between the source and the structure. The connection between the piezoelectric and the SMA (Shape Memory Alloy) cable. The functioning of the sensor when submerged or dipped in the referred fluid. Finally, the behavior of the sensor and the beams when subjected to load.

Once we obtained all these results, we proceeded to the sensor calibration section, which will be discussed in the following chapter. However, the piezoelectric are crucial components in various applications owing to their sensitivity to mechanical changes. Their efficiency and functionality can be influenced by factors like assembly techniques, beam spacing, and the medium they're placed in. In addition, we examine how the piezoelectric material behaves under various conditions and its influence when incorporated into a larger system, in order to clarify the complexity of these dependencies. The development of any innovative sensor, especially one with complexity such as a piezoelectric-integrated cantilever micro-beam, is rarely straightforward. From conception to realization, every step relies on iterations, trials, and constant refinement, informed by knowledge gained from prior experiences.

3.2 Evolution of the Sensor Design

Our concept evolved through a delicate balance between innovation and practicality. To begin with, we aimed to create a coherent synergy between form and function. The foundational structure of the micro-cantilever assembly bore dimensions of (500 x 120 x 40) μm^3 with a pitch of 180μm specifically for the cantilever. Our sensor's effectiveness is based on its precise dimensions, which ensure optimal functionality and responsiveness. However, the creation of this assembly was not without its complexities. A laser ablation procedure was used to achieve the fine details of the structure during the engraving process. During the engraving phase, we were able to maintain the integrity of the material thanks to this separated approach. Every decision, every measurement, and every procedure we made towards sensorial perfection became evident as we explored the technical aspects of our design. We retained the design that was proposed and validated in the theoretical and numerical sections as depicted in Figure 3.1. However, we adjusted the thickness and length of the beams to align with the precision of the laser ablation.

3.2.1 Initial Design and Challenges

Let's refer to the design in Figure 3.1. Critical considerations for the structure include: a design that is easy to manage and handle, ensuring a clean and uniform surface, having identical beams,

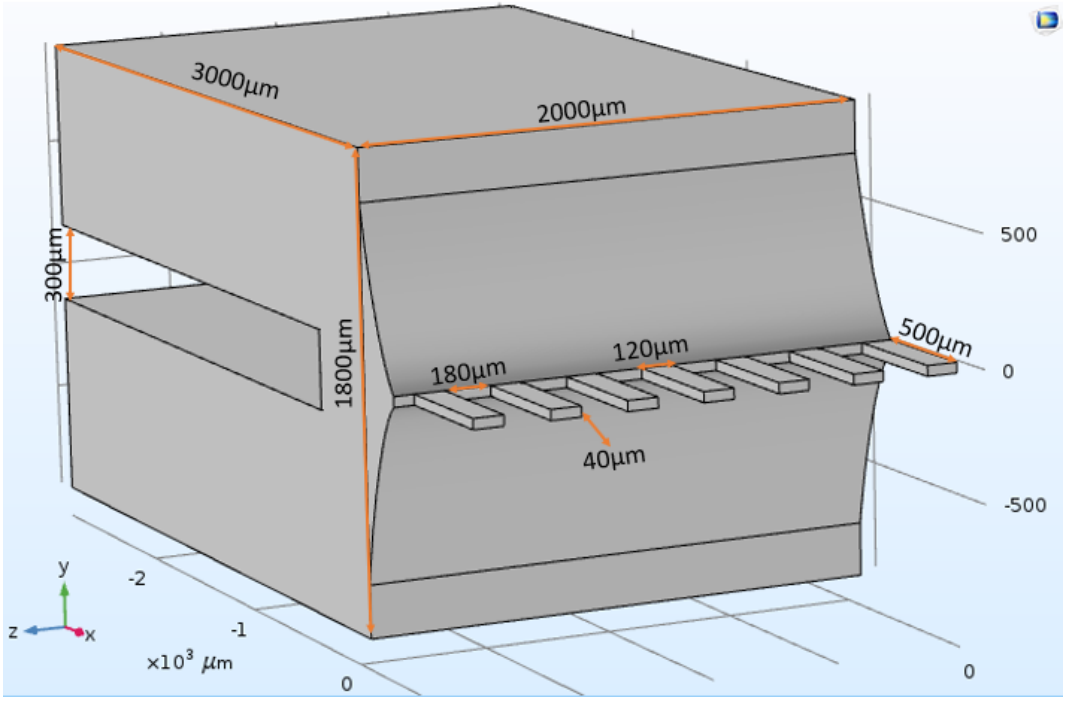

Figure 3.1: Our First Proposition - CAD Model

and achieving optimal and perfect contact between the piezoelectric element and the structure into which it is integrated. Consequently, we chose to manufacture the device using a femtosecond laser, as previously mentioned. Silicon devices were constructed using the Oxford JSeries laser as Figure 1.10 shows, which operates at a green wavelength. The device has a thickness of 2 mm, so we sourced a 2 mm thick silicon wafer for engraving.

The color (or wavelength) of the laser is essential for its interactions with various materials. A green light, as mentioned, typically has a wavelength of about 532 nm. Galvo lenses mounted on the Z-head (galvanometer-driven mirrors) are rapid motion mirrors capable of quickly redirecting the laser beam onto the work surface. They allow for the fast and accurate positioning of the laser beam. In many laser systems, these are utilized for high-speed engraving or marking without the need to physically move the object being engraved. The Z-head (or Z-axis control) adjusts the laser's focal depth, essential for focusing on surfaces at different heights or engraving at varying depths. For 3D engraving, precise Z-axis control lets the laser engrave at different material depths, creating a three-dimensional image. The XY jig is a motorized platform that can move the workpiece (or sometimes the laser head) in the X and Y directions. This setup allows for engraving larger designs or patterns beyond the galvo mirrors' immediate field of view and can also engrave larger pieces sectionally.

3D Engraving Process:

For 3D engraving over several iterations with the laser: The design to be engraved is first processed by a specialized software, in our case, Alphacam, to create a depth map. This map guides the laser on the depth to engrave for each design section. We have data from previous projects that detail the specific characteristics needed to cut certain materials of a given thickness. The laser starts the

engraving based on the depth map nad once the graving start we can see the reddot on the wafer as shown figure 3.2. The Z-head adjusts the focal depth according to the design's requirements, allowing for various engraving depths. For deeper engravings, the laser makes multiple passes, removing a bit of material with each iteration. The combination of precise Z-axis control and several passes enables the laser to produce detailed 3D engravings. Throughout this process, the galvo mirrors and the XY jig work together to ensure accurate laser beam positioning across the entire design. The first ablation focuses on the side view, and the second ablation targets the top view to achieve the desired shape.



Figure 3.2: Laser Oxford Etching Silicon Wafer With a Green Wavelength

There are two available laser micromachining setups, operating in the nanosecond and femtosecond pulse durations, respectively. The engraving process will be conducted in two stages. Firstly, on a silicon wafer with a thickness of 2mm, we will create the slot where the piezo will be integrated and carve out the exoskeleton of the device, as illustrated in Fig 3.3. Subsequently, the device will be placed on the laser's jig as depicted in Fig 3.2, where ablation will be performed on the beams, as shown in Fig 3.4.

We detailed the ablation process across multiple stages, with each stage having its unique ablation format, as delineated in the table 3.1 and visually presented in the attached photograph. The laser's specifications include Wavelength: 532 nm, Average Power: 7.01 W at 200 kHz, and Focus: 285.6. An airflow was maintained over the machining surface throughout the process. With this laser, we can achieve beam thicknesses ranging between 20µm and 40µm. Our goal is to identify a method that can consistently achieve these specifications while addressing all critical points.

Three tests were conducted on this model. The first step involves machining the device into a 2

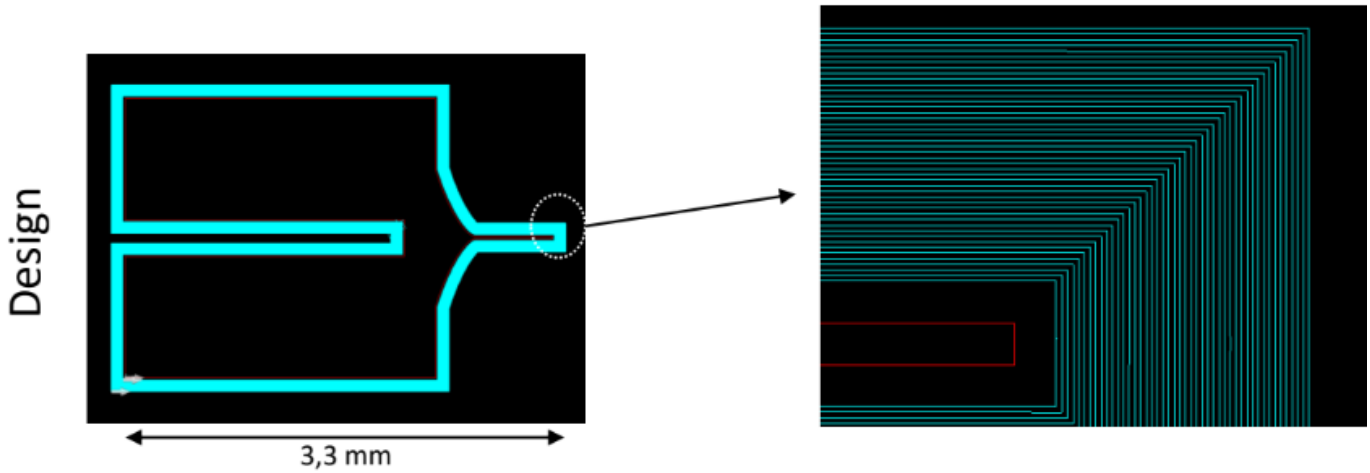

Figure 3.3: This is the structure transmitted in DXF format with the different laser passages for ablation for the first Etch.

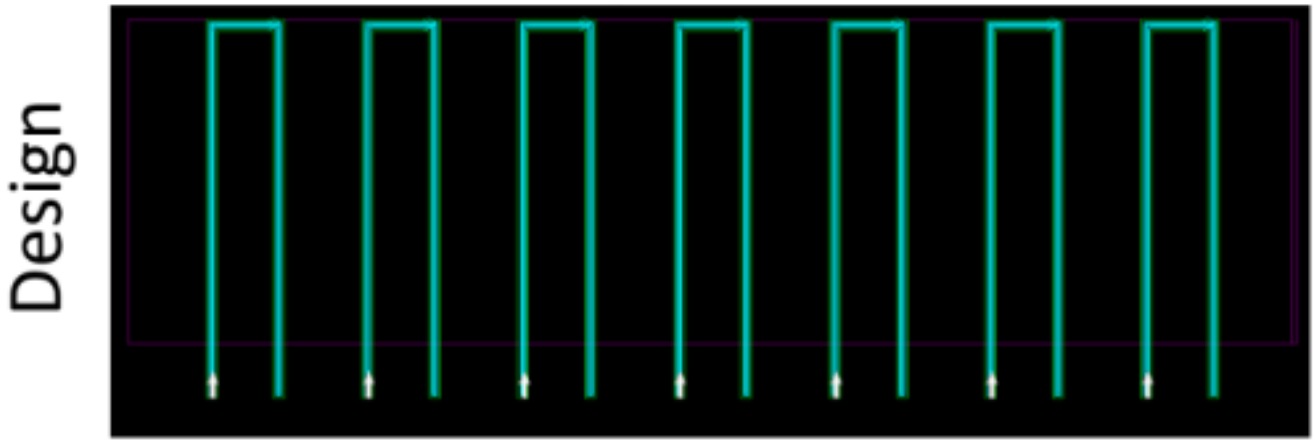

Figure 3.4: In the next step, the engraving will be done on the beam.

mm thick silicon wafer. The second step requires flipping the created device over and machining the slats on the edge.

Discussing **Step 1:** with the first test (see Figure 3.5): the device was machined into a 2 mm thick wafer. Width of the slat: 50 µm on the backside. *Note*: The sample was cleaned in an ultrasonic bath 3.12 (acetone + alcohol). Debris remains visible on the front. The cleaning Sonix 6MX machine vibrations likely caused the slat to break (as visible from the side view). With the second test (see Figure 3.6), adjustments were made to the ultrasonic power and rinsing. Here, there was no cleaning. We observe that the slat is not intact. Then, a second ultrasonic test was conducted at 40% power: ultimately, the sample broke.

	Repetition Frequency (kHz)	Number of passes	Power %	Movement speeds (mm/s)	Zpitch (µm)
Test n °1	33	160	100	10	12.5
Test n °2	33	150	100	11	13
Test n °3	33	150	100	11	12

Table 3.1: Machining parameters of the three tests

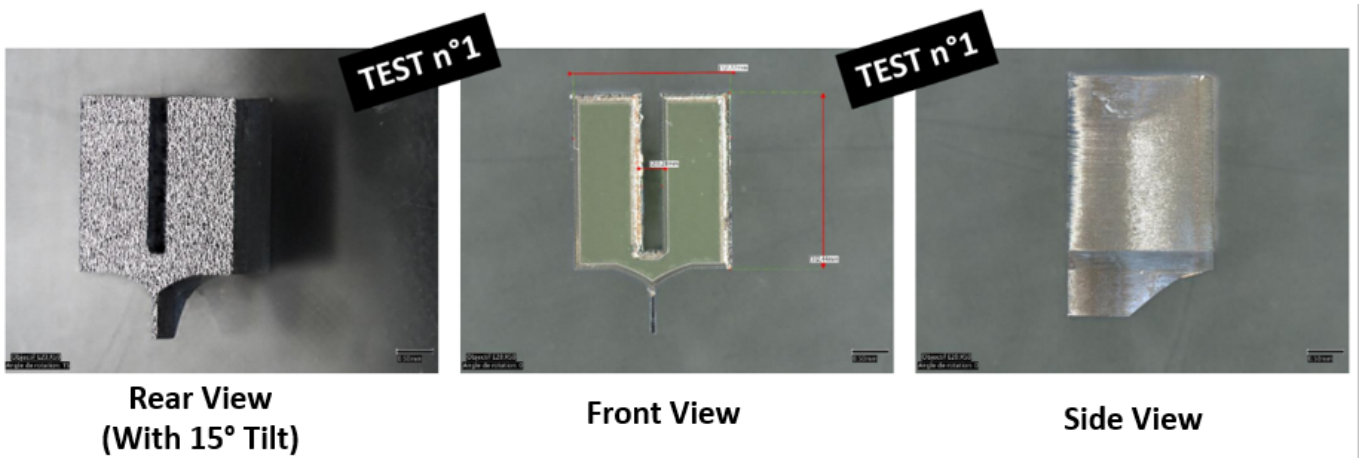

Figure 3.5: TEST 1 In 2D View

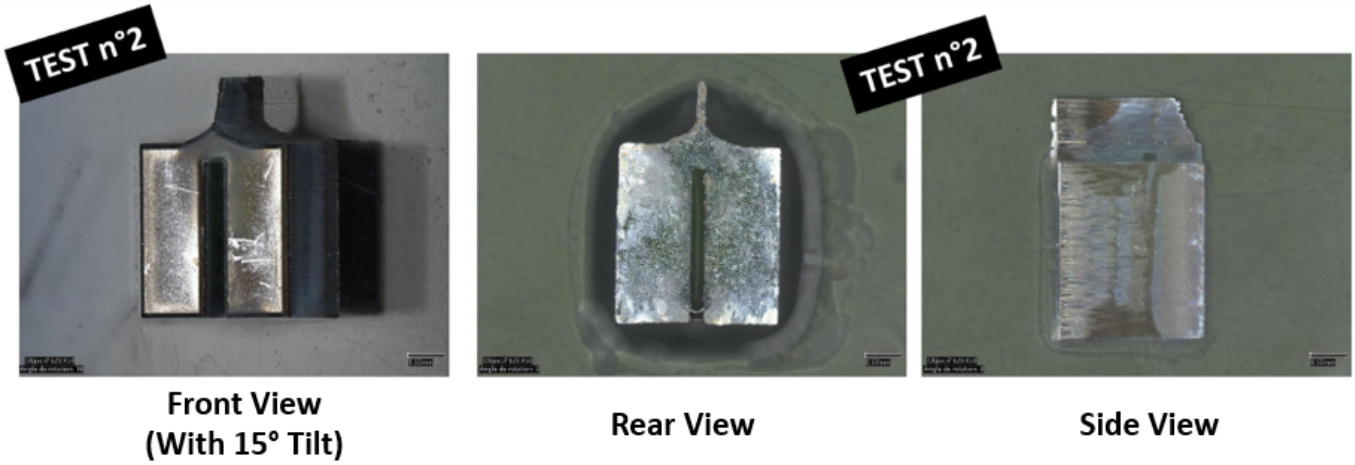

Figure 3.6: TEST 2 In 2D view

With the third test (see Figures 3.7, 3.8, and 3.9), cleaning consisted of a simple acetone/alcohol bath with a light cotton swab pass. The width of the slat is 38µm on the front and 78µm on the back.

Step 2: involves machining the slats onto the device, with no constraints. In conclusion, the device is manageable. Taking between 2 to 3 hours of total machining time, it is lengthy. Machining is done on the 2 mm thick Si. The aspect ratio is approximately 91.5° on the Si edges. We are sticking to the 2 mm model: the process is already lengthy for the 2 mm device, yet it remains manageable. The slat thickness is limited by the laser's capabilities. At best, a result of around 50 µm in thickness was achieved. This issue is related to the nature of the beam. With a Gaussian beam, it measures about



Figure 3.7: TEST 3 In 2D View

30 µm when focused; 2 mm lower, its diameter expands by several tens of micrometers. Therefore,

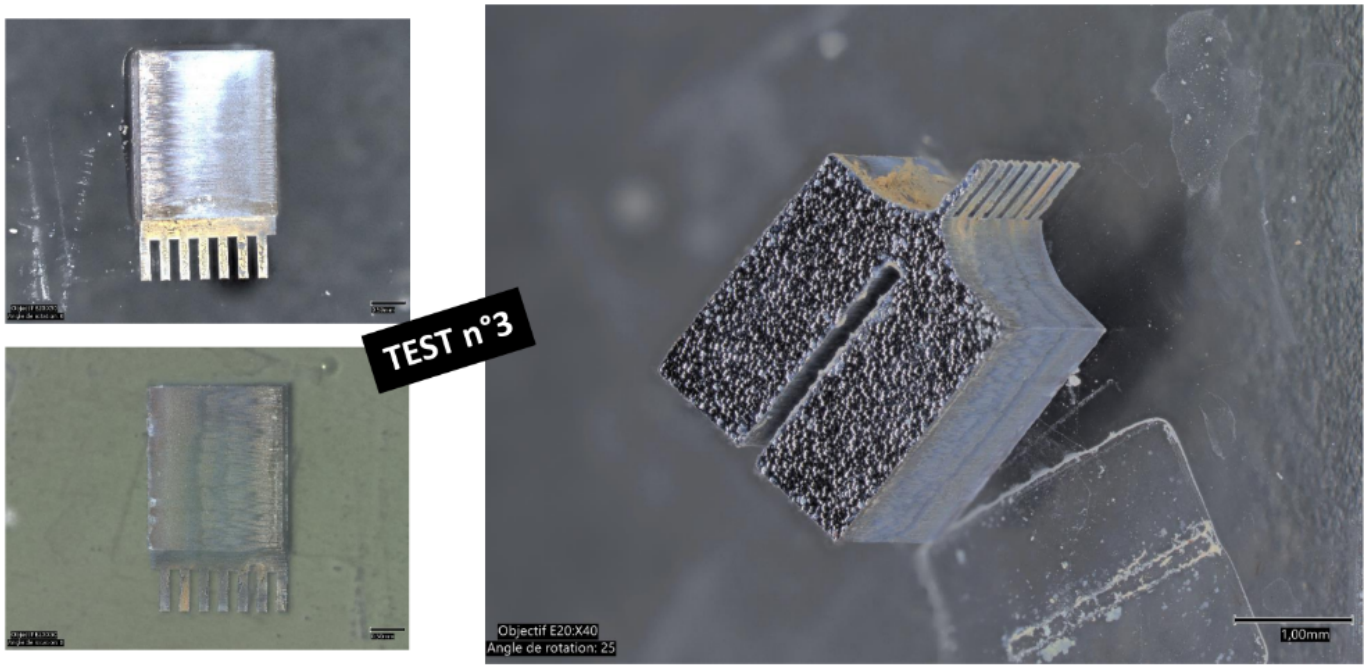

Figure 3.8: TEST 3 In 3D View

we always end up "trimming" the top of the slat when machining the bottom. We considered touch-ups using FIB, but after several attempts, it was deemed impossible: furthermore, there's too much surface to remove. Ultrasonic cleaning is not feasible: the vibrations are too strong even at the lowest power, resulting in a tuning fork effect. A different cleaning method must be found.

Additionally, as can be seen in the images 3.10 , the device includes six beams ranging from $89\mu m$ to $41\mu m$. To understand why we have to notice that the side of the laser beam is the side where the $41\mu m$ is so we can imagine the position of the wafer that the upper side that faces the galvanometric lens is the side of the $41\mu m$ and the while we go deep in the etching while the error is bigger.

In Figure 3.11, you will find the results of the cleaning. We began the cleaning process using

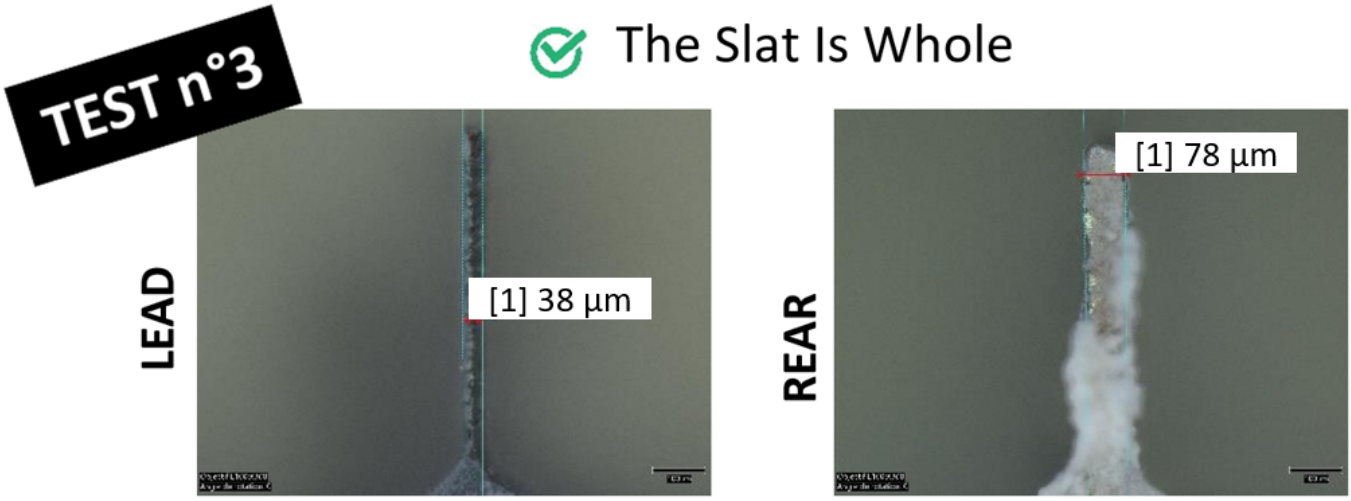

Figure 3.9: TEST 3 Slat Is Whole

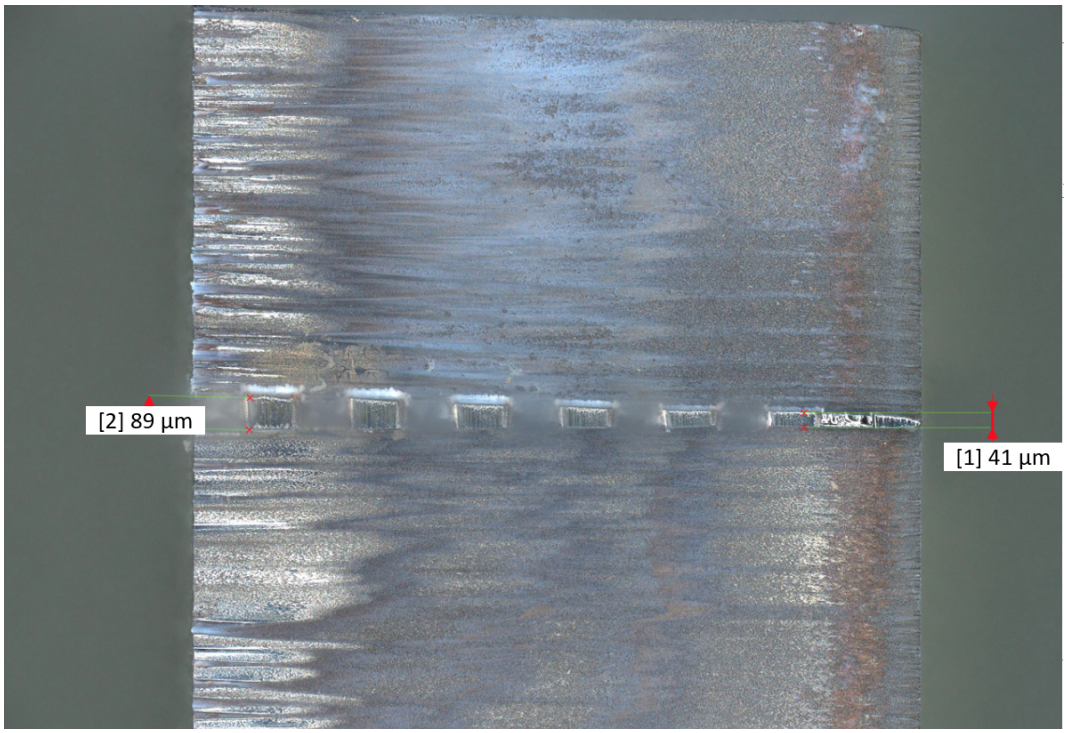

Figure 3.10: This Sample Includes Six Beams Ranging From 89μm to 41μm

a detergent as recommended by a colleague chemist. This cleaning requires some handling of the device. Even though we took many precautions, these manipulations resulted in the breaking of the thinnest slat (those less than 40μm). Some light debris remains, but most of the dust can be removed without the use of ultrasonics machine see in fig 3.12. Furthermore, as seen in Figure 3.11, the device comprises 6 slats ranging from 90 to 40 µm. We used it as a trial for initial handling and mainly to understand the device's fragility. Regarding the possibility of thinning down the structure, as I previously mentioned, it's impossible with FIB since there would be too much material to remove. Additionally, we employ a technique involving the XeF2 etching method. In this approach, silicon

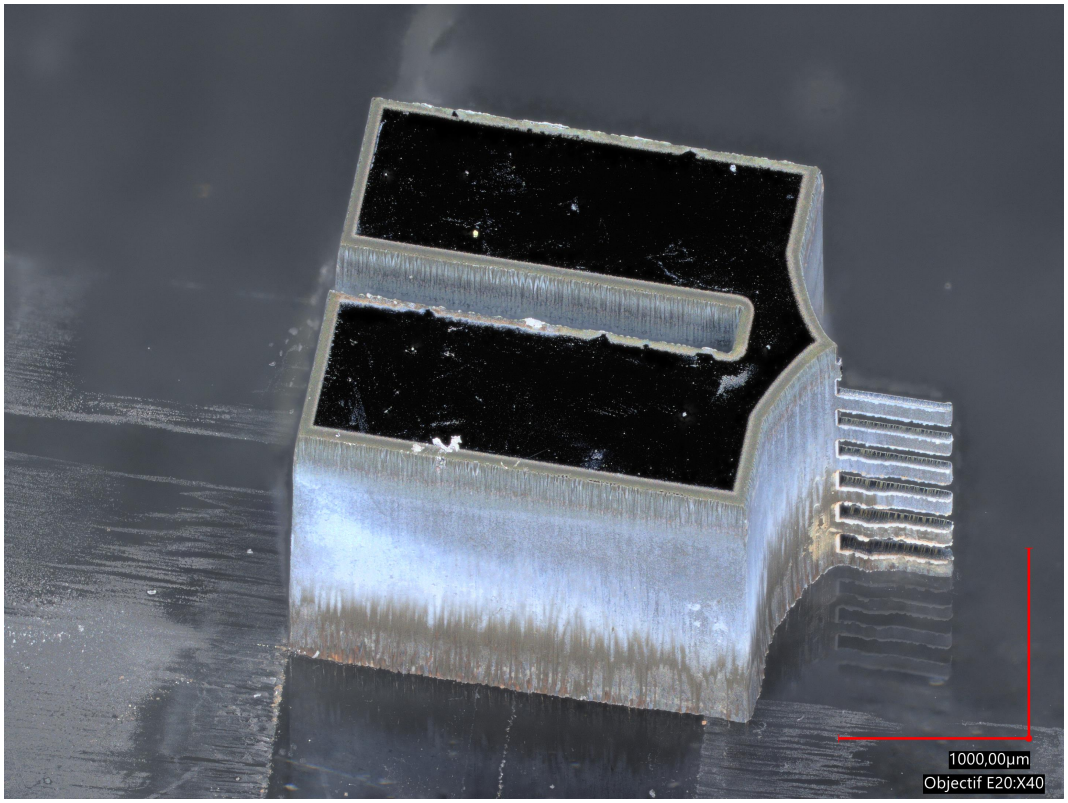

Figure 3.11: 3D view of the sample After Cleanig



Figure 3.12: Cleaning Samples with Ultrasound Machine

samples are subjected to cycles of XeF2 gas exposure. During this process, the etching chamber undergoes repeated pressurization (approximately 2 mbar) and subsequent evacuation. However, this method would require a lot of development and handling of the increasingly fragile device. We also conducted tests with the etching team to try to reduce the thickness of the slats. Unfortunately, these trials have not been conclusive so far (especially in terms of uniformity). The substrate to be diced is positioned on a flexible adhesive film and fixed on the chuck. After alignment between the cutting paths on the substrate and the blade, the substrate moves at a selected speed under the blade. The blade is cooled by a water jet, and its rotation speed is controlled. We faced several issues with this method. Among the most critical were the non-uniformity of the beams and the varying thickness of the slit within the box as we moved away from the ablation side, attributed to the functioning of the galvo lens. Additionally, the cleanliness of the beams was compromised due to the cleaning method which damaged the beams.

3.2.2 Proposed Design Using Thin Wafer Tiles

Methodological Adjustments

As a result of the limitations of the initial design and the challenges associated with the etching technique of the hall system using a single wafer in two steps, we adjusted our design approach. As a result, we have chosen a design with fewer beams, specifically five instead of eight. This reduction allowed us to allocate more space for the pitch between the beams, increasing the pitch to 400µm as shows Fig 3.13.

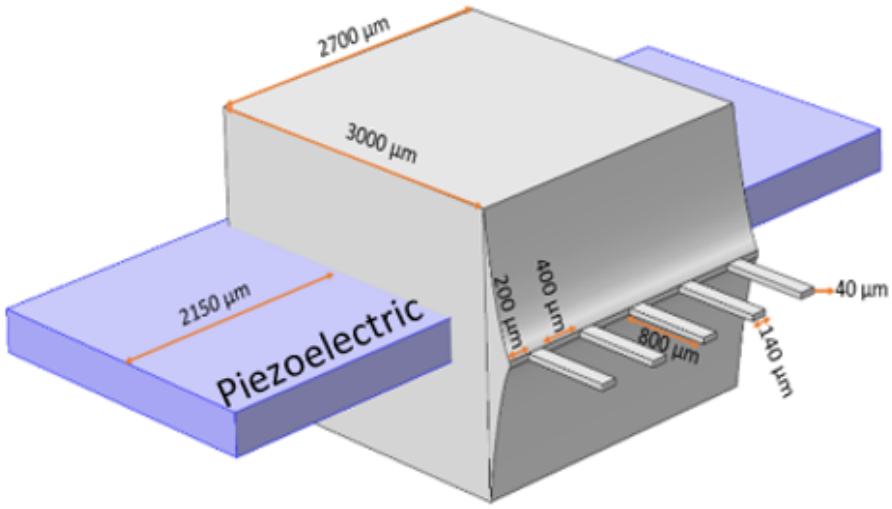

Figure 3.13: The new design after adjustment

After the first attempt, we identified several issues. We experienced low pressure due to the excessive thickness of the material that needed to be removed. Furthermore, during the system cleaning process, we found that ultrasonic cleaning was effective, but posed a risk of breaking the beams as they were quite fragile. Consequently, we decided to divide the structure shown in Figure 3.13into

multiple components. We chose to create four distinct pieces, with each piece having a specific role, as illustrated in Figure 3.14. We designed spacers with varying thicknesses. Two spacers, placed on either side of the two extremity beams to protect them (a and c in Figure 3.14), have a thickness of $200\mu m$. We also introduced a spacer with a thickness of $400\mu m$(b in Figure 3.14) positioned between the beams, and finally, the beams themselves have a thickness of $140\mu m$ (d in Figure 3.14). In essence, we increased the pitch to avoid the beams' frequency coupling and to provide more thickness to the tiles to be assembled, thus reducing assembly complexity. Figure 3.15 depicts the assembly of the

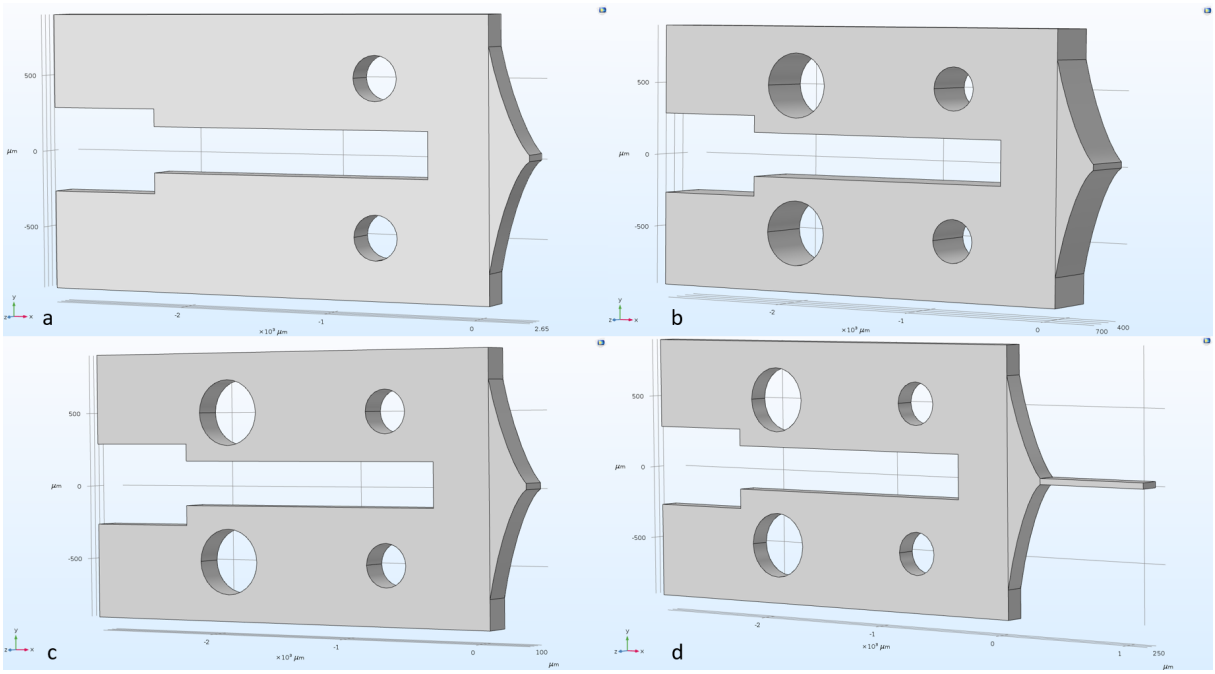

Figure 3.14: The different Tiles thickness: a and c represent the spacers with thickness $200\mu m$. b represent the spacer with thickness $400\mu m$. e represent the spacers with thickness $140\mu m$

components: part (a) highlighted in blue indicates the beams' position, part (b) in blue denotes the spacer positions, part (c) displays the piezoelectric section, and part (d) in blue represents the structure holding the piezoelectric component.

Alongside these major modifications, we implemented several other technical adjustments, although less significant, which we refer to as "pitch". Consequently, the length of the beams was adjusted from to 800µm. The modified design is presented in 3.15. Given the numerous issues encountered with the previous method, as discussed in the first section of this chapter, it became evident that ablating the entire structure in a single pass led to precision and uniformity challenges. In this section, we present an alternative approach aimed at minimizing these errors and ensuring greater accuracy in determining the dimensions of the beam and the slot in the sample. To address this, the decision was made to divide the structure into finer parts. Consequently, we procured wafers with a thickness of $400\mu m$ instead of $2mm$. For this segmentation, three primary components were considered: first, the beams; second, the spacers between the beams; and finally, the sample's edges. We settled on three different wafer thicknesses: $140\mu m$ for the beams as showed in Fig 3.16

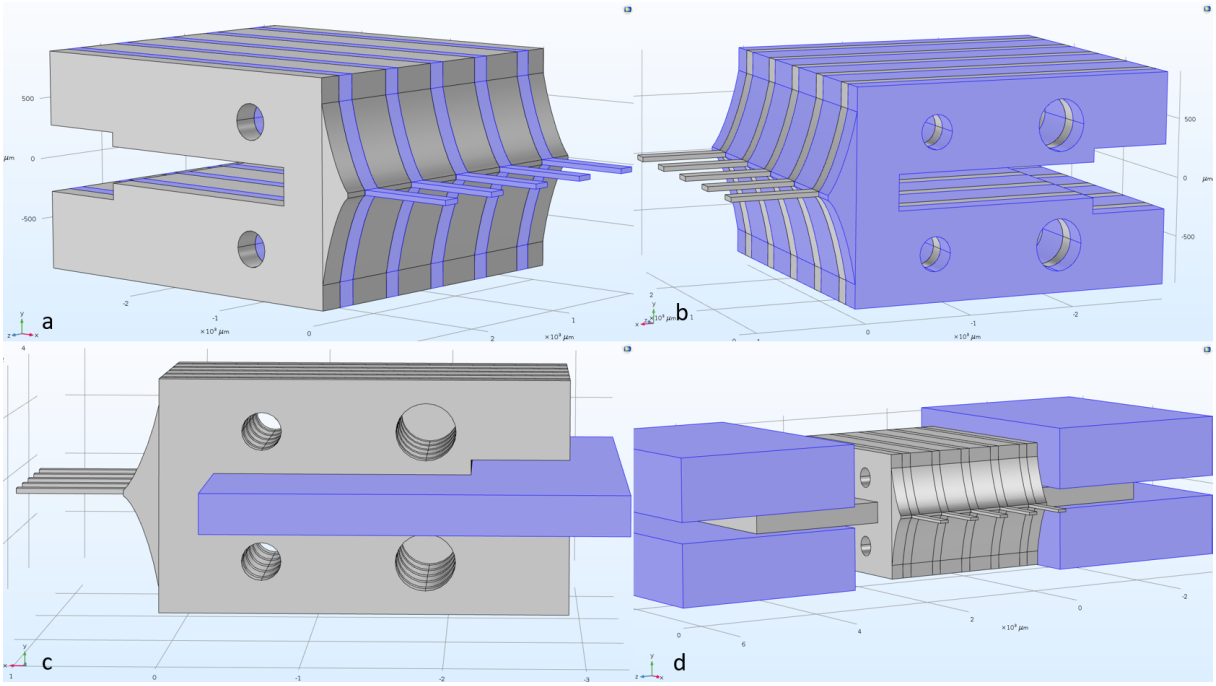

Figure 3.15: a: All beams are blue. b: All spacers are blue. c: The piezoelectric is blue. d: The piezoelectric holder

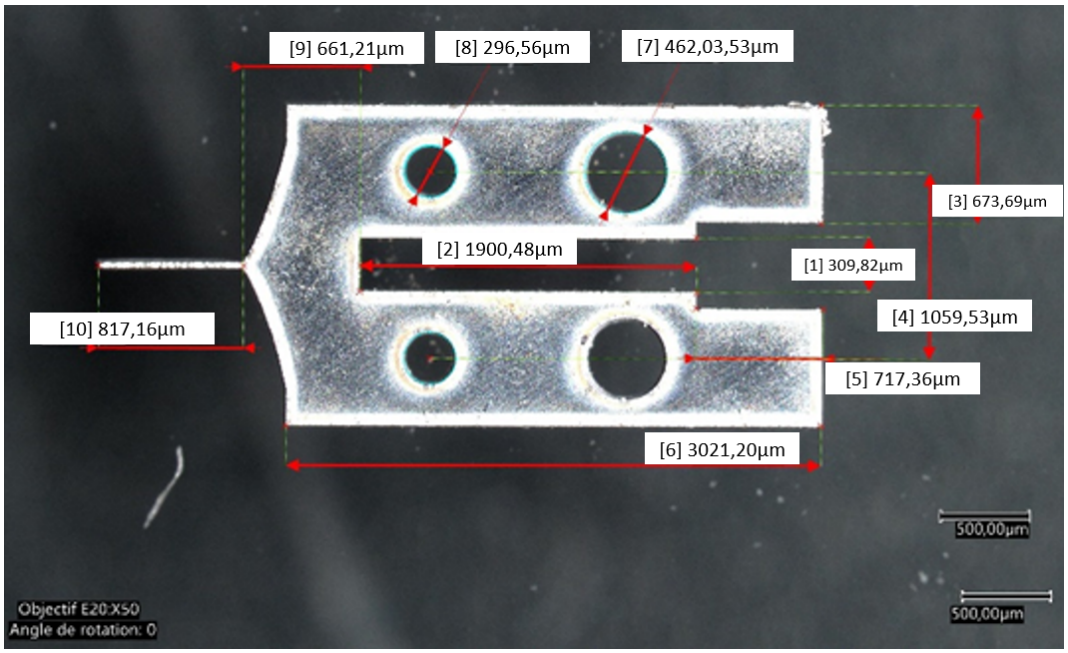

Figure 3.16: Details of The Tiles that Clamped a Beam

and the details of the beam in Fig 3.17, 200μm for the edge tiles of the sensor, and 400μm for the spacers situated between the beams.

The thickness of the spacer tile was increased intentionally to prevent coupling between the beams during vibration, thereby minimizing noise interference.

We can clearly observe that the piezoelectric slot is clean, uniform, and dust-free. As noted in the two images of the spacers, there is a slot at the end of the box which is wider than the piezoelectric

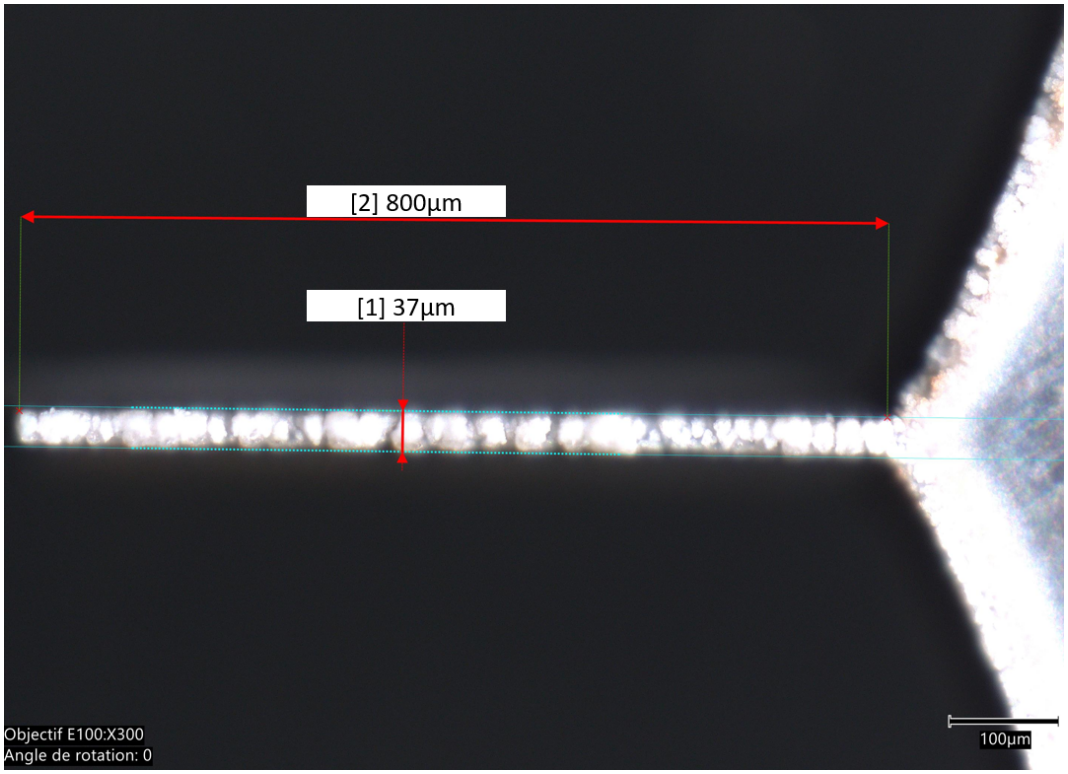

Figure 3.17: Beam Length and Thickness

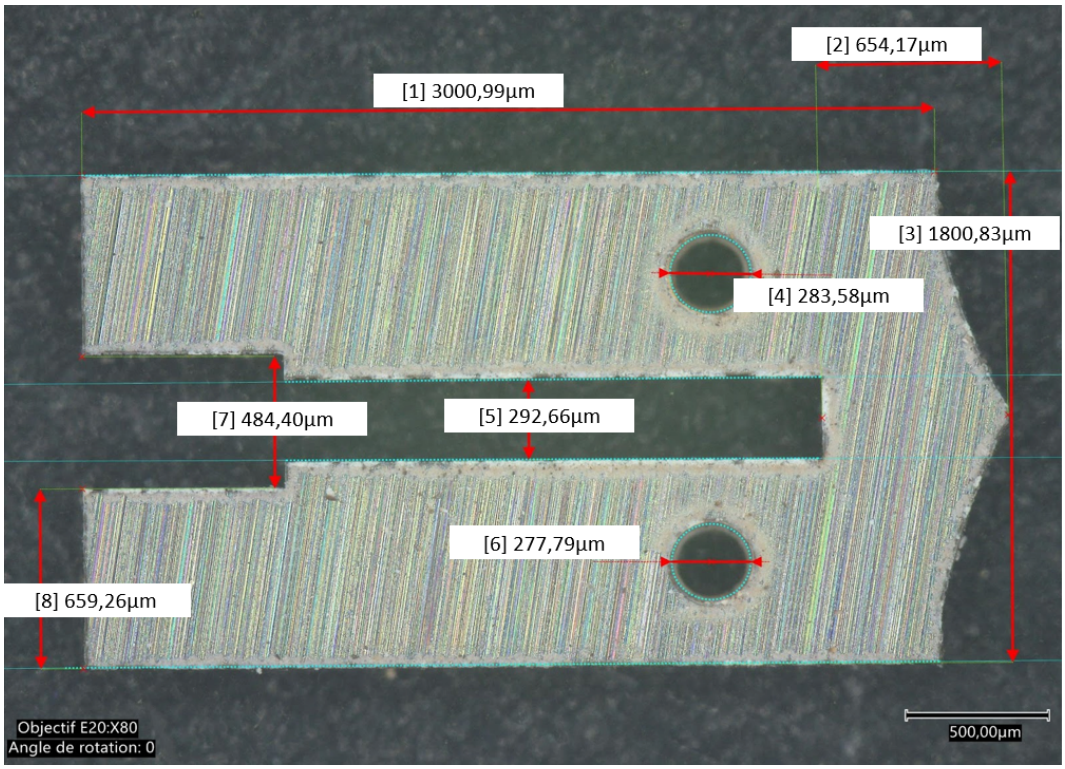

Figure 3.18: Description of The First Spacer With 2 Holes in The Device.

slot. We made this slot for two reasons: 1) to facilitate the integration of the piezoelectric material, and 2) to apply resin for adhesive purposes. For every device to be assembled, we require a piece

like that shown in photo 3.18, depending on the number of beams desired. However, it's important to note that photo 3.19 depicts the shape of two different pieces: one with a thickness of $200\mu m$ which is the final piece of the assembly, and another with a thickness of $400\mu m$ which acts as a spacer separating the beams.

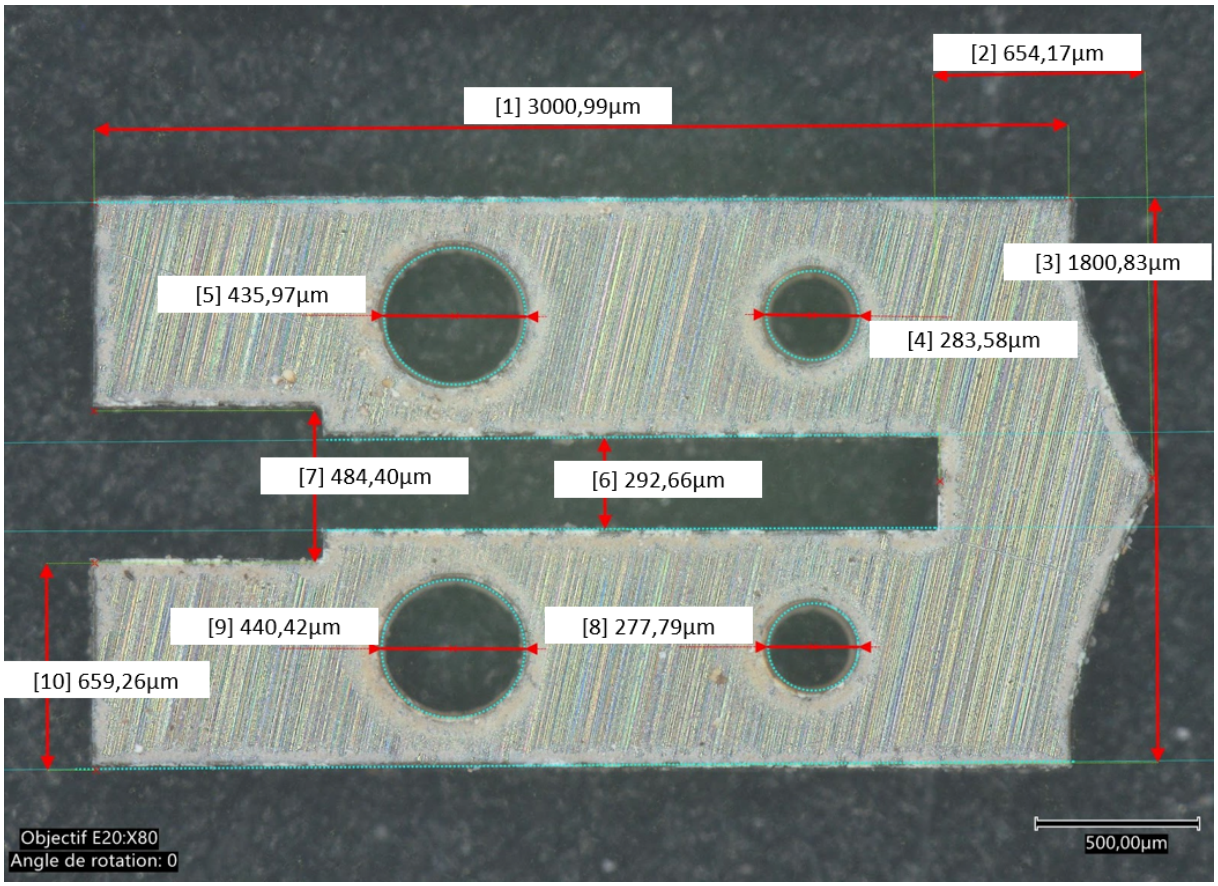

Figure 3.19: Details of The other Spacers With 4 Holes of The Device: We Have Two Spacers With The Same Shape But Different Thicknesses.

Upon crafting these tiles, the challenge then became how to stack them effectively, considering their micro-metric structures. We devised a stacking method using wire and resin. This necessitated a redesign of the tile structure to ensure that the adhesive and wire could be integrated seamlessly, thus facilitating the assembly process. Employing the same laser but with varied parameters, we began crafting the tiles. As previously mentioned, these tiles were differentiated based on their distinct thicknesses.

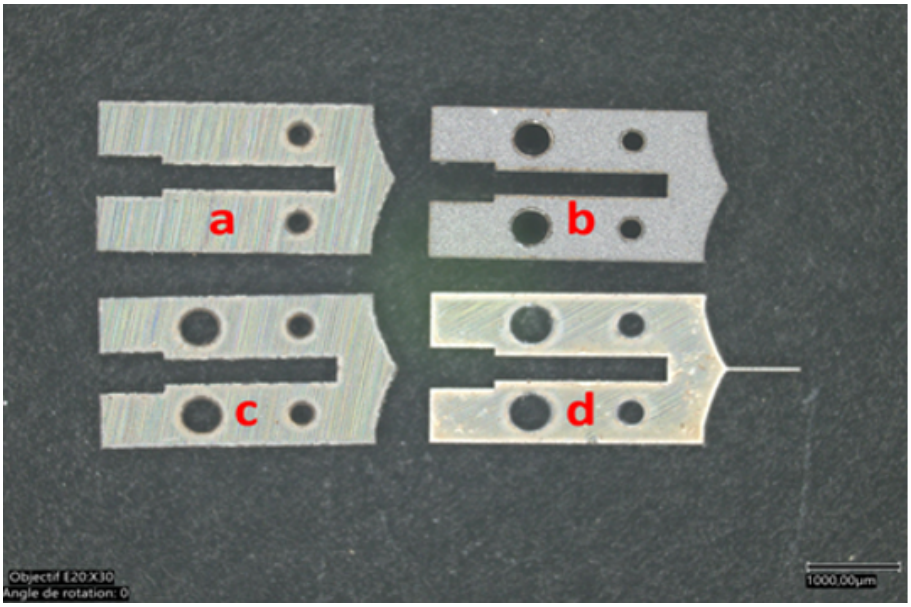

Figure 3.20: Four different tile shapes must be established in the device.

Given our prior challenges with cleaning, we decided to use propanol to remove dust and any thermal effects of laser ablation from the beams, avoiding ultrasonic cleaning to prevent breakage. However, for the spacers, we rinsed them with distilled water and then cleaned them using ultrasonics. As shown in the figure 3.20, we have tiles cleaned with distilled water where (a, b, and c are spacers of two different thicknesses; d is a tile embedded with a cantilever beam).

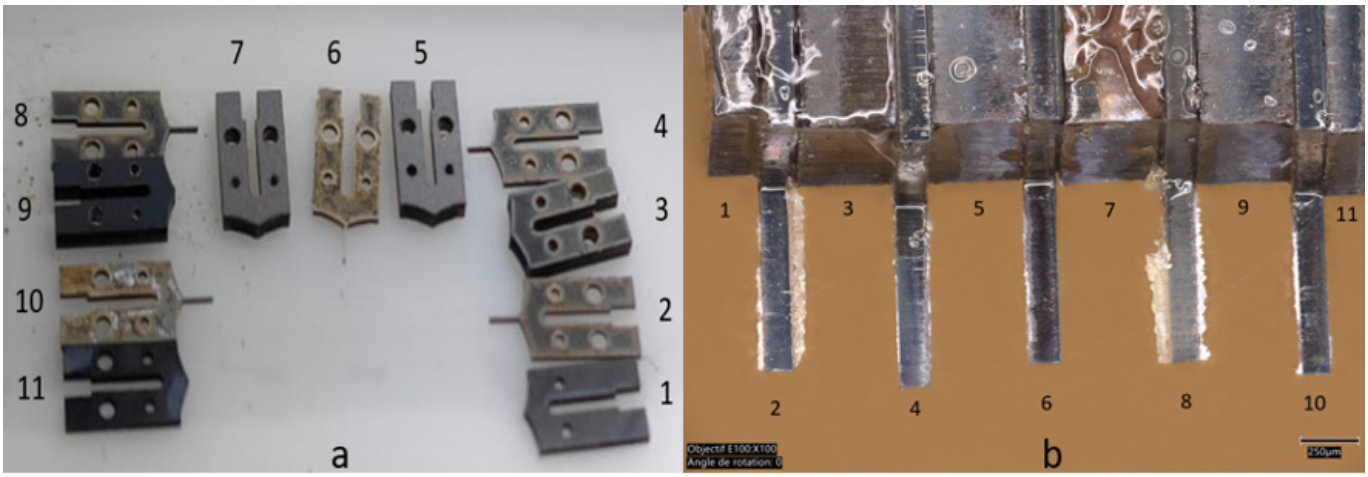

Figure 3.21: Assembly a

We etched two spacers onto a 200μm wafer, as depicted in the figure 3.20 with tiles a, b, c, and d for the structure's ends to provide the necessary protection for the beams. The first tile adopts the design of the 400μm spacers. However, the second tile is distinct because it lacks rear holes, as shown in the subsequent figure.

- 2 spacers of 200μm thickness on the edges (1, 11),

- 5 beams of 140μm thickness (2, 4, 6, 8, 10),
- 4 spacers of 400μm thickness separating the beams (3, 5, 7, 9),
- 1 Piezoelectric of 270μm thickness.

Initially, we etched four tiles with beams measuring 800μm in length and 30μm in width onto a 140μm thick wafer. Each tile etching takes about three minutes. Additionally, we etched three spacers (similar design but lacking beams) onto a 400μm thick wafer for assembly purposes. This step ensures proper spacing between the beams. As illustrated in the figure 3.14, each tile has four holes. The first pair of holes, each roughly 300μm in diameter, is specifically designed for stacking tiles. Steel wires will be threaded through these holes to ensure the tiles' linear stacking. The two rear holes, each about 460μm in diameter, are designed to inject resin once the tiles are stacked. This infusion process increases the sample's viscosity, making its handling more straightforward. One can observe that we have a tile, denoted as tile a in the figure, with only small holes for the steel wire to pass through and two other holes for the resin. When stacking the tiles, it is essential that the resin does not spill outwards; therefore, only the first stacking piece is closed on the resin pouring side, while the others have all four holes. Consequently, to stack a device with five beams, we need the components, which also indicates the assembly order. As illustrated in the figure 3.21, the stacking start from tiles 1 until 11 as they

The stacking starts with tile 1 and goes up to tile 11 in order as indicated in part (a) of the figure. Once assembled, it will have the shape illustrated in part (b) of the photo. To assemble it, several methods were proposed, and an analysis was conducted for each method, with the results shown in the table 3.2:

Table 3.2: Comparison of Different Methods of Joining Tiles.

Structure	**Number Of beams**	**Type Of Alignment**	**Types Of Temporary Bonding**	**Type of final bonding**	**Cleanliness**
D1	3	P	C	A′	-
D2	2	P	B+A	A′	++
D3	3	P	NTB	A′	-
D4	4	P	C	A′	+
D5	5	P′	B+A	A′	+++
D6	5	P	B	A′	+
D7	1	P	A	A′	+
D8	3	P′	B	A′	++

Legend:

- A: Assembly by resin pad.
- B: Syringe resin (A215nXT 50/50) dispensing assembly into rear holes.

- C: By spray.
- A': Dispense cyanolit by syringe on the top of the stacked tiles.
- P: Piezoelectric fixed first on the PCB support, then integrated the system stack in the piezo and provided cyanolit on everything to stick them.
- P': Integrate the piezoelectric after stacking with the temporary glue (resin), then put the cyanolit(Both That Showed in Fig 3.28) to fix the stacked tiles with the piezoelectric, then integrate the two in the PCB holder.
- NTB: No Temporary Bonding.

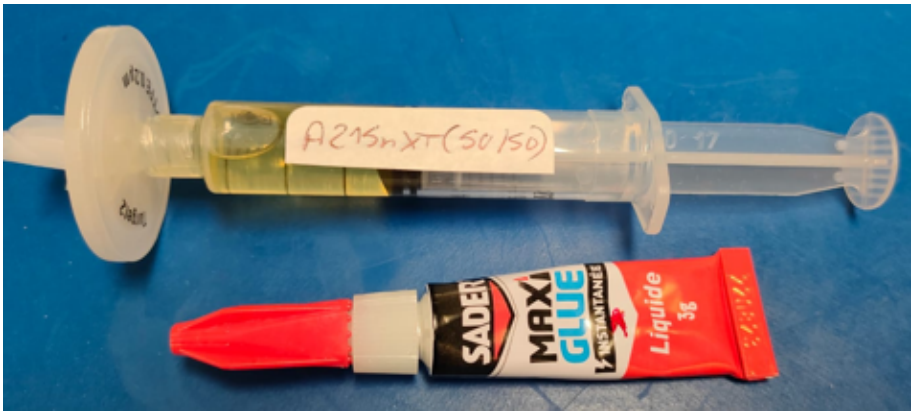

Figure 3.22: Resin (A215nXT 50/50) and Cyanolit Liquid

Most devices feature multiple beams, with having 1, 2, 3, 4, or 5 beams. The primary alignment technique employed is "P", where the piezoelectric is initially fixed to the PCB support. An alternative, "P"', integrates the piezoelectric after stacking and is observed in D5 and D8. Temporary bonding methods are diverse: "C" (spray bonding) is utilized for D1 and D4, a combination of syringe resin and assembly by resin pad (B+A) is observed in D2 and D5, D3 uniquely uses No Temporary Bonding (NTB), D6 and D8 employ syringe resin assembly (B), and D7 uses assembly by resin pad (A) exclusively. Intriguingly, all devices employ "A"', suggesting a standardized final bonding approach wherein cyanolit is dispensed atop the stacked tiles. In terms of results, D1 and D3 indicate a "-" outcome, pointing to potential suboptimal configurations. Conversely, D2 and D8 yield a "++" performance, with D5 topping the chart at "+++". D4, D6, and D7 present a "+" outcome, potentially signaling an average performance. These results underscore the significance of considering various external factors like cost, efficiency, and scalability in device assembly.

Support To Align the Tiles

The process involves the use of a wire that threads through the assembly tiles. We engraved a rectangular area where we made two small holes to hold or fix the wire in place. In addition,

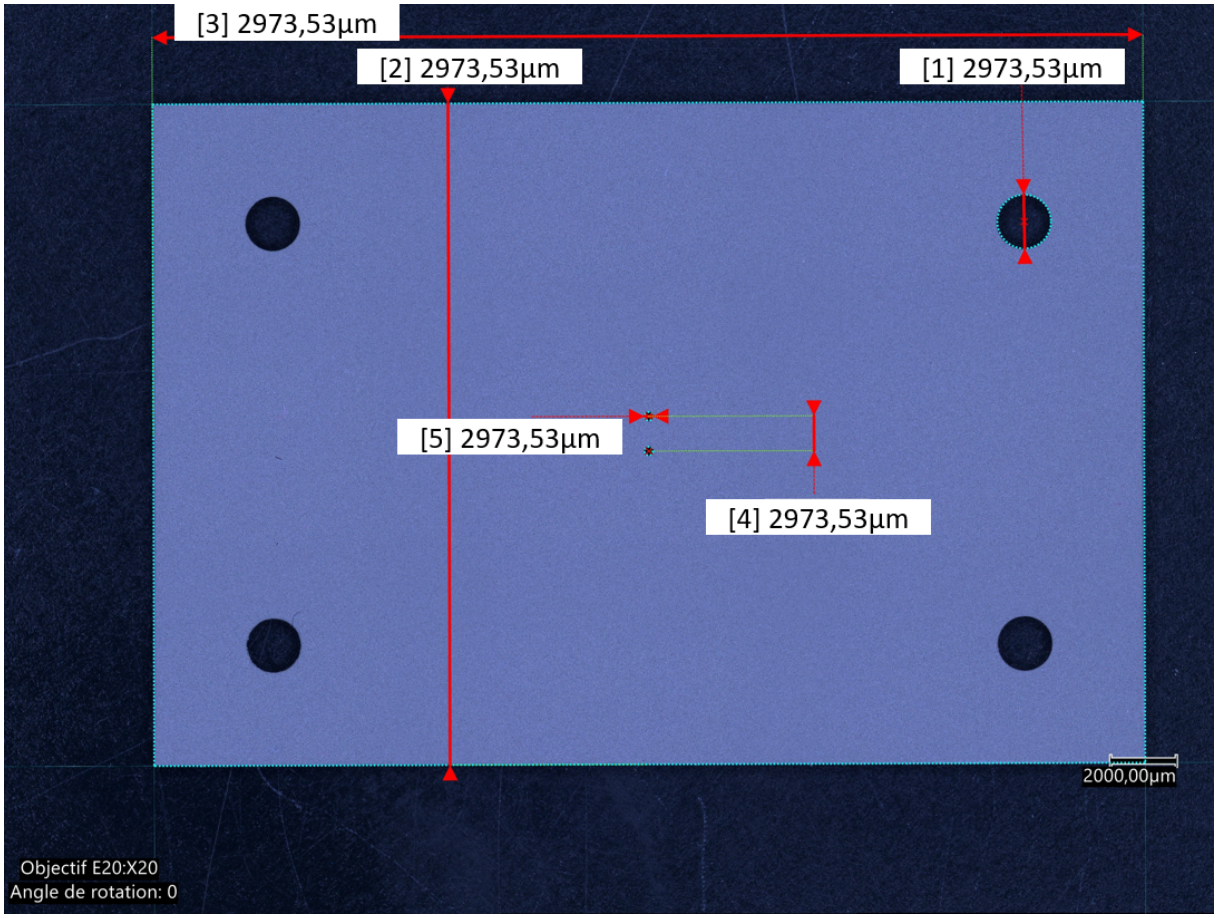

Figure 3.23: Rectangular Tile etched to establish a Support For Assembling Process

four larger holes were made at each corner of the rectangle, as illustrated in the figure. All of this was designed to create a working support, simplifying the tile assembly process. These tiles are stacked and connected using four metal rods, as depicted in the subsequent figure. When starting the assembly, one requires precision tweezers to handle the micrometric tiles, a microscope to see the holes and thread the lead holes with the wire, and it's essential to follow the assembly protocol with the adhesive, as explained in the previous section. It takes 20 minutes on average for a device with 4 cantilever microbeams to stack and assemble.

Piezoelectric Integration

PZT-5H wafer is used as source element. This wafer, with a commendable thickness of 270µm, is metallized on both surfaces to ensure optimal performance shown in Figure 3.26. Using the same laser techniques, the wafer is etched to produce a rectangular piezoelectric sample of dimensions 3×7 mm. The cyanolite, chosen for its optimal viscosity, is used during the assembly process to facilitate the integration of the piezoelectric element into the structure's slot. Once the piezoelectric element is aligned in the slot and the cantilever beams are level and aligned. Ensure that the piezoelectric element is well positioned on both sides to maintain the capacity to fix the piezoelectric while simultaneously obtaining an electrical connection from both sides. As we proceed with this

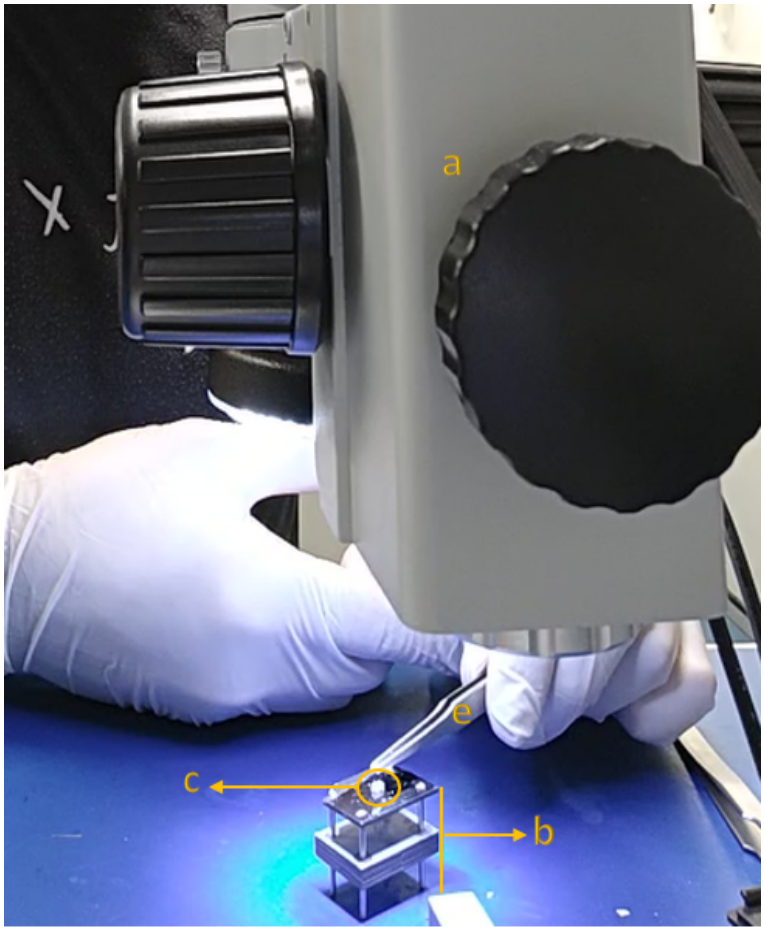

Figure 3.24: Stacking Tiles In order While using a Microscope and a Precision Tweezers with a: the microscope. b: the Support for assembly. c: the Cantilever micro beam structure. e: The Precision Tweezers

intricate assembly, special tools such as precision tweezers and microscopes are employed, ensuring that the integration process is both smooth and accurate. The outcome is a harmonious melding of the piezoelectric element with the overarching structure, ready to exhibit the desired functionalities while maintaining robustness.

Surface Condition Analyse

In this section, we dive into the detailed surface condition analysis of the fabricated structure, focusing primarily on the integrity of the piezoelectric element, the resin and cyanolite glue filling, as well as the conditions of the beams. The Scanning Electron Microscope (SEM) was employed to capture high-resolution images that enable us to identify and quantify the intricacies of the structure. The first SEM image (refer to Figure 3.29) illustrates the overall structure of the piezoelectric sensor. It was crucial to ascertain whether the resin and the cyanolite liquid glue completely filled the gaps, ensuring there is no space between the tiles. From this image, we can observe that the assembly procedure resulted in a well-stacked structure. Furthermore, it's evident that the piezoelectric element is seamlessly integrated, devoid of any extraneous material that could compromise its physical and electrical properties.

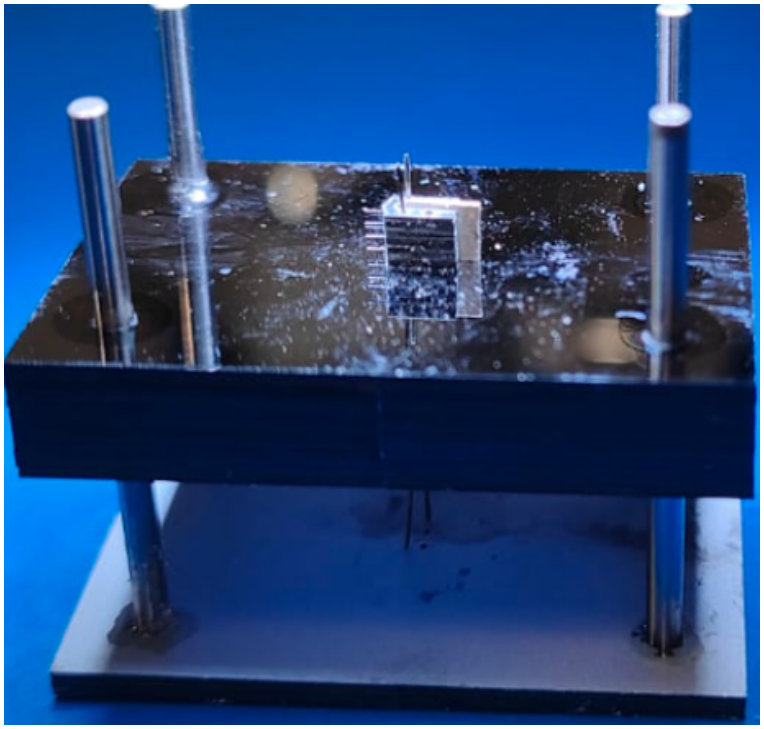

Figure 3.25: Support for Assembling with an array of four beams already stacked

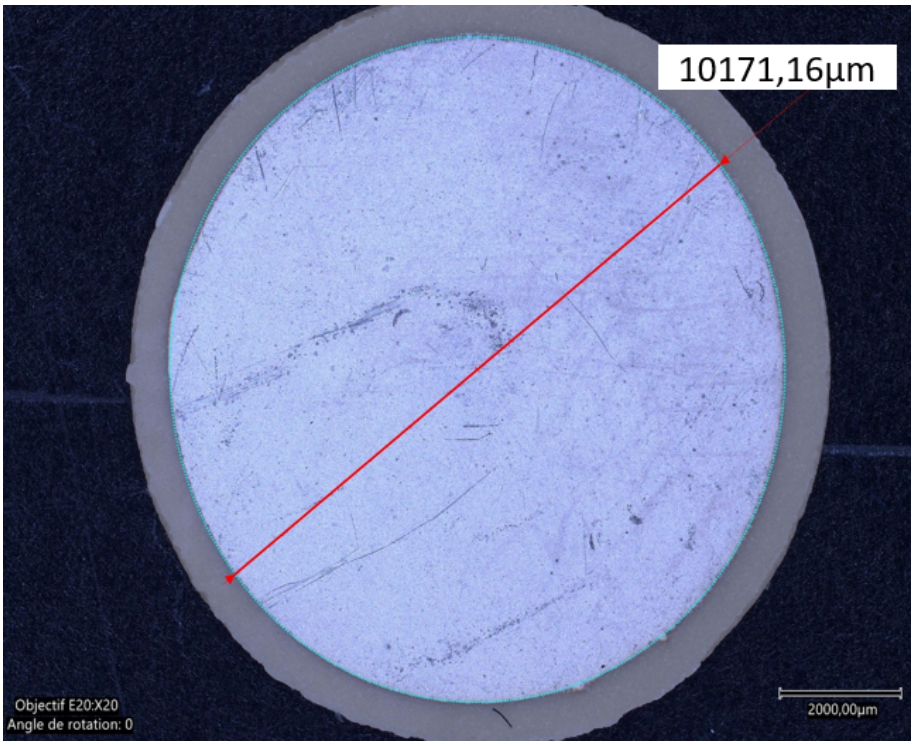

Figure 3.26: PZT-5H Homemade Wafer

Following this, three images were focused on the beam structures, specifically on their surface and border conditions. The second image (refer to Figure 3.30) highlights the front part of the beam. It becomes evident how the dust has welded onto the surface due to the thermal effects of the laser beam during cutting. Even though we employed a nozzle jet to expel a combination of nitrogen

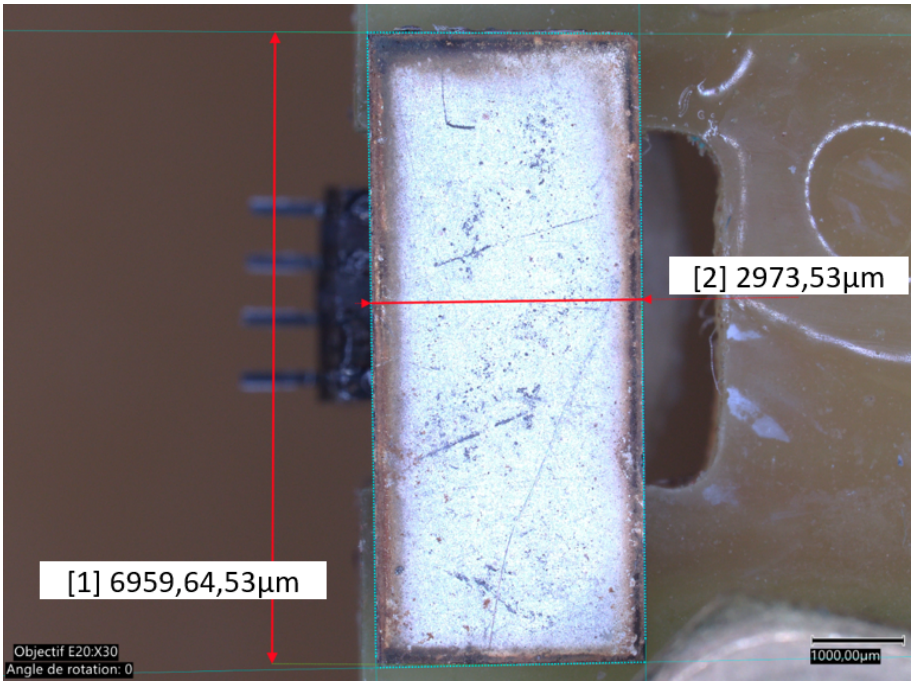

Figure 3.27: Details Of a PZT-5H Cut it in Rectangle Shape

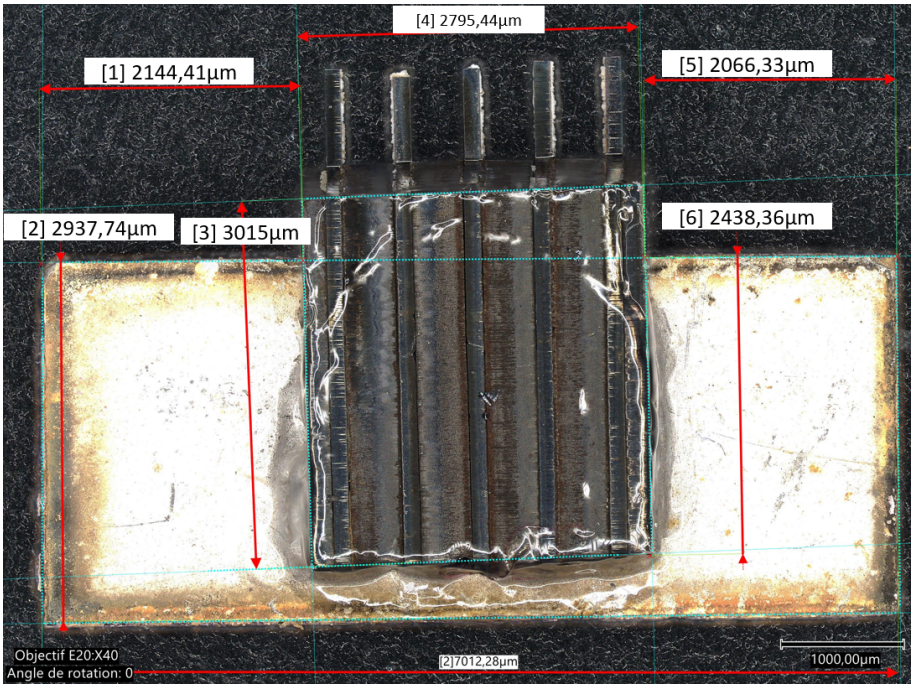

Figure 3.28: The Piezoelectric Is Integrated In The Assembly Structure

(azote) and air during the laser etching process, the thermal effects prove challenging to mitigate entirely.

The third SEM image (refer to Figure 3.31) demonstrates the side of the beam, particularly the side that doesn't face the direct airflow from the nozzle jet. This area is more susceptible to dust welding due to its relative shielding from the cooling effects of jetted nitrogen and air.

Lastly, the fourth image (shown in Figure 3.32) magnifies the condition of the welded dust. Upon

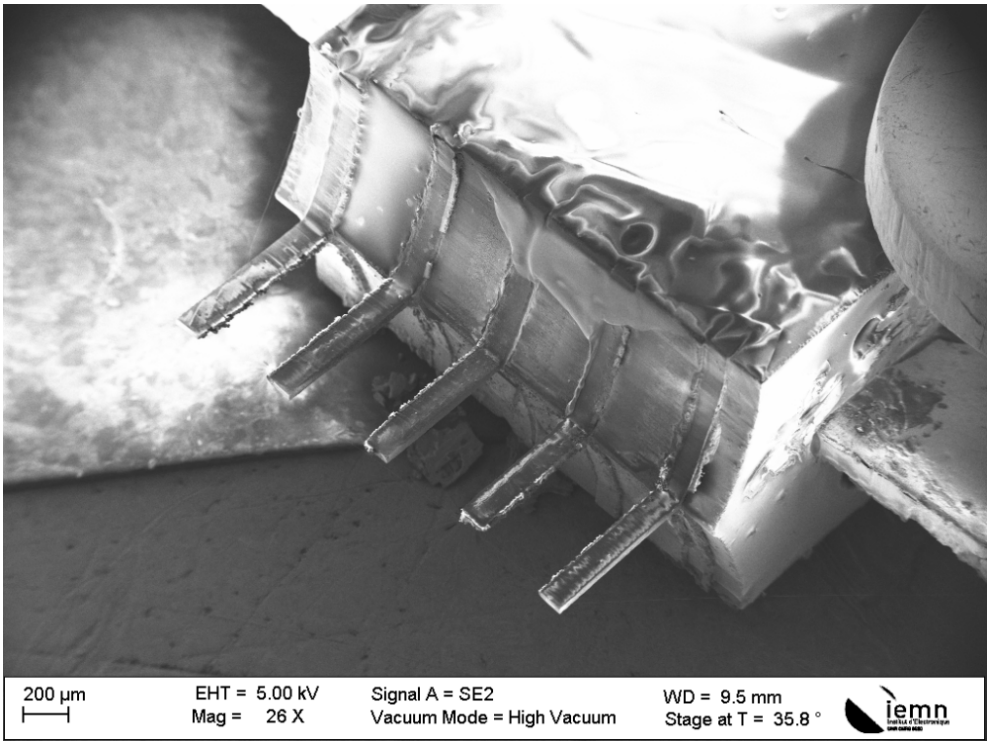

Figure 3.29: SEM image showing the overall structure with the piezoelectric element.

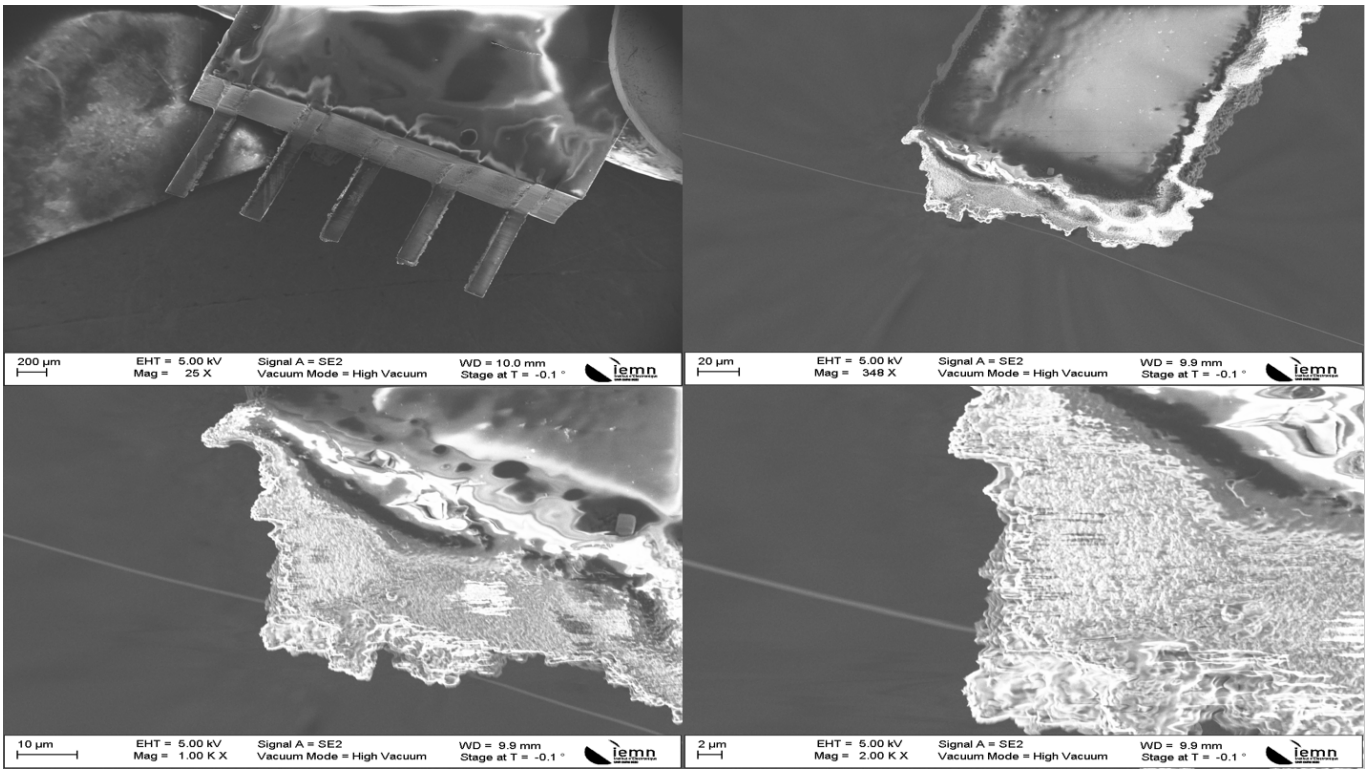

Figure 3.30: SEM image showcasing the dust welded on the front part of the beam.

close inspection, we can discern a porous surface structure. The implications of this porous surface are twofold: firstly, it could potentially affect the mechanical behavior of the beam, and secondly, the increased surface area due to porosity might lead to enhanced interactions with the medium in

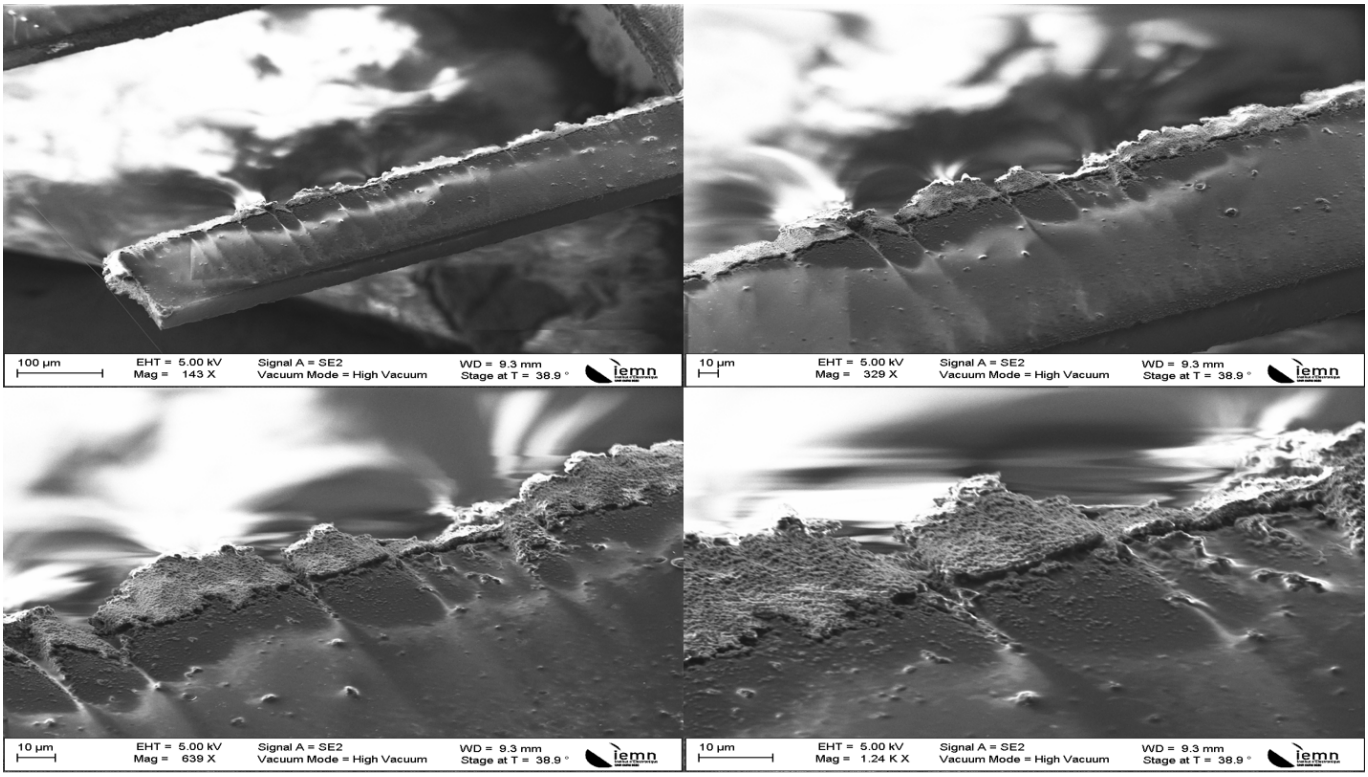

Figure 3.31: SEM image of the beam's side, indicating the dust welded away from the direct jet airflow.

which the beam is immersed.

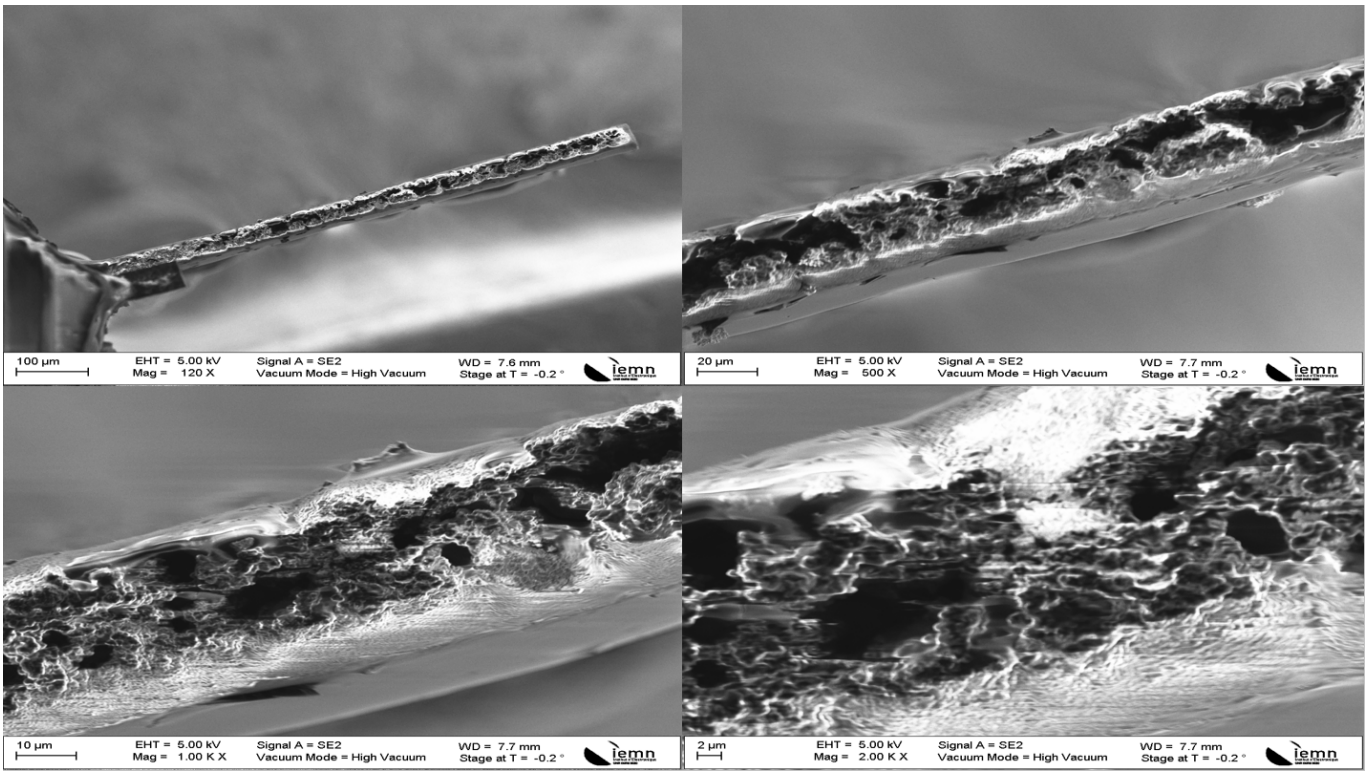

Figure 3.32: Close-up SEM image of the porous surface of the welded dust.

While the general structure and piezoelectric integration appear to be of high integrity, the beam

surfaces present challenges, especially regarding the welded dust and its potential impacts on the beam's behavior.

3.3 Support Structure and Connection

The success of the "beam sensor" device largely hinges on its supporting structure. Figure 3.34 illustrates the computer-aided design (CAO) of the sensor holder, meticulously crafted to achieve this purpose. Both support components are designed from a single-sided FR4 printed circuit board. This ensures uniformity and precision across components, with each part mirroring its counterpart to effectively encase the piezoelectric sensor.

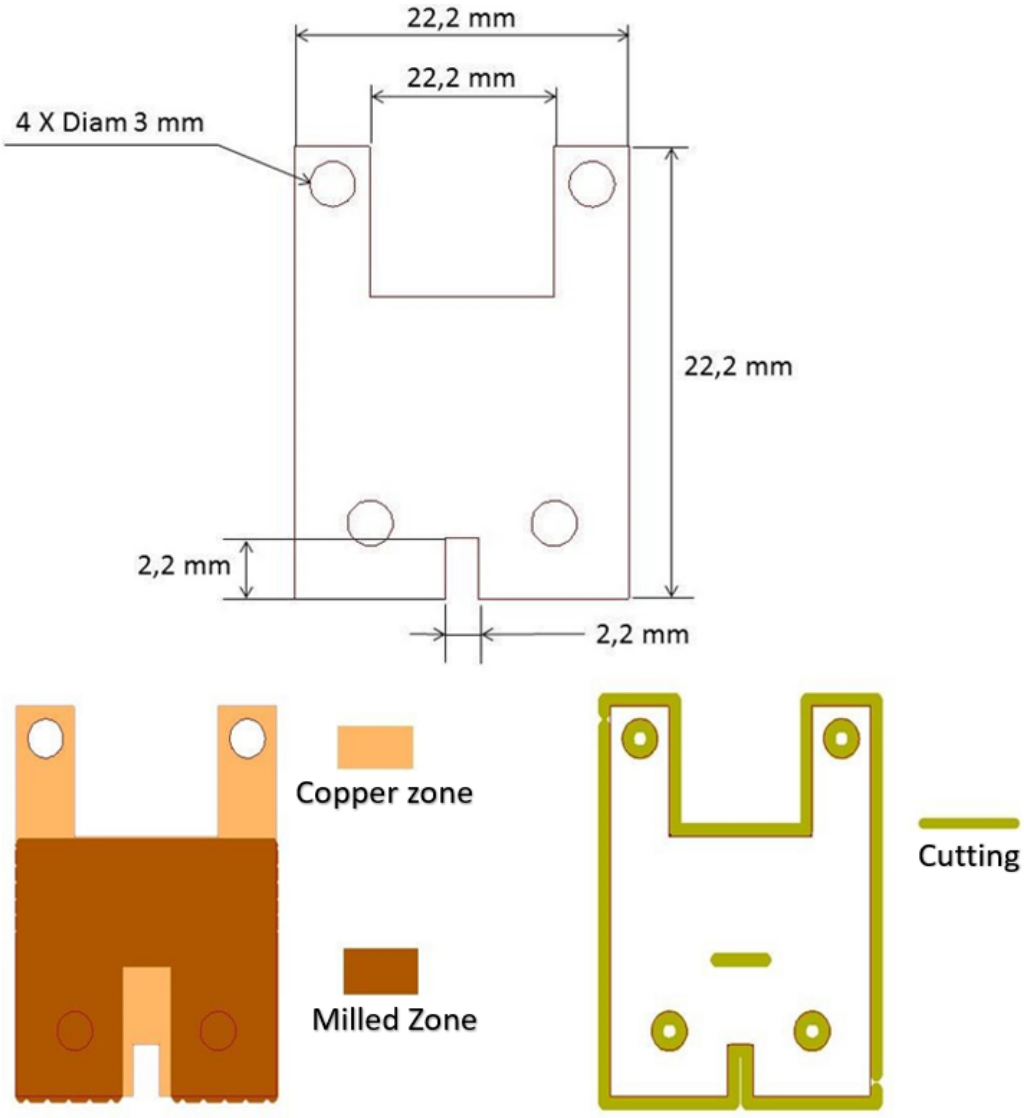

Figure 3.33: Computer-Aided Design (CAO) of the sensor holder.

The intricate design was realized using the Gerber Tool software, renowned for its precision. Within this framework, two primary layers are formed. The first focuses on milling, predominantly

for copper removal, while the second concerns the exact cutting of the board. This meticulous design phase, as showcased in Figure 3.34, produces guiding files crucial for subsequent fabrication.

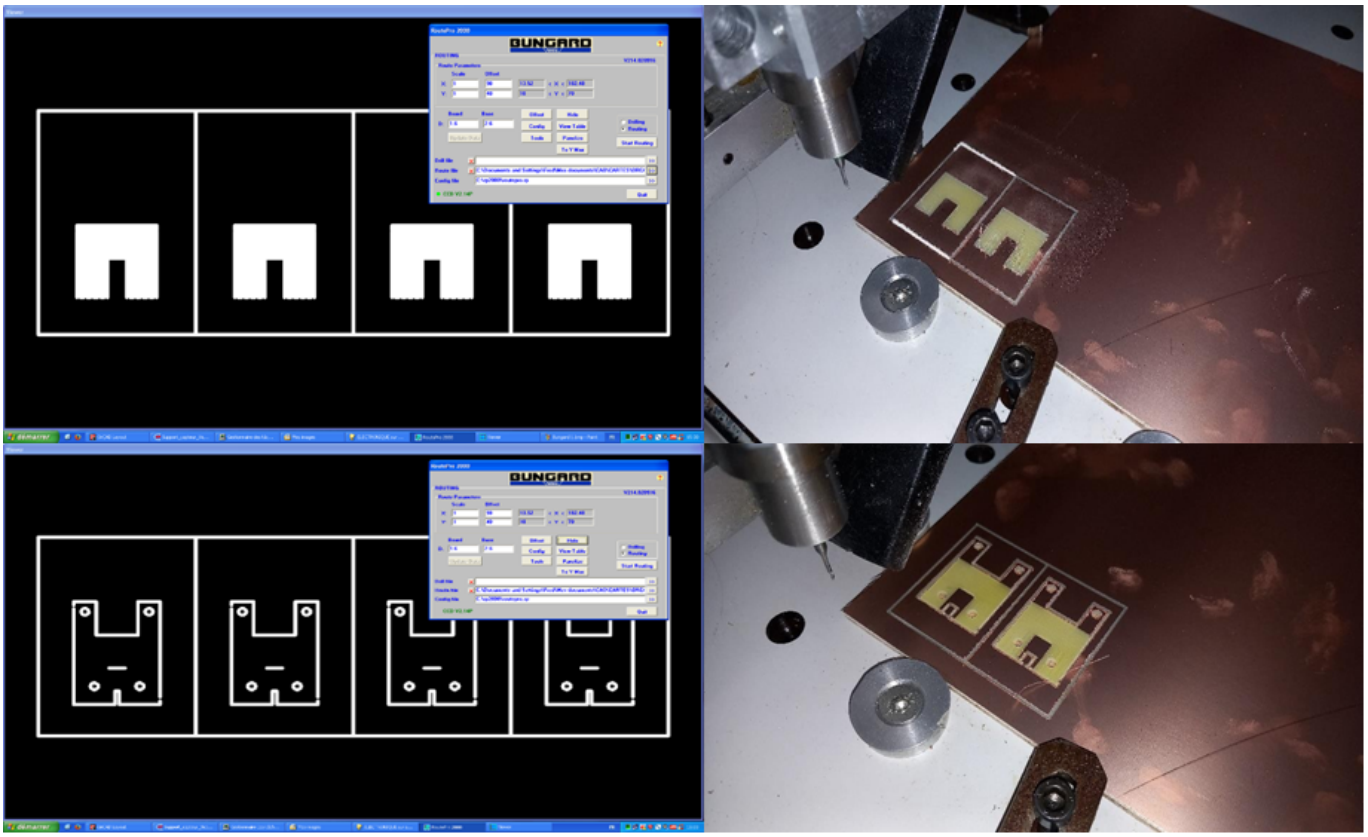

Figure 3.34: Detailing of the single-sided FR4 printed circuit board (PCB).

The Bungard CCD machine, a cutting-edge piece of equipment operated via the RoutePro 2000 software, brings these designs to life. Figure 3.35 displays the results post-copper removal, achieved using a 1mm diameter milling bit. This is followed by precision cutting, ensuring each part aligns perfectly with its initial design.

Post-fabrication, the emphasis shifts to assembly. As seen in Figure 3.36, the support's top and bottom are connected using a copper sheet, vital for ensuring optimal electrical conduction. This is complemented by an RG174 coaxial cable, complete with an SMA male connector.

To safeguard the assembly's longevity and resilience, both connections are reinforced with a robust epoxy adhesive, minimizing the risk of tearing or disconnection. Upon finalizing the assembly, it becomes crucial to ensure that the holder interfaces perfectly with the piezoelectric element, as this plays a pivotal role in the overall performance of the sensor. Figure 3.37 offers a detailed perspective of this interface. The image accentuates how the intricacies of the design converge in reality, highlighting the nuanced contact between the holder and the piezoelectric. Such precision ensures a consistent and optimal connection, minimizing interference and maximizing the sensor's efficiency and reliability.

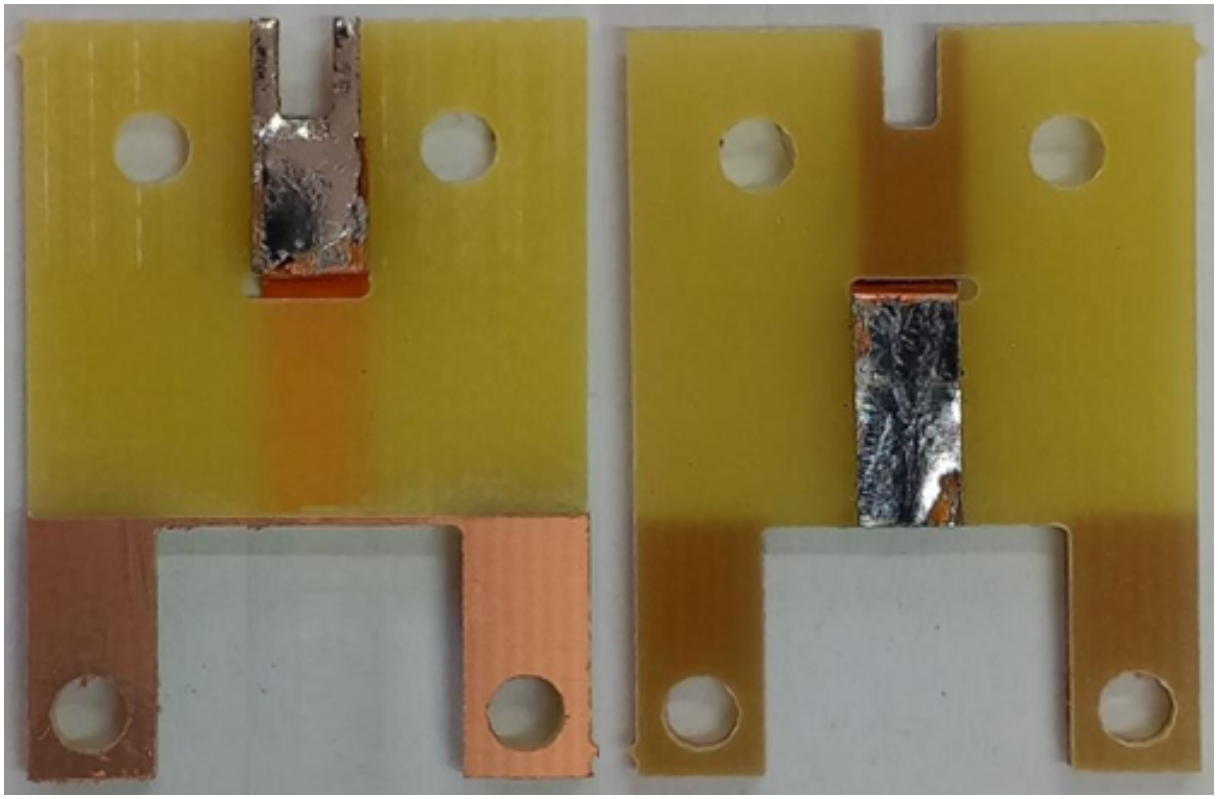

Figure 3.35: Fabricated structure post-copper removal process.

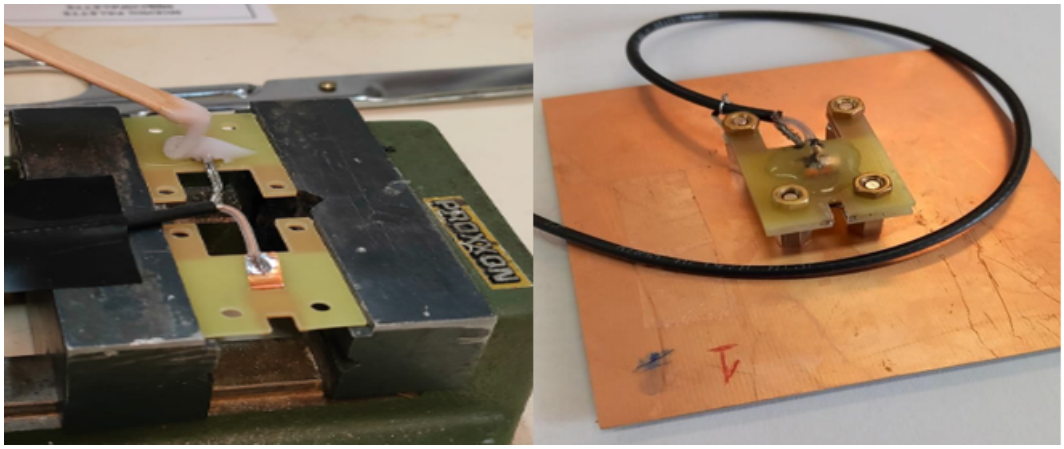

Figure 3.36: Detailing of the Coaxial Cable with an SMA Connector.

3.4 Creating Devices with Varied Beam Spacing

This section delves into the intricate design of devices characterized by different beam spacings, commonly referred to as "pitch". By studying and analyzing these devices, we aim to discern the significance of beam spacing on the device's performance.

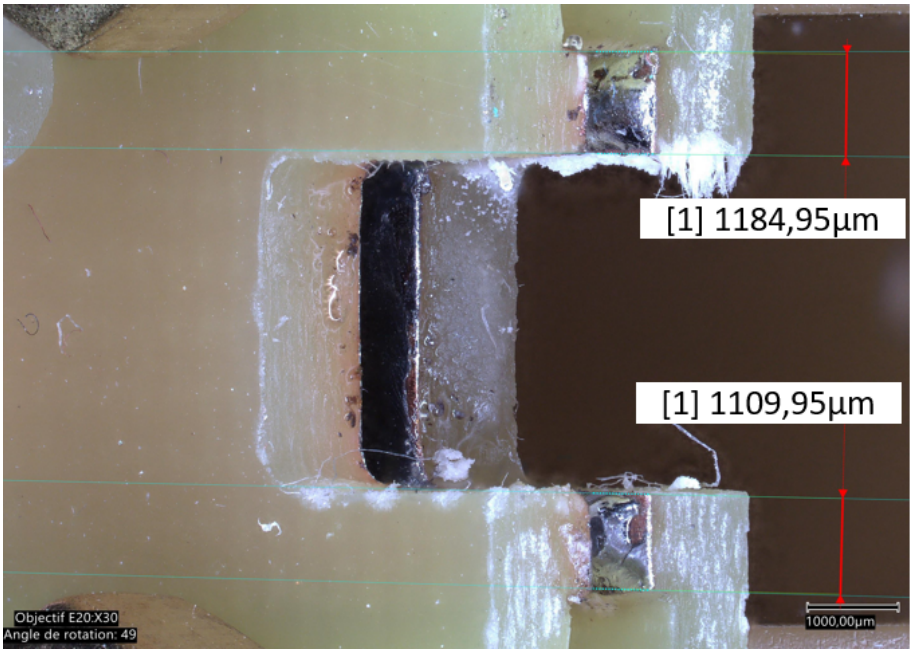

Figure 3.37: Detailed visualization of the precise interface between the holder and the piezoelectric element, emphasizing the importance of their aligned connection.

3.4.1 Variation in Beam Number and Spacing

The composite image in Figure 3.38 showcases four different devices, each varying in the number of beams present. Remarkably, all devices maintain the same width, ensured by a consistent number of tiles. The distinction arises in their assembly, as outlined in Table 3.2, and the differing beam counts.

The single-beam device serves as a reference to assess the benefits (or lack thereof) of incorporating multiple beams into the design. With the two-beam devices, the pitch varies, either being spread across the structure's extremities (yielding a pitch of 800 µm) or brought closer with a single tile spacing (400 µm). Lastly, the four-beam device introduces a dual pitch system, with spacings of 400 µm and 300 µm, to further probe beam coupling effects during peak frequency vibrations. Each device also represents a means of assembly mentioned in Table 3.2.

Cracked Structure Analysis

A serendipitous incident during assembly led to the development of a cracked device, as depicted in Figure 3.39. This unintentional outcome offered a unique opportunity to study the resonance frequency's sensitivity to structural deformities.

Figure 3.40 presents the D5 device. With its impeccable cleanliness and assembly, coupled with five beams spaced at our reference pitch of 400µm, this device represents the zenith of our fabrication efforts.

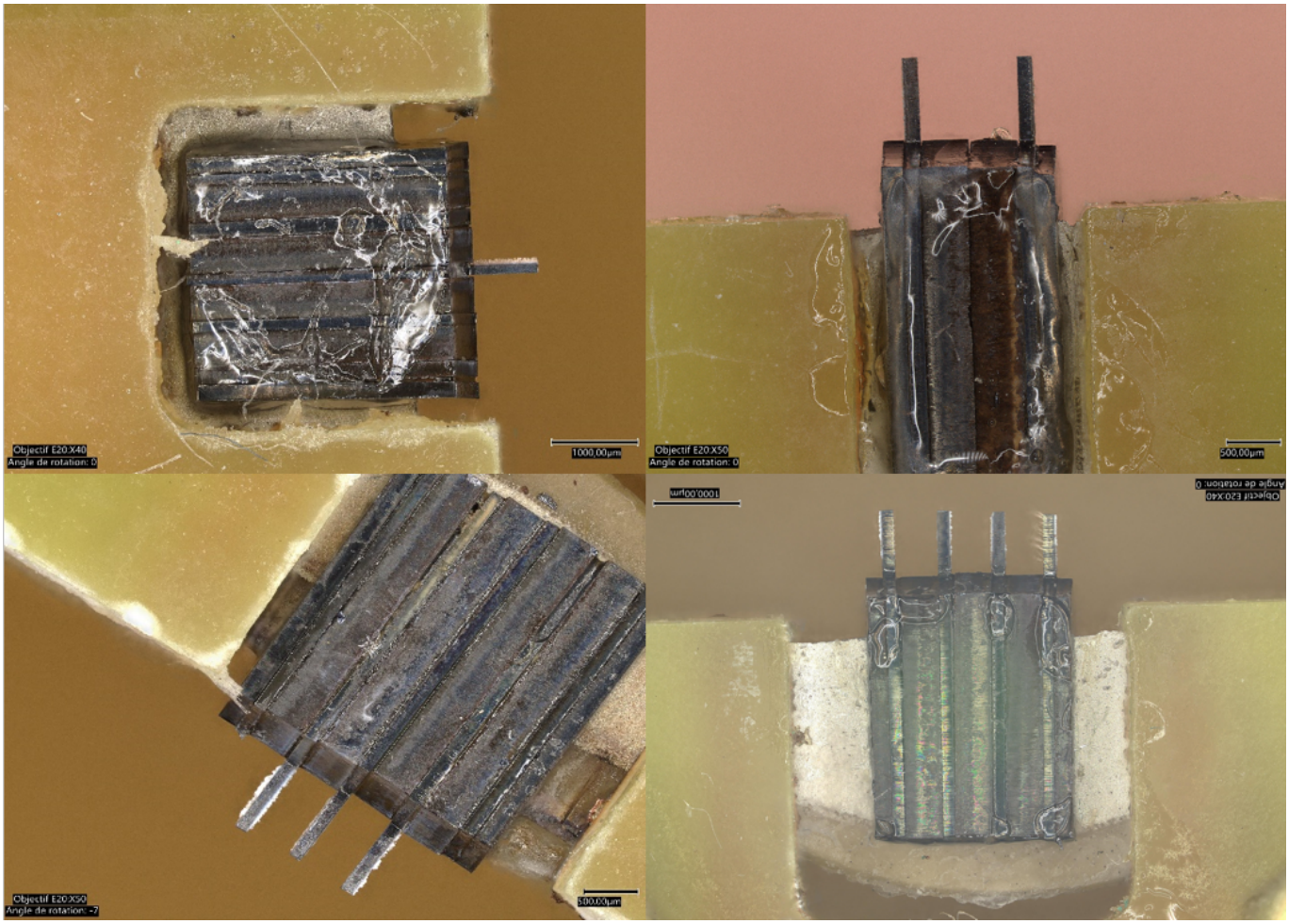

Figure 3.38: Devices with varied beam numbers and spacings.

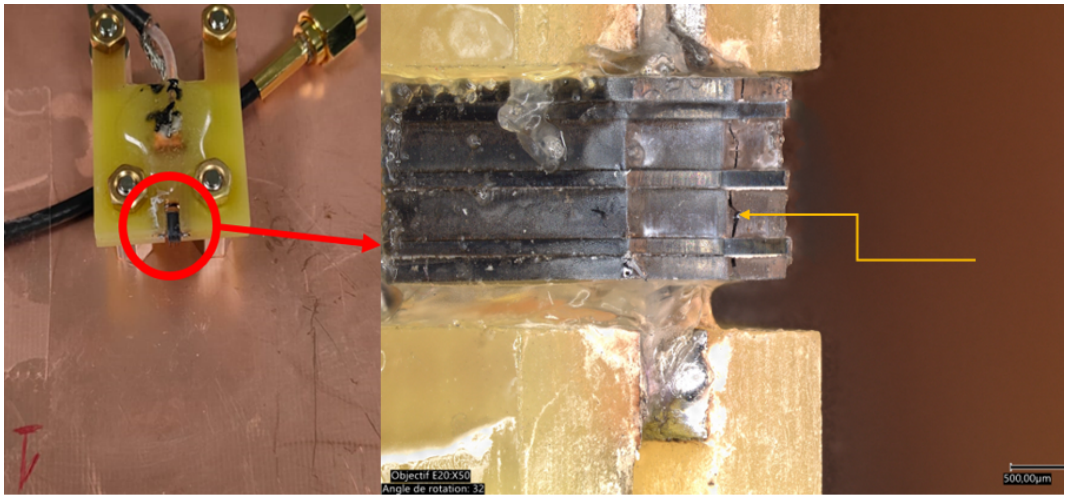

Figure 3.39: Device with a crack along its structure.

Complete Sensor Assembly

Finally, Figure 3.41 illustrates a comprehensive view of our sensor, integrated with its support holder and electrical connectors, encapsulating the culmination of our design and assembly endeav-

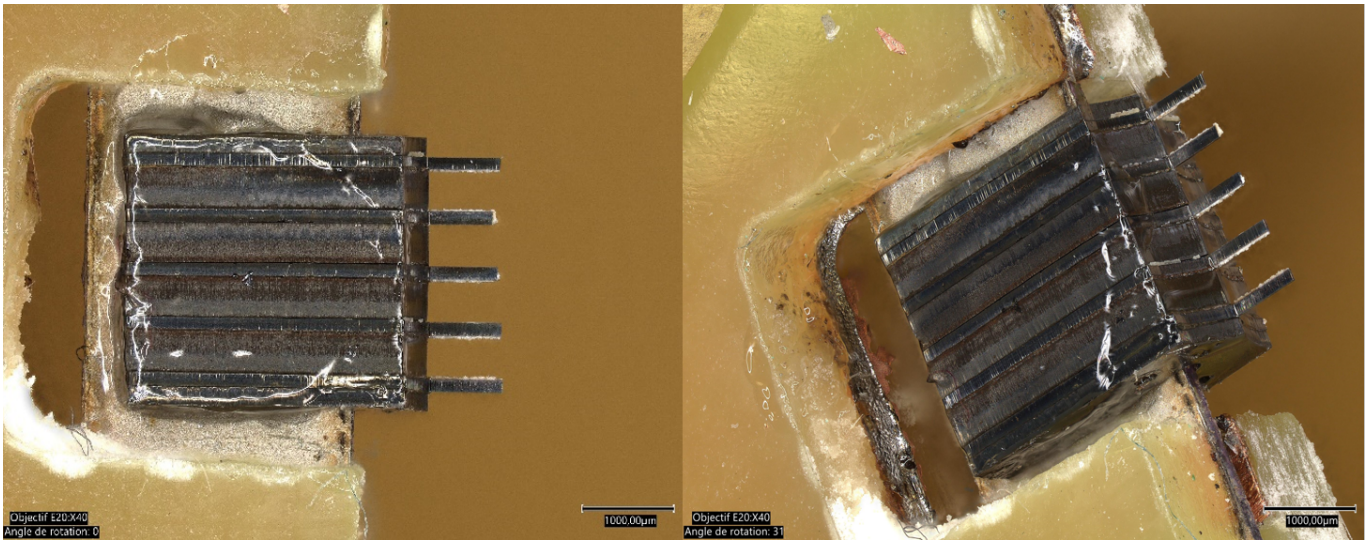

Figure 3.40: D5 device with optimal cleanliness and assembly.

ors. Through this exhaustive study, we aim to glean insights into how beam spacing and assembly techniques influence device performance, paving the way for optimized piezoelectric sensor designs in future endeavors .

3.5 Device Characterization and Validation

Using Comsol, Impedance Analyzer, and laser PSV 400 Polytech, the process is divided into three distinct phases: piezoelectric preparation and initial characterization, sensitivity assessment in different media, and final device integration and validation.

3.5.1 Numerical Analysis

For an effective application of these microbeams in sensing environments, it's imperative to comprehend their mechanical behavior under applied loads. Factors such as the maximal stress the beam can endure without deformation, and the maximum displacement it can experience before breaking, become pivotal for its operation within its limits. This part embarks on a journey through the strength of materials approach, better known as Résistance Des Matériaux (RDM), to define the mechanical constraints of a given silicon cantilever microbeam. With dimensions of $800\mu m$ in length, $120\mu m$ in width, and $40\mu m$ in thickness, the beam's mechanical response is evaluated under point loads. The material's innate properties, including Young's modulus and yield strength, play a crucial role in determining these limits.

Strength of Materials Calculation for a Silicon Cantilever Microbeam

Given Data:

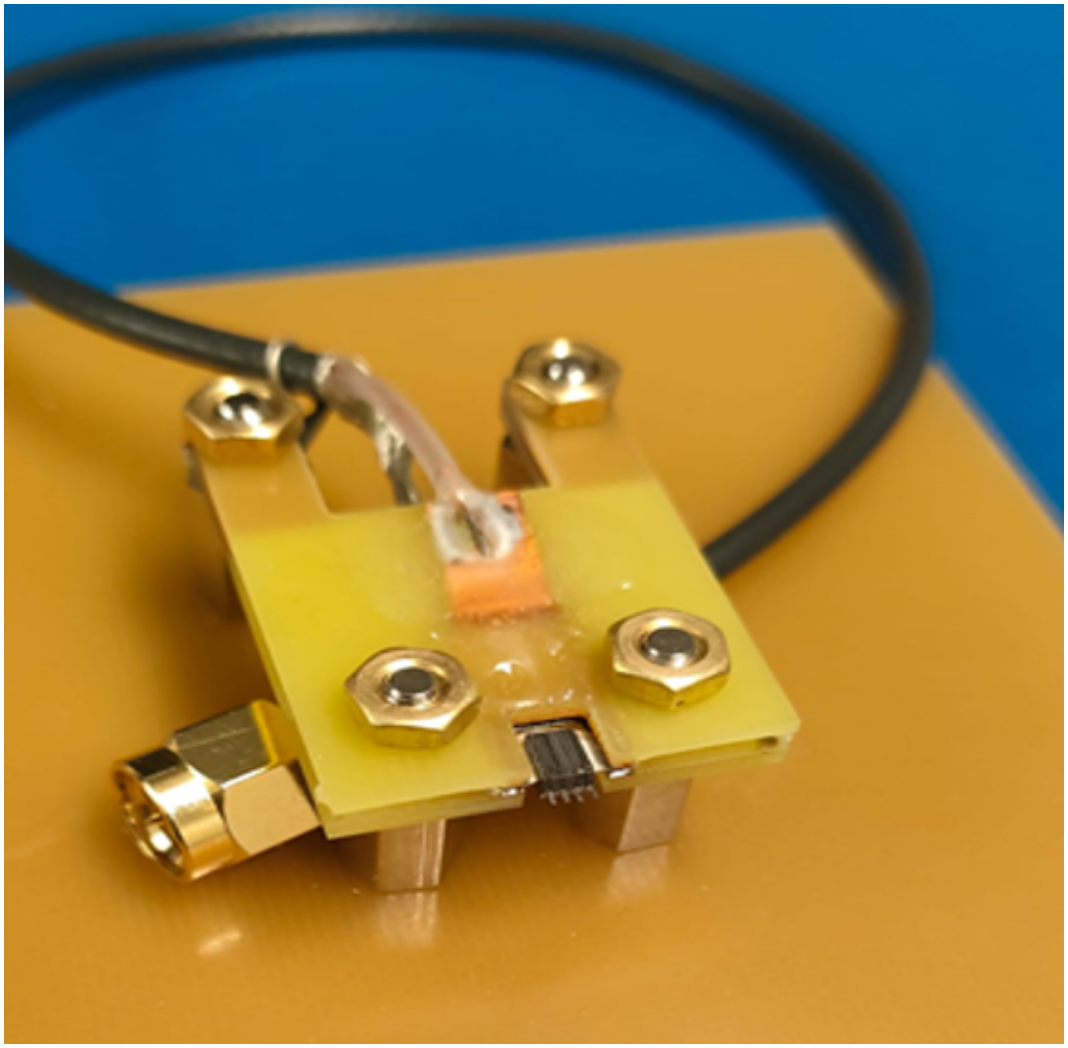

Figure 3.41: The full sensor setup with support holder and electrical connector.

- Length (L): 800μm
- Width (b): 120μm
- Thickness (h): 40μm

Material Properties (Silicon):

- Young's Modulus (E): is 100 GPa for monocrystalline silicon.
- Yield Strength (σ_y): Approximately 7 GPa.

1. Moment of Inertia Calculation

For a rectangular cross section, the moment of inertia, I, is given by:

$$I = \frac{b \times h^3}{12}$$

Substituting the given values:

$$I = \frac{120 \times 10^{-6} \times (40 \times 10^{-6})^3}{12} = 6.4 \times 10^{-16}\, m^4$$

2. Maximal Stress in the Beam

For a cantilever beam with a point load P at its free end, the maximum stress σ occurs at the fixed end and is given by:

$$\sigma = \frac{P \times L}{I} \times \frac{h}{2}$$

The beam can handle a maximal force of P without undergoing plastic deformation:

$$P = \frac{\sigma_y \times I}{L \times \frac{h}{2}} = 2.8 \times 10^{-3}\, N$$

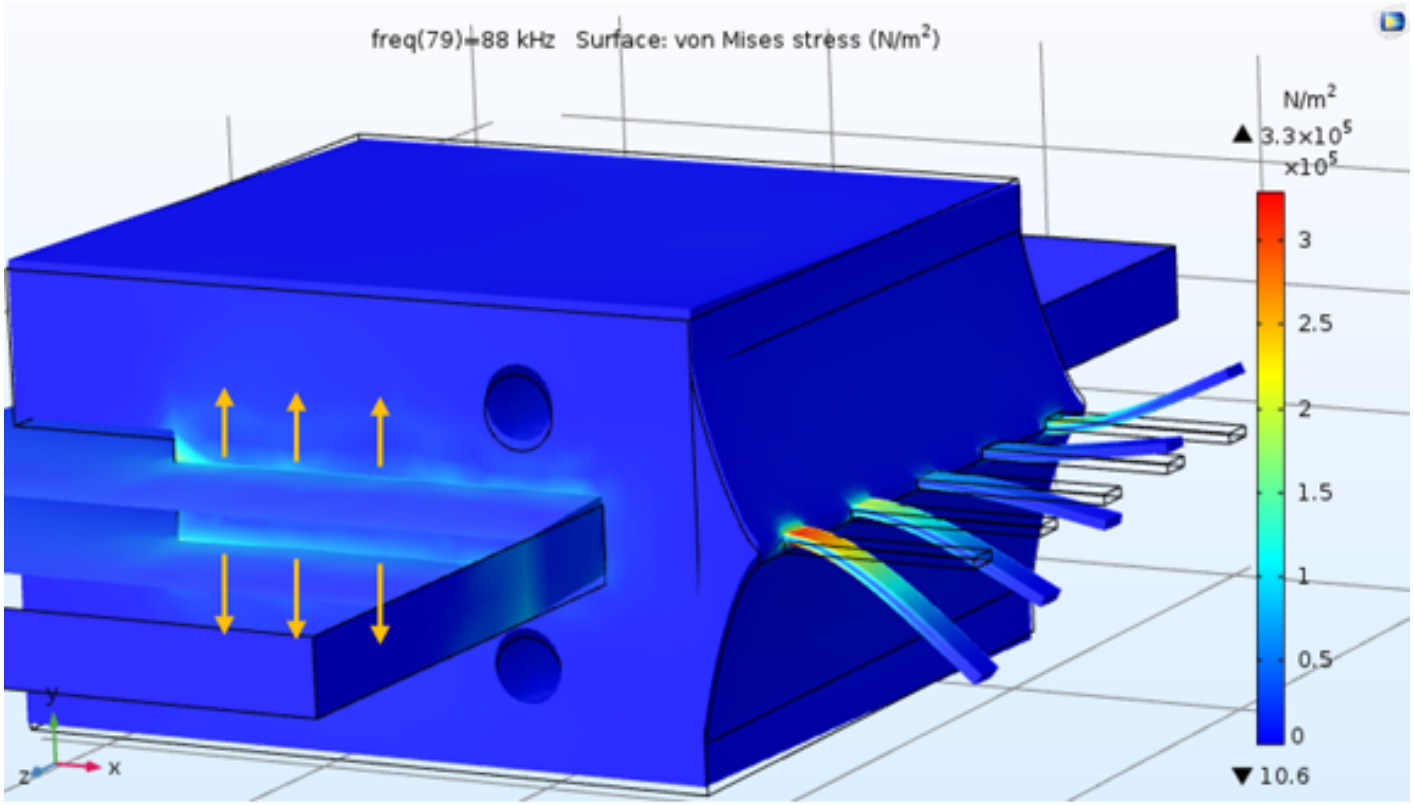

Figure 3.42: Electrical Excitation of Piezoelectric at Fundamental Frequency

3. Maximal Displacement Before Breaking

Given that we've defined breaking in terms of exceeding the yield strength, the maximum displacement at the free end, $\delta_{\max}$, can be found as:

$$\delta_{\max} = \frac{P \times L^3}{3E \times I}$$

Using $E = 150\,GPa$ as a representative value:

$$\delta_{\max} = \frac{2.8 \times 10^{-3} \times (800 \times 10^{-6})^3}{3 \times 150 \times 10^9 \times 6.4 \times 10^{-16}}$$

$$\delta_{\max} = \frac{2.8 \times 10^{-3} \times (800 \times 10^{-6})^3}{3 \times 150 \times 10^9 \times 6.4 \times 10^{-16}}$$

$$\delta_{\max} \approx 4.979 \times 10^{-6}\,\text{m}$$

$$\delta_{\max} \approx 4.979\,\mu\text{m}$$

This displacement represents the beam's limit before undergoing permanent deformation. In the context of our cantilever microbeams' mode shapes, the design intricacy becomes particularly evident when considering the integration of the piezoelectric element. This element, when sandwiched, undergoes compressive and tensile stresses upon the application of an electric field. This stress is subsequently conveyed to the beams, leading to distinct vibrations, as can be observed in Figure 3.42.

Piezoelectric materials inherently produce an electric charge under mechanical stress and the inverse is also true. In our design, this piezoelectric material is closely coupled with the beams, ensuring an efficient energy transfer. When the piezoelectric receives an electrical pulse, the beams vibrate, which can be visually confirmed by examining the rear side of the piezoelectric, shown in Figure 3.43. However, caution is paramount in such setups. Excessive electrical input can push the beams' stress levels beyond the silicon's yield strength. Thus, maintaining the system's structural integrity necessitates awareness and operation within these limits.

3.5.2 Piezoelectric element charaterics

The piezoelectric element, after its laser cut as depicted in Fig 3.27, was secured and fix it to the designated support as shown Fig 3.44. Its connection was established using the SMA cable, which was then linked directly to the impedance analyzer (Wayne KERR 6520A). As seen in Figure 3.45, the piezoelectric's resonance frequency stands at approximately 10.6 MHz after exciting the piezoelectric. With the impedance analyzer, we apply the self-sensing mode(3.45). A subsequent analysis using MATLAB facilitated the plotting of both impedance reactance and resistance for the piezoelectric, which can be observed in Figure 3.46. Describe how you used an impedance analyzer

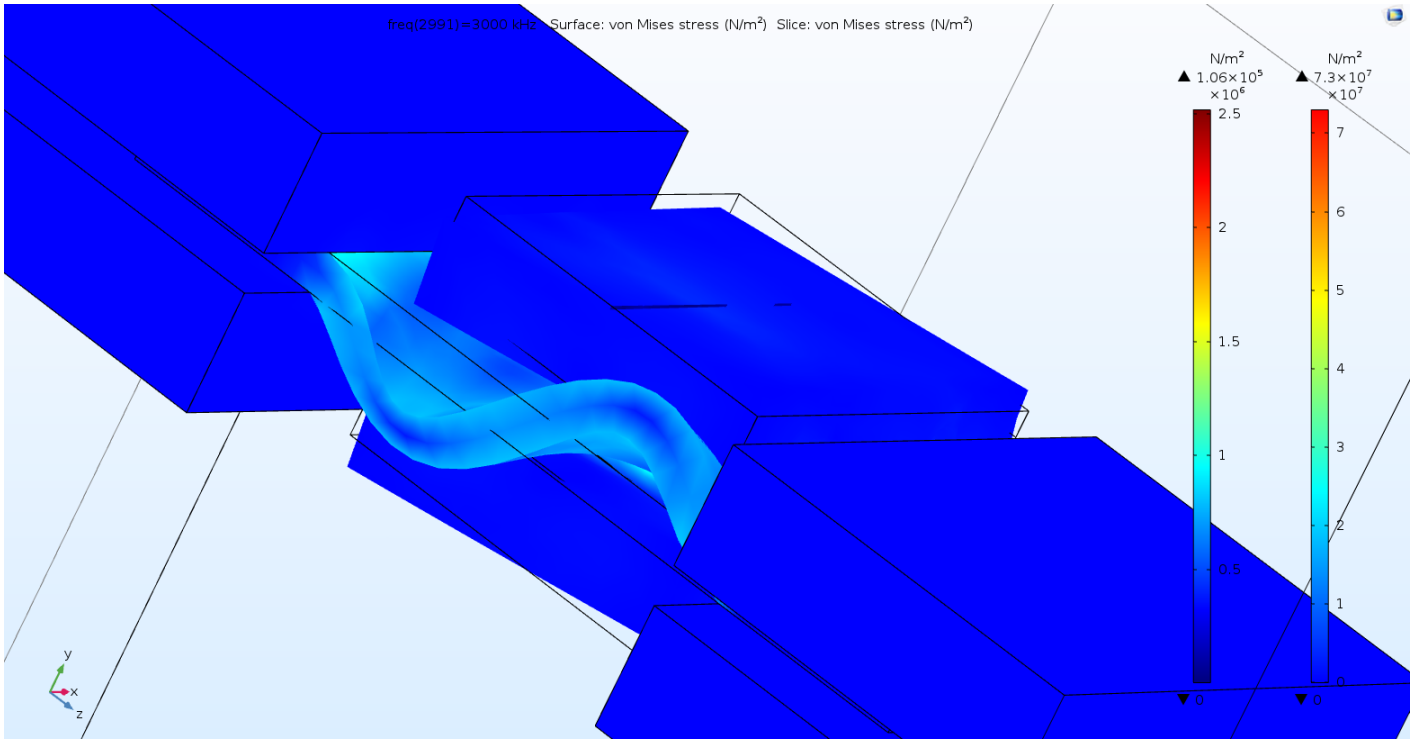

Figure 3.43: Unfixed Rear View of the Piezoelectric Element

to validate the electrical connection and interaction between the piezo and the device. Analyzing the sensitivity of a piezoelectric material is crucial for understanding its performance when incorporated into a larger system. Resistance measurements for the piezoelectric element in different mediums ranged from a vacuum to water with incrementing concentrations of NaCl, as shown in Figure 3.47. Analyzing the sensitivity of a piezoelectric material is paramount to understanding its subsequent behavior when integrated into a larger system. This section delves into an analysis of resistance measurements under different conditions to determine the sensitivity of the piezoelectric used in the sensor's structure. Figure 3.47 displays this features variations in various mediums. The mediums range from a vacuum to water with varying concentrations of NaCl. The salient features of the graph are:

Table 3.3: Resistance measurements in different environments

Environment	Concentration of NaCl (%)	Resistance (Ω)
Vacuum	-	175.2270
Ethanol	-	87.3576
Water	-	65.7446
Water + NaCl	0.5	21.3492
Water + NaCl	1.0	15.1946
Water + NaCl	1.5	14.7418
Water + NaCl	2.0	10.5798
Water + NaCl	2.5	7.7381
Water + NaCl	3.0	5.7097

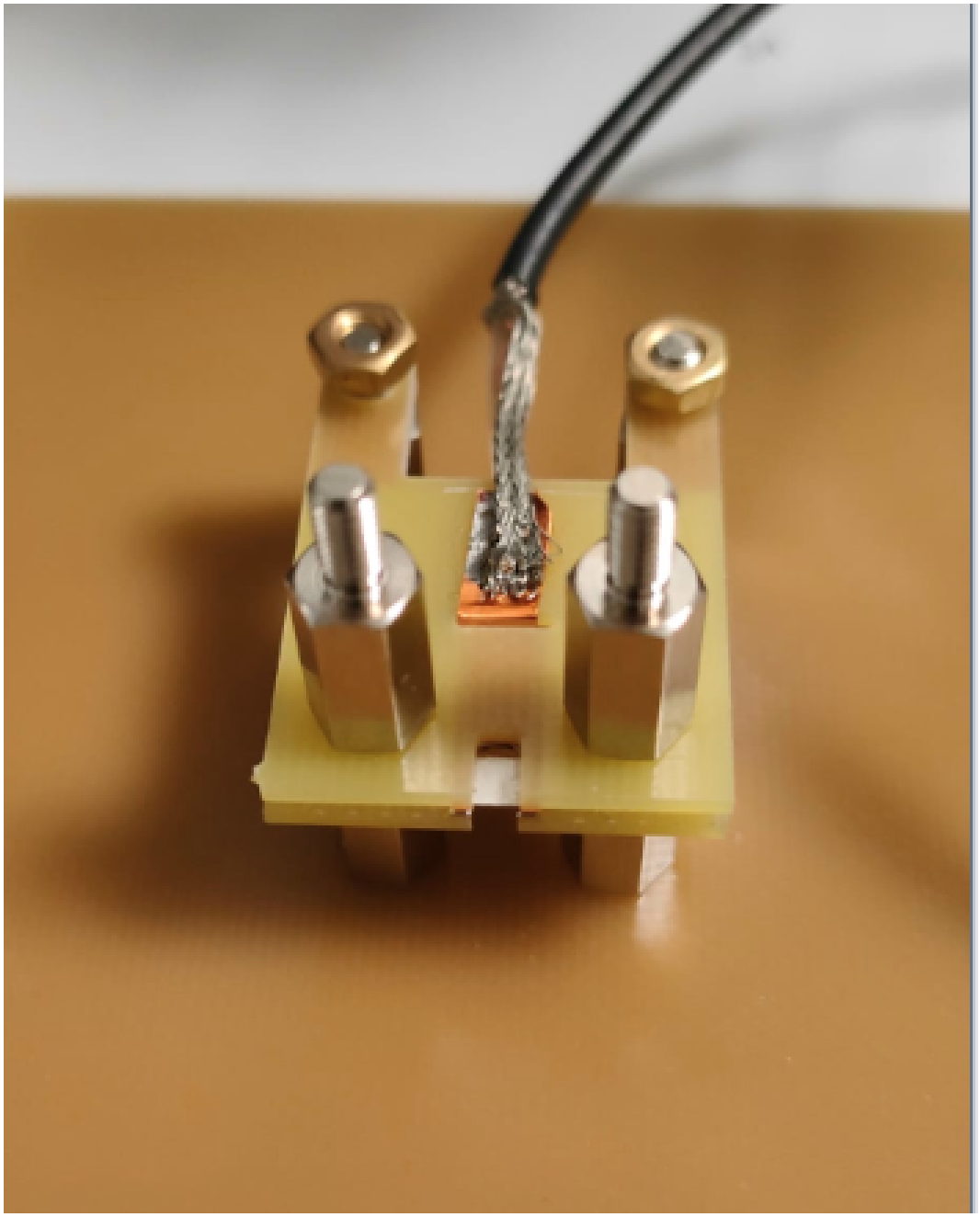

Figure 3.44: The Piezoelectric fixed in the holder

- The yellow line represents measurements taken in a vacuum, with the maximum resistance being 175.2270 ohms.
- In an ethanol environment, represented by the black line, the resistance drops significantly to a minimum of 87.3576 ohms.
- The resistance continues to decrease in a water medium, denoted by the blue line, reaching 65.7446 ohms.
- The introduction of NaCl into the water further diminishes the resistance. The red line indi-

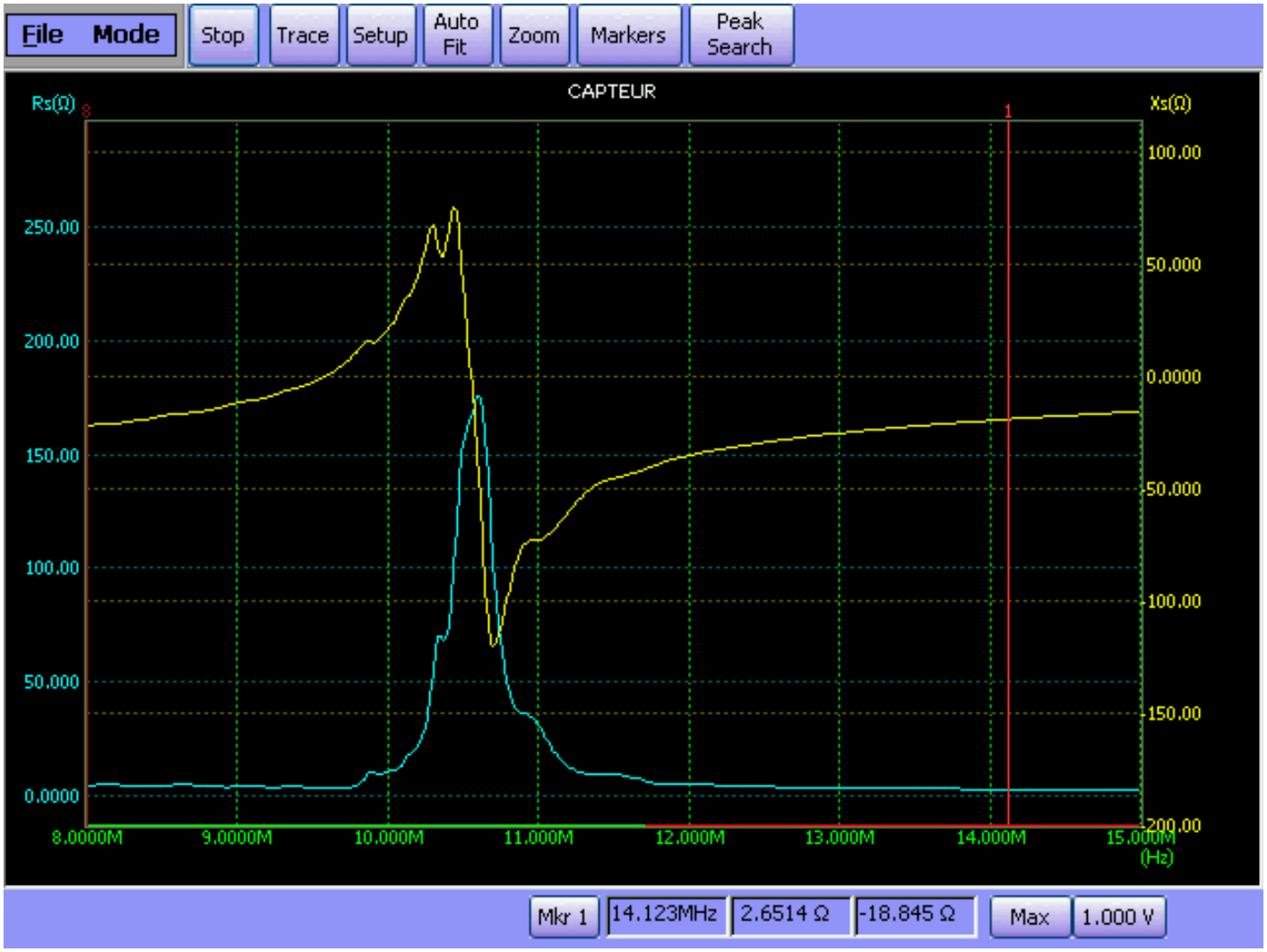

Figure 3.45: Resonance frequency of the piezoelectric via the impedance analyzer.

cates a resistance of 21.3492 ohms for a 0.5% concentration of NaCl, while the green line and purple line show readings of 15.1946 ohms and 14.7418 ohms for 1% and 1.5% concentrations, respectively.

- As the concentration of NaCl increases to 2%, 2.5%, and 3%, represented by the cyan, gray, and olive lines, the resistances drop further to 10.5798 ohms, 7.7381 ohms, and 5.7097 ohms respectively.

From these observations, it's evident that the piezoelectric element exhibits varying sensitivity based on the medium. The presence and concentration of NaCl in water significantly affect its resistance, suggesting that the piezoelectric is highly sensitive to changes in salinity. When the piezoelectric is integrated with the cantilever beam, it will provide insights into the beam's behavior and its influence on the piezoelectric.

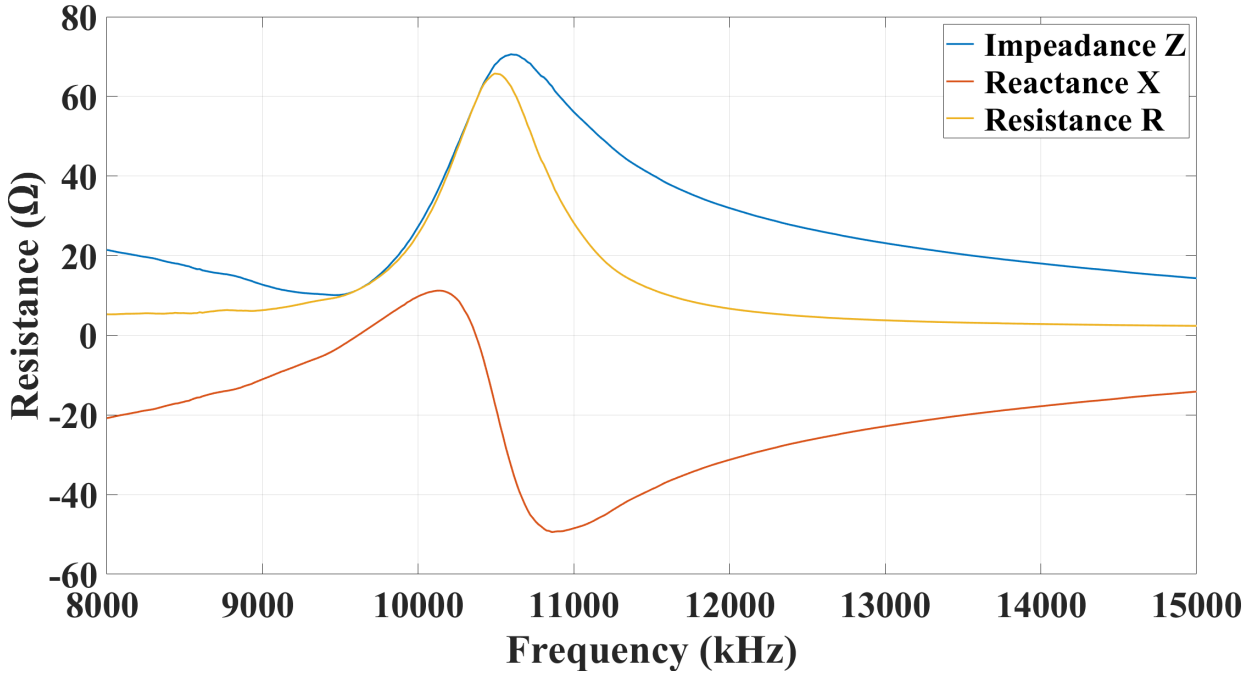

Figure 3.46: Impedance reactance and resistance plot using MATLAB.

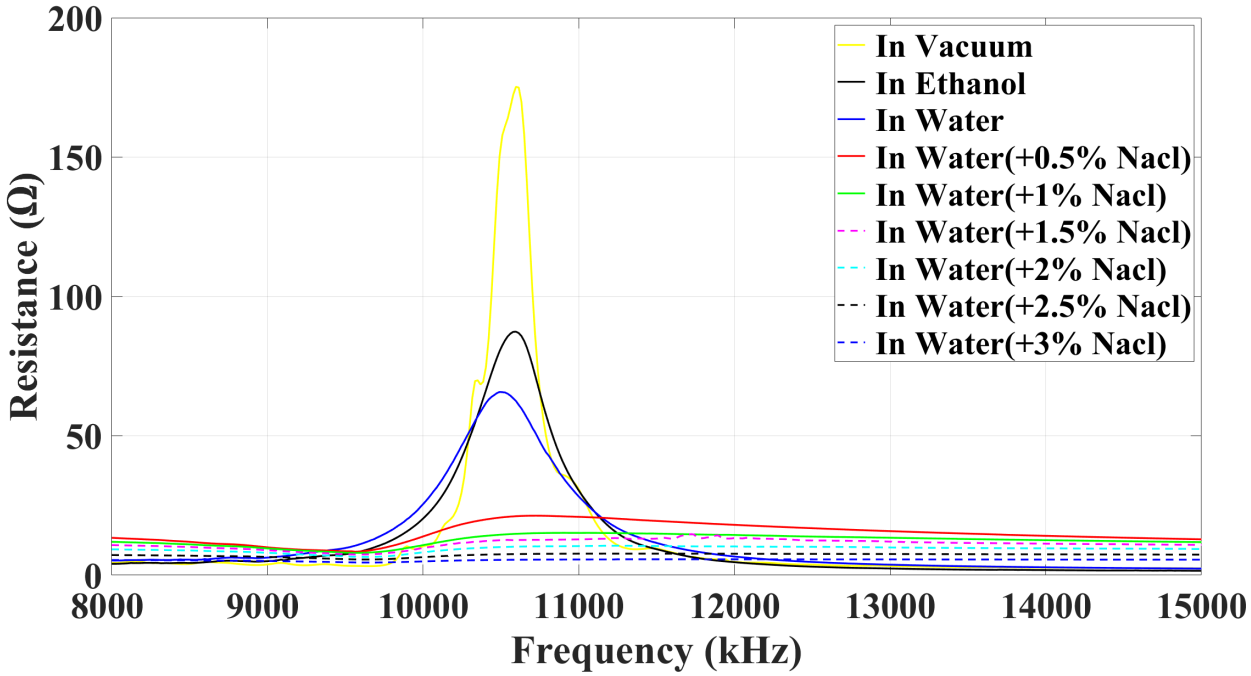

Figure 3.47: Resistance measurements of the piezoelectric in various mediums.

3.5.3 Device Integration

After successfully establishing the connection between the piezoelectric component (often referred to as the piezo) and its supporting structure, and subsequently gaining insights into the piezo's sensitivity and resonance frequency, we proceeded to integrate the assembled structure for testing

using an impedance analyzer. A frequency sweep ranging from 10 kHz to 15 MHz was conducted. The initial resonance frequencies appeared in Figure 3.48 between 200 kHz and 500 kHz, which likely signified the impact of the structure's load on the piezo. When we immersed the beams in water, an

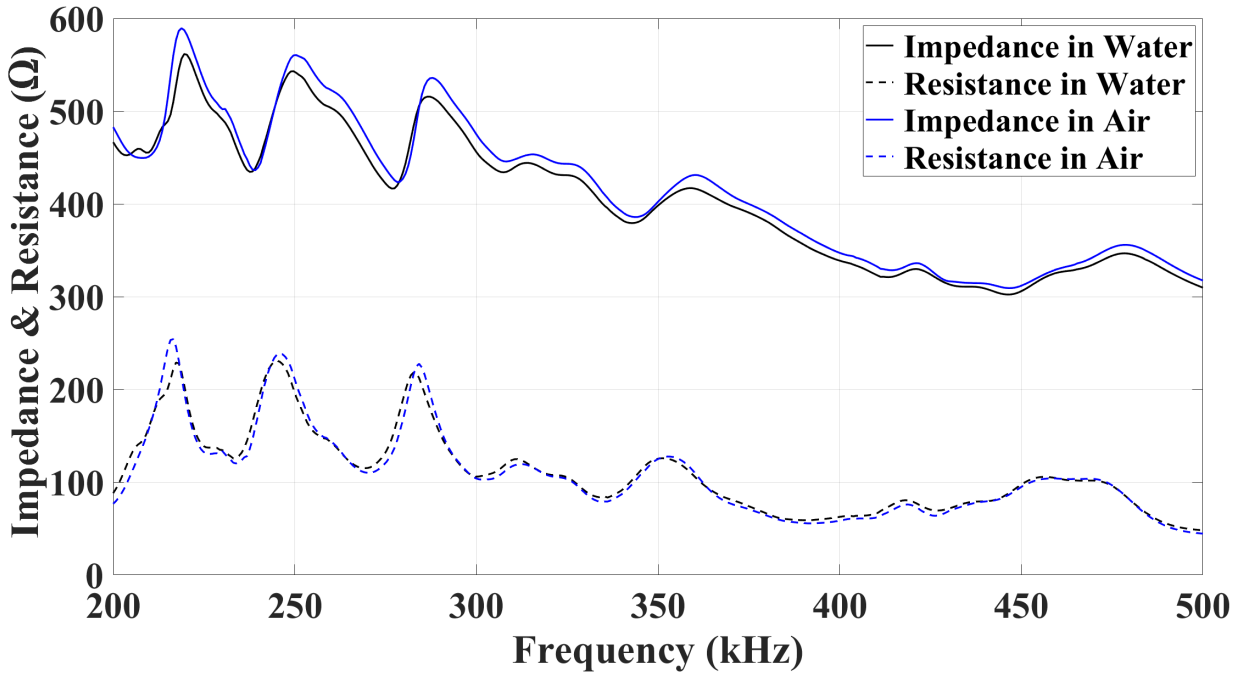

Figure 3.48: Shift in Impedance and Reactance (ΔZ) Upon Immersion of Beams in Water

impedance shift was observed, manifesting as a frequency offset. Motivated by this observation, we attempted to delve deeper into the detection and quantification of fluid environments through this frequency shift, anticipating its potential significance as discussed in Chapter 2. However, our attempts were unsuccessful. I surmise that the structure might be too large to effectively convey its behavior to the piezoelectric component.

3.6 Investigation of Piezoelectric-Structure Interaction Via PSv-400

The exploration of the dynamic interaction between microbeam structures and piezoelectric elements is critical for various applications, especially in MEMS (Micro-Electro-Mechanical Systems) devices. The piezoelectric components, when excited, can exert mechanical stresses on adjacent structures, leading to vibrations in these structures. Understanding this interaction can help in predicting and managing the behavior of such systems under different conditions. This section delves into the interaction between the cantilever microbeam structure and the sandwiched piezoelectric component. Utilizing the PSV 400 LASER Polytec and its associated PSV Presentation software, the behavior of the structure and beams under piezoelectric excitation was studied. The Laser Doppler Vibrometer's operation and the analysis methodology are subsequently discussed. Several tests were carried out to explore different aspects of this interaction. The Laser Doppler Vibrometer (LDV) is

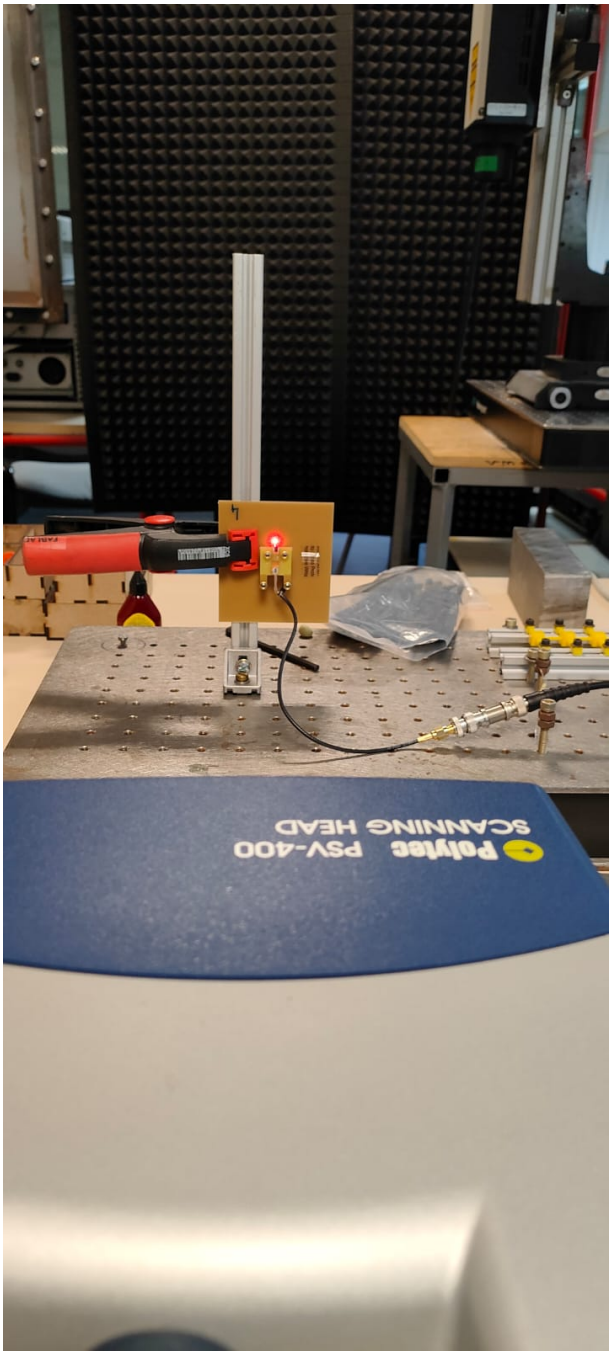

Figure 3.49: Laser PSV-400 Polytec

a non-contact instrument that uses laser interferometry to gauge the velocity and displacement of vibrating objects by emitting a laser, reflecting it off the target, and measuring the interference with a reference beam. This interference is then converted into an electrical signal by photodetectors, revealing the object's velocity, from which displacement is derived. The LDV's data, showcasing velocity and displacement over time, is analyzed through a systematic approach involving the PSV Presentation software. This involves capturing raw data, transforming it to the frequency domain via Fast Fourier Transform (FFT) for insight into dominant vibration frequencies, identifying mode shapes, examining time-domain data, and creating visual animations of vibrational behavior. Ultimately,

LDV results are compared with other analytical models to ensure accuracy and understanding of the vibrating structure's behavior.

3.6.1 Structure Mechanical Behavior

Primary Structural Resonance Test

In our initial test, the scanning focus was directed at the structure housing the beams. This was undertaken to ensure the presence of vibration and to affirm impeccable contact between the piezoelectric and the structure. Results indicated that the structure's resonance frequency is approximately 700Khz. In this study, we employed the Polytec PSV 400 Scanning head to systematically investigate the mechanical interactions between the piezoelectric element and the silicon structure. Our primary objective was to confirm the presence and characteristics of vibrations within the beams. All the measurements were conducted using the PSV 400 laser polytec. The PSV presentation software was utilized for both measurement and analysis. It's notable that the vertical bending was determined post-animation via the software, highlighting the beam bending. In the following, we focus on the intricate interaction between the cantilever microbeam-holding structure and the piezoelectric element embedded within it. Utilizing the PSV 400 LASER Polytec in conjunction with the PSV Presentation software, we meticulously measure and analyze the structural and beam behaviors upon piezoelectric excitation. This study aims to elucidate the mechanical stress introduced by the piezoelectric element onto the structure and ascertain the consequent stress transfer that culminates in beam vibrations.

Additionally, the subsequent validation step employed the laser PSV 400 Polytech, targeting the beam structure. This method, illustrated in a series of photos and graphs, effectively measured the structure's primary peak frequency (roughly 700KHz) as shown in figure 3.50.

The introduction of water markedly affect the resonant frequencies. Among the beams, the blue specter resonates at the most elevated frequency, while the beam demonstrating the highest sensitivity is the first. It is crucial to note that these measurements may not be entirely accurate, as the water droplet's influence on the beam could vary.

Frequency Analysis of Device 6 (D6)

The second scan we focused measures scanned the beam movement, detecting vibrations and ensuring interactivity in the electric-mechanical coupling (PZT - Beams).

Multiple tests conducted on devices D6 (with 5 beams) and D8 (with 3 beams) revealed specific harmonic mode shapes and fundamentals, which were visualized in MATLAB-generated graphs. Details include [specific frequencies and respective colors for each beam, as you previously mentioned]. In a curious endeavor, a water droplet was placed on a beam, with results indicating a frequency shift in the fundamental mode by approximately 35kHz for the beams on D8.

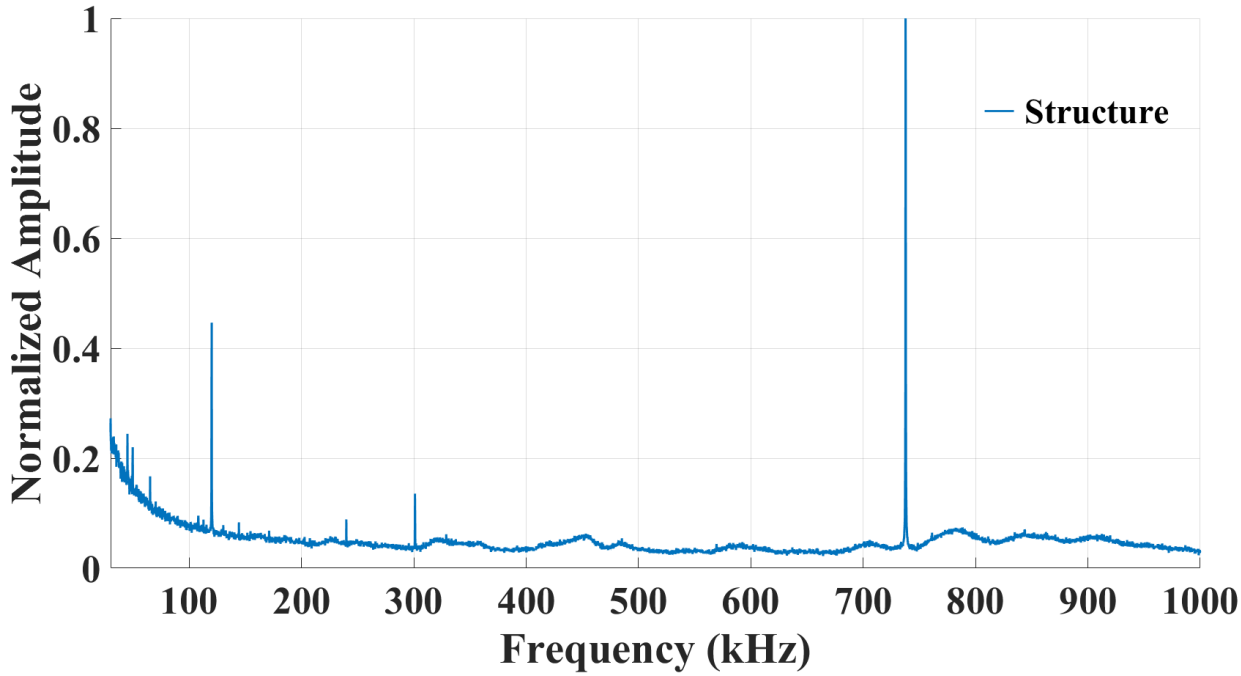

Figure 3.50: The peak frequenciesof the structur measured by the PSV 400 laser

Beam	1st vertical Bending	2nd Vertical bending
1st beam (Red specter)	84,53	515,78
2nd beam (Yellow specter)	92,03	560
3rd beam (Blue specter)	92,656	558,12
4th beam (Purple specter)	96,25	568,438
5th beam (Green specter)	82,5	505,62

In fact, the case of Device D5, the purple specter beam shows the highest frequency for both vertical bending modes. Interestingly, the first vertical bending frequencies are relatively close to each other, while the second vertical bending frequencies show more variability. For Device 6 (D6), which comprises 5 beams, we carried out a frequency sweep from 10Khz to 600Khz. The objective was to discern distinct mode shapes. Our observations led us to identify three mode shapes: two of them exhibited pronounced amplitude while the third was relatively subdued. The PSV Presentation software's animation further revealed the detection of the first flexural mode around 90KHz, the second flexural mode near 530kHz, and an elusive third mode around 200kHz. Due to our specific scanning position, categorizing this third mode as torsional, longitudinal, or lateral posed challenges.

Frequency Assessment of Device 8 (D8) Without load Effect

Turning our attention to Device 8 (D8), which is outfitted with 3 beams, we replicated the previous frequency sweep parameters, ranging from 10Khz to 600Khz. Results bore a resemblance to those of D6, albeit with notable amplitude variations in the second and third modes when juxtaposed with D6's outcomes.

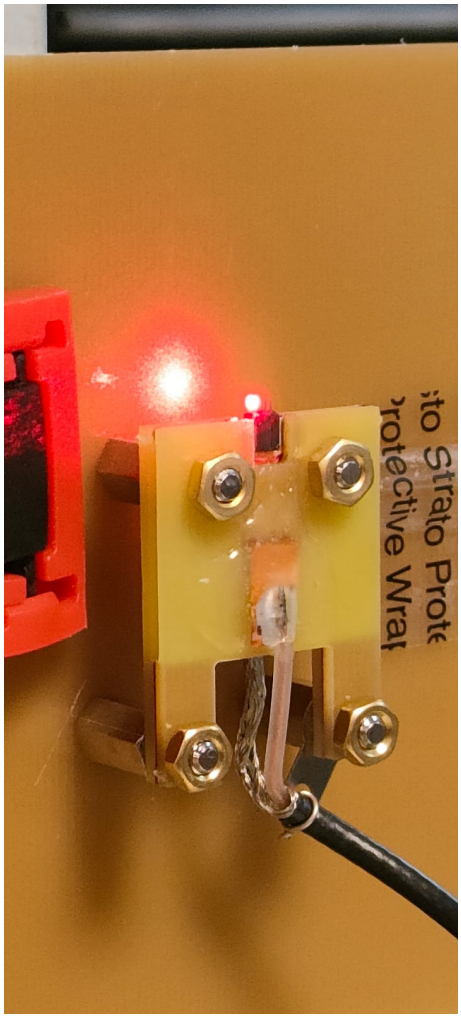

Figure 3.51: PSV laser scaning the beam while the beam is vibrating

Beam	1st mode shape	2nd mode shape	3rd mode shape
1st beam (yellow specter)	87,81 Khz	194,688 Khz	510,93 Khz
2nd beam (red specter)	94,6875 Khz	200,78 Khz	540 Khz
3rd beam (Blue specter)	90,15 Khz	214,06 Khz	575,05 Khz

The resonant frequencies of beams in air differ from one another. The second beam exhibits the highest frequency in the first mode, whereas the third beam dominates in the latter two modes.

Analysis of Device 8 (D8) With Load Effect

For a more comprehensive understanding, Device 8 (D8) was subjected to a charging effect to gauge frequency-responsive behaviors. This entailed the precise deposition of a water droplet atop the beams, followed by a sweep focusing on the fundamental frequency between 30Khz and 100khz. Our observations spotlighted an approximate frequency shift of 30KHZ.

Carefully, we precisely deposited a droplet of water onto a beam, resulting in a water bubble surrounding the beam. The primary objective of this water droplet was to induce a charging effect by either modifying the surrounding medium or incorporating the water's mass. This was undertaken

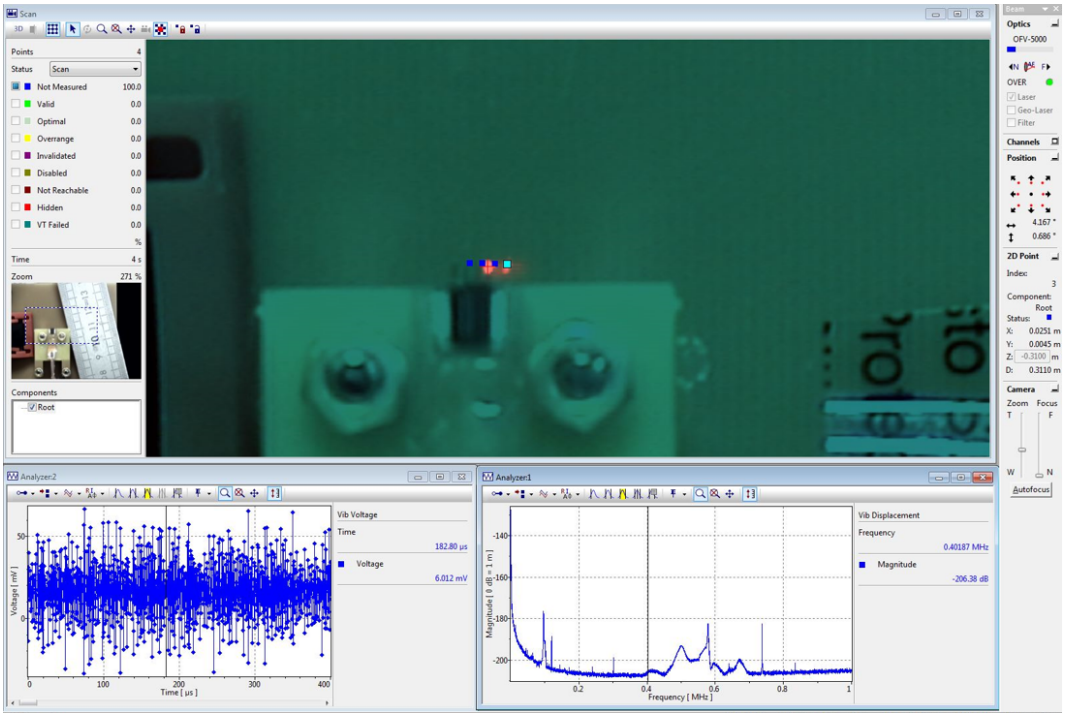

Figure 3.52: This shows how to register a point to be scanned with PSV software.

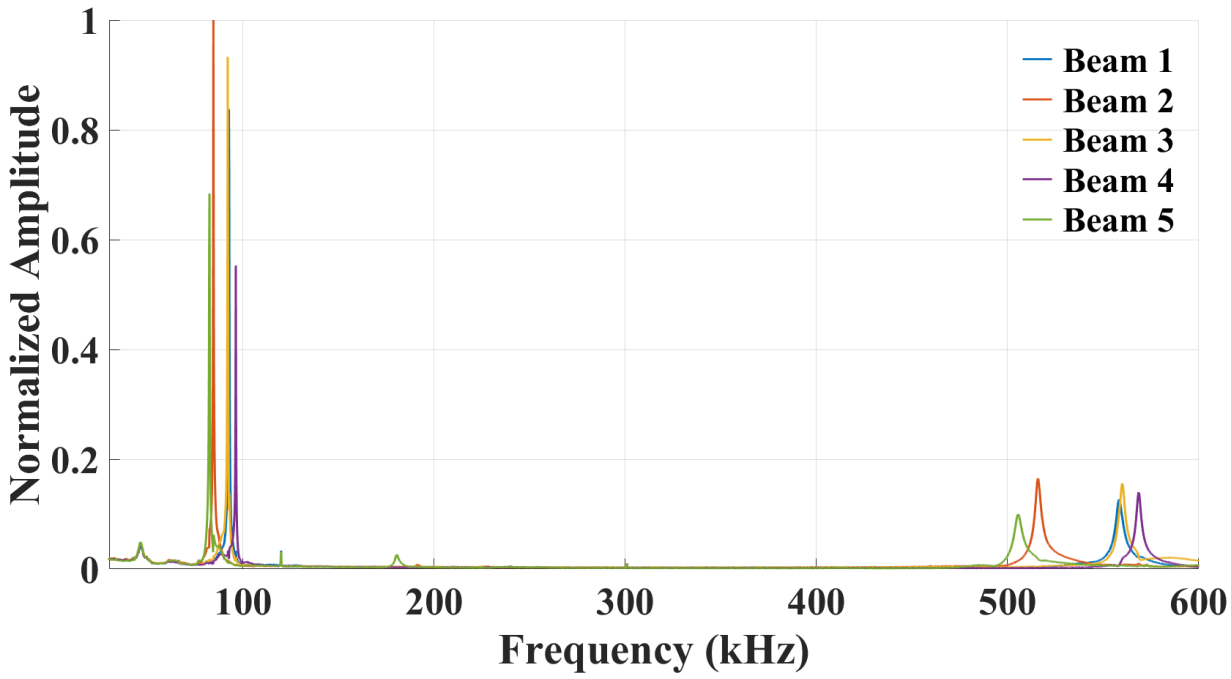

Figure 3.53: The Peak frequencies of the D5 measure with PSV-400

to determine if there would be any alteration in the natural frequency. Subsequently, we conducted a frequency sweep ranging from 30Khz to 100Khz, aiming to pinpoint the fundamental frequency. In Figure 3.55, the spectrum of the three beams is depicted. The first, second, and third beams correspond to the blue, red, and yellow specters, respectively. Figure 3.56 showcases the droplet of water on the beams. By introducing this droplet, we were able to induce a mass charging effect on the

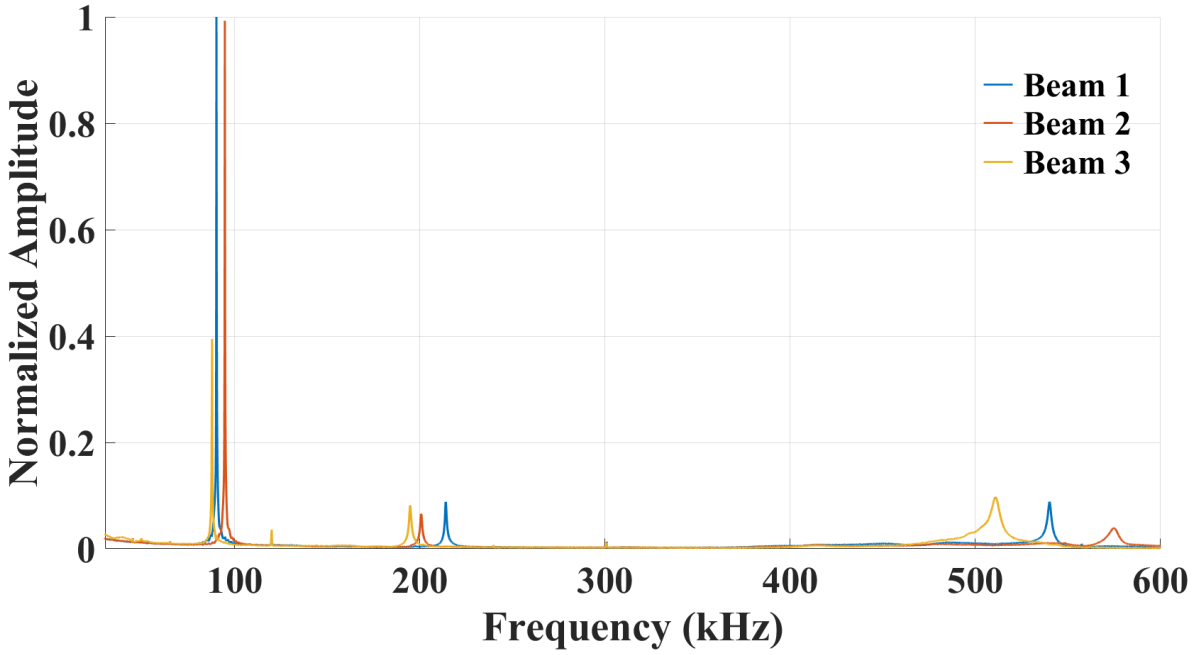

Figure 3.54: D8 In Air Sweeping frequency from 10 to 600Khz

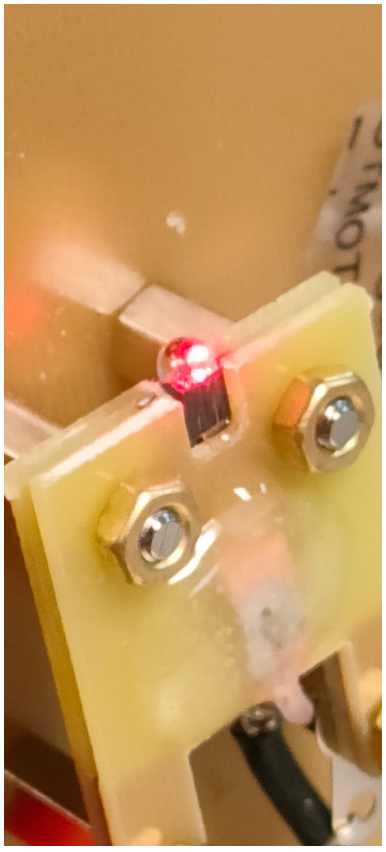

Figure 3.55: The sweeping frequency in water from 30Khz to 100Khz

beam's surface.

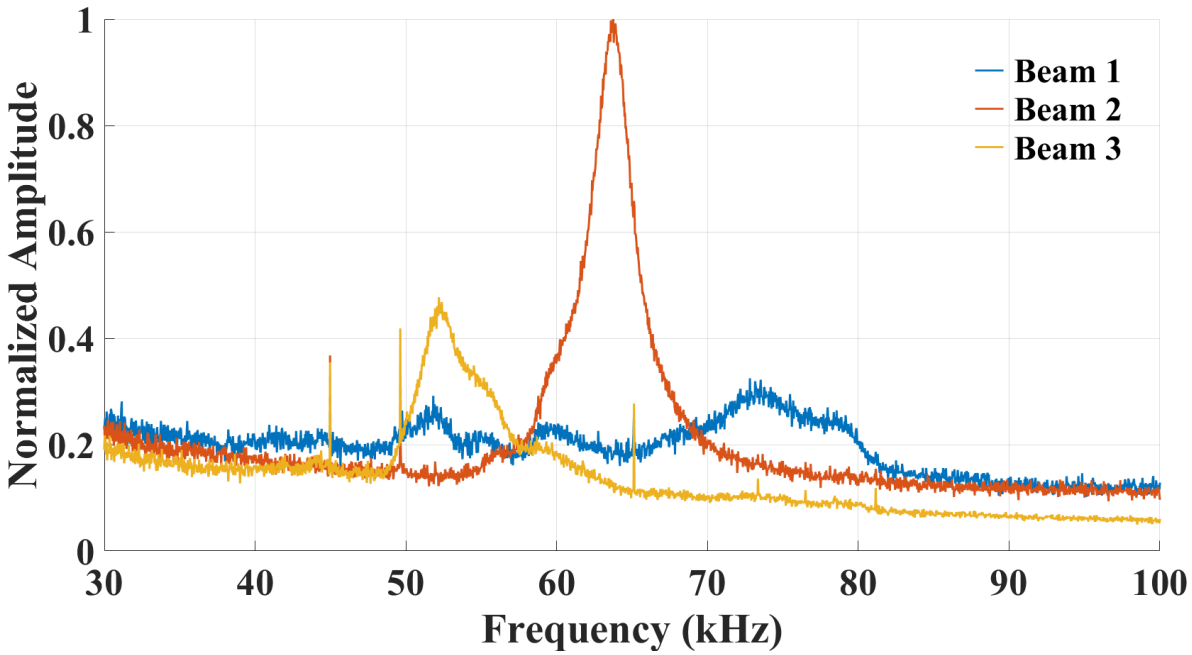

Figure 3.56: Water drops on the beams landing on the three beams

Beam	1st mode shape
1st beam (yellow specter)	52,18 Khz
2nd beam (red specter)	63,75 Khz
3rd beam (Blue specter)	72,81 Khz

Based on the mass of a water droplet, the 3.56 illustrates the shift in fundamental frequency from air to water. We can compare the 1st mode without and with added effect charging to notice the shifting of frequency which is roughly 30kHz.

3.7 Conclusion of the Interaction Study

The investigations detailed in this section offer valuable insights into the intricate interactions between the cantilever microbeam structure and the piezoelectric component. The Laser Doppler Vibrometer proved to be an effective tool in capturing the vibrations and resonances of the structure and beams, with the resonance frequency of the holding structure being identified around 700KHz. The tests on Device 6 (D6) and Device 8 (D8) showcased the significance of mode shapes and their variations in the presence and absence of charging effects. Particularly, the introduction of a droplet of water on D8 underlined the sensitivity of the system to external factors, evident from the frequency shift observed. The findings from these tests can serve as a foundation for further studies and enhancements in designing and managing MEMS devices with piezoelectric interactions. The comprehensive examination of the cantilever microbeam sensor revealed invaluable insights into its performance, behavior, and intricacies. We have discerned that the behavior and sensitivity of the piezoelectric material are heavily influenced by its surrounding medium, with significant differ-

ences observed in various mediums, especially when NaCl concentrations are altered. Furthermore, the laser validation process played an indispensable role in confirming the sensor's functionality and efficacy. As technology advances, the findings from this study will undeniably be instrumental in guiding optimized piezoelectric sensor designs in future endeavors. These insights not only reinforce the importance of meticulous design and testing but also pave the way for next-generation sensor devices that can be even more efficient, reliable, and versatile. In our pursuit to develop silicon devices using the femtosecond laser, our primary aim was the integration of a piezoelectric membrane to subsequently excite the piezo. The device's design was intricate, resembling a box that housed cantilever microbeams. Despite our best efforts and precautions during the cleaning process, there were challenges in maintaining the integrity of the finest lamella. Furthermore, attempts to reduce the thickness of the beams through engraving were, unfortunately, not successful. The substrate positioning process presented another layer of intricacies, particularly with alignment. The final surface state of the beams was not optimal, and the placement of the piezo was challenging. This often led to partial contact between the piezo and the box, jeopardizing the functionality of the system. In reflection, engraving within a 2mm wafer thickness proved to be excessively thick, especially given the fine structure of the Galvo lens used. Moving forward, a more intricate calibration and perhaps a reevaluation of the engraving depth might be necessary for optimizing the device's performance and structural integrity.

Chapter 4

Modal Analysis and Frequency Shifts in Fluidic Environments

Introduction

After successfully navigating the challenges of sensor assembly and validation in the previous chapter, we now move to the next crucial phase of methodology. Essentially, calibration ensures that our sensor operates with maximum accuracy and sensitivity by connecting theoretical predictions and empirical observations.

The purpose of this chapter is to plunge our assembled sensor into a variety of Newtonian fluidic environments housed within an incompressible chamber. The immersion is not just intended to test the sensor's resilience but also to determine its sensitivity and response to varying fluid conditions. A series of tests were conducted to achieve this goal. It was our goal to dissect the nuances of our sensor's reactivity by holding the density constant while varying the viscosity, and then holding the viscosity steady while altering the density.

To conduct these experiments, we upgraded our toolkit. Our testing conditions were incompatible with the PSV 400, so we switched to the LDV-UHF-120 Polytec doppler vibrolaser. Microstructures can be determined precisely with this advanced instrument, which has been tailored to scan the entire surface of the beam.

However, our exploration does not end there. We made an effort to evaluate the impact of additional mass on the beam since we understood that sensitivity is a complex quality. Additionally, seeing that every assembly process has its own character, we created a variety of devices that varied in terms of how components were attached, the distance between beams (or pitch), and the quantity of cantilever beams. Some even had defaults included on purpose to test the effects on performance.

4.1 Harmonic Mode Shapes Analysis

For many applications in microsystem technology, an understanding of the vibrational patterns, or mode forms, of cantilever microbeams is essential. The beam vibrates in a certain way for each mode shape, and the environment can have a big impact on these vibrational patterns. The vibrational behavior of the beam provides information on its interactions and limitations, whether it is in the air or submerged in a fluid. In this section, we explore the many modes of our cantilever microbeam. We will investigate the behavior of each mode under various environmental conditions. Our goal is to figure out the minute but essential dynamics that control the beam's performance, particularly when we alter the density and viscosity of fluid media. It was considered necessary to first carry out a numerical simulation before starting the experimental phase, where we used the piezoelectric to cause vibrations in the beams over different media. This first step was to determine the beams' eigenfrequencies, which gave us a clear understanding of both the in-plane and out-of-plane modes. We could define the correct frequency range for our sweep and ensure the best mode shape identification of the cantilever microbeam by knowing where peak frequencies are located. A numerical study was carried out with COMSOL Multiphysics to guarantee consistency and accuracy. Using this platform, we were able to precisely duplicate the circumstances and factors related to the assembly process that were fully described in Chapter 3, to guarantee that our experimental efforts were supported by a solid theoretical foundation, speeding our follow-up research and enhancing the validity of our conclusions.

4.1.1 Numerical Analysis:

In the field of microsystem technology, numerical analysis is a crucial tool, especially when working with cantilever microbeams. This method allows us to obtain insight into anticipated peak frequencies and identify potential mode shapes in advance of future experimental studies. Furthermore, knowing the simulation results enables us to understand how mechanical stresses, brought on by electric pulses on the piezoelectric element, appear as vibrations on the cantilever beams. This analytical framework simplifies our experimental process and allows a more thorough and reliable interpretation of data from real-world applications.

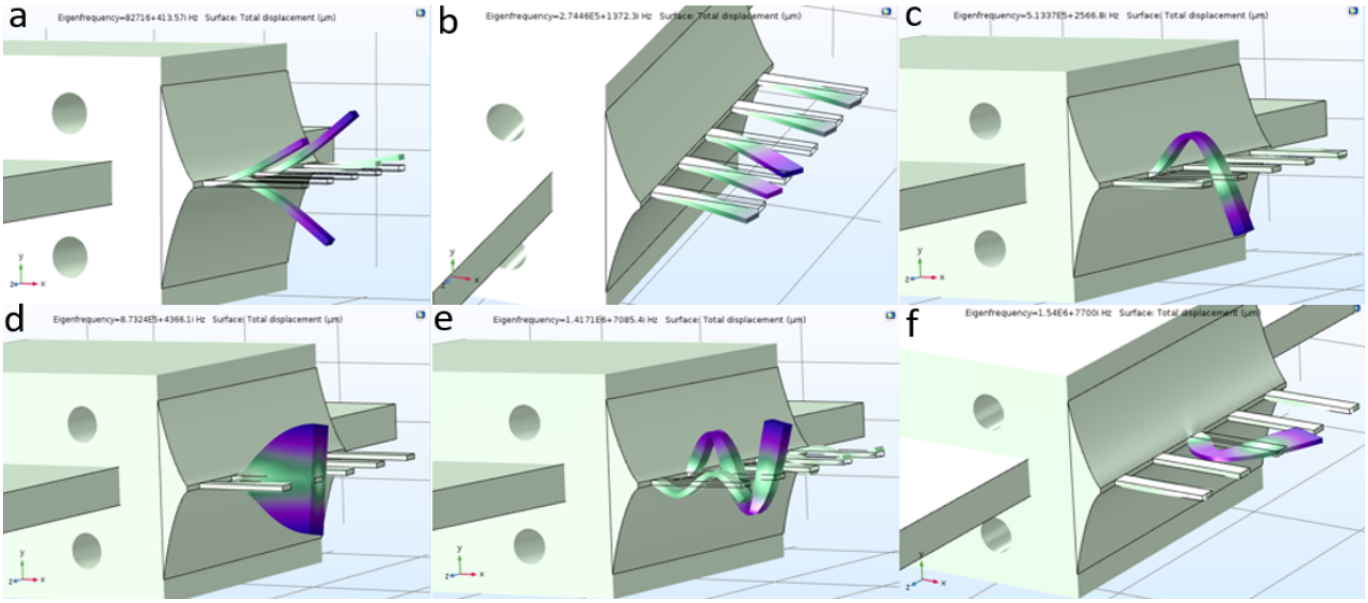

Figure 4.1: Mode Shapes

It is crucial to go further into the details of the mode forms related to cantilever microbeams, building on this fundamental understanding from numerical simulations. Referring to Figure4.1, we can observe two distinct mode shapes. The in-plane mode demonstrates lateral bending by emphasizing the oscillations of the beam from side to side, which are comparable to a board being pushed from its sides. On the other hand, the out-of-plane mode clarifies additional important dynamics by encompassing both flexions with modes a, c, and e (first, second, and third), as well as torsional bending with mode d (first, torsion mode). We are now in a great position to design and build our experimental setup, having gotten a thorough knowledge and having identified various modes that could appear during our experimental measurements. Our preliminary studies' basis assures that we enter this phase with a clear road map. This configuration must incorporate the insights and information learned thus far since it will form the basis for our testing phase. Each element and tool we select will be in line with our study goals as we proceed, ensuring a smooth transition from theoretical analysis to practical testing.

4.2 Experimental Setup

The following figure4.2 describes an experimental setup designed to investigate beam vibrations. The LDV-UHF-120 serves as the setup's mainstay. This device connects to a PC via which the PSV 9.3 software, which controls the acquisition process, is run. The PSV Presentation program and MATLAB may be used to see and analyze the experiment's data. The signal generator is also managed via MATLAB. An amplifier is attached to the signal generator's output. In turn, this amplifier is connected to a piezoelectric component built right inside the sample. Beams inside the sample can be stimulated and their subsequent vibrations examined by activating the piezoelectric element. This step is ensured by a global chain mainly composed of:

1. **LDV-UHF-120:** Likely refers to a Laser Doppler Vibrometer with ultra-high frequency capabilities. It measures vibrations of structures using a non-contact approach by measuring the Doppler shift of a laser beam reflected off a vibrating structure.

2. **PC with PSV 9.3 Acquisition Software:** A unit allows data acquisition, storage, and management from the LDV-UHF-120.

3. **PSV Presentation Software:** Used for visualizing, analyzing, and presenting data acquired through the PSV 9.3 system.

4. **MATLAB:** A high-level programming language and environment for numerical computation, data analysis, and visualization. In this setup, MATLAB controls the signal generator and can also analyze and visualize data.

5. **Signal Generator:** An electronic device producing signals in waveforms, controlled via MATLAB.

6. **Amplifier:** Amplifies the output signal from the signal generator for the piezoelectric element.

7. **Piezoelectric Element:** Generates vibrations in the sample when an electric field is applied.

The evaluation of cantilever beams' vibrational behavior utilized a state-of-the-art optical approach, specifically the *Polytec UHF-120 Laser Doppler Vibrometer (LDV)*. This heterodyne-type apparatus is specifically designed for non-contact assessments, capturing the out-of-plane vibrational components within the expansive DC-1.2 GHz frequency spectrum. For these assessments, the cantilever beam, anchored to a PCB support, was positioned on the LDV's motorized stage. This setup permitted finely controlled displacements across a 200 x 200 mm span, achieving an impressive resolution precision of 0.5 μm.

The LDV's capability extends to conducting spatial acoustic field scanning in a methodical point-by-point mode. The positioning of scanning points was efficiently determined through video imagery of the beam array, facilitated by the UHF-120's integrated microscope camera. This scanning resolution was meticulously calibrated, ensuring comprehensive and clear delineation of all the structural resonance modes inherent to the beam structure.

For these intricate measurements, a *Mitutoyo M Plan Apo 20x/0.42* infinity-corrected objective lens was employed. This high-resolution lens, boasting a 20x magnification capability, provides an unparalleled resolution of 0.7 μm and a depth field of 1.6 μm. This ensured a meticulous and precise acquisition of both spatial field distribution and nuanced vibrational data.

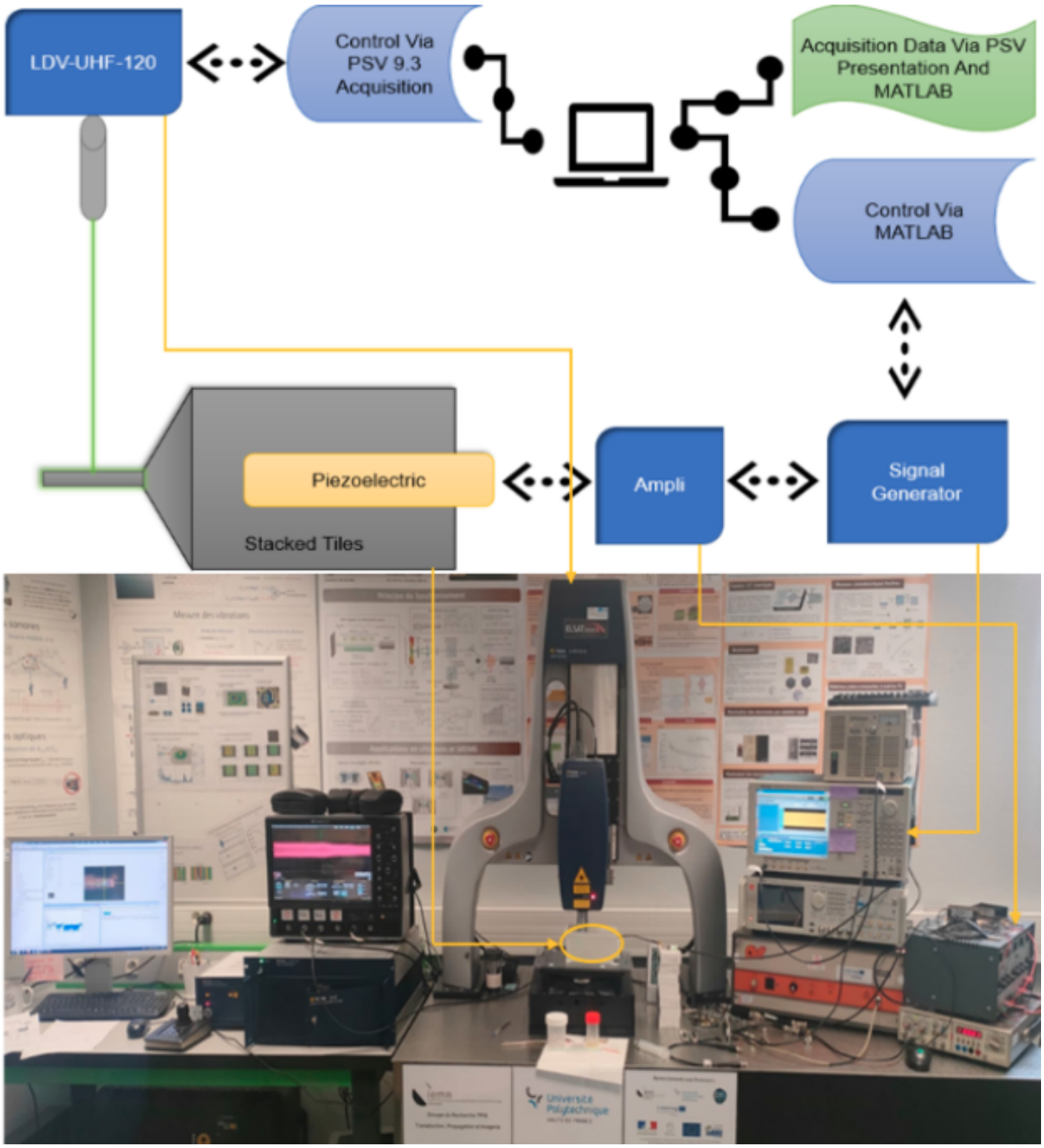

Figure 4.2: Experimental Setup for Investigating Beam Vibrations Using LDV-UHF-120 and MATLAB-Controlled Signal Generation

To extract comprehensive vibrational data across a vast frequency spectrum, the cantilever beams were excited with pulsed signals that linearly spanned from 10 kHz to 4 MHz within a concise 4 ms window. The *Amplifier Research 50W1000A* was employed to amplify these signals, outputting

an impressive 5 W of electrical power to a consistent 50 Ohm load. The collected acoustic displacement data, set in the spectral domain, utilized a detailed 128,000 fast Fourier transform (FFT) lines, recorded at an astoundingly swift 1 Gs/s sampling rate within a compact 320 μs duration. This achieved a frequency resolution granularity of 3.125 kHz. With this advanced methodology, data elucidating the root mean square (RMS) of the spatial field distribution could be sourced directly from FFT data. Moreover, this also facilitated the generation of time-resolved imagery, depicting the structural resonance modes via inverse FFT, encompassing the entire excitation frequency range from 10 kHz to 4 MHz.

The Protocol for Measurements and Data Collection:

1. **Setup:**
    - Position the LDV-UHF-120 at an optimal distance from the sample.
    - Turn on the PC and launch the PSV 9.3 Acquisition software.
    - Initialize MATLAB with the required scripts for controlling the signal generator.
2. **Calibration:**
    - Calibrate the LDV-UHF-120 using a reference sample.
    - Test and adjust the signal generator and amplifier using MATLAB.
3. **Measurement Process:**
    - Use MATLAB to initiate the signal generator.
    - The LDV-UHF-120 captures the sample's vibrations.
    - Transfer data to the PC via PSV 9.3.
4. **Data Collection and Analysis:**
    - Store raw data for each session.
    - Visualize data using PSV Presentation and analyze in MATLAB.
5. **Repeat Measurements:** Conduct multiple sessions and average results.
6. **Data Backup and Report:**
    - Back up the collected data.
    - Generate detailed reports using PSV Presentation and MATLAB.

4.3 Harmonic Mode shapes: Flexion and Torsion Analyses in Air

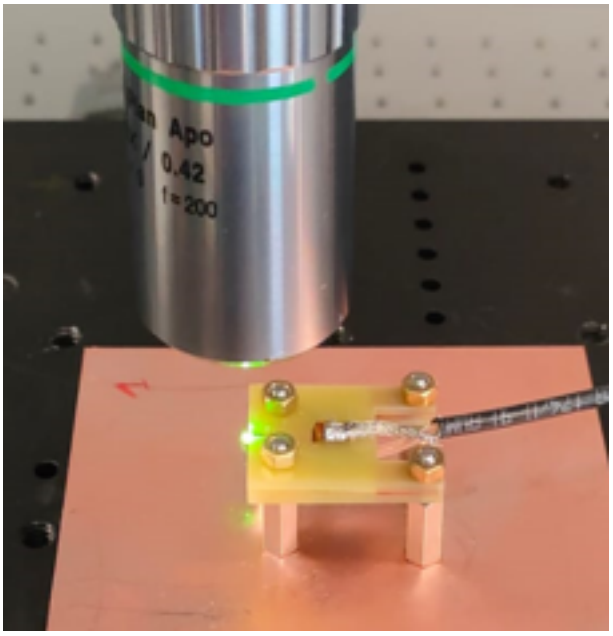

Figure 4.3: Vibrational Analysis of Microbeam using LDV-UHF-120 Laser Doppler Vibrometer

A Laser Doppler Vibrometer (LDV-UHF-120), seen as the cylindrical device at the top of the picture4.3, is actively scanning a center microbeam using a green laser dot in this high-tech experimental setup. An incorporated but barely perceptible piezoelectric component vibrates this microbeam, which is securely held between supports. The entire system is supported by a strong base plate with a grid design that is probably fastened to a sturdy platform to reduce outside influence. The fact that the test is conducted in an air environment is crucial since the surroundings can change how the microbeam vibrates. This exact configuration is intended to non-intrusively examine the vibrational behavior of the microbeam under piezoelectric activation.

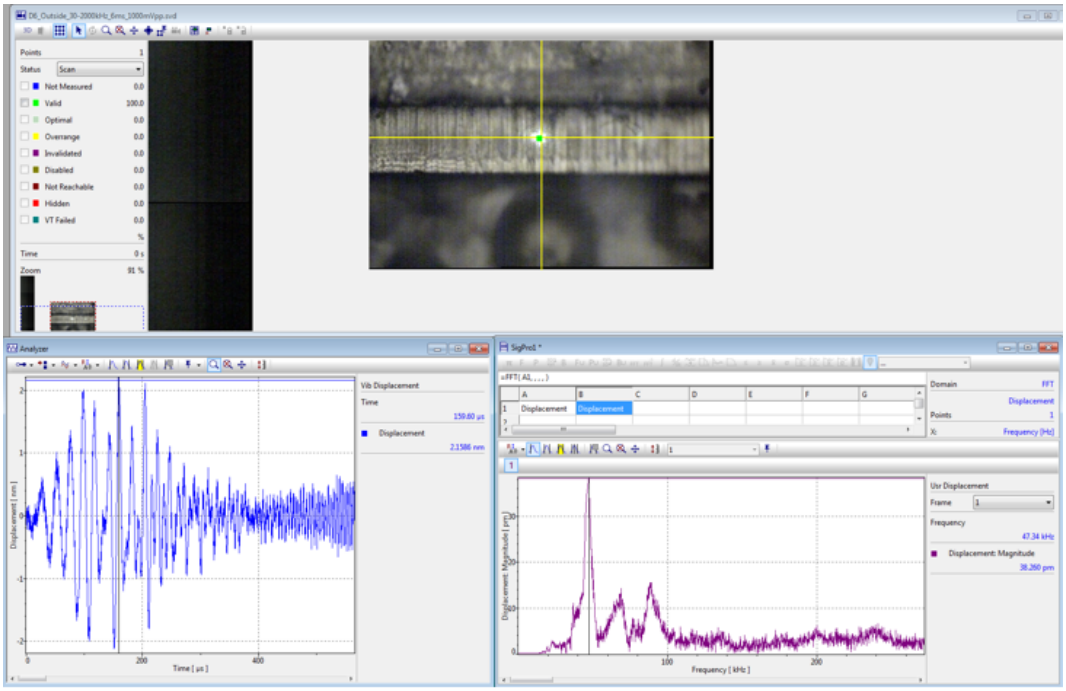

Figure 4.4: Workings of the LDV-UHF-120 Laser Doppler Vibrometer via the PSV presentation software, including real-time monitoring of the reflected laser signal.

The picture4.4 displays the PSV presentation software's user interface while simultaneously showcasing the LDV-UHF-120 Laser Doppler Vibrometer's capability. With the precise location of laser contact indicated, the top portion shows a microbeam being actively scanned. This demonstrates the Vibrometer's capacity to observe vibrational action without intervening. A thorough status panel next to it lists the different operational phases of the scanning procedure. The vibrational data is depicted in great detail in the sequence of graphs below. A time-domain, on the left, depicts the varying displacements throughout a period, capturing transitory vibrating patterns. An study of the data in the right segment's frequency domain reveals sharp peaks that correspond to the vibration's primary frequencies. This dual representation guarantees a thorough comprehension of the dynamic behavior of the microbeam. Integrated controls, seen throughout, allow for real-time adjustments, thereby ensuring accuracy in capturing the reflection signal emitted by the laser. In the field of mechanical and structural engineering, it is crucial to comprehend how a system behaves under different excitations. Two of the most fundamental and varied ways a system might bend are flexion and torsion modes. Torsion focuses on the twisting of structures, whereas flexion primarily deals with their bending. In addition to providing information on the system's resilience and weaknesses, a thorough study of each of these modes helps designers make adjustments for the best possible performance and safety.

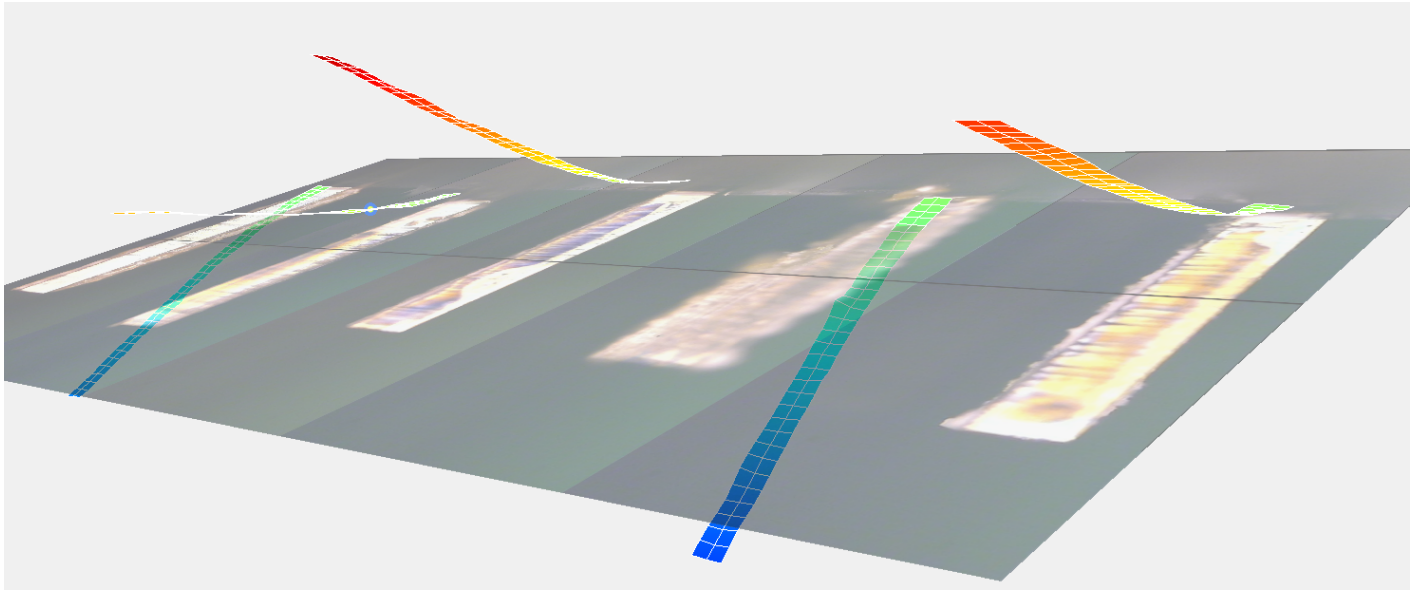

Figure 4.5: 1st bending mode with the 5 beams

We begin by defining flexion and torsion modes before analyzing out-of-plane harmonic mode forms in air. We derived a number of dynamic representations from the PSV program, each depicting a different mode form, using our laser scanning system. Beginning with flexion modes, Figure 4.5 depicts the initial bending mode for a system equipped with five beams.

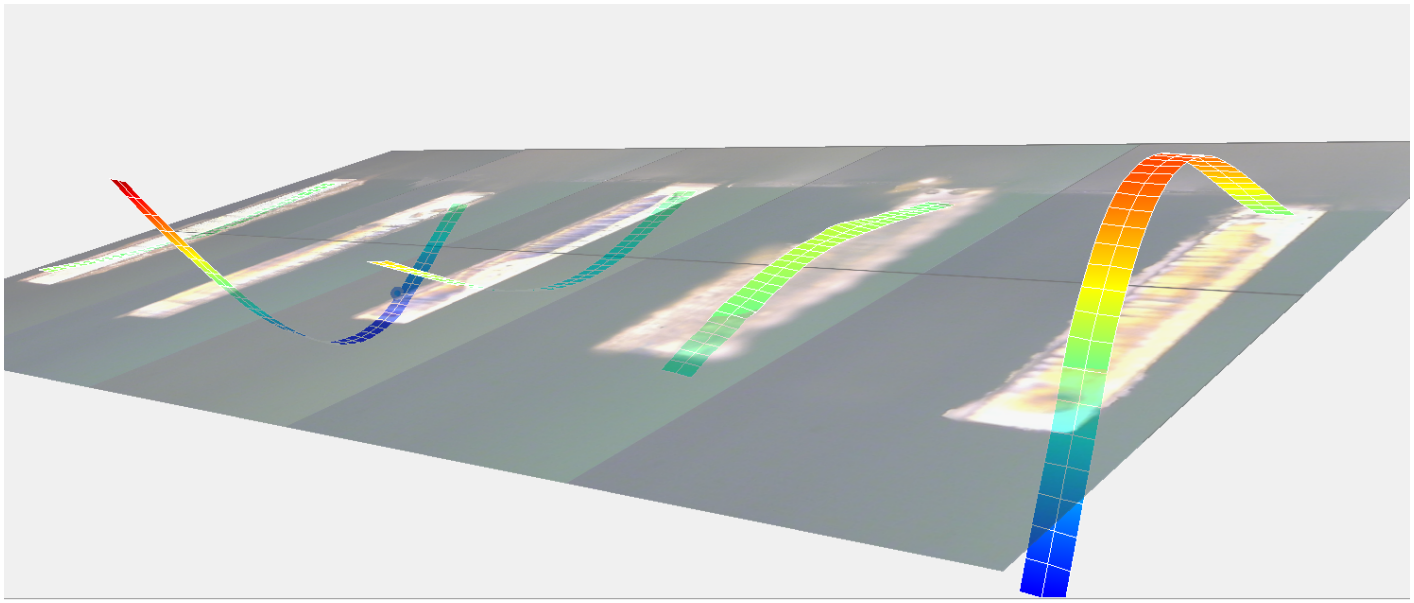

Figure 4.6: 2nd Bending mode with the 5 beams

This foundational pattern progresses to a more complex state as shown in Figure 4.6, illustrating the 2nd bending flexion mode. Our exploration into torsional dynamics is captured in Figures 4.7 and 4.8, which display the 1st and 2nd torsion modes, respectively.

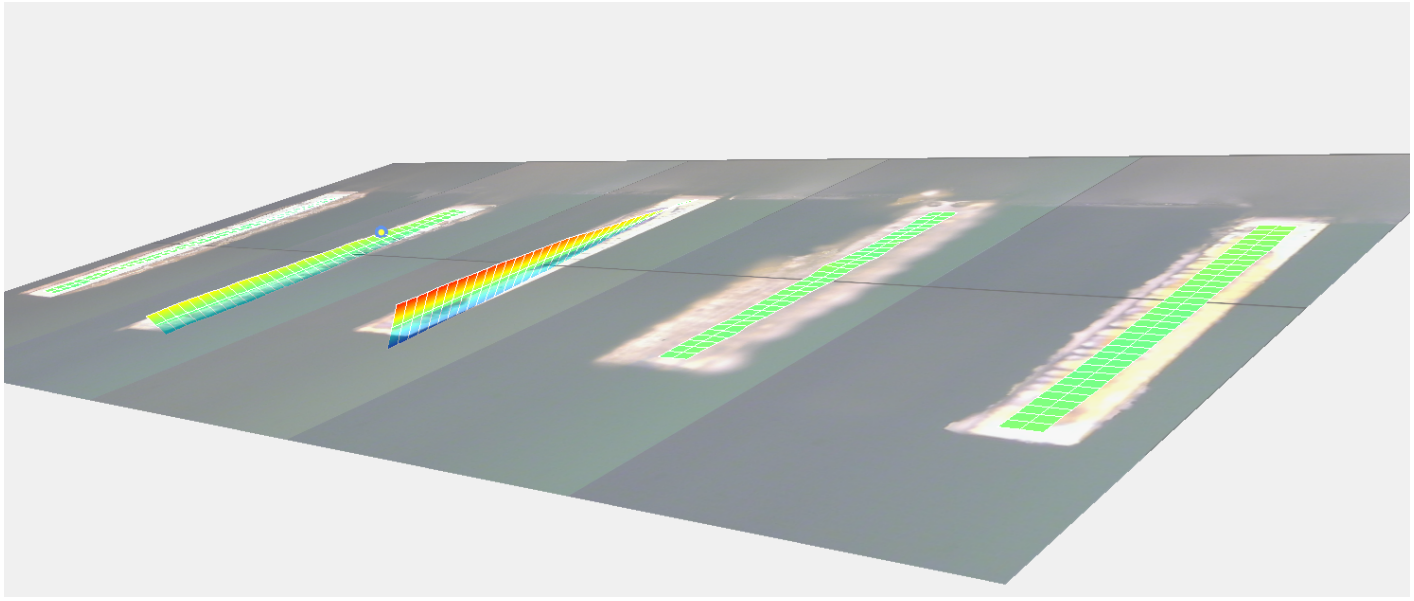

Figure 4.7: The 3rd beam shows the 1st Torsion mode with the device with 5 beams

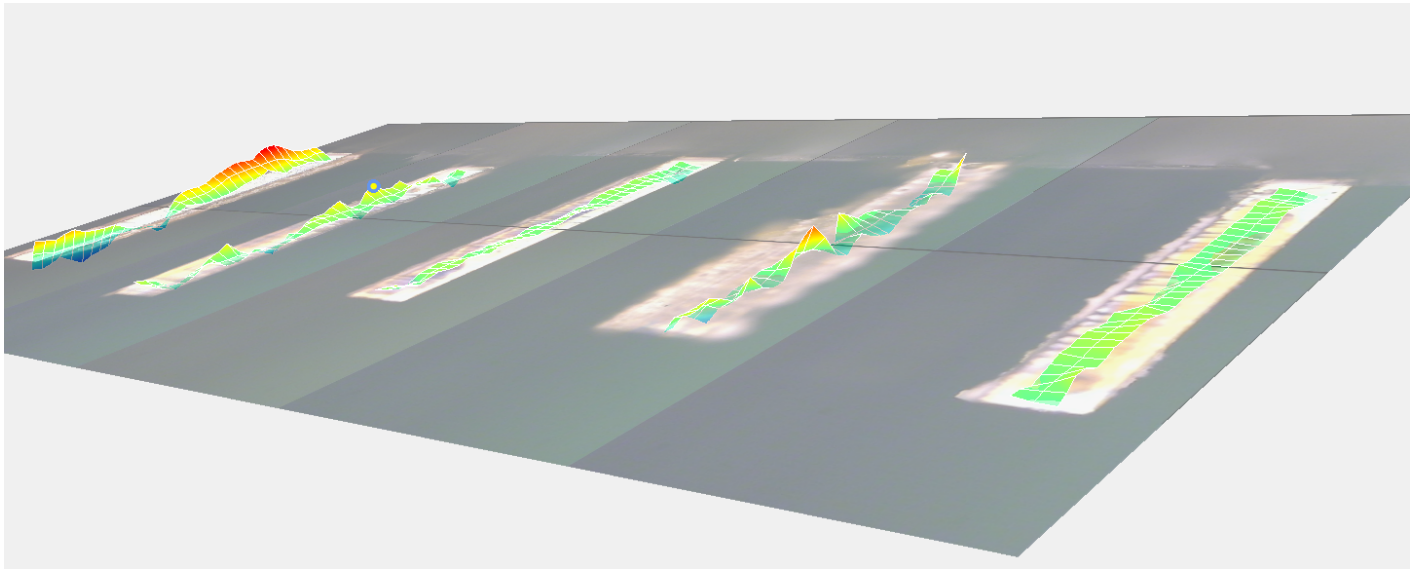

Figure 4.8: The 1st beam shows the 2nd Torsion mode with the device with 5 beams

The transition from one mode to another, for as from the first to the second bending mode, involves more than modes evolution. Each succeeding mode results in a deeper pattern of deformations and frequency, exposing possible stress points and regions of the structure's vulnerability or strength. A full vibrational design is essentially revealed as we move up the mode numbers, with each mode providing a different viewpoint on how the structure could respond to various external stimuli.

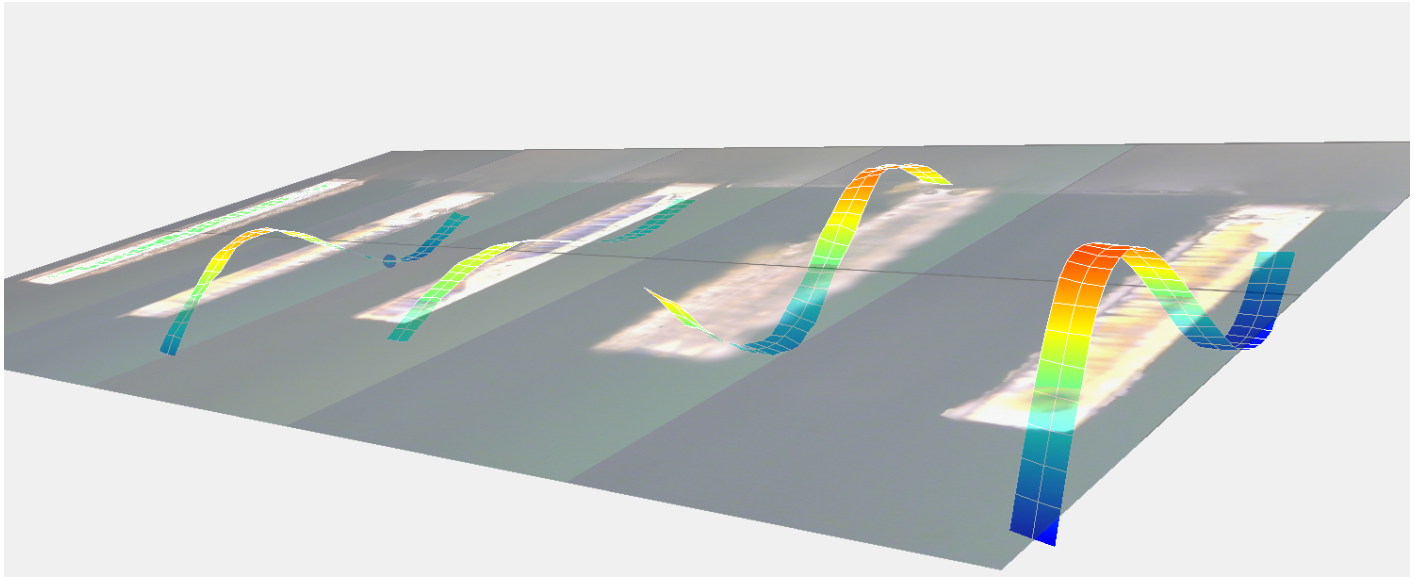

Figure 4.9: 3rd Bending mode with the 5 beams

A later transition into the 3rd bending flexion mode is clearly showcased in Figure 4.9.

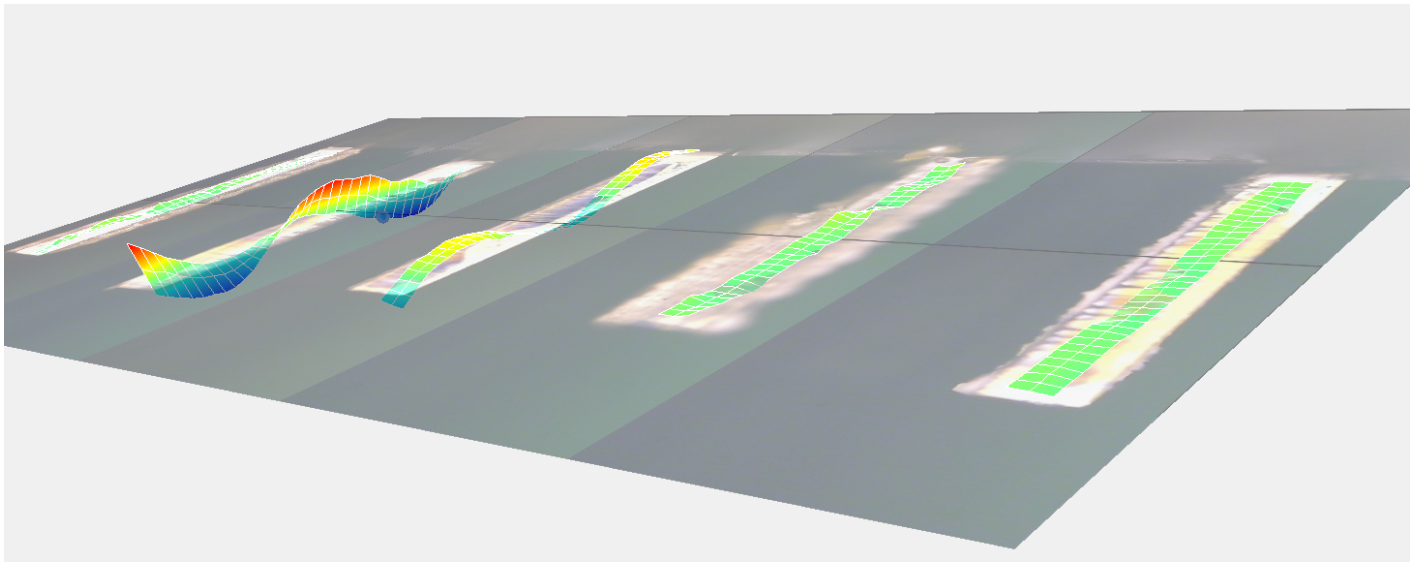

Figure 4.10: Using the devices with 5 beams, the 2nd beam shows the 3rd Torsion mode

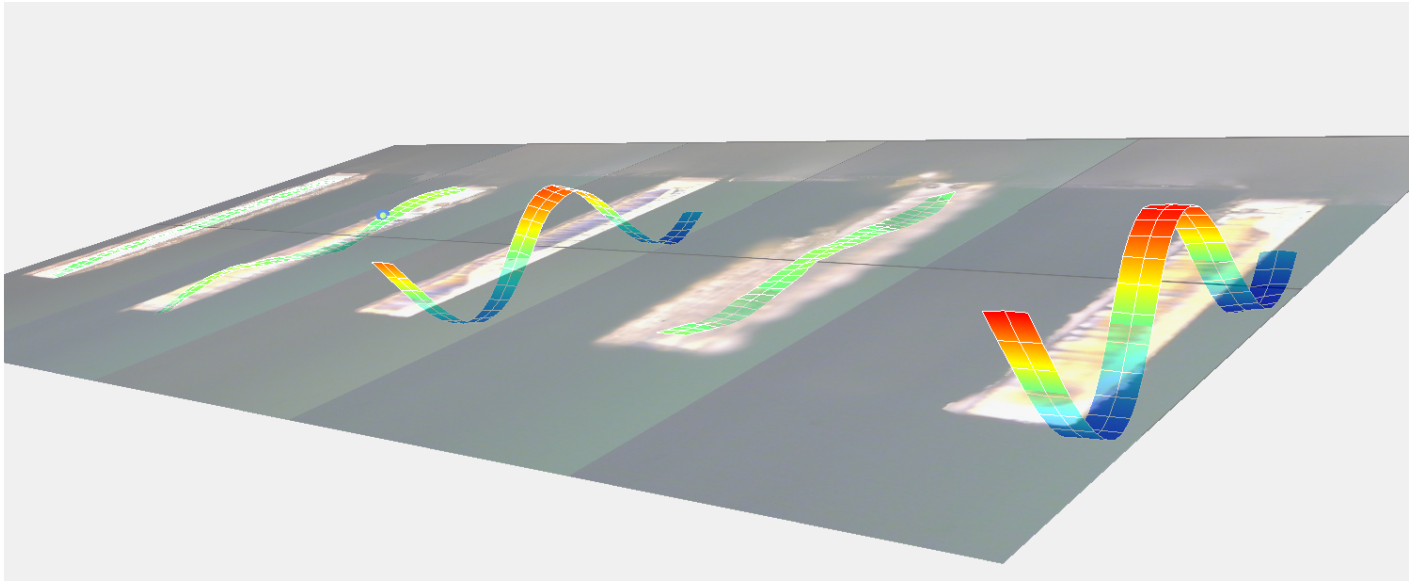

Figure 4.11: Using the devices with 5 beams, the 3rd and the 5th beams shows the 4th flexion mode

Additionally, the torsional behavior intensifies in Figure 4.10, representing the 3rd torsion mode. Our visual exploration concludes with Figure 4.11, which encapsulates the 4th bending flexion mode, adding depth to our understanding of the system's vibrational intricacies.

4.3.1 Frequency Shift Analysis in Air and Water

The Figure 4.12 shows parts of the machine partially submerged in what looks to be a container filled with water in the left image. The device's green illumination it's an indication of active laser scanning. The submerged microbeam in the right image can be seen up close, highlighting the way the laser light highlights the underwater beam. This arrangement appears to improve the underwater visibility of the vibrational behavior of the beam, which makes it a valuable tool for researching the impact of fluid dynamics on material properties.

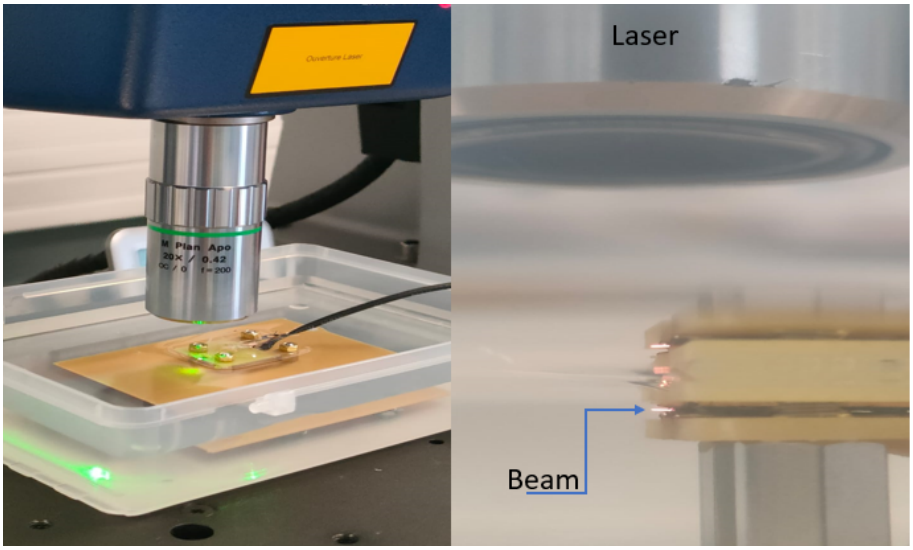

Figure 4.12: Laser-Assisted Underwater Analysis of Microbeam Vibrations

Figure 4.13 showcases the vibrational analysis of a multi-beam device in its fundamental mode. The five beams' behaviors in the air and water are shown. The upper portion of the image's 3D visualization sheds light on the mode shapes in these two different environments. There is a noticeable vibration pattern in the left frame (air), which is significantly changed in the right frame (water) under the damping effect of the denser and more viscous water medium.

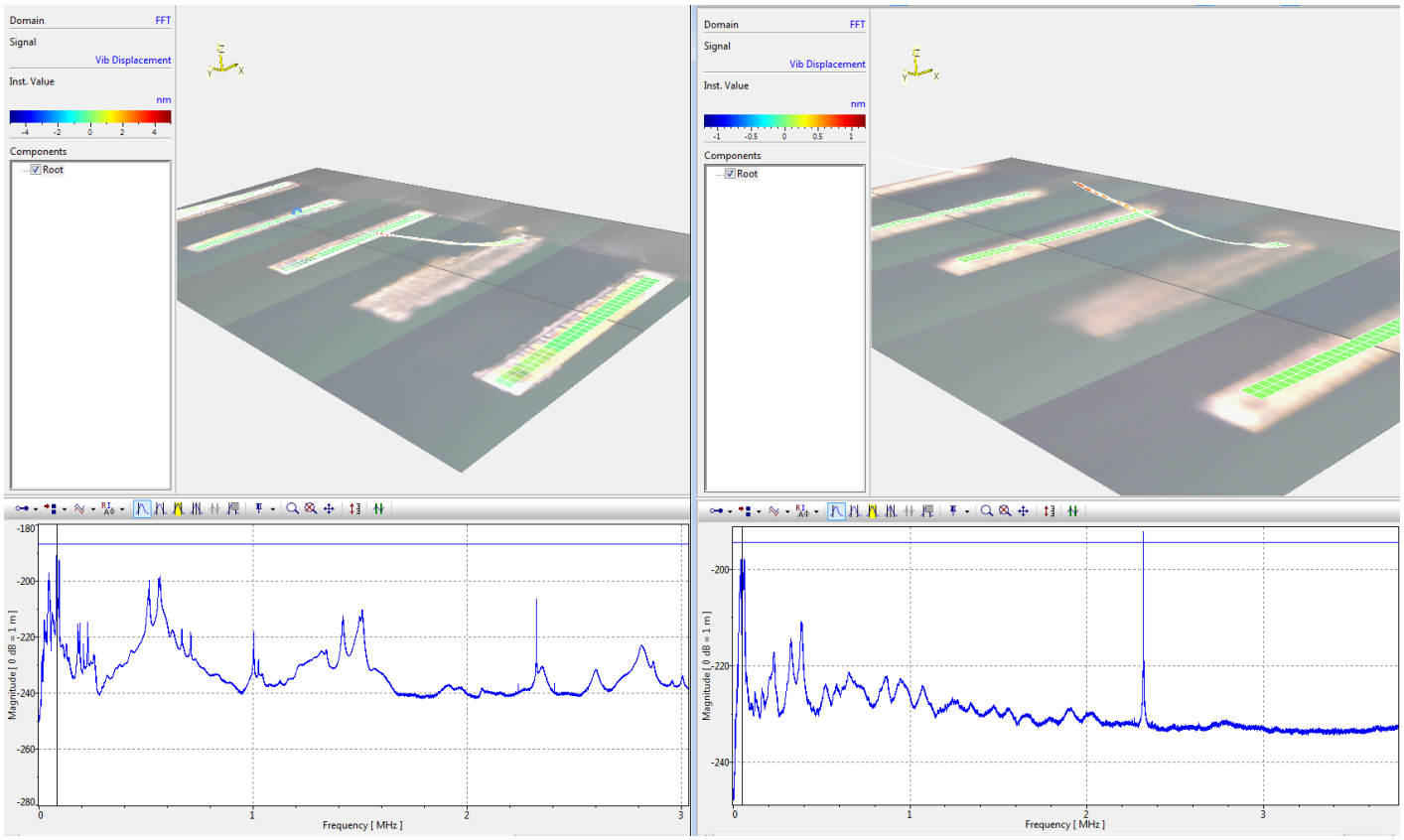

Figure 4.13: Comparative Resonance Analysis of Multi-beam Device: Air vs. Water Environments (First Mode in Air Vs Water with resonance frequencies 84Khz and 51Khz, respectively)

These visual interpretations are further supported by the frequency analysis charts below, which offer numerical data regarding the beams' resonance frequencies. The inherent frequency of vibrating structures at mode 1 is affected by the damping properties of the water medium and the added mass effect, which are responsible for the observed frequency shift from 84 kHz in air to 51 kHz in water.

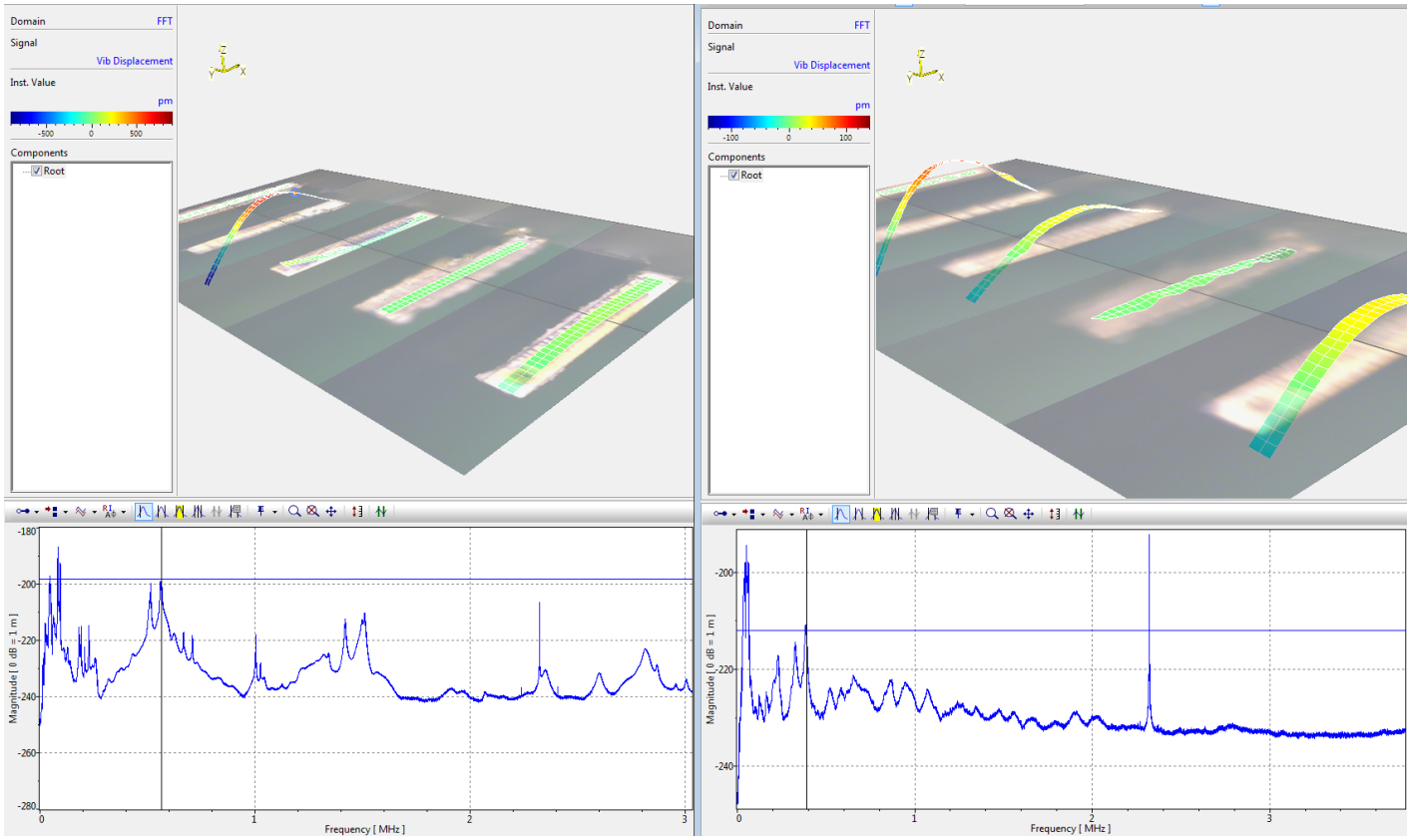

Figure 4.14: Flexional Mode 2 Resonance Shift Analysis: Multi-beam Device in Air vs. Water Environments (566Khz and 391Khz for Air and Water, respectively)

Figure 4.14 demonstrates the second flexional mode (Mode 2) of a five-beam device. It compares and contrasts the vibrational reactions in environments with and without water. The 3D depiction highlights the striking differences in vibrational characteristics between the air (left frame) and water (right frame), with the added mass effect and damping qualities of the water producing a muted vibrational pattern. The resonance frequency charts, which show a peak frequency shift from 566 kHz in air to 391 kHz in water, support this visual interpretation even more.

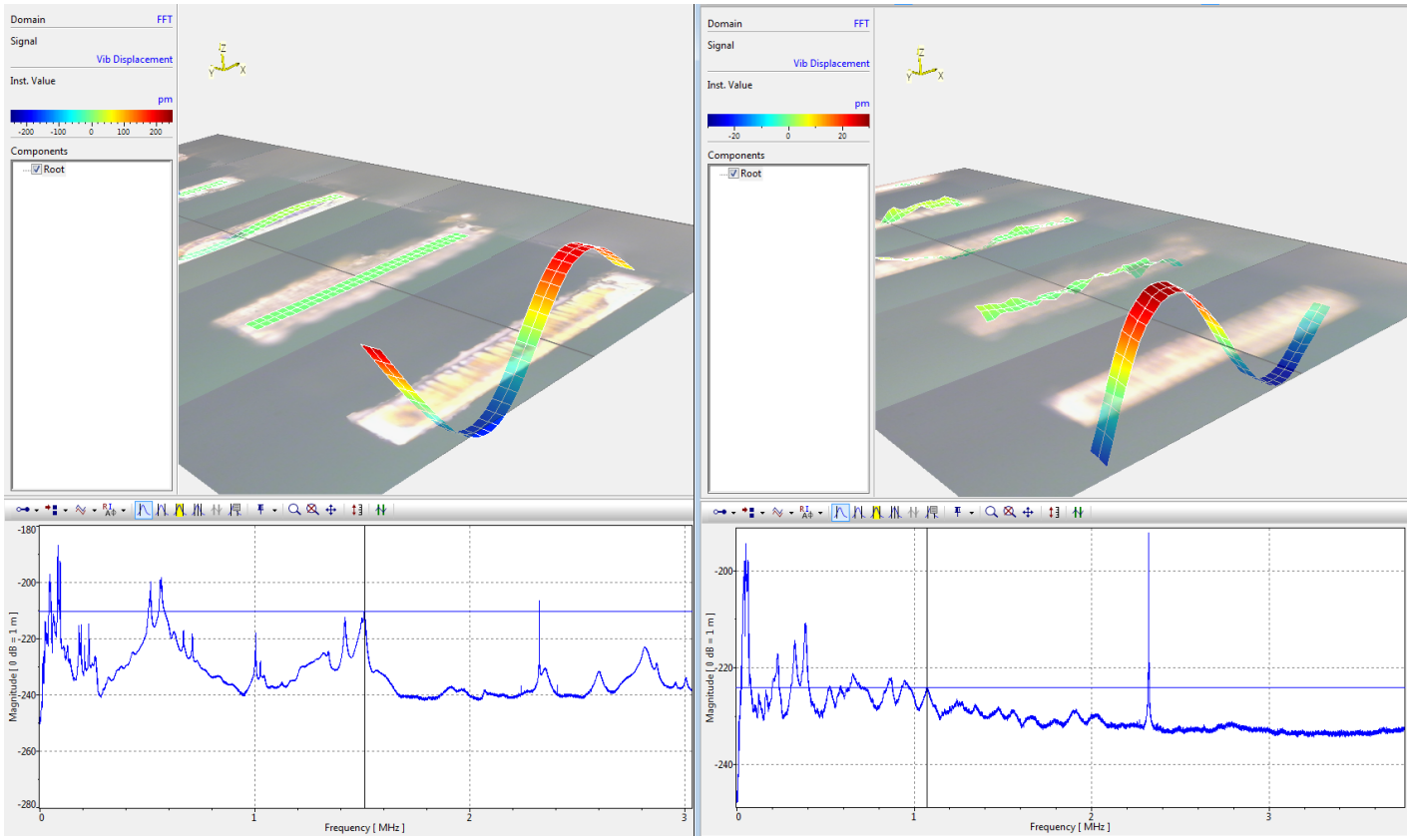

Figure 4.15: Third Flexional Mode Analysis: Resonance Shift of Multi-beam Device in Air and Water (1.509Mhz and 1.070 Mhz for Air and Water, respectively)

The figure 4.15, delineates a five-beam device in its third flexional mode, evident from the two nodal points on the beam. The three-dimensional illustrations contrast the vibrational patterns of water (right frame) and air (left frame). A characteristic flexional pattern with a larger amplitude is seen in the air environment. On the other hand, the amplitude decreases in the water environment, demonstrating the damping effect of water. These findings are further quantified by the frequency response charts, which identify a peak resonance frequency shift from 1.509 MHz in air to 1.070 MHz in water.

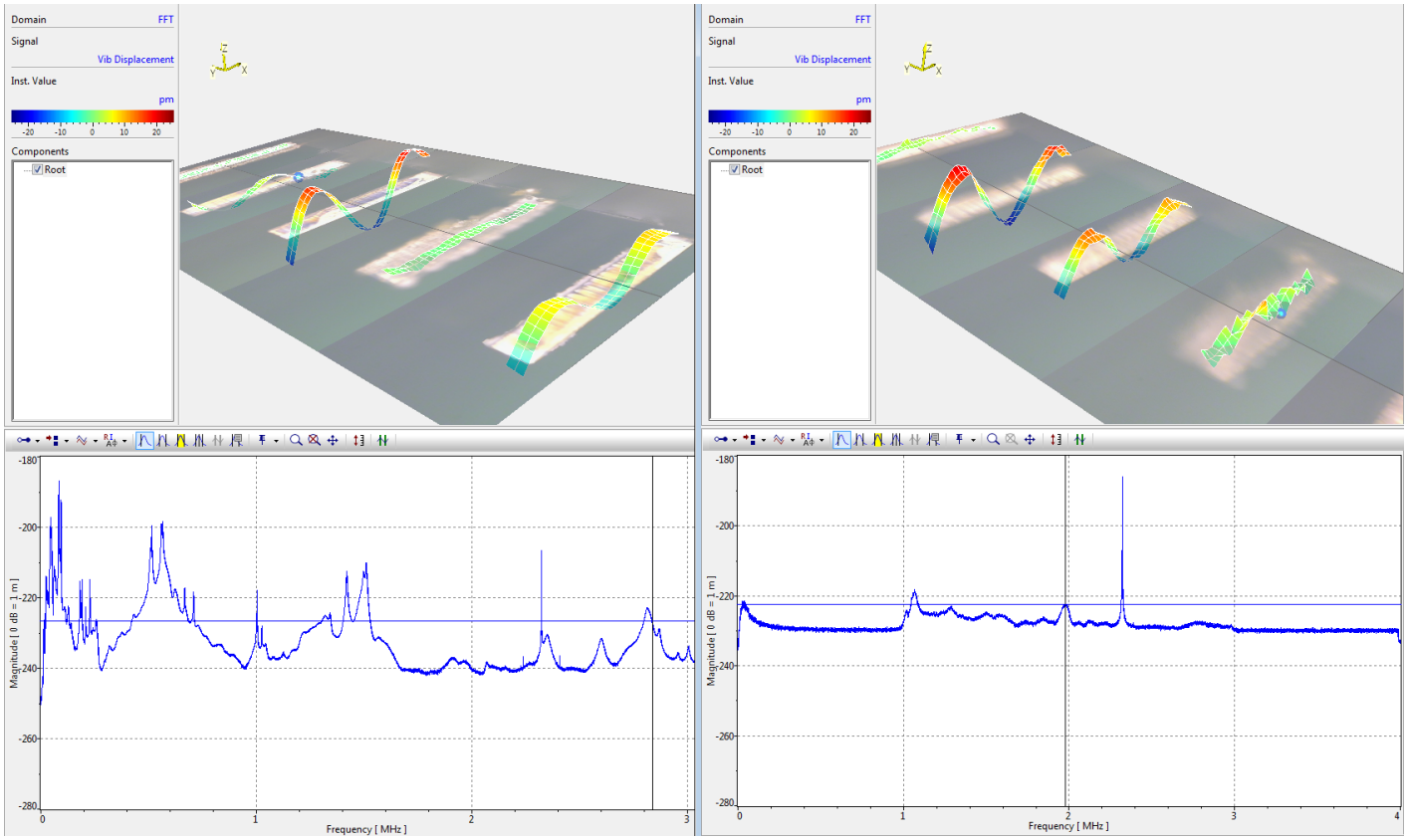

Figure 4.16: Fourth Flexional Mode Shift: Air to Water Frequency Transition in Multi-beam Device (2.834Mhz and 1.978 Mhz for Air and Water, respectively)

Lastly, Figure **??** demonstrates the fourth flexional of a five-beam device. The three nodal points on the beam clearly identify it as the fourth mode. The vibrational patterns in water (right frame) and air (left frame) are contrasted in the three-dimensional representations. A larger amplitude in the air indicates more flexibility and less resistance; however, in the water (right frame), the amplitude is noticeably reduced, highlighting the damping effect of the water. These visual observations are explained by the frequency response charts below, which show a shift of about 856 kHz from 2.834 MHz in air to 1.978 MHz in water.

It is impossible to overestimate the importance of experimental research in the study of cantilever microbeams. The scene was set by numerical simulations that predicted possible peak frequencies, interpreted mode shapes, and demonstrated the mutually beneficial relationship between beam vibrations and electric pulses on piezoelectric materials. These theoretical insights were validated in part by the ensuing experimental phase.

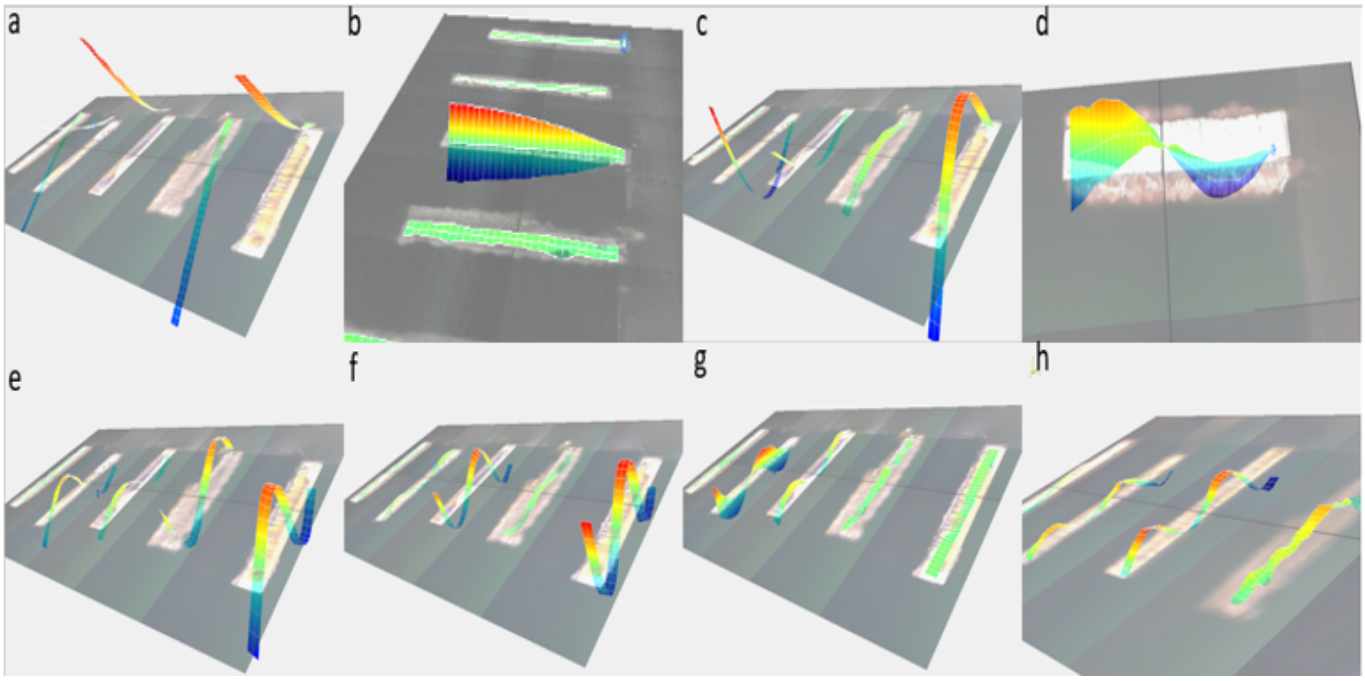

Figure 4.17: Depiction of the out-of-plane mode shapes observed during the experimental phase. Flexion bending mode shapes are encapsulated in sub-figures (a, c, e, f, and h), and torsion mode shapes in sub-figures (b, d, and g).

The different mode shapes were easily distinguished and identified after a careful analysis of the experimental data. The Figure 4.17 elucidates that the out-of-plane mode shapes were observed, a consequence of the inherent constraints of the vibrolaser, which is optimized for measuring displacements along the z-axis. The flexion bending mode shapes can be discerned in sub-figures a, c, e, f, and h of Figure 4.17. On the other hand, sub-figures b, d, and g represent the torsion mode shapes. We obtained observations over a wide frequency range (10 kHz–4 MHz) and identified eight different mode shapes from them. Our experimental design made it easier to go from numerical predictions to concrete experimentation, guaranteeing the precision of our results. The following sections provide a more thorough explanation of the techniques used, a thorough analysis of the results, and an interpretation of the relevance and effects of these mode shapes for the field of microbeam research.

4.3.2 Beam behavior under design

Dust aberration

According to Figure 4.18, the figure illustrates how dust can affect a beam's behavior, especially in torsion mode. Dust particles have the ability to affect the mechanical characteristics and behaviors of materials, particularly microscale components. According to the description given, the laser's thermal effects could cause localized "welding" in the presence of dust. This welding effect may cause the dust-ridden beam side to become fixed or restrained, impairing its ability to move correctly. On the other hand, unopposed torsional forces will cause the clean side on the other side to rotate or

flip.

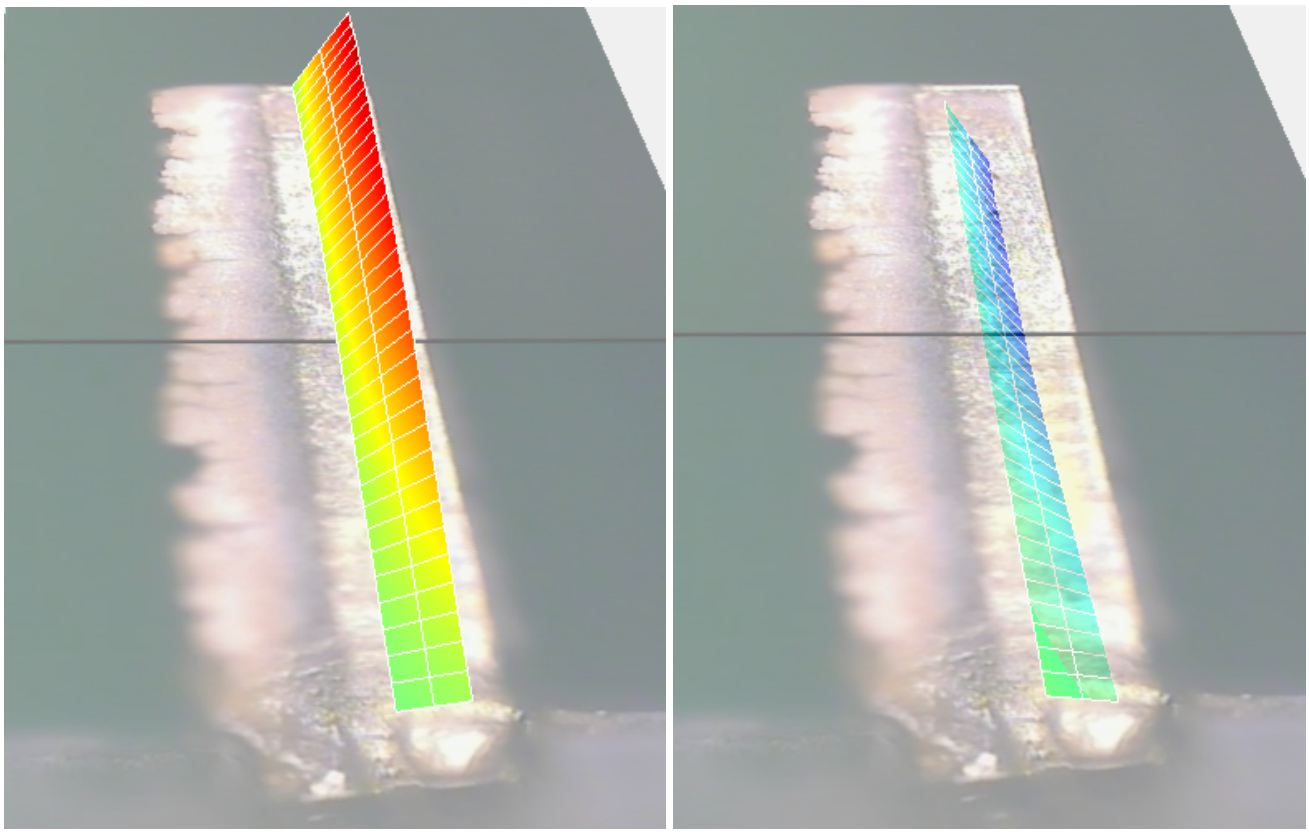

(a) (b)

Figure 4.18: Dust influence on torsion mode.

As was explained previously in the chapter with the images from the Scanning Electron Microscope (SEM), surface conditions have a big impact on how a material behaves. Traditionally, the presence of dust on the material as shown in Figure3.32 a result of the thermal effects of the laser—has been seen as a barrier. But this dust, with its natural porous morphology, could prove surprisingly useful. Increased interactions with the surrounding medium are made possible by this porous texture, which may result in new functionalities or better material qualities. Such a nuanced viewpoint changes our understanding because it allows us to view these surface irregularities as opportunities for creative applications and optimizations rather than as simple defects. This emphasizes how crucial it is to take advantage of these features, particularly when doing so can help a project or study achieve its larger objectives.

Effect of Spacing

The device depicted in Figure 3.38 consists of two beams. The aim with this design is to explain how the beam spacing affects the frequency coupling.

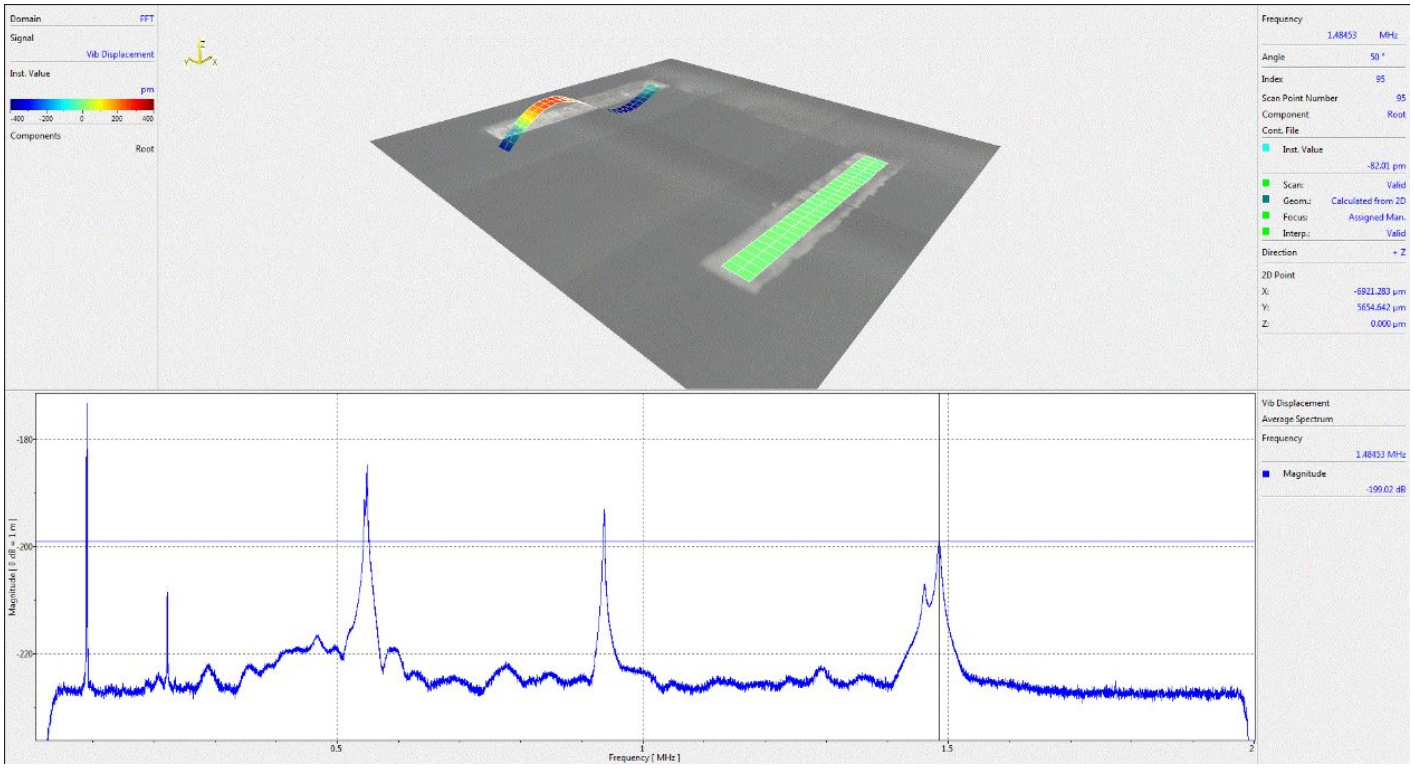

Figure 4.19: Spacing between the beams set at $800\mu m$

Upon examining Figure 4.19, presented in PSV Presentation softwar, it's apparent that there are two distinct peaks for each mode. Moreover, there is no apparent frequency coupling exists between the beams. This highlights the fact that every beam has a distinct peak frequency that is particular to its mode.

4.3.3 Physical affects of beams characterisation

After a thorough analysis of different beam devices, it has been found that the precision of results is positively impacted by an increase in the number of beams. The fact that not all beams need to operate in all harmonic modes leads to this conclusion. Over the course of our investigation, a few beams failed. After extensive testing, the device with the most beams, Device 5, consistently produced the clearest results. As a result, this particular device was chosen for calibration. The plan was to carefully examine every beam in Device 5 and select the one with the highest quality factor and maximum sensitivity. This criterion for selection was predicated on the notion that a beam of that type would exhibit all required harmonic mode shapes.

The methodology involved using a vibro laser to scan a set of 5 beams from Device 5 to record their responses post excitation by the electromechanical embedded element. As previously outlined, the frequency sweep ranged between 10kHz and 4MHz and utilized a voltage of chirp signal 7.5 volts. It was observed that the beam modes became less clear and masked after 3 MHz. With extreme caution, the voltage was maintained at a constant level to prevent any possible damage to the fragile beams. It is commonly known that these beams are unable to support high loads. After this scanning

process, the results are thoroughly discussed in the section that follows.

In Air

Air	Beam 1 (kHz)	Beam 2 (kHz)	Beam 3 (kHz)	Beam 4 (kHz)	Beam 5 (kHz)	Bending
Mode 1	93	84.25	93	96	83	flexion
Mode 2	207.25	191.75	227.25	228	182.5	lateral
Mode 3	559	515	561	566.25	508	flexion
Mode 4	1175	993	1000	1004	709	torsion
Mode 5	1509	1418	1513.7	1496	1342	flexion
Mode 6	2810	2150	2825.5	2772.5	2349	flexion
Mode 7	3002	2597.6	2955	2867.5	3160	torsion

Table 4.1: Vibration mode data for different beams in air

The table4.1 summarizes the experimental results accrued from frequency sweeps between 10kHz and 4MHz across a five-beam array, revealing seven distinct harmonic modes. Modes 1, 3, 5, and 6 are classified under the "flexion" category; Mode 2 represents "lateral" movement, whereas Modes 4 and 7 are termed as "torsion". A prominent trend is Beam 2's frequency, which consistently sits above that of Beam 3 but below Beam 1, indicating a potential hierarchy in beam stiffness. In contrast, Beams 4 and 5 display unique frequencies for Modes 4 and 5. Specifically, Beam 4 registers a dramatic drop in frequency for Mode 4 to 1kHz. Simultaneously, Beam 3 shows a pronounced frequency increase in Mode 5 when juxtaposed with its adjacent modes. The differences could be the result of inherent structural variations or variations in the materials used to make the beams, or they could be a sign of possible measurement errors. The table shows a consistent trend, as is common in vibrational analyses, where an increase in frequency values is followed by a rise in the mode number. It is important to remember that the array of five beams under investigation is the focus of this study, and the data clarifies the peak frequencies of each beam over the measured harmonic modes.

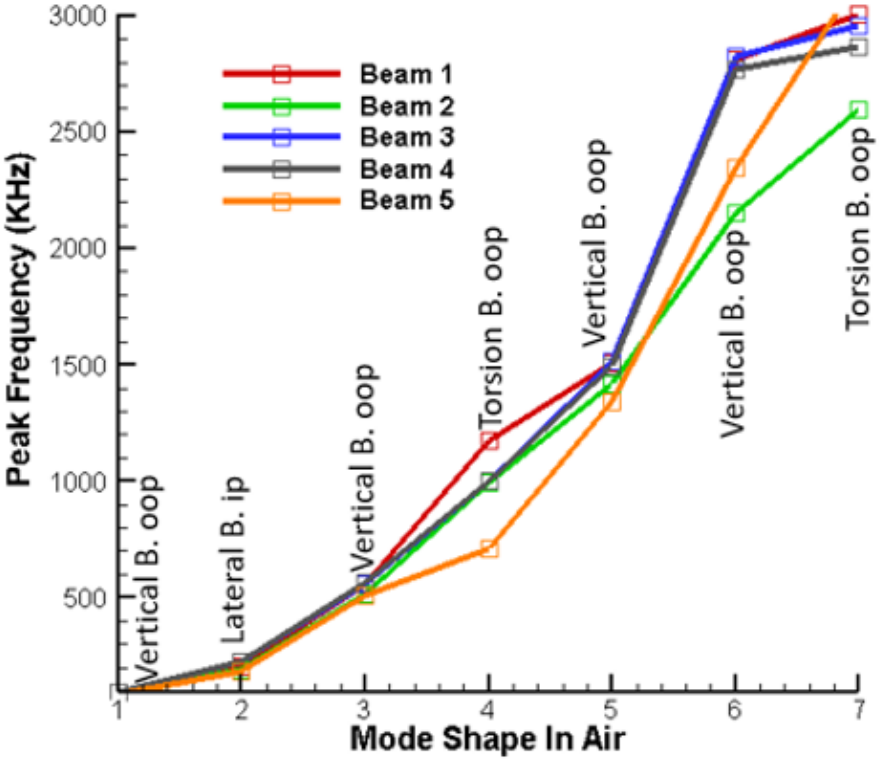

Figure 4.20: Mode shape Beams In Air

A graphical representation of the mode shapes of beams in air is depicted in Figure 4.20 below. This figure provides a visual understanding of the beam behavior and supports the trends and observations explained in the table.

In Fluid Surrounding

Water	Beam 1 (kHz)	Beam 2 (kHz)	Beam 3 (kHz)	Beam 4 (kHz)	Beam 5 (kHz)	Bending
Mode 1	62.25	50.55	64.2	64	51.33	Flexion
Mode 2	163	166.2	160.5	160	161	Lateral
Mode 3	385.6	323.5	384.75	389.25	324	Flexion
Mode 4	598	459	602	603	602	Lateral
Mode 5	1067.5	936	1068.5	1027	854	Flexion
Mode 6	2020	1798	1988.2	1888	1770	Flexion
Mode 7	3320	3250	3330	3310	3290	Flexion

Table 4.2: Vibration mode data for different beams in water

The study further investigated the vibrational behavior of beams when submerged in a fluidic environment, specifically in water. It was postulated that the surrounding fluid would impart a dampening effect, altering the natural frequencies of the beams. To validate this hypothesis, each beam was assessed under identical testing parameters, as previously utilized for the air trials.

The summarized vibrational data in Table 4.2 offers insights into the harmonic mode frequencies of beams when submerged in water. Just as observed in the air trials, Mode 1, Mode 3, Mode 5, Mode 6, and Mode 7 are categorized under the "Flexion" bending type, while Mode 2 and Mode 4 demonstrate "Lateral" motion. Interestingly, while the fluidic environment did lead to a general reduction in the recorded frequencies, the pattern and behavior of each beam relative to others remain congruent with the air trials.

Furthermore, the graphical representation of these modes is visualized in Figure 4.21. The curves elucidates the comparative mode shapes of the beams in water, enabling a tangible comparison of the beam frequencies in relation to each mode. Notably, the enveloped frequency trajectories reflect the dampening effects of the fluid medium, especially when juxtaposed against their counterparts in air, as depicted in Figure 4.20.

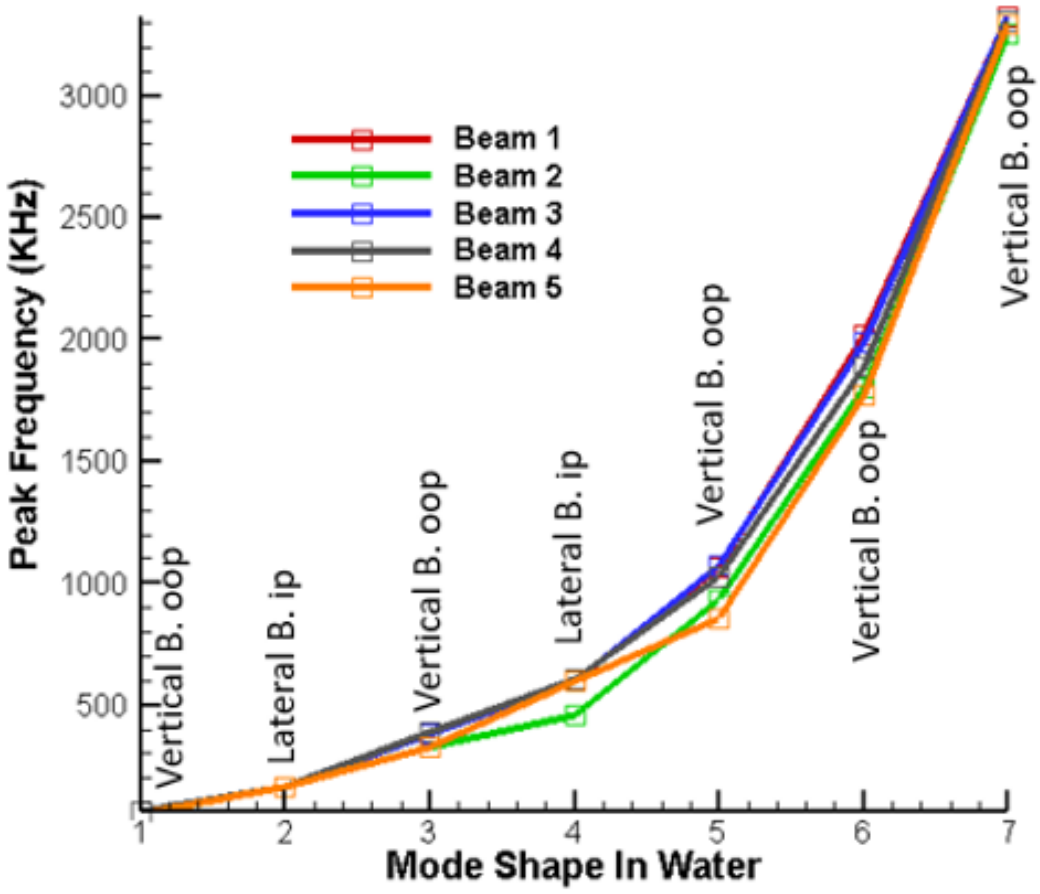

Figure 4.21: Beams In Water

Discussion

Beams, notably those from Device 5, showed significant differences in vibrational behavior in air and fluidic environments. Beams showed harmonic modes up to Mode 7 in both cases, but the frequency values of the water-filled beams were lower, probably as a result of the water's additional

mass and damping properties. Curiously, "Flexion," "Lateral," and "Torsion" mode shapes were displayed in beams in air, but the "Torsion" mode was clearly absent in water, indicating that water is resistant to rotational vibrations. This variation highlights the intrinsic properties of the beams as well as possible disparities brought about by inaccurate measurements or microstructural variations. The trajectory plots highlight the damping effect of water even more, particularly when considering the absence of the "Torsion" mode.

4.3.4 Quality Factor Evaluation

The quality factor, often denoted as Q, is a dimensionless parameter that characterizes the energy losses of a resonator. It is defined as:

$$Q = \frac{\left(\frac{4\rho_t s_i}{\pi \rho_{air} b}\right) + \Gamma_r(f,n)}{\Gamma_i(f,n)} \tag{4.1}$$

A higher value of Q indicates a lower rate of energy loss and a more narrow bandwidth.

The Quality Factor Of The Beam's in Air

Air	Beam 1	Beam 2	Beam 3	Beam 4	Beam 5	Bending
Mode 1	203.3	252.5	262	194.5	298	flexion
Mode 2	230.1	222.4	228.5	198.3	215.6	lateral
Mode 3	105.3	119	124.3	98.7	106.8	flexion
Mode 4	492.1	462.7	509.3	489.5	501.2	torsion
Mode 5	223.3	249.2	259.3	210.5	250.3	flexion
Mode 6	27.5	21.8	18.49	27.6	31.5	flexion
Mode 7	84.8	69.5	81.3	101.2	75.6	torsion

Table 4.3: Quality factor data for different beams in air

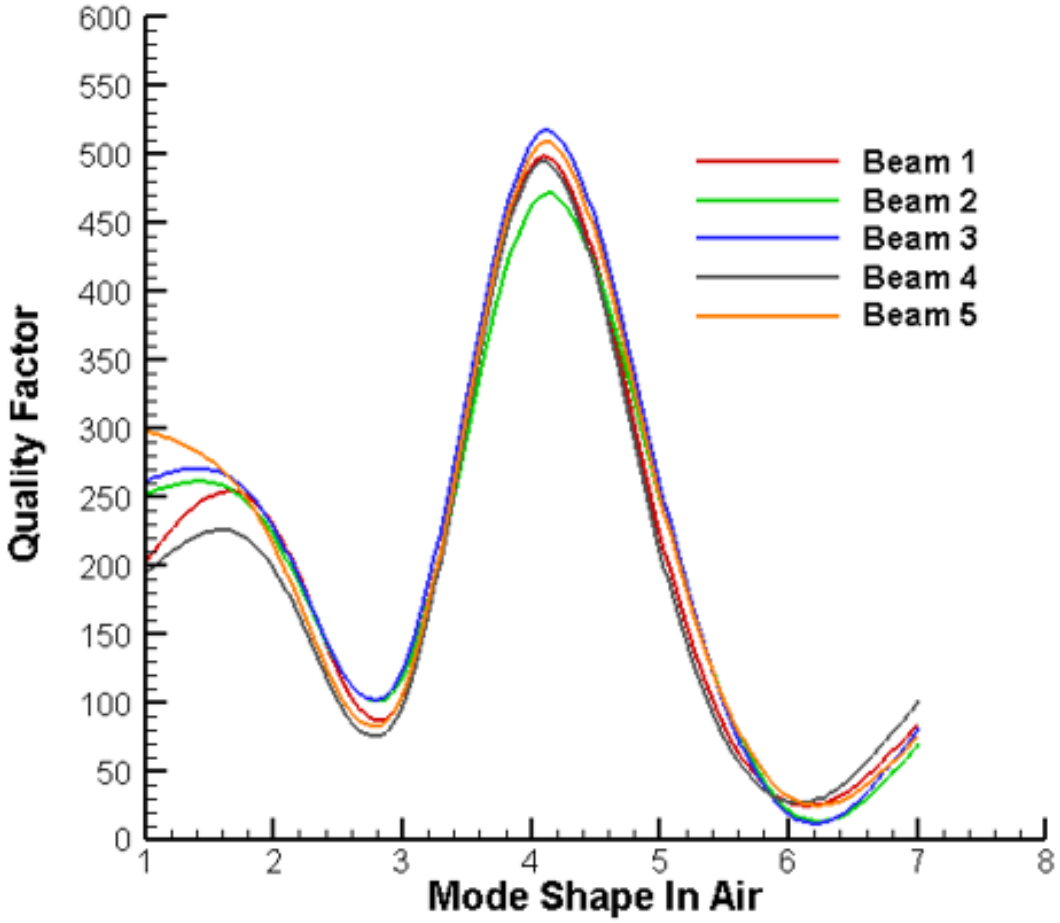

Figure 4.22: Quality Factor Air

Fig. 4.22 illustrates the quality factor (Q-factor) of five distinct beams across different mode shapes when exposed to air. The Q-factor indicates the extent of energy loss in resonators, where higher values suggest decreased energy losses and a more restricted bandwidth. Analyzing the graph and cross-referencing it with the accompanying table, several observations can be made. Beam 3, represented in blue, stands out by achieving the highest Q-factor during Mode 4, corresponding to torsion, with a precise Q-factor value of $Q = 509.3$, the peak among all beams for this mode. In the initial modes, Beam 3 consistently demonstrates superior Q-factor values but witnesses a decline beyond Mode 5. In contrast, Beam 5 begins with a prominent Q-factor in Mode 1, yet it eventually converges with other beams by Mode 7. Predominantly, modes such as Mode 1 (flexion), Mode 2 (lateral), Mode 4 (torsion), and Mode 5 (flexion) consistently record elevated Q-factors across all beams. However, Mode 6 consistently registers the lowest Q-factor values, with Beam 3's value dropping to its nadir at $Q = 18.49$. A discernible pattern emerges, with beams amplifying their Q-factor up to Mode 4, after which a decline is observed. Most beams reach their zenith at Mode 4, underscoring that torsion results in the least energy loss in this scenario. Beam 4 showcases a stable performance across modes, hovering around average values. However, Beam 3, while displaying top values in Modes 1 and 4, also portrays the lowest in Mode 6, emphasizing its variable performance. In essence, the Q-factor showcases variations across beams and mode shapes. Beam 3, especially in torsion, exhibits optimal

energy conservation properties, making it the foremost choice for applications where sensitivity is crucial.

The Quality Factor Of The Beam's in Water

Water	Beam 1	Beam 2	Beam 3	Beam 4	Beam 5	Bending
Mode 1	12.3	13.5	15.7	17.2	16.6	Flexion
Mode 2	11.8	13.1	10.93	8.1	10.5	Lateral
Mode 3	29.5	31.2	35.92	33.2	28.9	Flexion
Mode 4	10.5	12.3	9.38	7.2	10.32	Lateral
Mode 5	33.3	32.8	34.48	30.9	31.9	Flexion
Mode 6	31.2	32.5	36	35.3	32.7	Flexion
Mode 7	27.9	26.59	27.7	27.33	25.8	Flexion

Table 4.4: Quality factor data for different beams in water

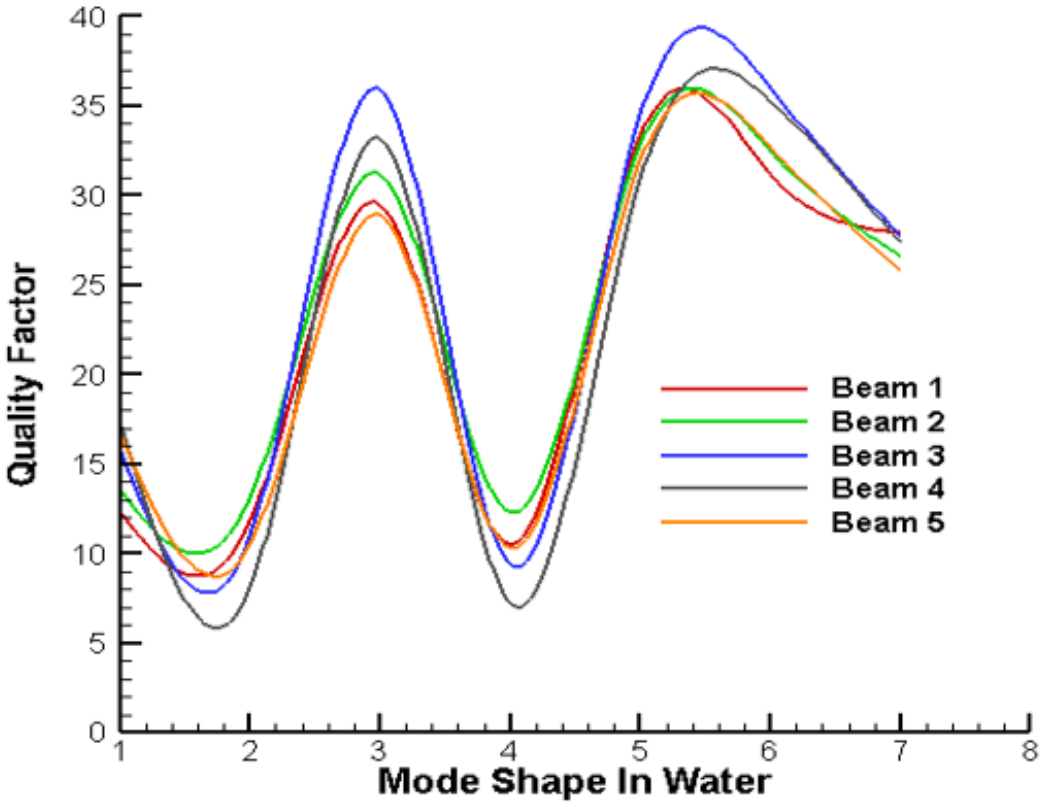

Figure 4.23: Quality Factor Water

Fig. 4.23 displays the quality factor (Q-factor) of five beams across different mode shapes in water. Compared to their performance in air, these beams manifest reduced Q-factor values in water, a phenomenon likely driven by the amplified damping effects of the aquatic environment. Beam 3,

highlighted in blue, excels by reaching its Q-factor zenith at $Q = 35.92$ during Mode 3, a flexion bending mode. This beam consistently outperforms others in most modes but slightly lags in Mode 2. Conversely, Beam 4 registers the lowest Q-factor for Mode 2, a lateral mode, at $Q = 8.1$. Beams 1 and 5 present analogous trends, yet their Q-factor magnitudes differ. Flexion modes, namely Modes 1, 3, 5, 6, and 7, recurrently exhibit higher Q-factors than their lateral counterparts, Modes 2 and 4, suggesting that beams in flexion modes are adept at minimizing energy loss in water. An overarching pattern discernible across the beams entails an uptrend in Q-factor values up to Mode 3, succeeded by a downturn and a subsequent ascent around Modes 5 and 6, with Mode 5 predominantly in the lead. Such oscillations potentially arise from the interplay between the beams' material attributes and the characteristics of water. Given Beam 3's remarkable Q-factor metrics, particularly in flexion modes, it is inferred to be the optimal choice for energy retention in aquatic settings, making it ideal for high-precision underwater operations. Collectively, the graphical representation and table synthesize the performance metrics of these beams, providing insights into their energy conservation capabilities in different bending configurations under water.

Discussion

The quality factors (Q-factors) of beams, in conjunction with their mode shapes, play an instrumental role in determining their energy conservation and sensitivity characteristics in different environments. Analyzing these factors, it becomes evident that different harmonic modes are optimally suited for different mediums, thereby underscoring the critical interplay between a beam's mode shape and its surrounding environment.

The torsion mode shape in air, corresponding to the fourth harmonic mode, appears to be the most ideal for obtaining high sensitivity, according to the data. The strong Q-factor values found for beams in this mode serve as proof of this. In the fourth harmonic mode, Beam 3, for example, has a Q-factor value of Q = 509.3, demonstrating the improved energy-saving properties of beams during torsional movements in an airborne setting. The higher Q-factor values, which indicate lower energy losses, suggest that the torsion mode is more effective at reducing energy dissipation in air. These findings highlight the fact that beams operating in the 4th harmonic torsional mode are the most promising options for applications requiring increased sensitivity in an aerial setting. On the other hand, when it comes to maximizing sensitivity in water, the vertical mode shape—which corresponds to the fifth harmonic mode—comes to light. The high Q-factor values corresponding to beams operating in this mode support this claim. For example, Beam 3 achieves excellent Q-factor metrics in the 5th harmonic mode despite the surrounding medium being water, which is known to have amplifying damping effects. The beams' remarkable performance metrics highlight their ability to reduce energy loss during vertical movements in water. Because the vertical mode is more common in water, beams operating in the 5th harmonic vertical mode have the best chances for underwater applications where high sensitivity is critical.

4.3.5 Sensitivity in Terms of density and viscosity variation

The process of combining water with glycerol is performed using a magnetic stirrer, which is captured in a series of three stages. Initially, a 600ml beaker, half-filled with 300ml of the water and glycerol mixture, is placed on the stirrer. Upon activating the stirrer, the liquid medium is mixed for about five minutes. This continuous stirring leads to a homogeneous mixture, evidenced by the uniform appearance of the solution with no visible separation between the water and glycerol components.

Mixture	**Density (g/cm^3)**	**Viscosity (Pa.s)**
300 ml of water	1	1×10^{-3}
300 ml of water + 30g of NaCl	1.165	1×10^{-3}
300 ml of ethanol	0.789	1.1×10^{-3}
270 ml of water + 30 ml of glycerol	1.026	0.149
225 ml of water + 75 ml of glycerol	1.065	0.3725
150 ml of water + 150 ml of glycerol	1.13	0.7445

Table 4.5: Density and viscosity measurements of various mixtures

The mixtures produced exhibit varying densities and viscosities, as shown in Tab. 4.5. Additionally, the viscosities of the first three mixtures are nearly the same regardless of having different densities. The latter three, on the other hand, show varying viscosities but relatively stable densities.

A uniform solution is ensured by this thorough mixing. By examining this, one can gain insight into how the mixture's density and viscosity affect beam 3's sensitivity, particularly with regard to frequency shifts. These experiments have yielded important insights into the behavior of the beam in a variety of fluidic environments. These results may have an impact on designs and applications in the future when similar beams are used in comparable situations.

Based on the quality factor results discussed in the previous section, we have chosen beam 3 of device 5 to calibrate the sensor in rheological terms. Beam 3 exhibited the best quality factor and showed a presence for all harmonic modes. The table 4.6 lists the harmonic modes of beam 3 along with their peak frequencies in air.

3rd Beam Mode Shape	**Peak Frequencies in Air (kHz)**
Mode 1 (1st Mode of Flexion)	93
Mode 2 (1st Mode of Lateral)	227.25
Mode 3 (2nd Mode of Flexion)	561
Mode 4 (1st Mode of Torsion)	1004
Mode 5 (3rd Mode of Flexion)	1513.7
Mode 6 (4th Mode of Flexion)	2825.5
Mode 7 (2nd Mode of Torsion)	3003

Table 4.6: Mode shapes and their corresponding peak frequencies in air for Beam 3

We began our viscosity and density study to investigate the beam's sensitivity to changes in density and viscosity. We identified 7 modes, and we need to select the most suitable mode in a fluid medium based on the greatest frequency shift, while also considering the quality factor and the mode shape. For each test we will conduct, by preparing a 300ml mixture to be able to immerse the entire structure in the fluid mixture, as shown in the figure (Figure 4.12: Laser-Assisted Underwater Analysis of Microbeam Vibrations). Consequently, we prepared mixtures as indicated in the table (Table 4.5: Density and viscosity measurements of various mixtures). Measurements were taken with the LDV-UHF-120 vibro-laser. We scanned the beam with the laser at multiple points. The estimated time to scan the entire beam is about 20 minutes. It takes a considerable amount of time because when the laser moves from one scanning point to another, we must wait for the fluid medium to stabilize to obtain a clear and perfect reflection for the signal since we are working in a Newtonian fluid.

	3rd Beam Mode Shape						
Medium (300ml)	**Mode 1**	**Mode 2**	**Mode 3**	**Mode 4**	**Mode 5**	**Mode 6**	**Mode 7**
100% Ethanol	66	205	408.75	841.25	1090	2682	3740
100% Water	64.2	202	384.75	678	1068.5	1988.2	3330
100% Water with 30g of Nacl	61.8	201.8	378	659.3	1072.8	1953.5	3290
90% Water 10% Glycerol	60.75	187	360.5	626.5	1029	1839	3230
80%Water 20% Glycerol	56	170	339	592.5	955	1700	3110
50%Water 50% Glycerol	44	123	294.25	499.75	841	1404	2820

Table 4.7: Mode shape data for the Beam 3 in different mediums

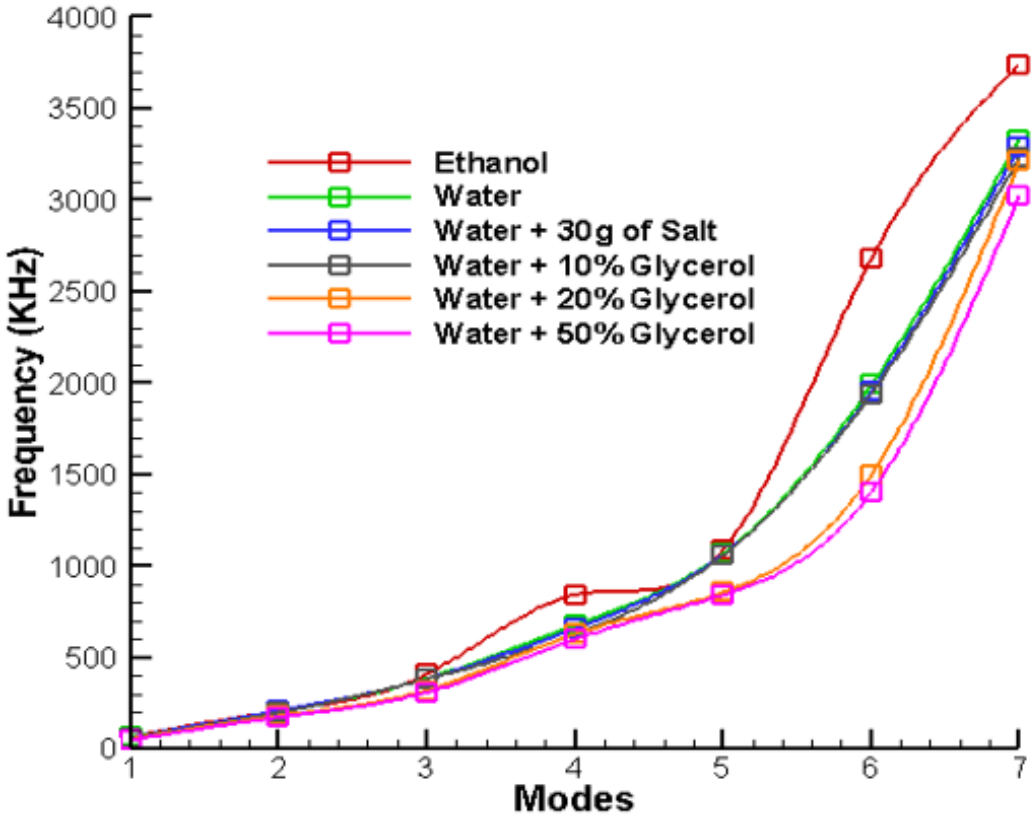

Figure 4.24: Frequency Shift for each Harmonic Modes

The table 4.7 showcases the peak frequencies of the 3rd Beam Mode Shape across various mediums. An observation of these outcomes, particularly when employing water as the standard, elucidates the beam's sensitivity to alterations in medium viscosity and density. The graph in Figure 4.24 depicts the frequency of harmonic modes across various fluids with different densities and viscosities. As the mode number increases, so does the frequency, indicative of the natural progression of harmonic modes. Ethanol, with its lower viscosity and density, shows a sharper increase in frequency, underscoring the influence of fluid physical properties on vibrational characteristics. The addition of salt to water and the incorporation of glycerol in varying percentages elevate the density and viscosity, resulting in a corresponding shift to higher frequencies. This shift evidences the direct correlation between the physical attributes of fluids and the energy required to sustain vibrational modes. The quality factor, although not depicted, plays a crucial role in defining the resonance sharpness and energy dissipation within the system. Higher quality factors would result in more pronounced frequency shifts and clearer distinctions between modes. The last proper harmonic mode, appearing without coupling at higher frequencies, represents the most unadulterated vibrational state before harmonic overlap ensues. This comprehensive analysis demonstrates the intricate balance between fluid characteristics, vibrational energy, and harmonic clarity, culminating in the distinct frequency patterns observed in the graph.

4.4 Analysis of Frequency band Shifting

- **Density variation relating to the shifting frequency**:

  The graphical representation in Figure 4.25 highlights amplitude variations over a frequency range from 10 kHz to 2 MHz for three mediums: Air, Water, and Water with Salt. Zones 'a' through 'e' depict mode shapes 1 to 5 achieved in the frequency sweep. Zone 'a', representing the fundamental mode, shows a marked shift in frequencies, with the blue line (Air) as a benchmark. Comparing it to the red (Water) and yellow (Water with Salt) lines, distinct amplitude and frequency variations are evident. Specifically, the amplitude in dB for the water medium deviates from that in air, and the addition of salt amplifies this difference. Similarly, frequency shifts in zone 'a' are evident when comparing the water-based mediums to air. Progressing to higher mode shapes, from zones 'b' to 'e', the peak shifts become more noticeable, growing pronounced with increasing mode number. This shifting intensity, especially against the backdrop of air, underscores the mediums' critical role in influencing frequency and amplitude. Such insights into the frequency-amplitude dynamics across various mediums are crucial for applications requiring meticulous control over these parameters.

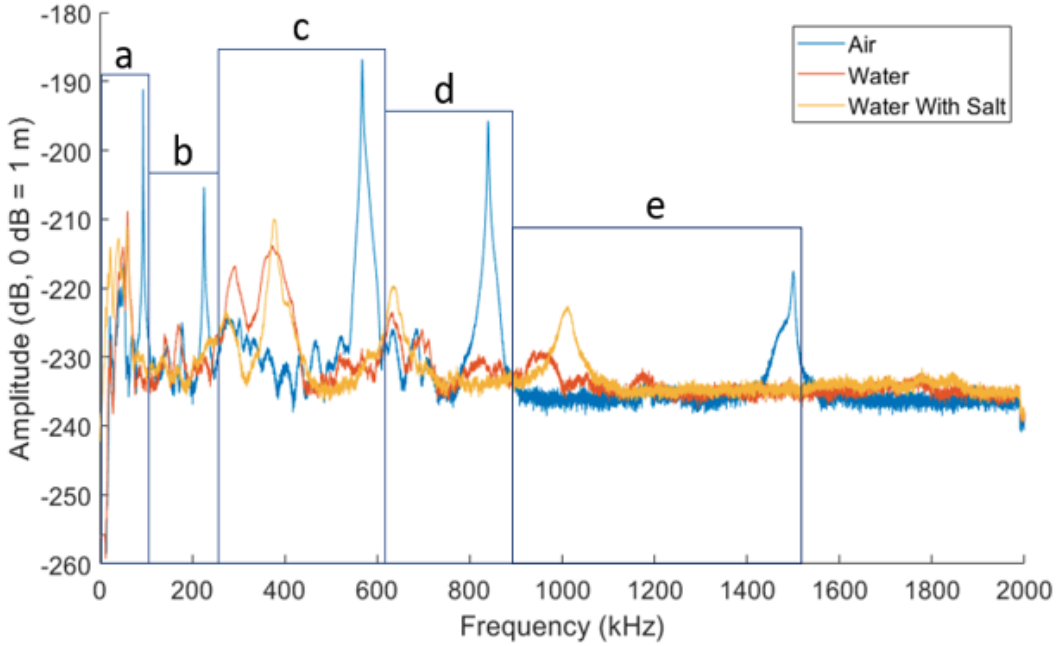

Figure 4.25: Amplitude and Frequency Variations Across Different Mediums: A Comparative Analysis from 10 kHz to 2 MHz

1. **Water with 10% of NaCl vs. Pure Water vs. Air:** Introducing salt augments the density of water without considerably transforming its viscosity. When contrasting the peak frequencies in pure water and salted water, we discern a conspicuous shift in frequency across all modes. This variation implies a direct correlation between the medium's density and the resonance frequency of the beam.

2. **Ethanol vs. Air:** Even though ethanol and water share akin viscosity's, ethanol possesses a lesser density than water. The data suggests that when the density diminishes (as observed in ethanol), the peak frequencies correspondingly recede across all modes.

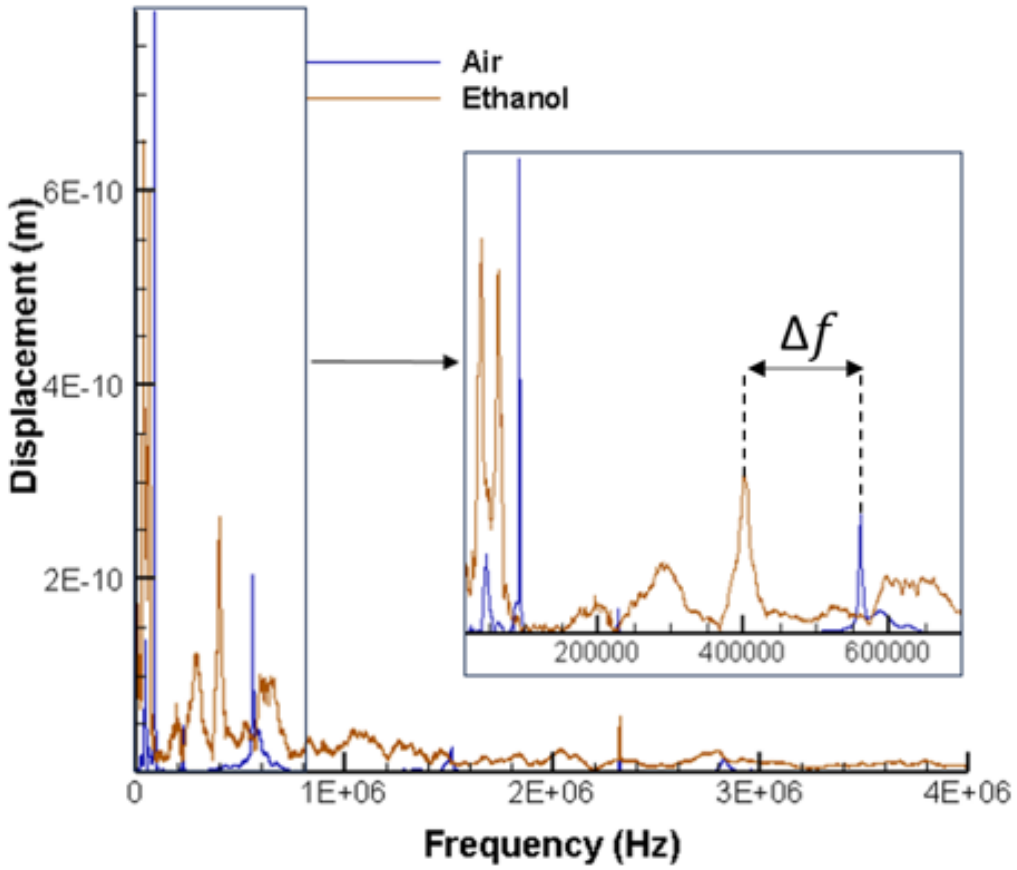

Figure 4.26: Displacement Variations in Air and Ethanol over a Specified Frequency Range

The graphical representation in Figure 4.26 showcases the displacement measurements for two mediums: Air and Ethanol, over a specified frequency range.

From the figure, one can readily discern a pronounced frequency shift, particularly for the third mode, which corresponds to the second flexural mode. The Air, represented by the blue line, can be used as a reference. Upon juxtaposition of this curve with the one representing Ethanol (orange line), the frequency shift or '*décalage fréquentiel*' becomes evident.

This noticeable shift emphasizes the varying vibrational characteristics the sensor undergoes when transitioning from a medium like air to a denser medium like ethanol. Such observations could have significant implications, especially in applications requiring precise frequency measurements in different mediums.

Discussion

For harmonic mode 3 (the second flexion mode shape):

1. Frequency for 100% Ethanol: 408.75kHz
2. Frequency for 100% Water: 384.75kHz
3. Frequency for 100% Water with 30g of NaCl: 378kHz

From the second table:

1. Density of 100% Ethanol: 0.789g/cm^3
2. Density of 100% Water: 1g/cm^3
3. Density of 100% Water with 30g of NaCl: 1.165g/cm^3

Now, let's compute the frequency and density differences:

$$\begin{aligned}
\Delta f_{\text{Ethanol-Water}} &= 408.75 - 384.75 = 24\text{kHz} \\
\Delta f_{\text{SaltedWater-Water}} &= 378 - 384.75 = -6.75\text{kHz} \\
\Delta \rho_{\text{Ethanol-Water}} &= 0.789 - 1 = -0.211\text{g/cm}^3 \\
\Delta \rho_{\text{SaltedWater-Water}} &= 1.165 - 1 = 0.165\text{g/cm}^3
\end{aligned}$$

For a density change of -0.211g/cm^3, the frequency changes by 24kHz. For a density change of 0.165g/cm^3, the frequency changes by -6.75kHz.

To establish a definitive relationship or check its linearity, a detailed analysis incorporating material properties and boundary conditions, and potentially a linear regression on a larger dataset would be necessary.

- **Viscosity variation relating to the shifting frequency**:

  1. **Water-Glycerol Mixtures vs. Pure Water:** For this segment, the table conveys data for three concoctions:
     - 90% Water & 10% Glycerol
     - 80% Water & 20% Glycerol
     - 50% Water & 50% Glycerol

With these mixtures, the fraction of glycerol escalates while maintaining the aggregate volume at 300ml constant. Owing to its pronounced viscosity, the overall viscosity of the medium surges as the proportion of glycerol swells.

Contrasting the peak frequencies of the concoctions against pure water reveals an unambiguous downward trend in frequencies across all modes with the escalation in viscosity. This indicates that an ascent in viscosity (while preserving the density relatively stable) leads to a descent in the beam's resonance frequencies.

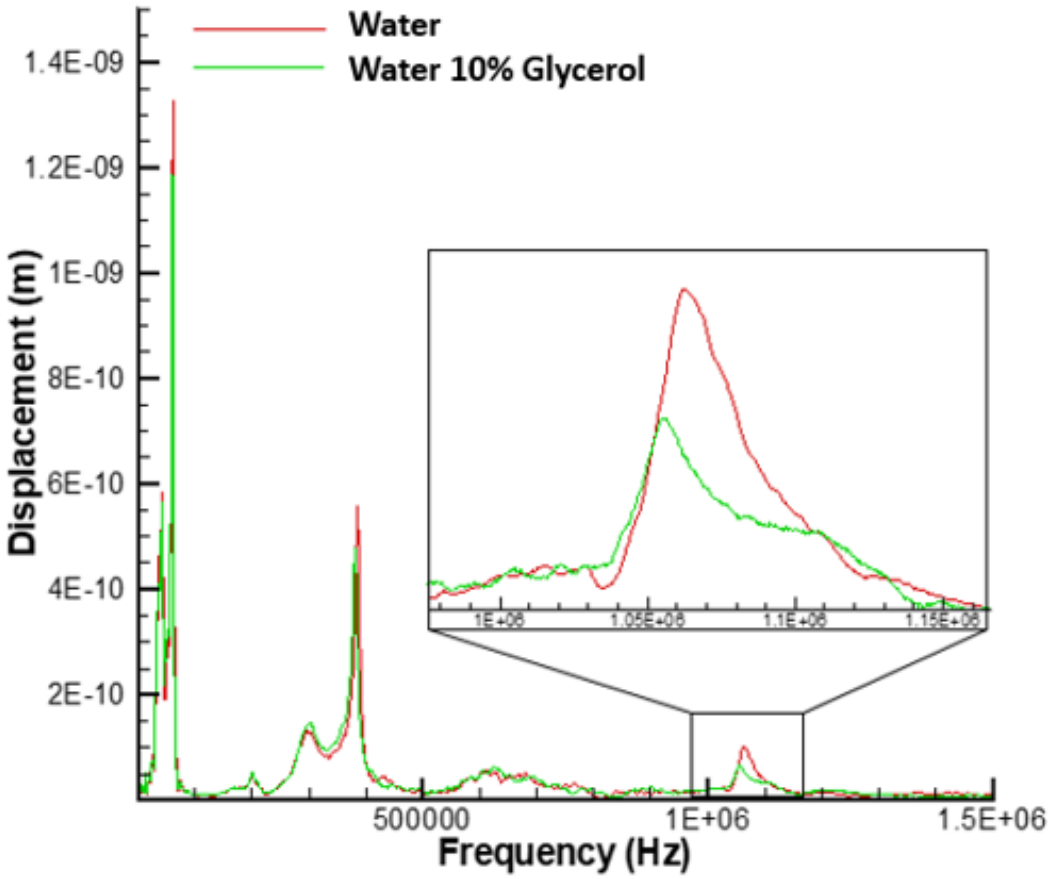

Figure 4.27: Frequency Shift by variation of 25% of Viscosity On the Third mode of Flexion Bending

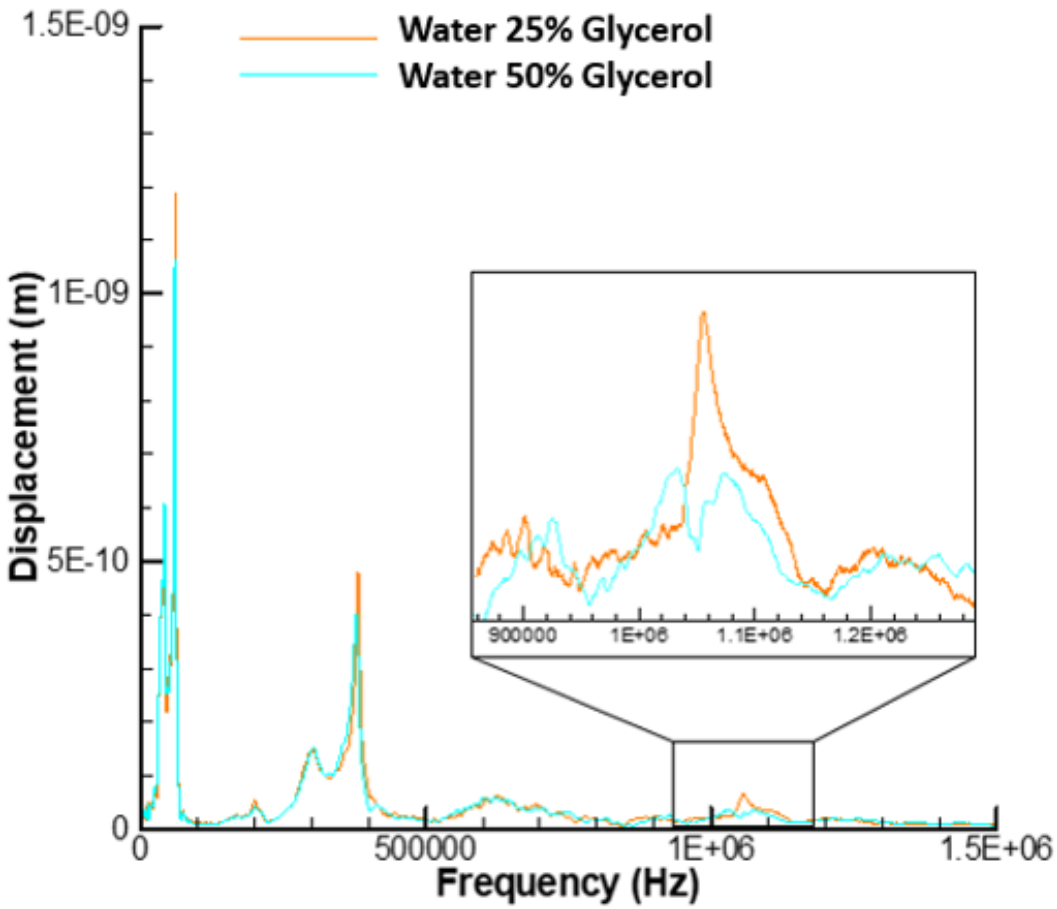

Figure 4.28: Frequency Shift by variation of 25% of Viscosity On the Third mode of Flexion Bending

Discussion

To determine the relationship between the shift in frequency and viscosity, the difference in frequency and viscosity for the mixtures can be computed:

$$\Delta f_{10\%-20\%} = 1029 - 955 = 74\text{kHz}$$
$$\Delta f_{10\%-50\%} = 1029 - 841 = 188\text{kHz}$$
$$\Delta f_{20\%-50\%} = 955 - 841 = 114\text{kHz}$$

$$\Delta \eta_{10\%-20\%} = 0.149 - 0.3725 = -0.2235\text{Pa.s}$$
$$\Delta \eta_{10\%-50\%} = 0.149 - 0.7445 = -0.5955\text{Pa.s}$$
$$\Delta \eta_{20\%-50\%} = 0.3725 - 0.7445 = -0.372\text{Pa.s}$$

To establish a definitive relationship or check its linearity, a detailed analysis with material prop-

erties, boundary conditions, and potentially a linear regression on the data-set would be necessary.

4.4.1 Sensitivity

The beam's susceptibility to variations in the attributes of the medium is apparent. Augmenting the density typically results in a dip in the resonance frequencies, as demonstrated by the infusion of salt into water. Similarly, elevating the viscosity, illustrated by the inclusion of glycerol to water, also induces a decline in the resonance frequencies. These observations stress the significance of discerning the behavior of the beam in multifarious mediums, especially if it's to be deployed in fluctuating environmental circumstances or for bespoke applications wherein the properties of the medium might undergo alterations. Effect of Density and Viscosity: The decrease in frequencies when transitioning from ethanol to water and then to water-glycerol mixtures suggests the influence of fluid density and viscosity on the resonant frequencies. As glycerol is added, the mixture's viscosity and with approximately the same density , leading to a decrease in frequencies.

Given the table, we're asked to understand the sensitivity of the sensor for each 1 kHz change in relation to the density and viscosity changes.

1. **Sensitivity to Density**:

   For the mediums of Ethanol and Water+Salt, we can calculate the sensitivity of the sensor in terms of the change in density for each 1 kHz shift in frequency.

   - **Ethanol**: Change in density (Δd) is approximately -0.211 g/cm^3, and the corresponding frequency shift (Δf) is -21 kHz. Therefore, the sensitivity of the sensor with respect to density based on the ethanol test is:

   $$\text{Sensitivity}_{\text{Ethanol}} = \frac{\Delta d}{\Delta f} \approx \frac{-0.211}{-21} \approx 0.01 \text{ g/cm}^3/\text{kHz}$$

   - **Water + Salt**: Change in density (Δd) is greater than 0.165 g/cm^3 for a frequency shift (Δf) of 16.2 kHz. Therefore, the minimum sensitivity of the sensor with respect to density based on the water+salt test is:

   $$\text{Sensitivity}_{\text{Water+Salt}} = \frac{\Delta d}{\Delta f} \approx \frac{0.165}{16.2} \approx 0.0102 \text{ g/cm}^3/\text{kHz}$$

2. **Sensitivity to Viscosity**:

   For the mediums with glycerol (10%, 25%, and 50%), we can calculate the sensitivity of the sensor in terms of the change in viscosity for each 1 kHz shift in frequency.

   - **10% Glycerol**: Change in viscosity (Δv) is 0.148 Pa.s, and the corresponding frequency shift (Δf) is 39.7 kHz. Therefore, the sensitivity of the sensor with respect to viscosity

based on the 10% glycerol test is:

$$\text{Sensitivity}_{10\%\,\text{Glycerol}} = \frac{\Delta v}{\Delta f} \approx \frac{0.148}{39.7} \approx 0.0037\ \text{Pa.s/kHz}$$

- **25% Glycerol**: Change in viscosity (Δv) is 0.371 Pa.s, and the corresponding frequency shift (Δf) is 113.5 kHz. Therefore, the sensitivity of the sensor with respect to viscosity based on the 25% glycerol test is:

$$\text{Sensitivity}_{25\%\,\text{Glycerol}} = \frac{\Delta v}{\Delta f} \approx \frac{0.371}{113.5} \approx 0.0033\ \text{Pa.s/kHz}$$

- **50% Glycerol**: Change in viscosity (Δv) is 0.7435 Pa.s, and the corresponding frequency shift (Δf) is 227.5 kHz. Therefore, the sensitivity of the sensor with respect to viscosity based on the 50% glycerol test is:

$$\text{Sensitivity}_{50\%\,\text{Glycerol}} = \frac{\Delta v}{\Delta f} \approx \frac{0.7435}{227.5} \approx 0.0033\ \text{Pa.s/kHz}$$

In summary:

- The sensor has a density sensitivity in the range of $0.01 - 0.0102\ \text{g/cm}^3\text{/kHz}$ based on the tests with ethanol and water+salt.
- The sensor has a viscosity sensitivity of approximately $3.3 \times 10^{-3} - 3.7 \times 10^{-3}$ Pa.s/kHz based on the tests with varying glycerol concentrations.

Note: The values calculated are approximations based on the provided data. Actual sensitivity may vary based on experimental conditions, calibration, and other factors.

Medium	**3rd Beam Δf(kHz) in mode 5**
Air	-445.2
Ethanol	$-21.$
Water	0
Water + Salt	16.2
Water +10% Glycerol	39.7
Water +25% Glycerol	113.5
Water +50% Glycerol	227.5

Table 4.8: Frequency deviation (Δf) in mode 5 of the third beam for different mediums

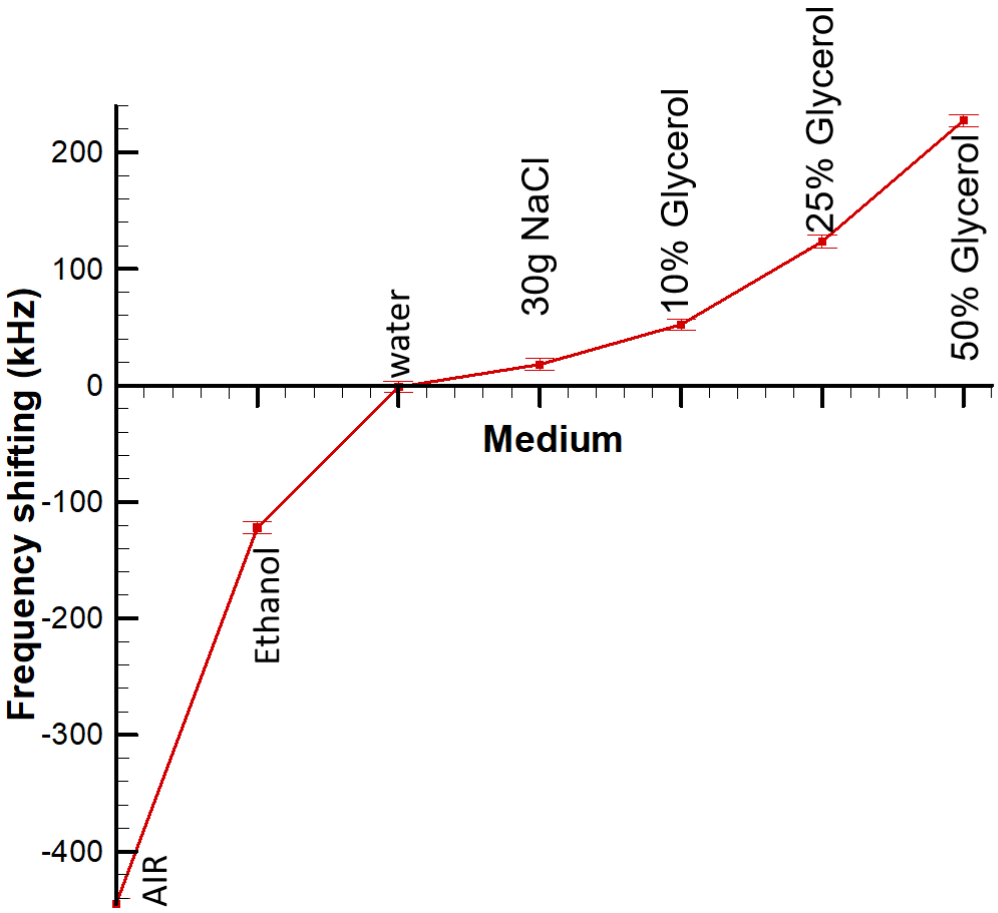

Figure 4.29: Delta f For The third Beam

Medium	Δd**Density (g/cm^3)**	Δv**Visc. (Pa.s)**	Δf **in Mode 5 (kHz)**
Air	—	—	-445.2
Ethanol	≈ -0.211	—	$-21.$
Water	0	0	0
Water + Salt	> 0.165	—	16.2
10% Glycerol	—	0.148	39.7
25% Glycerol	—	0.371	113.5
50% Glycerol	—	0.7435	227.5

Table 4.9: Density, Viscosity, and Frequency Shift for Various Mediums.

Trend across Modes: Across all mediums, the frequencies increase from Mode 1 to Mode 7. However, the rate of increase isn't constant; the differences between consecutive modes vary.

Medium-wise Comparison: For the same mode, frequencies in ethanol are higher than in water, and those in water are generally higher than in water-glycerol mixtures. The presence of salt in water slightly reduces the resonant frequencies compared to pure water.

Discussion

To analyze the data, we need to split the mediums into two categories based on your description: Constant Viscosity & Varying Density (First three mixtures): Ethanol, Water, and Water with salt. Varying Viscosity & Constant Density (Last three mixtures): Water with 10% Glycerol, Water with 25% Glycerol, and Water with 50% Glycerol. Constant Viscosity & Varying Density: Looking at the second table, we observe that the viscosities of these three mediums are approximately the same order of magnitude , but their densities vary. As we progress from Ethanol (least dense) to Water with salt (most dense), the frequencies across all mode shapes decrease. This suggests that as the density of the medium increases, the resonant frequencies tend to decrease. The frequency drop from Ethanol to Water is more pronounced in higher modes (Mode 4 onwards). For instance, for Mode 7, the frequency difference is a substantial 410 kHz between Ethanol and Water. Varying Viscosity & Constant Density: For these mixtures, the density is approximately constant (around 1 g/cm3), but the viscosity changes with the addition of glycerol. As we increase the glycerol content (and consequently increase the viscosity), there's a consistent decrease in frequencies across all mode shapes. The effect of viscosity is more pronounced in the higher mode shapes, suggesting that the damping effects of increased viscosity play a more significant role at higher frequencies. For instance, the frequency shift from Water + 10% Glycerol to Water + 50% Glycerol in Mode 7 is a substantial 410 kHz. Effect of Density: An increase in density (while keeping viscosity constant) tends to reduce the resonant frequencies of the beam. This can be attributed to the increased inertia imparted by the denser medium, which results in lower frequencies. Effect of Viscosity: An increase in viscosity (while keeping density approximately constant) also reduces the resonant frequencies. Higher viscosity leads to more damping, which results in the reduction of frequencies. The pronounced reduction in higher modes suggests a higher damping effect at those frequencies. Interplay between Density and Viscosity: By comparing the two sets of mixtures, it's evident that both density and viscosity play pivotal roles in determining the resonant frequencies. However, based on the provided data, viscosity seems to have a more pronounced effect, especially in higher mode shapes.The tables provide valuable insights into how the density and viscosity of different mediums influence the vibrational behavior of the 3rd Beam. Understanding these effects is crucial for applications where the beam operates in varying fluid environments. The inclusion of both density and viscosity in the analysis paints a comprehensive picture of the beam's response characteristics.

Added Mass

The amplitude displacement for each mode shape has been simulated. Fig. 4.30 (a) displays the peaks of each mode in relation to their respective frequencies via COMSOL Multiphysics. As previously demonstrated by the theoretical calculations, Fig. 4.30 (b) shows a good agreement between the observed displacement amplitude and the simulated values. This facilitates the simulation of beam sensitivity for a specified added mass.

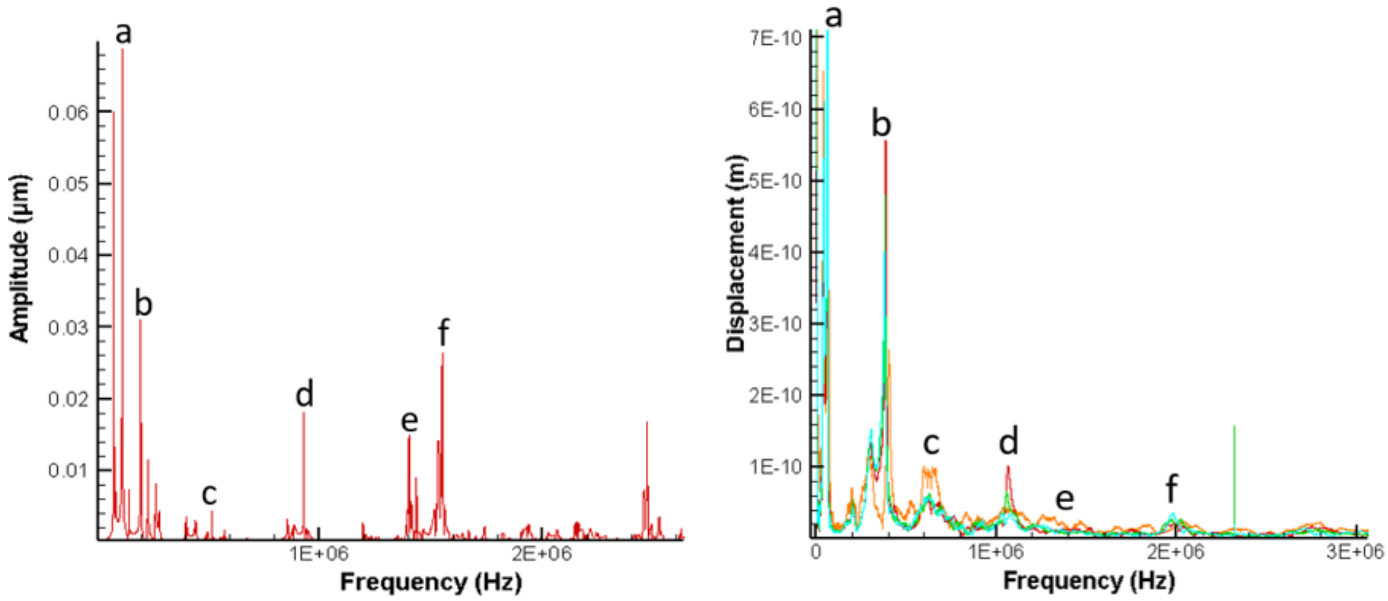

(a) Modeling Displacement

(b) Experimental Displacement

Figure 4.30: Comparison of modeled and experimental displacement amplitudes as a function of frequency.

Fig. 4.31 shows the amplitude response of beam 3 in both vacuum (black) and water (blue) mediums. The higher-order modes show a significant frequency shift, in which the sensitivity can then be calculated in a vacuum and water medium when mass is added.

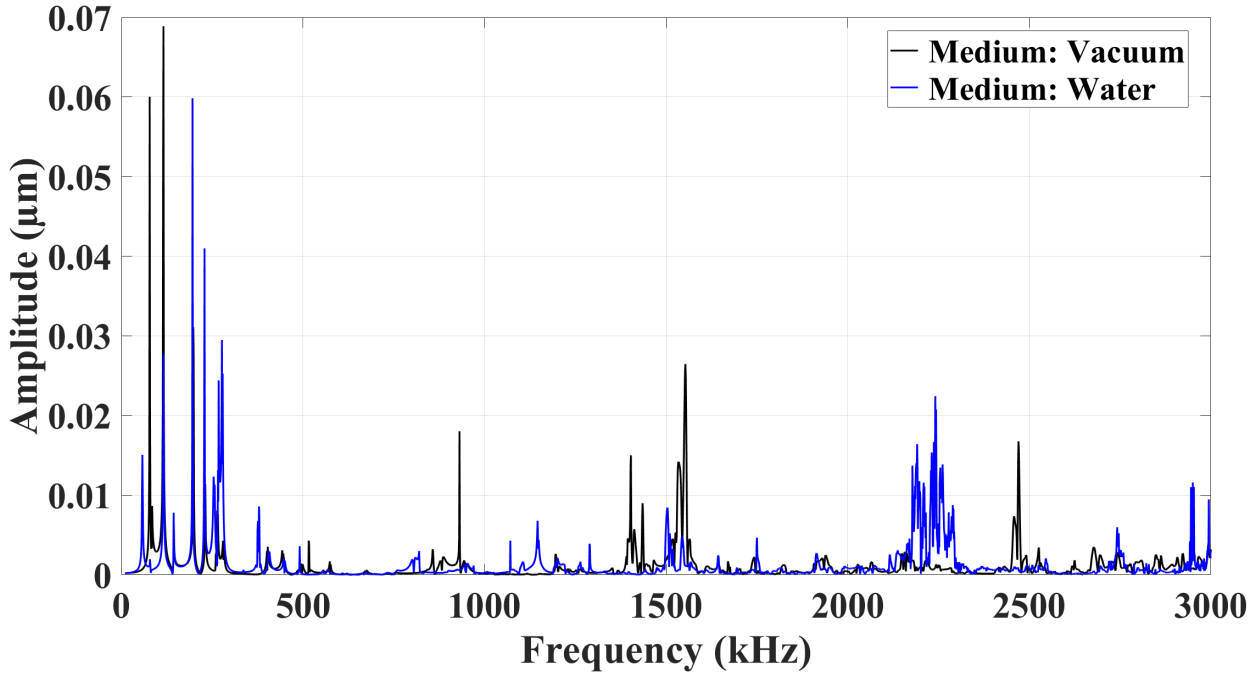

Figure 4.31: Amplitude response in water (blue), and in vacuum (black).

Fig. 4.32 presents the amplitude response of beam 3 in vacuum when 8 μg is added to the beams. The fundamental modes are observed at 78 kHz without frequency shift. On the other hand, the

higher order modes show a frequency shift from 1553 kHz to 1403 kHz for mode 5, and 2470 kHz to 2163 kHz for mode 6 when 8 μg is added, indicating a frequency shift of $\Delta f_{mode5} = 150\ kHz$ and $\Delta f_{mode6} = 307\ kHz$ and therefore sensitivity of 18.75 $kHz/\mu g$ and 38.375 $kHz/\mu g$ respectively.

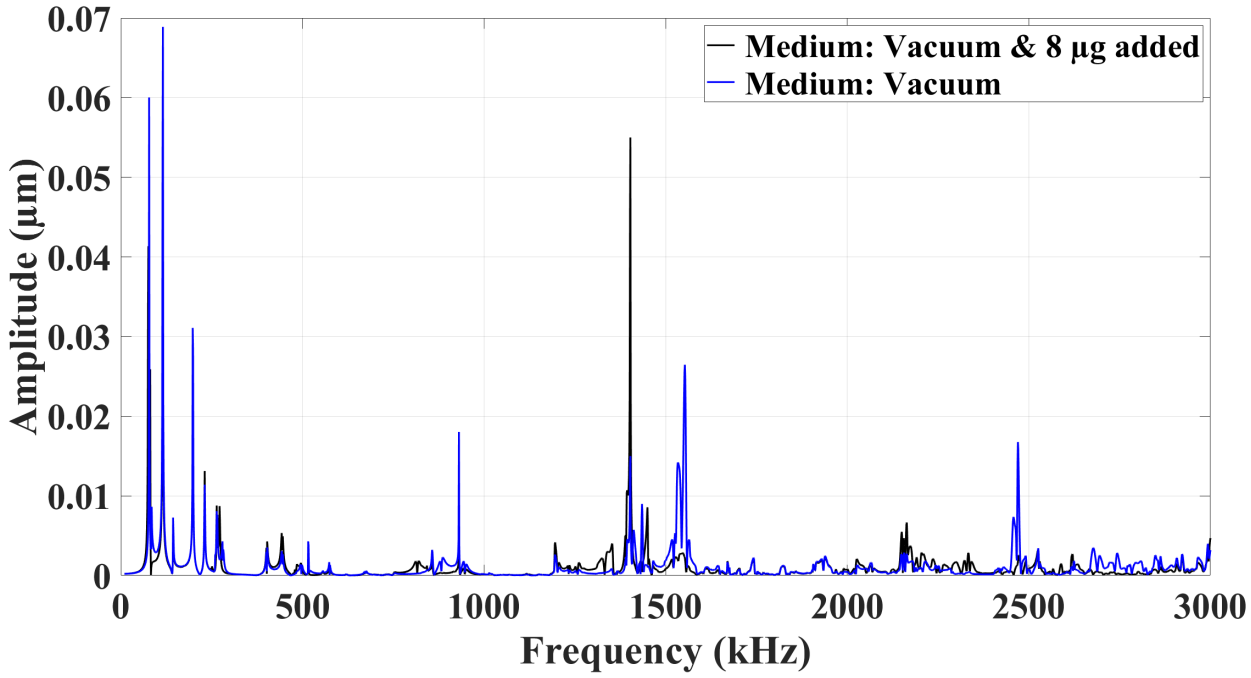

Figure 4.32: Amplitude response in vacuum (blue), and with 8 μg added to the beams (black).

A similar simulation is done in a water medium, the effect of the added mass in the water medium is presented in Fig. 4.33. A frequency shifting of $\Delta f_{mode5} = 107\ kHz$ and it is noted for the higher order modes when 8 μg is added to the beams. The proportionality of the frequency shift and the added mass led to a numerical conclusion about the sensitivity of the designed structure in water, which has a frequency sensitivity of 13.375 $kHz/\mu g$ and 8 $kHz/\mu g$ for modes 5 and 6 respectively.

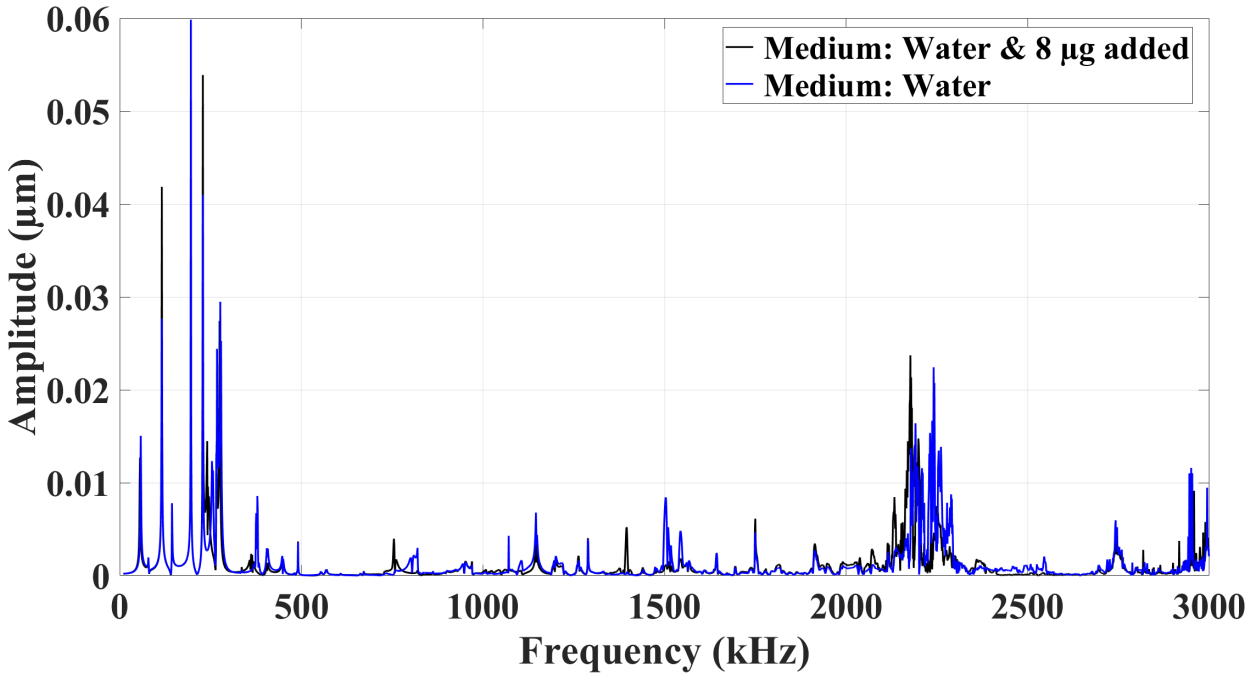

Figure 4.33: Amplitude response in water (blue), and with 8 μg added to the beams (black).

In concluding, the amplitude displacements for different mode shapes have been effectively simulated and assessed. The simulated peaks of each mode correspond well with their frequencies, affirming the theoretical calculations previously established. This alignment between observed and theoretical values demonstrates the model's accuracy in simulating beam sensitivity, particularly when additional mass is introduced to the system. The simulations highlight the distinct behaviors of the beam in vacuum and water mediums, especially under the influence of added mass. Fundamental modes maintain their frequency in a vacuum, while higher-order modes exhibit notable frequency shifts proportional to the added mass, enabling the calculation of beam sensitivity in both mediums. These findings not only confirm the model's predictive capability but also provide valuable insights into the beam's sensitivity characteristics, which are crucial for precise applications in various environmental conditions. The proportionality observed between frequency shifts and added mass in both mediums allows for a conclusive numerical determination of the structure's sensitivity, offering a robust framework for future designs and simulations in similar systems.

General Conclusion

In conclusion, our thesis has successfully established criteria for optimizing the dynamic sensitivity of measurement techniques. We have focused on micrometric concepts, particularly the dynamic and vibratory analysis of microbeams functioning as sensors with an integrated source. A solid correlation was found between analytical and numerical approaches, resulting in the adaptation of an experimental device. We have identified an effective method for the microresonator concept utilizing a laser ablation machine. Calibration processes addressed various biophysical and biochemical fluid properties, such as density and viscosity. The ongoing development of a micrometric prototyping device heralds the exploration of a multitude of application domains, marking a significant stride in micrometric technology. Building on this approach, our research focused on refining a micrometric concept that relies on analyzing dynamic and vibratory characteristic variations of microbeams, which are treated as sensors through the effect of applied loads. Initially, an analytical study, bolstered and validated through numerical methods, enabled us to substantiate our experimental design choices. This includes the resonance induction of the beams by integrating an electromechanical source (piezoelectric transducer, PZT) into the overall structure, ensuring optimal coupling. Consequently, this integration led to a continuity in dynamic displacement and a controlled vibratory amplification.

The overarching goal of the thesis was to harness the nuanced understanding of these dynamic and vibratory characteristics to develop a highly sensitive and precise lab-on-chip sensor. The sensor's design capitalizes on the microbeams' inherent properties, transforming minute mechanical disturbances into measurable electrical signals, thereby facilitating the detection of biomolecular interactions. Clearly, this has profound implications in the field of medical diagnostics, which requires such high precision and sensitivity to detect some physical content variations, which can be applied to early cancer detection. By methodically iterating through design, simulation, and experimental validation, the thesis aims to bridge the gap between theoretical mechanics and practical application in biomedical sensing technologies.

A strategic shift from traditional cantilever support structures to an integrated piezoelectric design facilitated an improved stress transfer, as confirmed through meticulous numerical and theoretical analysis using COMSOL Multi-physics. Despite the complexities that surfaced with microfabrication techniques like wet and dry etching in crafting the newly proposed model, the project pivoted to laser micro-machining, which proved less expensive and less complicated, allowing pre-

cise construction of the sensor structure. Upon assembling the sensor, the piezoelectric device was meticulously integrated, and the assembly's surface quality was examined using Scanning Electron Microscopy (SEM). A custom support was developed to maintain and electrically connect the piezoelectric device to the machinery used for its excitation. The functionality and sensitivity of the sensor were substantiated through impedance analysis to identify the resonance frequency of the piezoelectric element in various fluid mediums. Experimental validation was further extended to the full structure and the interaction with the piezoelectric device, even under immersion conditions. Through iterative prototyping and testing in different media, the optimal configuration for the sensor was established, leading to the selection of the third flexural mode for calibration purposes. The sensor was calibrated using mixtures that simulated serum characteristics, with a focus on varying density while maintaining constant viscosity, to assess sensitivity to changes in both properties.

On the technological way, the calibration of the microbeam cantilever sensor has yielded significant results that underscore its potential in precision measurements in biomedical applications. The sensitivity observed in mode 5 flexion bending on beam 3 of the device, with a viscosity sensitivity of 0.0037 Pas/kHz, indicates that the sensor is highly responsive to changes in the viscous properties of the fluid medium. This is particularly relevant in physiological fluid analysis where viscosity changes can be indicative of disease states or the presence of specific biomolecules. Furthermore, the density sensitivity of $0.01 g/cm/kHz$ suggests that the sensor can detect subtle changes in mass density, which could be crucial for applications like early disease detection where changes in fluid density could signal the presence of pathological conditions or the effect of therapeutic interventions.

The added mass sensitivity in water, quantified as 13.375 $kHz/\mu g$, demonstrates a remarkable ability of the sensor to detect minute mass changes. This sensitivity level is instrumental in applications requiring the detection of low-concentration biomarkers, which are often present in early stages of diseases such as cancer. The precision of mass change detection could therefore play a vital role in developing point-of-care diagnostics and real-time monitoring systems for various health conditions.

The cantilever microbeam sensor developed in this research exhibits exceptional sensitivity and specificity in the measurement of viscosity, density, and added mass in fluid mediums. These characteristics make it an innovative tool for the analysis of physiological fluids, providing critical insights into the underlying biomolecular interactions and changes within these fluids. The reoholgical qualities paves the way for the sensor's application in detecting and monitoring various medical conditions that manifest through alterations in the physical properties of body fluids. Moreover, the sensor's capability to detect minute mass changes holds great promise for advancing the fields of early disease diagnosis and therapeutic monitoring.

In this thesis, we present a comprehensive approach to enhance micro-cantilever sensor technology. We detail the application of standardized biochemical coatings to accurately estimate the mass adsorbed by the microbeams, refining the calibration of sensors for biomedical applications. Pioneering etching technologies are harnessed to meticulously refine the microbeam structures, reducing

their scale to substantially improve sensitivity—a vital attribute for precision-dependent applications. Furthermore, we delve into the integration of an autonomous microsystem capable of analyzing physiological fluids using microchambers or microcapillaries, which are instrumental for the precise and continuous control of biological environments. The culmination of this research is the scale-up of our technology to create lab-on-chip systems. These compact, integrated platforms are set to revolutionize biological and chemical analyses, offering speed and efficiency in a miniaturized form. Each of these technological strides is a testament to our commitment to advancing microfluidic technology, steering us towards a future where it becomes central to scientific and medical progress. As a culmination of this research, the microbeam cantilever sensor stands as a testament to the effectiveness of micro-vibration-based technologies in enhancing biomedical diagnostics. Future studies could focus on expanding the sensor's capabilities to detect a broader range of biomarkers, as well as integrating the sensor into a lab-on-chip platform for comprehensive point-of-care testing. The findings from this calibration phase are a crucial step towards the practical application of the sensor in clinical settings. Continued development and testing will be key to transitioning from the experimental phase to real-world applications, where the sensor's high sensitivity and precision can make a tangible difference in patient outcomes and healthcare delivery.

Abstract & Resume

Abstract:

In a world of continuous technological evolution, micro-electromechanical system (MEMS) sensors are becoming increasingly prominent in various fields such as biomedicine, the aerospace industry, and information and communication technologies. At the heart of this revolution, cantilever microbeams provide exceptional sensitivity, allowing the detection of minute physical variations. This thesis is dedicated to the design of a new cantilever microbeam sensor architecture aimed at optimizing their sensitivity and expanding their practical applications. The work undertaken focused on developing a theoretical model and experimental validation of a cantilever structure immersed in an incompressible Newtonian fluid, characterized by precise dimensions and an innovative design. The numerical part of the study allowed for testing the sensitivity of the proposed architecture against external loads, while the practical experiments involved the meticulous fabrication and assembly of the sensor components, including the integration of piezoelectric materials. Innovation does not stop here; the future envisions the incorporation of biochemical coatings for specific detection and the use of microfluidic techniques for real-time analysis, thereby marking a significant step forward in MEMS research and development. The quest for increased sensitivity in cantilever MEMS sensors has led us to the design and creation of an optimized structure, explored through this thesis work. The successful integration of the exponential architecture into the cantilever microbeam and the application of cutting-edge techniques in fabrication and numerical testing represent significant advancements in MEMS research. The results obtained open exciting prospects for the improvement and application of these sensors in complex environments. Future work, including the application of biochemical coatings and the development of microfluidic chambers, promises to further extend the scope of application and effectiveness of these sensitive devices.

In summary, this thesis contributes to the advancement of science and technology in MEMS sensors, proposing innovative solutions for current and future challenges in fields requiring precise detection and increased sensitivity. It thus lays the groundwork for future developments that will undoubtedly benefit many scientific disciplines and industrial applications.

Resume:

Dans un monde en constante évolution technologique, les capteurs micro électromécaniques (MEMS) prennent une place prépondérante dans divers domaines tels que la biomédecine, l'industrie aérospa-

tiale et les technologies de l'information et de la communication. Au cœur de cette révolution, les micro-poutres cantilever offrent une sensibilité exceptionnelle, permettant la détection de variations physiques infimes. Cette thèse se consacre à la conception d'une nouvelle architecture de capteurs à micro-poutres cantilever, visant à optimiser leur sensibilité et à étendre leurs applications pratiques. Le travail entrepris s'est focalisé sur l'élaboration d'un modèle théorique et la validation expérimentale d'une structure cantilever plongée dans un fluide newtonien incompressible, caractérisée par des dimensions précises et une conception innovante. La partie numérique de l'étude a permis de tester la sensibilité de l'architecture proposée face à des charges externes, tandis que les expériences pratiques ont impliqué la fabrication et l'assemblage minutieux des composants du capteur, y compris l'intégration de matériaux piézoélectriques. L'innovation ne s'arrête pas là ; l'avenir envisage l'incorporation de revêtements biochimiques pour la détection spécifique et l'utilisation de techniques microfluidiques pour une analyse en temps réel, marquant ainsi un pas en avant significatif dans la recherche et le développement des MEMS. La quête de sensibilité accrue dans les capteurs MEMS cantilever nous a menés à la conception et à l'élaboration d'une structure optimisée, explorée à travers ce travail de thèse. L'intégration réussie de l'architecture exponentielle dans la micro-poutre cantilever et l'application de techniques de pointe en fabrication et en tests numériques représentent des avancées significatives dans la recherche en MEMS. Les résultats obtenus ouvrent des perspectives fascinantes pour l'amélioration et l'application de ces capteurs dans des environnements complexes. Les futurs travaux, incluant l'application de revêtements biochimiques et le développement de chambres microfluidiques, promettent d'étendre encore davantage le champ d'application et d'efficacité de ces dispositifs sensibles.

En résumé, cette thèse contribue à l'avancement de la science et de la technologie des capteurs MEMS, en proposant des solutions innovantes pour les défis actuels et futurs dans les domaines nécessitant une détection précise et une sensibilité accrue. Elle pose ainsi les bases pour les développements futurs qui bénéficieront sans aucun doute à de nombreuses disciplines scientifiques et applications industrielles.

Publications

Elias, Victory, et al. "An autonomous acoustic collar to quantify the severity of COVID-19 effects by analyzing the vibratory components of vocal and respiratory systems." 2021 IEEE International Conference on Design & Test of Integrated Micro & Nano-Systems (DTS). IEEE, 2021. The conference was held over the period 07-10 June 2021. The proceedings were subsequently added to IEEE Xplore on 02 August 2021. The document's Digital Object Identifier (DOI) is 10.1109/DTS52014.2021.9498235, and it was published by the Institute of Electrical and Electronics Engineers (IEEE).

Elias, Victory, et al. "Investigation of the Eigen Frequency of a Cantilever Microbeam Immersed in a Fluid Under the Piezoelectric Effect." (2021). 254 (7), pp.31-37. ffhal-03564209

Elias, Victory, A. Rabih, and Georges Nassar. "Early Breast Lump Detection Using the Intelligent Bra" IN-bra"." Acta Scientific Women's Health 4.8 (2022): 43-49. DOI : 10.31080/ASWH.2022.04.0412